5-2018

Fluid Phase Separation via Nanochannel Array

John Lee
University of Arkansas, Fayetteville

Fluid Phase Separation via Nanochannel Array

A dissertation submitted in partial fulfillment
of the requirements for the degree of
Doctor of Philosophy in Engineering

by

John Bishop Lee
Oklahoma Christian University
Bachelor of Science in Mechanical Engineering, 2008

May 2018
University of Arkansas

This dissertation is approved for recommendation to the Graduate Council.

_____
Po-Hao Adam Huang, PhD.
Dissertation Director

_____   _____
Ingrid Fritsch, PhD.   Larry A. Roe, PhD.
Committee Member   Committee Member

_____   _____
Uchechukwu C. Wejinya, PhD.   Jeff Wolchok, PhD.
Committee Member   Committee Member

ABSTRACT

Microelectromechanical systems (MEMS) and nanoelectromechanical systems (NEMS) generate ideas and techniques for creating new devices at the micro/nano scale. This dissertation study designed a gas generator system utilizing nanochannels for phase separation that is useful for micro-pneumatic actuators, micro-valves, and micro-pumps. The new gas generator has the potential to be an integral part of a propulsion system for small-scale satellites. Nano/picosatellites have limited orientation capability partly due to the current limitations of microthruster devices. Development of a self-contained micro propulsion system enables dynamic orbital maneuvering of pico- and nano-class satellites.

Additionally, the new gas generator utilizes a high efficiency, green propellant that is less harmful to the environment. This dissertation study tested aqueous antifreeze solutions to verify vapor pressures and establish previously unknown kinematic viscosities. A viscometer, developed expressly for this study, measured kinematic viscosity values between 1E-2 and 1E-4 m^2/s for water solutions mixed with propylene glycol, ethylene glycol, methanol, and glycerol.

CubeSats, 10-centimeter cube satellites, are volume limited, and high strain expansion of water during crystallization could destroy the structure. Validation of the freezing point depression and measurement of previously unknown percent expansion with increasing concentration are valuable for setting safe design specifications. A 7.5 %w/w propylene glycol-water solution reduces the overall expansion by 2% while 20 %w/w PG reduces the expansion 4%.

Potassium hydroxide etched silicon micro/nanochannels regulated vaporization of aqueous propylene glycol to a vacuum environment. Sequential still images captured with a Basler Scout camera were used to measure mass flow rates, representative of Washburn capillary flow. Magnitude of single channel flow rates ranged from 1E-10 mol/s to 1E-8 mol/s for 600nm channels

up to 12μm channels, respectively. Although the flow rate increased using nanochannel arrays, it was 35% slower than expected based on single nanochannel measurements.

A system utilizing nanochannel arrays for fluid phase separation, with propylene glycol as the propellant, is feasible in a low-cost, green, non-toxic, and non-pressurized CubeSat propulsion system. Depressing the freezing point of water by adding antifreeze creates a wider liquid working range, decreases power requirements, but also maintains appreciable flow rates for thrust generation (micro-millinewton). Successful nanofluidic research on an aqueous antifreeze solution is foundational for future propulsion system research and pushes CubeSats in the right direction.

ACKNOWLEDGMENTS

DEDICATION

This dissertation is dedicated to my beautiful wife Nicole, wonderful daughter Zoey, and amazing son Zane who have brought so much joy into my life. Words cannot begin to express what these three people mean to me. My family is the reason why I kept pushing forward against what seemed like an insurmountable amount of work. They brighten my day in the darkest nights of research. Every setback and hurdle in life is washed away in their unconditional love and support. I owe more to my family than anyone else combined. And while they may have lengthened my time for completion of this dissertation, they have made these years immeasurably more fulfilling.

PUBLICATIONS

Lee, John and Huang, Adam, "A "Green Cold-Gas" Propulsion System for Cubesats." 31st Annual AIAA/USU Conference on Small Satellites, Logan, UT, Aug. 8, 2017.

Lee, John and Huang, Adam, "Aqueous Propylene Glycol Solution Characterization for Cold Gas Thruster Development." Arkansas Academy of Science 100th Annual Meeting, Fayetteville, AR, Apr. 1-2, 2016.

Lee, John B., Kempf, Brandon W., and Huang, Adam, "Time-of-Flight Based Sonic Speed Measurements for Cold Gas Thruster Development." Arkansas Academy of Science 100th Annual Meeting, Fayetteville, AR, Apr. 1-2, 2016.

Lee, John and Huang, Adam, "Water Based Propellant for Cold Gas Thruster." 2015 International Mechanical Engineering Congress and Exposition, IMECE2015-52776, Houston, TX, Nov. 13-19, 2015.

Lee, John and Huang, Adam, "Fatigue analysis of FDM materials." 2013 Rapid Prototyping Journal, Vol. 19 Iss: 4, pp.291 – 299

Lee, John and Huang, Adam, "Propellant Vaporization via Nanochannel Array for Space Application." 2012 International Mechanical Engineering Congress and Exposition, IMECE2012-93685, Houston, TX, Nov. 9-15, 2012.

Lee, John, "Suitability of R-134a for use in Micro-Thrusters." Poster presented at Abstract to Contract, Fayetteville, AR March 2011.

Lee, John, McMullen, Matt, and Huang, Adam, "Thrust Measurements of Different Gases in a Micro Nozzle." 2010 International Mechanical Engineering Congress and Exposition, IMECE2010-40009, Vancouver, BC, Nov. 12-18, 2010.

Lee, John and Huang, Adam, "Microthruster Knife Edge Thrust Stand." 2009 International Mechanical Engineering Congress and Exposition, IMECE2009-11854, Lake Buena Vista, FL, Nov. 13-19, 2009.

Lee, John and Huang, Adam, "Characteristics of Two Phase Fluids as Microthruster Propellant." 2009 International Mechanical Engineering Congress and Exposition, IMECE2009-11853, Lake Buena Vista, FL, Nov. 13-19, 2009.

Lee, John, "Microthruster Knife Edge Thrust Stand." Poster presented at AAME Graduate Research Symposium, Fayetteville, AR, March 2009.

TABLE OF CONTENTS

LIST OF FIGURES

1   INTRODUCTION

In 2013, Actor/comedian Bill Murray stated, "My iPhone has 2 million times the storage of the 1969 Apollo 11 spacecraft computer. They went to the moon. I throw birds at pig houses." Mr. Murray's observation makes light of how frivolously modern technology is used, but it also subtly points out how far technology has advanced over the last 50 years. The question then becomes, if landing on the moon was possible with the limitations to technology in 1969, what engineering feats are now possible with our current rapidly evolving propulsion and maneuverability nanotechnology capabilities?

Advances in technology have allowed for new ideas in the space exploration field. Ideas previously impossible or unachievable are now possible. The Hubble telescope, a modern engineering achievement launched into space in 1990, was approximately the size of a school bus (diameter of 4.2 meters and a length of 13.2 meters) with a mass of 11,110 kilograms (kg) ("Hubble essentials," n.d.). A replacement to the Hubble telescope, the James Webb Space Telescope (JWST), launches in 2019. At a length of 22 meters and width of 12 meters the JWST is considerably larger than the Hubble, and has a size comparable to a Boeing 737 airplane ("The James Webb Space Telescope," n.d.). However, the JWST has a mass of just 6200 kilograms, which is slightly over half the mass of the Hubble, but it also has a 6.5-meter diameter mirror, which is significantly larger than the 2.4-meter mirror on the Hubble. The difference in mirror size gives the JWST a collecting area of around 7 times larger than that of the Hubble while also allowing the JWST to view a larger wavelength spectrum, 0.6 to 28 micrometers, than what is possible with the Hubble telescope, 0.1 to 2.5 micrometers ("The James Webb Space Telescope," n.d.). Therefore, the JWST is larger yet lighter and will be able to observe developing stars that emit in the infrared spectrum, which previously was impossible.

In conjunction with the transition from the Hubble telescope to the JWST, and of particular importance to this research, is the development of technology for small satellites. A main advantage for the development of small satellites is minimizing the cost of the satellite, which is a two-part process. First, the smaller size of the satellite allows for a streamlined easier design process, cheaper fabrication, and even mass production. Multiple companies provide various base models to build small satellites from kits as well as provide systems for easy integration with the standardized satellites ("Pumpkin Price List," n.d.; "Spacecraft power management," n.d.; "Space Electronics," n.d.; "Nano-satellite systems," n.d.). The reduced satellite size means a lower weight, which in turn means smaller and cheaper launch vehicles. Decreased satellite development cost allows a wider global population to pursue space exploration.

Despite all the advantages, small satellites also have several limitations and challenges. Currently these satellites have a limited orientation capability and cannot perform orbital maneuvers. For example, a satellite could potentially use electro-magnetically charged coils in conjunction with earth's magnetic field to maintain a desired orientation. However, current methods of orientation are extremely slow to damp out oscillations due to low power (minutes) and cannot execute out of orbit maneuvers, which is particularly problematic for small satellites. Satellites need dynamic movement when, where, and how the mission objectives dictate.

The biggest hurdle, primarily because of the associated cost, with small satellites is simply delivery to space. Growing global interest in small satellite technology results in declining launch costs, but they remain in the tens to hundreds of thousands of dollars. Traditionally, space exploration runs through NASA and other government agencies, but recently public companies like SpaceX and numerous start-up companies (Rocket Lab, bSpace, and Spaceflight) enable more

satellites the ability to reach space. With all small satellite launches, the main method of delivery to space is through a ride-share environment.

In a ride-share, satellites launch with a collection of other small satellites, or they will "piggy-back" on with a primary payload. The designated "secondary payload" status results in restrictions not normally encountered on a mission with a primary payload. Restrictions on small satellites can even limit use of technology with known space heritage, especially when involving propulsion systems. Systems readily used on macro scale satellites like cold-gas thrusters and liquid/solid rockets become potential threats to primary and other secondary payloads.

Without an on-board propulsion system, secondary payloads are on an orbit dictated by the primary payload after deployment from the launch vehicle. The small satellite cannot change its orbital elements on command for the duration of its mission limiting its use for science missions. Thus, development of a micro propulsion system capable of full-authority attitude control and orbital maneuver would be extremely beneficial for the nano- and pico-satellite community.

2   BACKGROUND

2.1   SMALL SATELLITES

Most popular satellites are in the hundreds to thousands of kilograms: Hubble – 11,110kg, Voyager 815kg, Cassini-Huygens – 5600kg, Spitzer – 950kg, and MILSTAR – 4500kg. However, advancements in technology decreased the volume and mass necessary to conduct scientific missions. Now, modern satellites range in size from hundreds of grams to thousands of kilograms, Figure 1. Small satellites are technically defined as a satellite whose mass is between 100kg and 500kg ("Satellite classification," n.d.). For this research, satellites with a mass of less than 100kg are small satellites. Under the umbrella of small satellites are the following subcategories:

- Micro-satellite: 10kg to 100kg
- Nano-satellite: 1kg to 10kg
- Pico-satellite: 0.1kg to 1kg

Figure 1: Well-known satellites are typically on the micro/macroscale, but advances in technology have decreased the form factor necessary to conduct high impact space research. Advances in technology, particularly micro/nanotechnology, have further decreased the size of satellites to a handheld size. (Huang, Wilson, & Chan, 2014)

4

In addition to a decreased form factor, the smaller satellites are able to carry out missions that would be difficult for a larger satellite. These advantages include using formations to gather data from multiple points and in-orbit inspection of larger satellites. By flying in a synchronized formation, it becomes possible for multiple small satellites to record data from various locations simultaneously, whereas a larger satellite is limited to a single data point location. The cheaper cost and small-scale design enables university level research allowing for even more innovation in the field of space exploration and research. As of this writing, over thirty ("CubeSat launch initiative," 2012) university level programs exist in the United States alone, and even more exist in countries around the globe. Undergraduate and graduate research conducted for small satellites spans various scientific disciplines including aerospace ("AAU CubeSat," 2003; "XSAS microgravity project," 2010; Lokcu, and Ash, 2011) and biology ("GeneSat-1", 2007). Government programs ("To the stars: NASA selects small spacecraft technology demonstration missions," 2012; "NRL launches nano-satellite experimental platforms," 2010) and even the private sector ("Boeing successfully completes CubeSat mission to advance nano-satellite technology," 2007) developed small satellites for research with lower financial commitment and the potential for a high research return on investment. Nano/picosatellites have even successfully launched into low earth orbit, proving their viability for space research ("CubeSat ELaNa III launch on NPP mission," 2011; "Proving high-tech rocket systems, vega soars to space," 2012; "ULA atlas V finally launches with NROL-36," 2012) .

2.1.1 CubeSatellites

CubeSatellites, or CubeSats, are a specific classification of nano/picosatellites. The idea originated in 1999 between Jordi-Puig Suari (California Polytechnic Institute) and Bob Twiggs (Stanford University) to afford graduate students the ability to design, build, and test a spacecraft in space. Over time, the original idea developed as a standard for future satellites establishing a form factor of a 10cm wide by 10cm long by 10cm tall cube weighing less than or equal to 1kg, also known as 1U (one unit). Traditional CubeSats are scalable, albeit primarily in one direction to form 0.5U, 2U, and 3U satellites. All three forms have a 10cm by 10cm cross section with a varying length based on the 10cm unit. However, recent satellites have pushed the restrictions and uniquely stacked the 1U form to created 6U (2 by 1 by 3), 12U (2 by 2 by 3), and 27U (3 by 3 by 3) satellites.
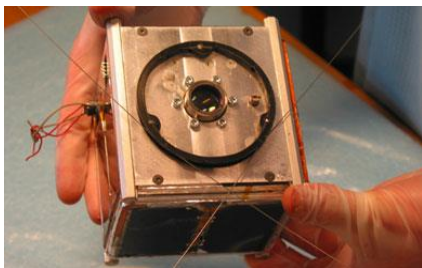
University of Aalborg (Denmark)

University of Tokyo

Stanford
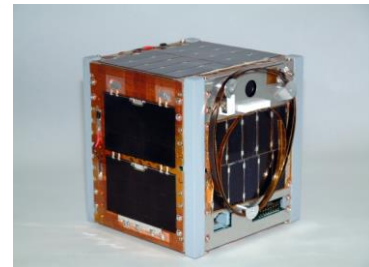
Cal-Poly San Luis Obispo
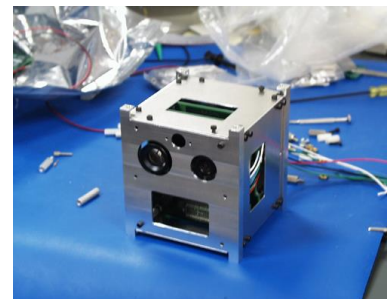
University of Toronto

Figure 2: CubeSats were developed for Universities with the aim of enabling doctorate, masters, or undergraduate level research. Universities from around the world have developed CubeSat programs. In the center is one of the CubeSat originators, Bob Twiggs. (Pappalardo, 2006; Nugent et al., 2008; Miller, 2001; Funase et al., 2005; Wells et al., 2002)

Initially developed primarily for academia, CubeSats enable student involvement in design, manufacture, and testing of a system used in lower earth orbit. In fact, universities across the globe developed CubeSat programs, operated with teams comprised of both undergraduate and graduate students, see Figure 2. However, since 2014, the commercial and amateur sectors account for most CubeSat launches.

With advancements in technology, CubeSats have the capability of much larger satellites at a fraction of the cost. While companies (Pumpkin, Clyde Space, Interorbital Systems, NanoRacks, etc.) offer CubeSat kits starting at around $5000, designing and building in-house further decreases costs. A fully assembled CubeSat with equipment runs in the tens of thousands of dollars, which is a fraction of the costs of typical satellites. However, custom CubeSats also can cost millions of dollars if the budget allows.

The low cost of CubeSats makes them useful for a wide variety of research. Initially the main function of CubeSats was limited to miniaturized earth observation missions or amateur radio satellites. Over time, the CubeSat form factor earned a place in other missions. High-risk missions with unproven or questionable theory are viable for CubeSat missions whereas larger satellites prove too costly for potential failure and loss. Biological research also utilizes CubeSats to study Escherichia coli bacteria in space (GeneSat 1), radiation effects on living organisms (BioSentinal), effects of space on yeast (PharmaSat), and microbe survival and activity (O Oreos). These low-cost experiments on a dedicated autonomous satellite obtain essential data, demonstrate the effectiveness of evolving technology, and open the door to a new world of innovation.

The University of Arkansas built the state's first satellite, ARKSAT-1, shown in Figure 3. The satellite's primary objective is to obtain LEO-to-Earth atmospheric composition measurements using an on-board xenon flash bulb. Secondary, the satellite will improve control of de-orbit rate using a solid-state gas inflation balloon, developed by a fellow University of Arkansas graduate student.
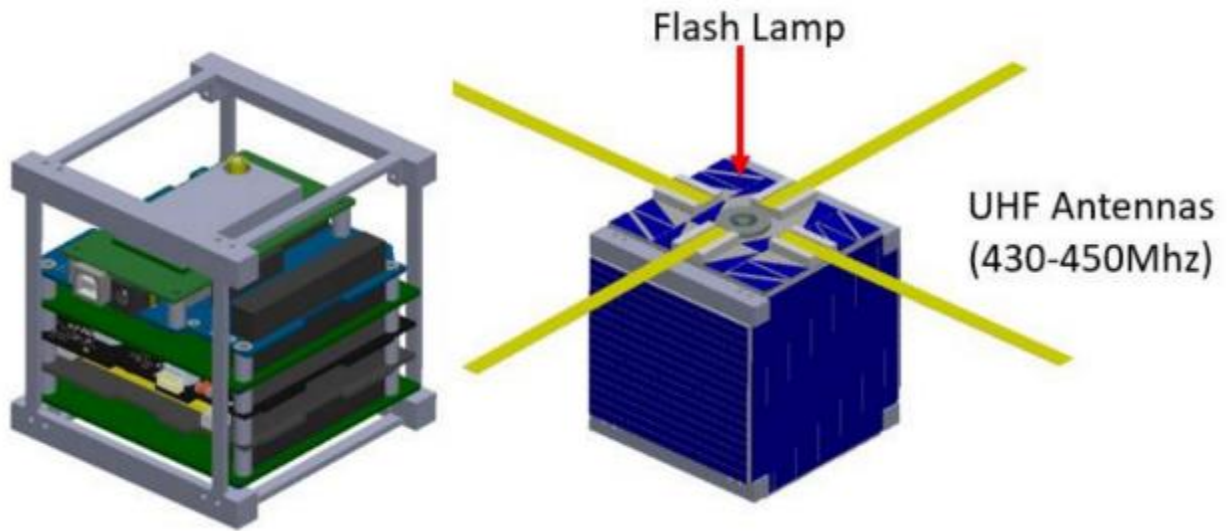
Figure 3: ARKSAT-1 is a 1U CubeSat that will demonstrate a solid-state gas inflation de-orbiter.

Shown in Figure 4, the University of Arkansas' second satellite is ARKSAT-2, which utilizes enhanced propulsion and maneuverability capabilities made possible, in part, through this dissertation research. ARKSAT-2 incorporates technology established by ARKSAT-1, but its primary objective is to demonstrate an agile, low-cost, non-toxic, and non-pressurized micro-propulsion system. The propulsion system enables control and manipulation of the satellite, not achievable with previous technology.
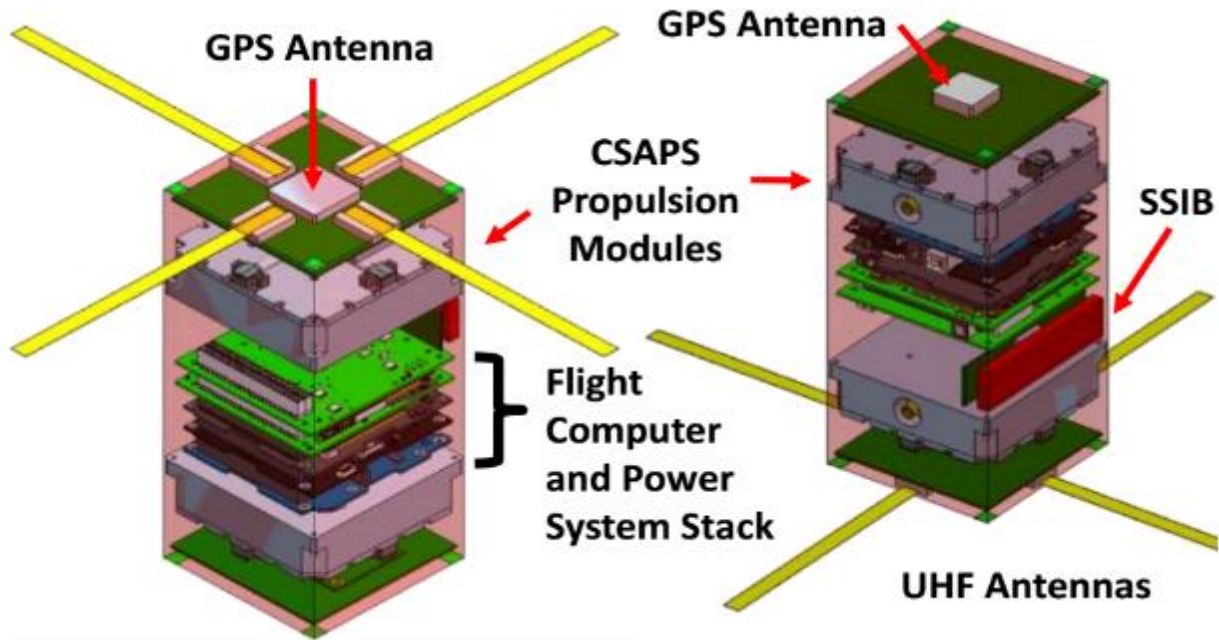
Figure 4: ARKSAT-2 is a 2U CubeSat that will demonstrate an innovative propulsion system.

Figure 5 shows the propulsion system schematic for ARKSAT-2. The general idea is for a liquid propellant to be stored at atmospheric temperature and pressure and contained by a MEMS-2 phase separator, which is the focus of this research. The system has the benefit of minimal moving parts and relatively inexpensive fabrication costs. Relying only on vapor pressure driven flow to vacuum, mass transfer is relatively small. However, small mass flow rates can have a big effect on CubeSats in the low atmosphere of space.
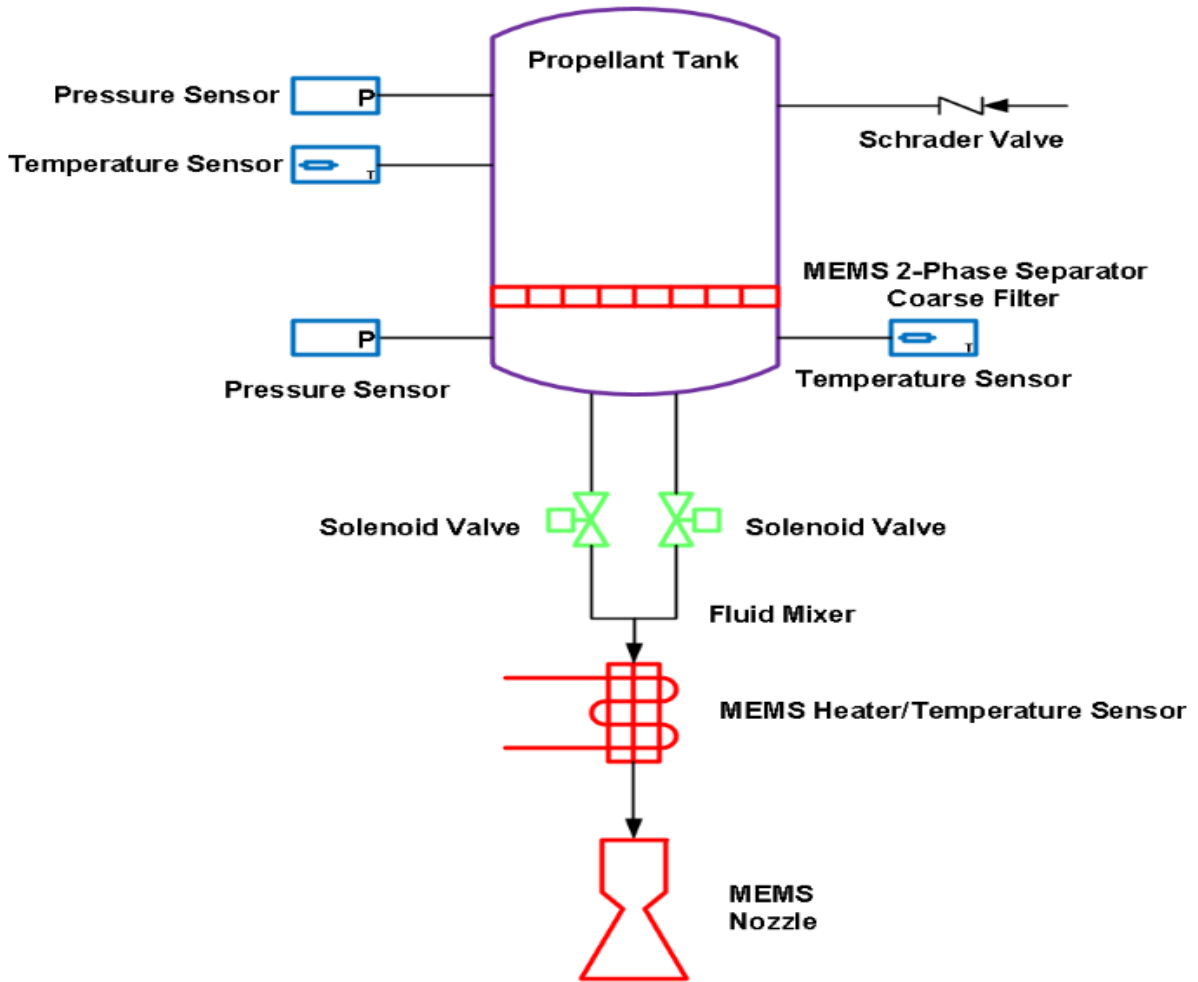
Figure 5: A propulsion system designed to be tested on ARKSAT-2 primarily utilizes equipment with space heritage. A novel liquid-vapor separator will be tested as an integral part in the non-toxic, biocompatible, and non-pressurized propulsion system.

Working in tandem, ARKSAT-1 and ARKSAT-2 will provide a satellite tracking and following system, which is the first step towards creating arrays and clusters of satellites for data collection. A macro scale satellite collects single spatial data points throughout its orbit. An array of CubeSatellites enables the collection of a more spatially complete and unique set of data, an enhanced capability that was never possible with larger satellites. Formation flying of CubeSats that communicate and track each other demonstrates application of new ideas and advances technology, see Figure 6.
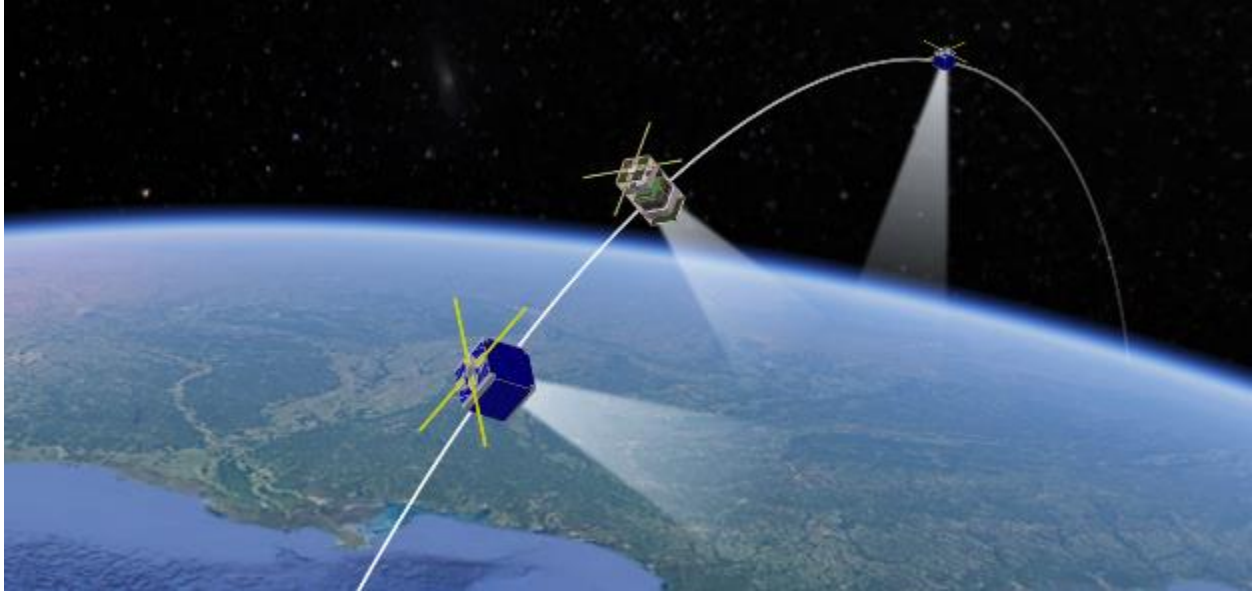
Figure 6: ARKSAT-1 and ARKSAT-2 will demonstrate formation flying with a novel, "green," cold-gas propulsion system.

2.1.2   Propulsion Systems

A variety of propulsion systems for attitude control and orbital maneuvers are utilized for micro/macro satellites. Scaling these propulsion systems down to the nano/picoscale is not a straightforward process due to power limitations and chemistry regulations. Thus, current orientation control of CubeSats is primarily accomplished through utilization of magnetorquers. Magnetorquers use the earth's magnetic field to alter the orientation of the satellite and are very slow (minutes). Dynamic movement of CubeSats is desirable and, at times, necessary to conduct science missions in space. Thus, propulsion for nano/picosatellites is an area of tremendous interest and focused research. A few of the more commonly explored methods of propulsion are cold gas, monopropellant, bipropellant, resistojet, and ion engine (Janson, Helvajian, Hansen, & Lodmell, 1999). Recent research has particularly focused on electric propulsion methods including Hall-Effect Thrusters, Field Emission Electric Propulsion, and Pulsed Plasma Thruster, (Polzin, 2014; Mason, Jankovsky, & Manzella, 2001; Szabo et al., 2012; Burton,. & Turchi, 1998; Guarducci, Coletti, & Gabriel, 2011).

Of particular interest to this research for CubeSats are cold-gas thruster systems because of their low cost and ease of use. Cold-gas microthrusters offer the ability for dynamic satellite orientation and potentially even out-of-plane maneuvers. Although many cold gas thrusters have been manufactured (Mueller, & Ziemer, 2008), there are currently no CubeSats in space utilizing the capability offered by microthrusters to deliver rapid movement with reasonable precision. So, this research focuses on development of a subsystem for a "cold-gas" CubeSat propulsion system.

CubeSat orbital maneuvers possible with a cold-gas propulsion system are illustrated in Figure 7. Attitude control and orientation of CubeSats require millinewton thrust levels while in-plane orbital maneuvers necessitate Newton level thrust. Out-of-plane orbital maneuvers require the same thrust levels as in-plane, but demand a higher Delta-V budget. Macro/microscale satellites require significantly more thrust to complete similar maneuvers, but a benefit of CubeSats is increased agility and mobility at a fraction of the thrust required for larger satellites.

Attitude Control
- 10's m/s total ΔV
- mN thrust levels
- μN impulse bits

Orbital Maneuvers Thrusters (OMT)

In-Plane
- 100's m/s total ΔV
- 0.1-1N thrust levels

Out-of-Plane
- Order of 1km/s total ΔV
- 0.1-1N thrust levels
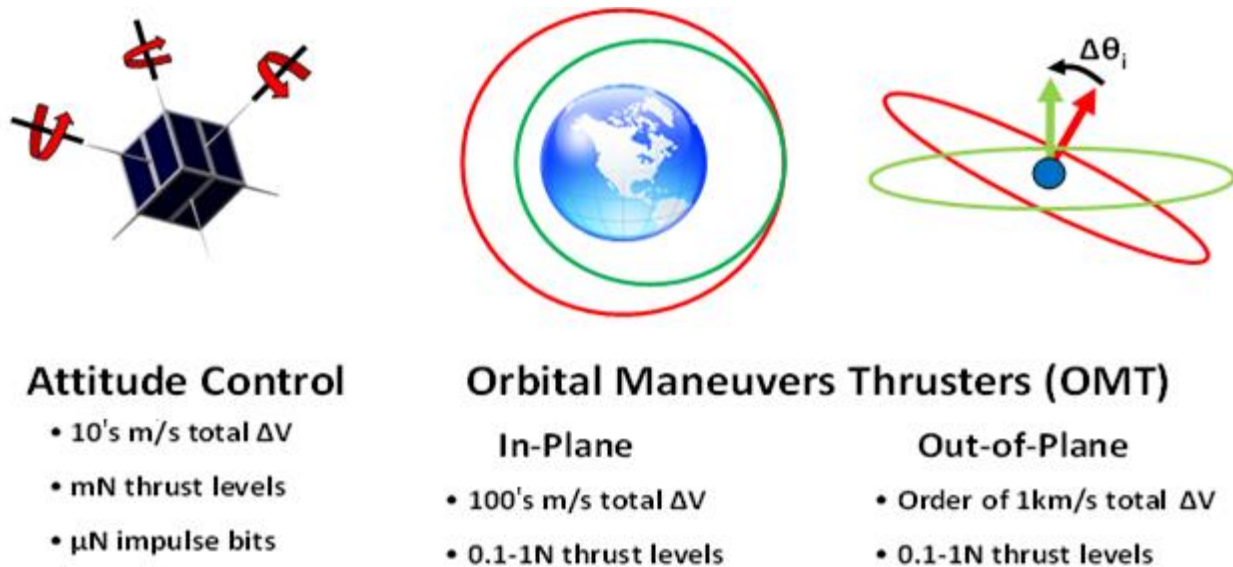
Figure 7: Cubesats have limited orientation control, but there exists a desire for more freedom of movement. Orbital maneuvers of interest are attitude control, in-plane maneuvers, and out-of-plane maneuvers. Thrust requirements vary based on the difficulty of the maneuver for CubeSats (Lee, & Huang, 2017)

When designing a cold-gas propulsion system, one of the first steps is to consider the Delta-V (ΔV) needed to conduct an orbital maneuver dictated by mission objectives, Figure 7. Delta-V, in space flight dynamics, is a measure of the velocity impulse necessary for launch, landing, or an orbital maneuver (Chobotov V, 2002). For these orbital maneuvers, one of the most important equations is the ideal rocket equation, or the Tsiolkovsky rocket equation, which states (Ward TA., 2010):

$$\Delta V = -\frac{F}{\dot{m}g_0} g_0 ln\left(\frac{m_f}{m_i}\right) \qquad \text{Equation 1}$$

For cold-gas propulsion systems, Equation 1 describes the effect of thrust on the motion of the small satellite through a conservation of momentum. The change in velocity (ΔV) of the satellite is related to the thrust generated (F), mass flow rate of the fluid at the exit ($\dot{m}$), and the final to initial mass ratio of the spacecraft while (g_0) is gravitational acceleration at the earth's surface ($9.8m/s^2$). Grouping terms from Equation 1 yields the following two equations:

$$I_{sp} = \frac{F}{\dot{m}g_0} \qquad \text{Equation 2}$$

$$efficiency = -ln\left(\frac{m_f}{m_i}\right) \qquad \text{Equation 3}$$

Both Equation 2 and Equation 3 are a measure of the efficiency of a rocket. Equation 3 relates the mass ratio, which describes how much heavier the spacecraft is with propellant than without. For an entire ΔV budget, the mass ratio relates the satellite's dry mass (satellite plus components) to the wet mass (satellite plus components and propellant). Orbital maneuvers require a ΔV which is relative to the mass before (m_i) and after the mass (m_f) after thrust. Equation 2 describes what is commonly known as specific impulse (I_{sp}) which is particularly interesting for thruster performance.

Specific impulse has units of seconds^{-1}, normalized versus standard gravity on earth (~9.81 m/s^2). Specific impulse is an indicator of the propellant flow rate necessary to generate thrust. For example, the higher the I_{sp}, the lower the mass flow rate necessary to maintain a given thrust. This specific impulse indicator is particularly beneficial when dealing with a limited volume of propellant, a common problem for small satellites. Table 1 shows a few common thruster types and expected specific impulse values. By comparison, cold-gas thrusters generally have a lower specific impulse than other types of microthrusters, but their ease of use and lower cost often make them an ideal choice for CubeSat propulsion.

Table 1: Common microthruster types and corresponding specific impulse ranges (Janson, Helvajian, Hansen, & Lodmell, 1999)

Thruster Type	Class	Specific Impulse	Typical Propellants
Cold Gas	Chemical	40 - 80s	Freon, N_2, Ar
Monopropellant	Chemical	180 - 220s	N_2H_4, H_2O_2
Bipropellant	Chemical	300 - 450s	$N_2H_4 + N_2O_4$, H_2, O_2
Solid	Chemical	100 - 290s	Nitrocellulose + Nitroglycerine
Resistojet	Electric	150 - 330s	H_2O, NH_3, N_2H_4
Arcjet	Electric	400 - 900s	NH_3, N_2H_4
Hall Effect	Electric	1400 - 2000s	Xe, Kr
Ion Engine	Electric	1600 - 5000s	Xe, Kr

For cold-gas vapor, specific impulse is proportional to the square root of the speed of sound and the inverse of square root of molecular weight. Table 2 shows that, in general, the specific impulse corresponds to the molecular weight of the propellant. A lightweight propellant like

hydrogen (2 kg/kmol) has a relatively high I_{sp} (296 seconds) while a much heavier propellant, Freon 12 (121 kg/kmol) has an I_{sp} of 46 seconds, or roughly 16% that of hydrogen. At standard atmospheric conditions, speed of sound is a function of the square root of temperature while molecular weight has a strong relationship with vapor pressure. Another factor that can influence specific impulse is the specific heat ratio. A common assumption is that the specific heat ratio remains constant during fluctuations in pressure and temperature, but this is not necessarily the case. The specific heat ratio can vary slightly with temperature resulting in significant changes to specific impulse.

Table 2: Common cold-gas propellants, molecular weight, density and specific impulse (Micci, & Ketsdever, 2000)

Propellant	Molecular Weight (kg/mol)	Density (gm/cm3)	Specific Impulse (s)	
Hydrogen	2.0	.002	296	272
Helium	4.0	.04	179	165
Neon	20.4	.19	82	75
Nitrogen	28	.28	80	73
Argon	39.9	.44	57	52
Krypton	83.8	1.08	39	37
Xenon	131.3	2.74	31	28
Freon 12	121	-	46	37
Freon 14	88	.96	55	45
Methane	16	.19	114	105
Ammonia	17	Liquid	105	96
Nitrous Oxide	44	-	67	61
Carbon Dioxide	44	Liquid	67	61

A few of the more commonly used cold-gas propellants are nitrogen, hydrogen, oxygen, argon, and Freon (Janson et al., 1999). In general, these propellants have a very useful specific impulse and are readily used in a space environment. However, to be stored in liquid form, these propellants require very heavy, pressurized and temperature controlled tanks (Platt, 2002). On a small satellite, volume and mass are at a premium, so minimization of propellant subsystem mass results in huge dividends for the overall system's capability and usefulness. Additionally, the pressurization necessary to store common cold-gas propellants is problematic for when considering launch restrictions.

2.1.3   "Poly Picosatellite Orbital Deployer" and Restrictions

Due to high launch costs, two "rideshare" methods developed: 1) grouping small satellites into one payload launched with a single rocket and 2) "piggybacking" onto a primary payload. As a secondary payload, it becomes feasible for universities and smaller research companies to launch a single satellite into orbit. Standardization of CubeSats to the 1U form factor reduces potential issues for launch since they fit in a "Poly-Picosatellite Orbital Deployer" (P-POD). A P-POD, shown in Figure 8, fits three 1U CubeSats, or any combination adding to 3U in length. The P-POD limits interaction between CubeSats and the primary payload while delivering the satellites to space. While P-PODs facilitate the transition to space and the "rideshare" methods result in cheaper launch costs, they also come with stringent restrictions.
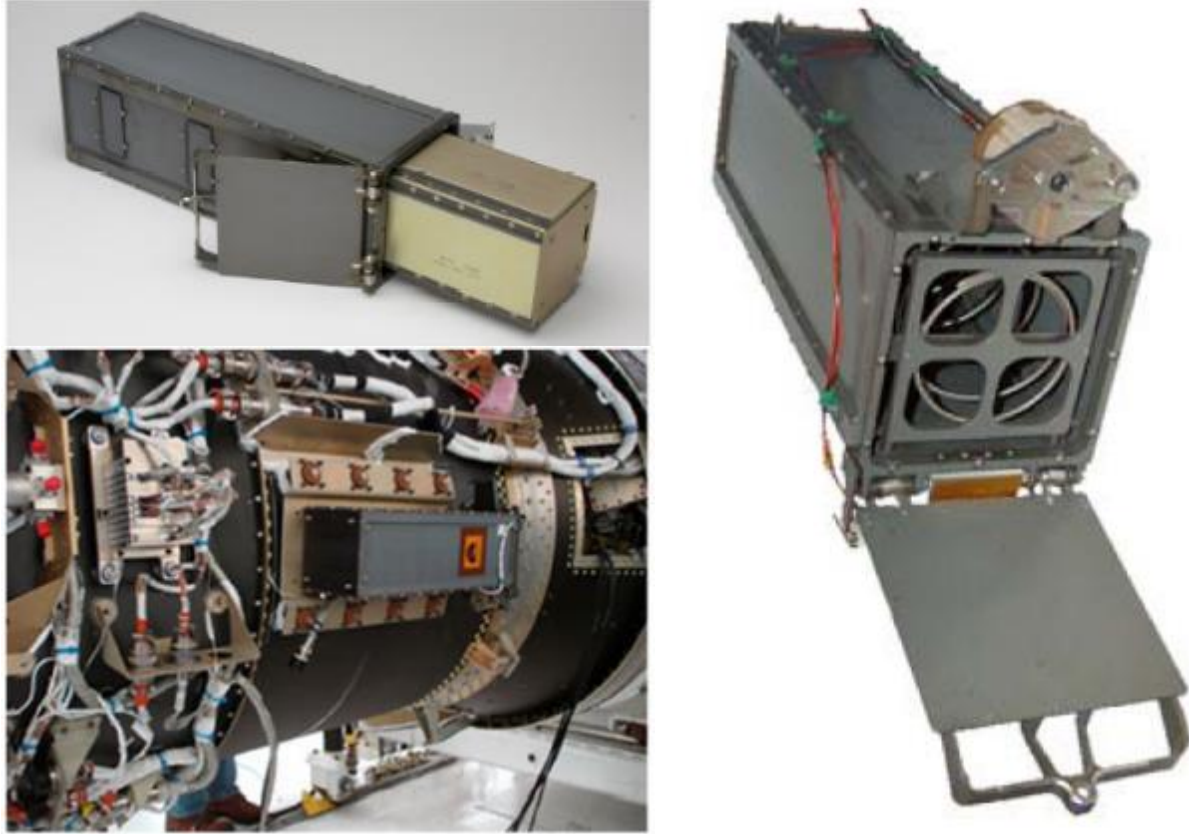
Figure 8: A Poly-Picosatellite Orbital Deployer (P-POD) is a launcher tube for deployment of CubeSats to space (Nugent et al., 2008). The P-POD developed at California Polytechnic University to safely carry CubeSats to space and minimize interaction with another payload.

Launching as an add-on results in deployment conditions dictated by the primary payload mission objectives. Thus, these satellites are typically restricted to the orbit of the deploying bus. Additionally, the secondary status means CubeSats must be as unobtrusive as possible and pose zero risk to the main/alternate payload(s). From the writer's experience, these limitations result in restrictions on satellite structure, overall satellite size/shape/weight, and propellant. The first two restrictions factor in the initial stages of satellite development, which have documented standards to follow. The restrictions on propellant, however, are not as black and white since the area of micropropulsion is still in its infancy and has not been thoroughly space-tested.

For CubeSats, it is undesirable for a propellant to be flammable as it could jeopardize the success of the primary payload mission. Unfortunately, flammability is usually a desirable property for a high-performance propellant, so this restriction significantly limits potential thruster systems. Additionally, it is undesirable for pressurization of the propellant prior to launch and the general limit is 1.2 atmospheres. A pressurized propellant, (i.e. common duster cans contain pressurized R-134a) can generate thrust, but is also considered an explosive limiting viability for space applications. The term "explosive" in this context refers to the pressurization of the propellant and not concerning the flammability of the liquid. For example, for R-134a the flash point is "not applicable" and the auto-ignition temperature is 750°C while the flash point and auto-ignition temperature of propylene glycol are 109°C and 371°C respectively. Even though R-134a is not flammable, it is still problematic because it requires pressurization to store in the liquid phase. The pressurization of the propellant on a small satellite triggers concern for the primary payload. A satellite review board scrutinizes any pressurized propellant tank for level of potential threat to the other mission payloads. Maintaining the satellite at ambient temperature and pressure prior to launch is desirable to minimize risk. Therefore, there is a critical need for a safe/efficient propellant/thruster system combination for use on small satellites.

Along with the advancements in technology has come a push for using safer forms of energy. Society globally is becoming aware of the limited resources available, but there is also a focus on the lasting effects of pollutants on the environment. Today's engineers must not only determine optimum performance conditions and design; they must also consider end of life of the design. Therefore, it is desirable for the propellant of small satellites to be "green" which means that it must be non-toxic and safe for the environment. Hydrazine is a commonly used liquid monopropellant for satellites of various sizes because of its high efficiency and ability to be stored

for long periods. However, it also has several limitations and liabilities regarding toxicity, environmental impact, and operational handling. Thus, it is desirable to find a non-toxic replacement to hydrazine and other toxic fuels while still maintaining a relatively high efficiency (Steitz, 2012). A proposed "green" alternative propellant, ammonium dinitramide (ADN), was developed in the Soviet Union circa 1970, but remained classified until 1989 when it was discovered by SRI International (Larsson,& Wingborg, 2011). Upon heating, ADN decomposes into nitrogen, oxygen, and hydrogen, which are not toxic or harmful to the environment. Unfortunately, ADN, like hydrazine, is combustive in nature and is therefore unacceptable as a propellant for a "piggyback" satellite due to its potential threat to the primary payload or other small satellites.

After reviewing other cold-gas and thruster systems it was determined that a new propellant was necessary to satisfy the stringent "rideshare" qualifications. Therefore, a water-based solution was developed as a non-pressurized and non-toxic propellant for CubeSat missions. Water has a neutral ph and is one of the "greenest" materials on earth. Additionally, the water based propellant stores in liquid form at ambient conditions satisfying even the strictest mission requirements.

2.2   PROPELLANT

2.2.1   Water

Water is one of the most common substances on earth, covering approximately seventy-one percent of the earth's surface. The average adult human body is fifty-five to sixty percent water. Nearly every day, water is commonly encountered in the solid, liquid, and vapor phase. Countless studies on water conducted in various fields generate a multitude of books and journal articles about water from a plethora of aspects. Yet, there is still so much more to learn about this chemical compound that humans consider so basic to everyday life.

19

Ideally, water is a prime propellant as it is readily available and neutral at standard temperature and pressure. When converted to vapor, water has a specific impulse of around 108s, which is comparable with other propellants currently used in cold gas systems. However, water has a very narrow working range with a freezing point at 0°C and boiling point at 100°C, which becomes problematic with space temperatures an orbiting satellite encounters.

A major concern with using water as a CubeSat propellant is the phase change from liquid to solid. During cooling, water reaches a maximum density at around four degrees Celsius (4°). At 4°C water molecules slow down and short length hydrogen bonds begin to form between pairs, packing the molecules tighter (Pietropaolo et al., 2008). Below 4°C ice crystals begin to nucleate, forming a hexagonal lattice crystal structure. A less commonly known benefit of the anomalous maximum density is cooling water actively mixes, preventing the bottom of freshwater bodies from freezing (Vernon, 1891). As water heats up or cools past 4°C it becomes less dense and rises leaving the bottom of lakes, ponds, etc. at around 4°C and unfrozen. During crystallization, water molecules form a repeating hexagonal pattern that is significantly less dense than liquid water; hence, the reason ice floats in a drink. This decrease in density results in an overall expansion of approximately 9% during freezing. Without a temperature regulation system in the propellant tank, water will freeze in the space environment, disrupt fluid flow as it crystalizes, and potentially crack and disable the satellite structure as it expands.

Since water alone is not a viable option due to the extreme working environment of space, the next logical step is to add a substance to modify the freezing/boiling point. Antifreeze reduces the freezing point of water and offers several potential advantages over other substances considered, such as salt. Salt can lower- the freezing point of water to -18°C, but is inadequate for the extreme temperatures of space. Additionally, salt can cause electrical connections to corrode, leading to

shorts or incorrect reading. Thus, this research focused on exploring aqueous antifreeze as a propellant for CubeSatellites.

2.2.2 *Primary Antifreezes: Propylene Glycol (PG) and Ethylene Glycol (EG)*

Propylene glycol (PG), $C_3H_8O_2$, is a viscous clear solution of an organic nature widely used in several applications such as anti-freeze coolant, food supplement for both humans and dogs, and bio-fuels ("Product safety assessment," n.d.). Propylene glycol's accessibility and nontoxic nature make it amenable for manipulation and utilization as a propellant for a CubeSat. Propylene glycol is an alcohol based compound that is generally recognized as safe (GRAS) thus making it an excellent candidate for an effective and safe propellant. Ethylene glycol (EG), $C_2H_6O_2$, is a viscous liquid commonly used as a precursor for polymers, antifreeze, coolant, and heat transfer agent. Unlike propylene glycol, EG is moderately toxic, affecting the nervous system and even leading to death, which limits use as a CubeSat propellant.

Ethylene glycol (EG), propylene glycol (PG), and water are among the few materials that satisfy the strict criteria dictated by the "rideshare" regulations. However, since pure water freezes at 0°C, PG and EG were analyzed as possible propellants. Both materials are alcohols with low freezing points. EG freezes at -12.9°C and while some discrepancy exists, PG is generally considered to have a freezing temperature of -59°C. The difference in freezing points of the two materials is due to their dissimilarity in molecular structure. By comparison, pure EG crystallizes at a higher temperature even though it has the same number of hydroxyl groups as PG. The difference between the two compounds is, propylene glycol contains a methyl group that prevents symmetric ordering at low temperatures (Ike, Seshimo, & Kojima, 2009).

At atmospheric conditions, pure propylene glycol has a liquid working range between -59˚C and 188.2˚C while ethylene glycol is liquid between -12.9˚C and 197.3˚C ("Product safety

21

assessment," n.d.). Relative to water, a larger working range is beneficial, but the higher boiling

point also requires more energy to vaporize. Further investigation of PG and EG reveals that the

latent heats of vaporization are 914 kJ/kg and 800 kJ/kg, which are significantly lower than water

(2257 kJ/kg). Thus, latent heat of vaporization could be a significant factor when considering

vaporization of the propellant.

Propylene and ethylene glycol vapor pressures are relatively similar in relationship with

temperature. Figure 9 illustrates the exponential relationship between vapor pressure and

temperature, which follows the Antoine Equation, Equation 4. When compared with water, both

EG and PG have relatively low vapor pressures around the CubeSat propellant storage

temperatures. At 30°C the vapor pressure of propylene glycol is 0.2 Torr and 0.14 Torr for ethylene

glycol. Unfortunately, the vapor pressure of EG and PG is significantly less than water (31.8Torr

at 30°C) at the same temperature indicating they are insufficient as propellants in the pure form.
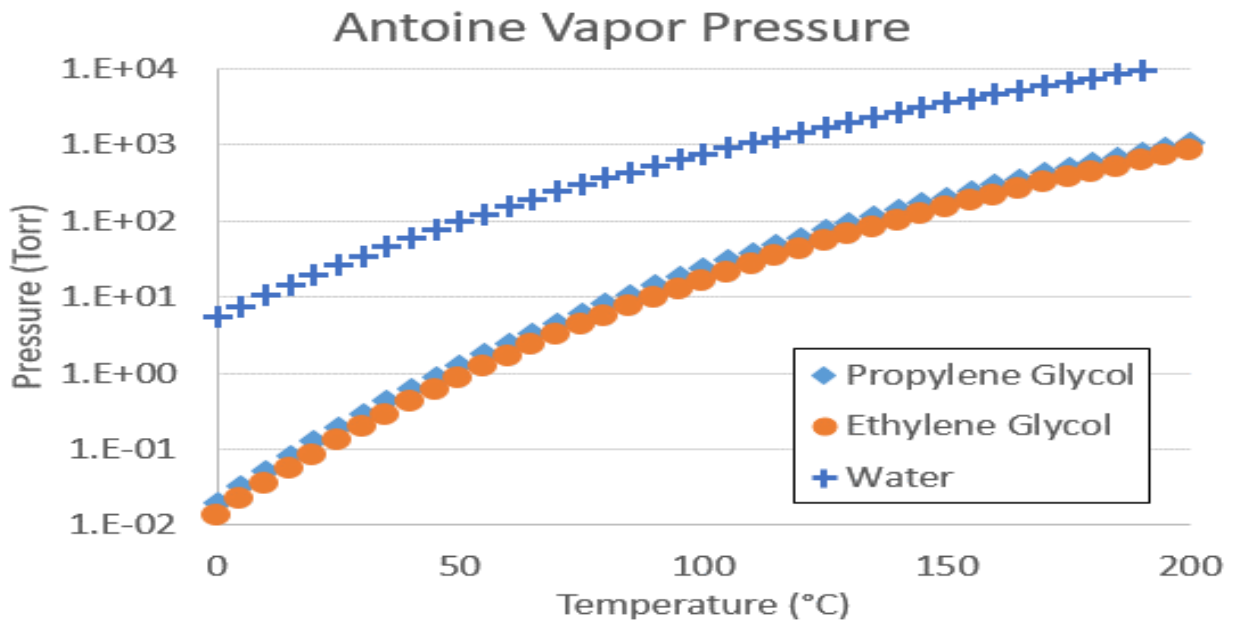
Figure 9: Vapor pressure is an important parameter when considering antifreeze as a propellant for
CubeSats. The Antoine Equation, Equation 4, describes the relationship between temperature and
vapor pressure for pure materials. At 30°C, ethylene and propylene glycol exhibit very similar
trends, but are both significantly lower than water vapor pressure.

$$P = 10^{A - \frac{B}{C+T}}$$

<div align="right">Equation 4</div>

P: Pressure
A, B, C: component specific constants
T: temperature

When combining water and antifreeze, properties are typically nonlinear. Figure 10 shows the boiling and condensation data for aqueous PG solutions. Adding water to EG and PG decreases both the boiling point and condensation point, decreasing the overall energy necessary to vaporize the propellant. For 70%w/w (weight of element/total weight) PG the boiling point is 110°C, a 78°C reduction of the 188°C boiling point of pure PG.
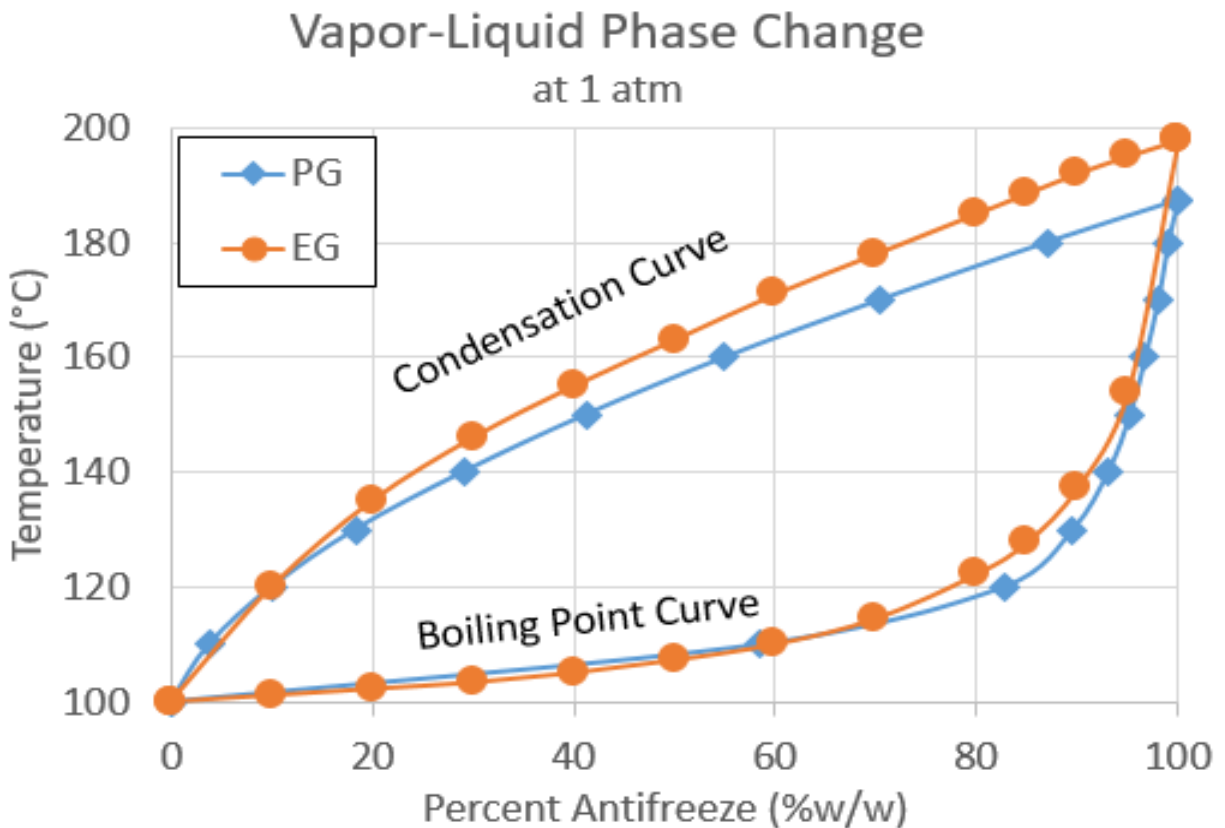
Figure 10: Water's boiling point (100°C) is much lower than the boiling points of ethylene glycol (197.3°C) and propylene glycol (188.2°C). Mixing ethylene/propylene glycol with water increases the boiling point of water, but also introduces a region where two phase flow might occur by separating the boiling and condensation curves.
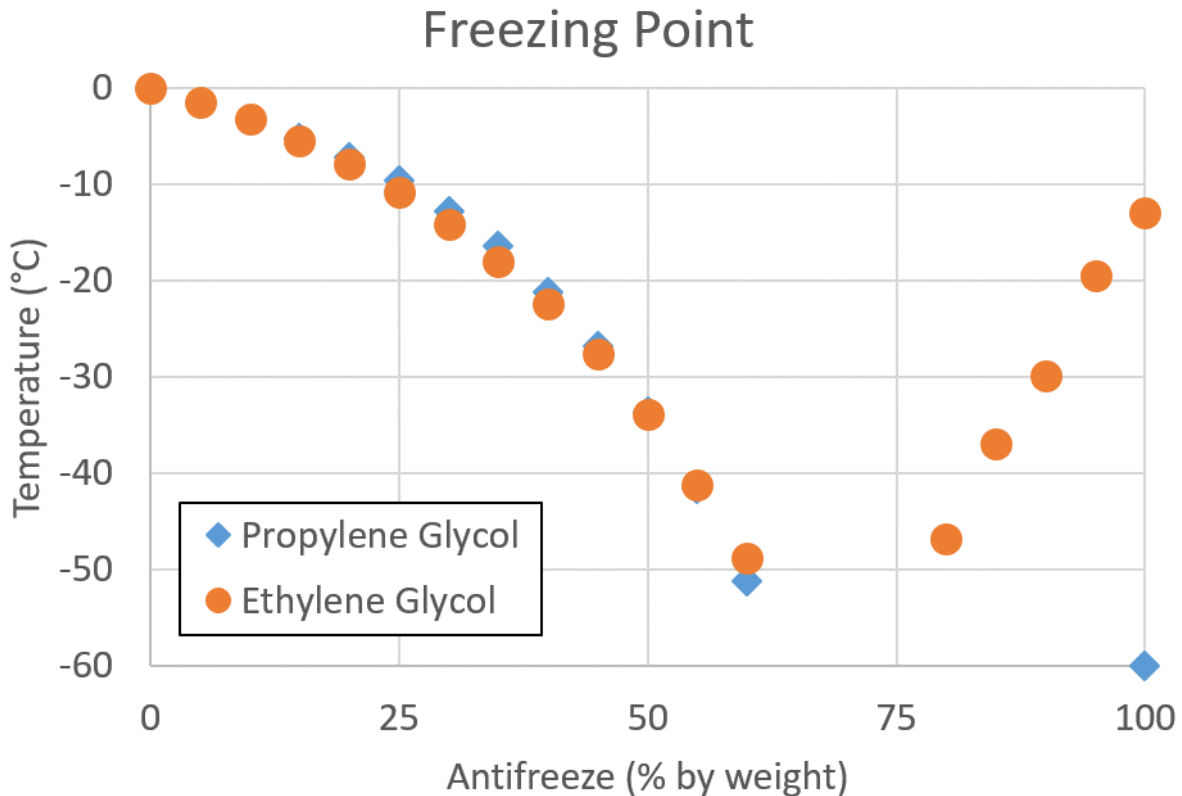
Figure 11: Water freezes at 0°C, but adding antifreeze disrupts hydrogen bonding and decreases the freezing point. With increased concentration of propylene glycol or ethylene glycol, the freezing point of aqueous antifreeze reaches a minimum at around 60%w/w. At this concentration the solution crystallizes at -50°C.

For CubeSat applications, the primary benefit of mixing antifreeze with water is freezing point depression. Homogenous PG does not have an intramolecular hydrogen bond because of the poor geometry for the expected hydrogen bond, and it has no detectable bond critical point between hydrogen and oxygen atoms of the two vicinal diols (Zhou Hu, Shen, Wu, & Cheng, 2009). However, when PG mixes with water the freezing point depresses dramatically. Likewise, mixing EG with water increases molecule structure complexity and makes the solution more difficult to crystallize (Ike, Seshimo, & Kojima, 2009). Water freezes at 0°C, but the freezing point begins to decrease with the addition of a cosolvent. Freezing point depression is a property alteration that is desirable for propulsion systems to function properly in the deep freezing space. Figure 11

24

shows the freezing points of both EG and PG when mixed with water ("Ethylene glycol and propylene glycol freezing points," 2011). The data was limited for aqueous PG, but the trend at lower concentrations of antifreeze was similar to that of EG. For EG, as weight percent solute increases the freezing temperature decreases until about 70 weight percent solute. At 70 percent EG, the freezing point begins to increase until reaching the freezing point of pure EG at -12.9°C. For PG, it appears that the freezing point is depressed reaching a minimum at a 70/30 ratio with water. Incomplete data is a result of the aqueous antifreeze solution failing to crystallize, but rather forming a "slurry" with no definitive freezing point.

Data is bountiful and well documented for aqueous PG and EG solutions. Curme and Johnston (1952) compiled an extensive collection of ethylene glycol and propylene glycol material properties necessary for CubeSat applications, such as specific heat, density, and viscosity. Yet, even though propylene glycol is a heavily researched material, there are still unknowns in the material properties that are necessary to understand before using PG or EG as propellants for satellites. For example, Curme and Johnson's collection of specific heats for PG-water solutions is incomplete beyond the boiling point; see Figure 12 (Curme, & Johnston, 1952).
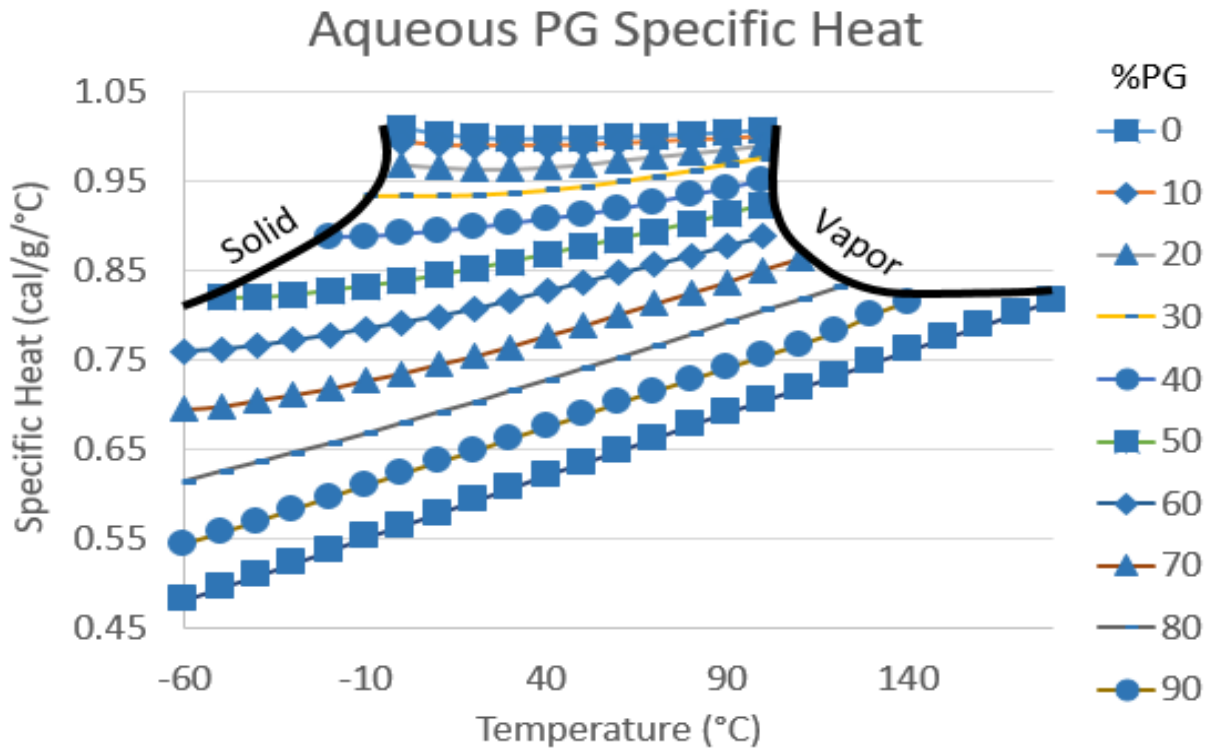
Figure 12: Specific heat data generated from research by Curme and Johnston (1952) is lacking data points outside of the liquid phase. The specific heat of vapor phase aqueous propylene glycol is necessary for determining the specific impulse of the propellant and predicting the thrust output when used as a cold-gas thruster.

Most charts regarding antifreeze are incomplete below the freezing point and above the boiling point. Figure 13 shows compiled data for density of aqueous propylene glycol solutions at varying temperatures and concentrations (Curme, & Johnston., 1952). The absence of data in the solid phase is evident when viewing Figure 13. Density is an important design parameter for volume limited CubeSats and clearly documented densities of liquid aqueous propylene glycol are useful. The lack of data below the freezing point is exacerbated by the fact that the density of water drops approximately 9% during the phase change. The density change during crystallization of the aqueous propylene glycols is an unknown variable in the design process. Similarly, aqueous antifreeze viscosity is unknown above the boiling point. Vapor phase viscosity is essential for cold-gas thrust characterization for CubeSats.

26
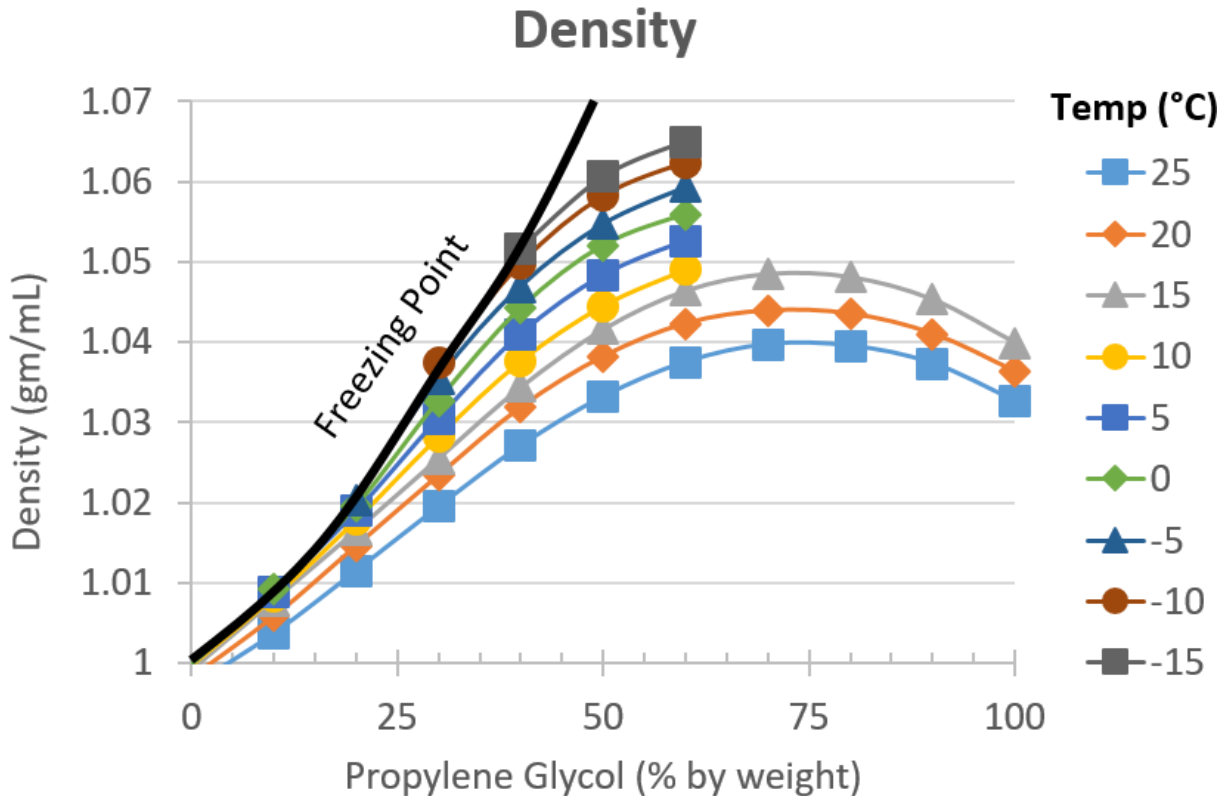
Figure 13: Aqueous propylene glycol liquid density curves generated from research by Curme and Johntson (1952) lack data in the solid and vapor phases. The solid and liquid densities are essential for CubeSat design.

Regarding expansion, water expands approximately nine percent during crystallization. CubeSats are extremely volume limited and researchers utilize every cubic centimeter. Liquid propellants already account for a large portion of the volume, but there is not any extra space to allow for expansion during crystallization. Additionally, expansion of propellants on a satellite is potentially catastrophic if the stress it imposes on the structure is not established. Yet, the expansion characteristics of antifreeze solution are not available in literature.

The Dow Chemical Company is the largest supplier of propylene and ethylene glycol. Safety guidelines do not report expansion data during crystallization of aqueous antifreeze solutions. Instead, the "Freeze Protection" identifies the freezing point of the aqueous solution, while the

guidelines recommend an offset working temperature identified as "Burst Protection." Freeze protection is the recommended temperature/composition values if the system is running constantly. Burst protection is required whenever the system will remain dormant for extended periods or if exposed to sub-freezing temperatures for extended periods. Both descriptors do not account for what will occur if the system does actually freeze. Instead, based on working temperature, the guidelines suggest concentrations for using the fluids in pipes. Figure 14 and Figure 15 illustrate the guidelines from Dow Chemical for propylene glycol and ethylene glycol, respectively.

DOWFROST – Propylene Glycol Solidification Limits
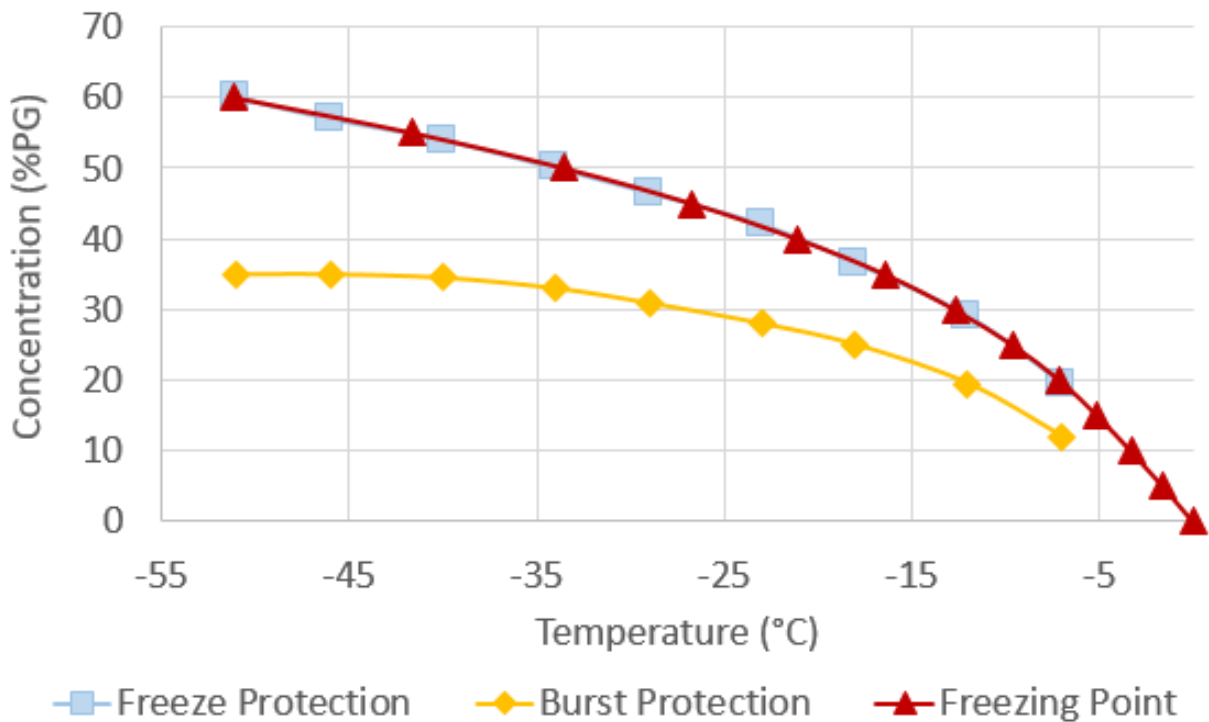
Figure 14: Antifreeze is used to prevent freezing, particularly in pipes. DOW Chemical suggests a minimum concentration of propylene glycol based on temperature to prevent freezing, and a lower concentration as an added protection to prevent pipe bursting. Freezing and burst protection curves are generated from DOWFROST data provided Dow Chemical Company (2018).

DOWTHERM – Ethylene Glycol Solidification Limits
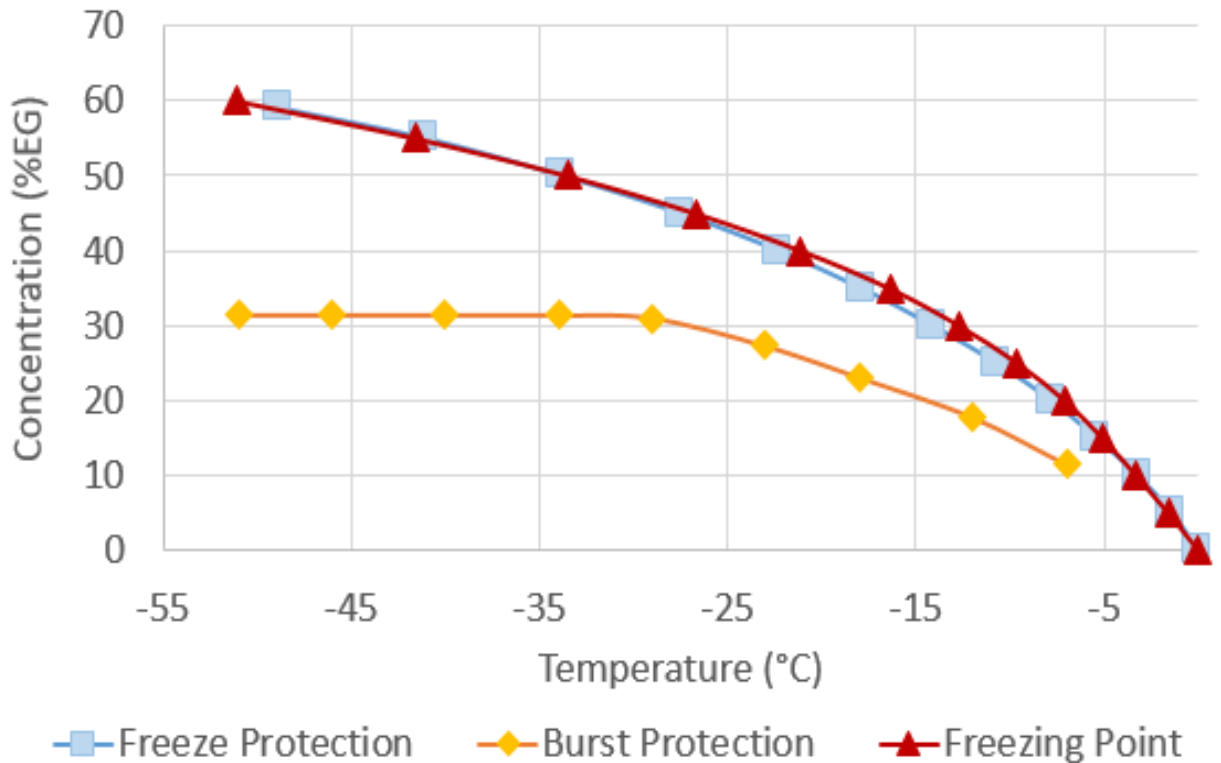
Figure 15: Antifreeze is used to prevent freezing, particularly in pipes. DOW Chemical suggests a minimum concentration of ethylene glycol based on temperature to prevent freezing, and a lower concentration as an added protection to prevent pipe bursting. Freezing and burst protection curves are generated from DOWTHERM data provided Dow Chemical Company (2018).

Instead of limiting the use of ethylene and propylene glycol as coolants to prevent freezing, the aqueous solutions show potential for use as propellants for small satellites. Therefore, knowledge of freezing points is insufficient. Instead, understanding expansion characteristics of the aqueous solutions at various concentrations is necessary. Hydrogen bond disruption depresses the freezing point, but it also limits crystallization from propagating across the entire solution. Quantitatively evaluating expansion enables more effective accounting of the limited volume allowed in a CubeSat, leading to better utilization and more successful missions.

2.2.3   Secondary Antifreeze Fluids: Glycerol and Methanol

Methanol and glycerol are additional reference antifreeze agents to examine and compare with the propylene glycol and ethylene glycol solutions. Commonly found in windshield washing fluid, deicer, and gasoline additives, methanol, CH_3OH, is the simplest alcohol. Methanol's use as a propellant for CubeSats is limited due to its volatility, flammability, and poisonous nature. Yet, methanol is a notable benchmark material due to its high specific impulse and vapor pressure.

Glycerol, $C_3H_8O_3$, is a non-toxic antifreeze commonly found in the food industry as a humectant, sweetener, and preservative. The e-cigarette industry use glycerol and propylene glycol as vaporizing agents to deliver nicotine to the user because of their non-toxic and safe classification. While safe for the environment and non-volatile, glycerol has limitations for CubeSat propulsion due to its high viscosity, high freezing point, and low vapor pressure.
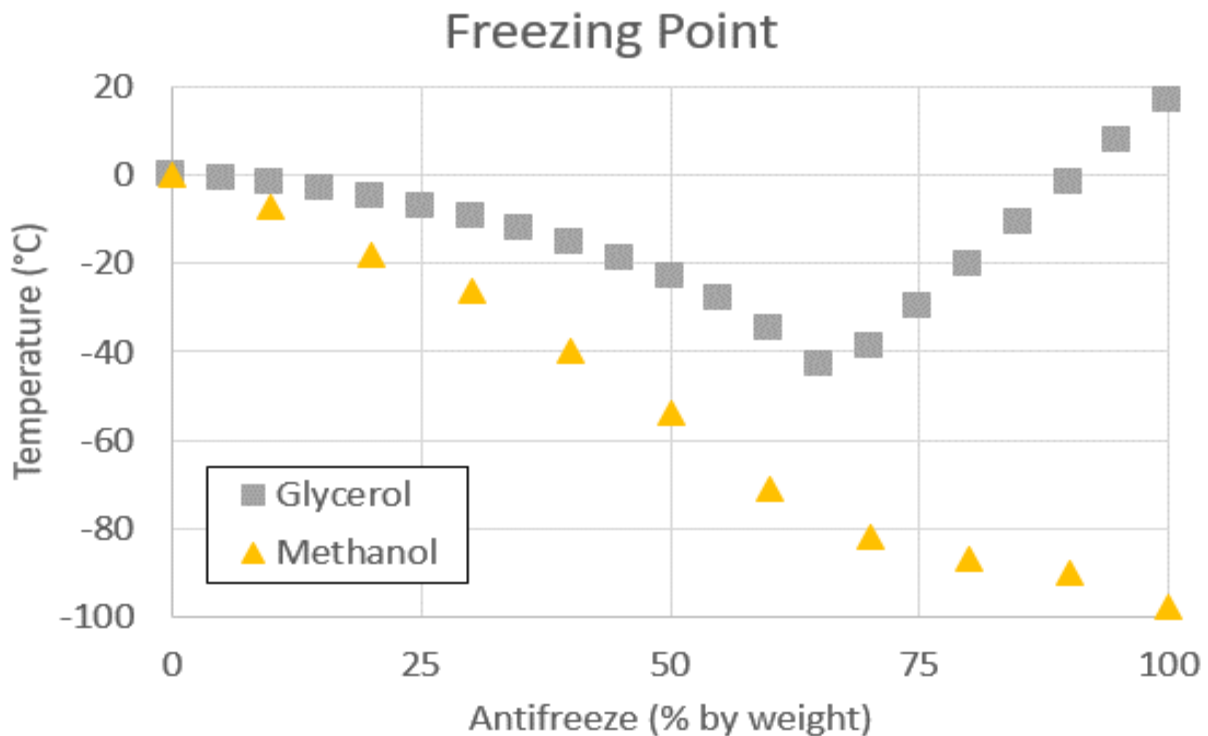
Figure 16: Similar to propylene glycol and ethylene glycol, glycerol and methanol depress the freezing point when mixed with water. Glycerol exhibits a minimum freezing point of -43°C at 65%w/w while methanol has a lower freezing point than water.

30

Methanol has a freezing point significantly lower than water, -97.6°C, but glycerol's freezing point is higher than water, 17.8°C. Figure 16 shows that when added to water; both liquids depress the freezing point. Glycerol reaches a minimum freezing point of -43°C at 65 %w/w glycerol 35%w/w water. Methanol depresses the freezing point of water until reaching a minimum at 100% methanol.

Theoretically, vapor pressures for methanol and glycerol, Figure 17, vary greatly from the primary antifreeze solutions. Methanol's vapor pressure is significantly higher than all other antifreeze solutions studied. At working temperatures, methanol's vapor pressure is approximately 500-1000 times that of ethylene and propylene glycol. Conversely, glycerol vapor pressure is 500-1000 times lower than that of ethylene and propylene glycol. Additionally, glycerol freezes at 17.8°C, limiting its use for vaporization. The varying vapor pressures establish a range of working pressures for cold gas thruster evaporation.
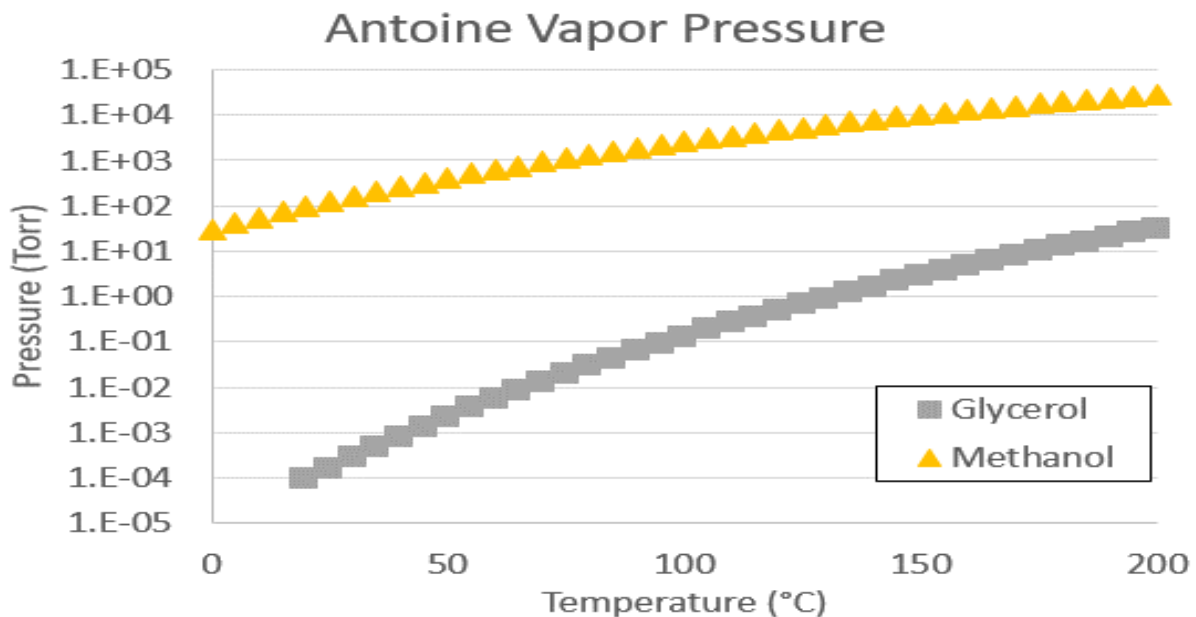
Figure 17: Vapor pressure of a pure material is determined using Equation 4. Methanol has a vapor pressure higher than water, so mixtures will all have a higher vapor pressure than pure water. Glycerol has the lowest vapor pressure compared to the other antifreezes, limiting use as a CubeSat propellant.

31

2.3   NANOFLUIDICS

Usable volume is a major constraint when working with small satellites. Miniaturization of devices creates the impetus for innovations to meet the needs of smaller systems on CubeSats. An evolving area of research of particular interest to this author is nanofluidics because it holds potential for advancing capabilities of small satellites. Nanofluidics is the study and application of fluid flow in and around nanosized (10^{-9}m) objects (Eijkel, & van den Berg., 2005). These structures have increased in popularity because of their unique capability in biomolecular manipulation and control. The biological applications include separation of biomolecules, drug delivery, and single molecule detections (Mao, & Han, 2005). The size of nanochannels provides an ideal experimental platform for well controlled, model-based study of molecular fluidic transport processes in confined space (Mao, & Han, 2005). Nanochannels aid in studying, sorting, and filtering polymer molecules. Nanofluidics shows tremendous potential for use in small satellites and is a major focus of this research.

Nanofluidics examines fluid behavior in geometric structures at the nanometer characteristic scale typically (1-100nm). While nanofluidics has been around for decades, recent interest pushes into a new frontier previously unrealized (Xu, 2018). Recent research, due in large part to advances in nanofabrication, abetted the growth in nanofluidics (Sparreboom, van den Berg, & Eijkel, 2009; Boquet, & Tabling, 2014; Haywood, Saha-Shah, Baker, & Jacobson, 2015; Mawatari et al., 2014; Mukhopadhyay, 2006). Accessibility to nanoscale fabrication methods ignited nanofluidic research in chemistry, physics, biology, and engineering. Fabricated nanochannels and nanopores, used to form new nanofluidic devices, have well-defined geometries enabling high-level controllable, reproducible, and predictable research (Xu, 2018). Of particular interest to Cubesatellites, recent research in nanofluidics focused on applications in carbon nanotubes

32

because of inherent desirable properties. Carbon nanotubes are atomically smooth and controlling the growth parameters influences their size. Holt et al. (2006) successfully grew carbon nanotubes with a diameter between 1 to 2 nanometers and measured the volumetric flow rate of water.

To date, most understanding of nanofluidic flow stems from molecular dynamics simulations, since experimentally nanochannel flow is rather difficult to quantify (Tang, & Advani, 2006; Chen et al., 2008; Han, 2008; Xu, Zhou, & Xu, 2004; Tuzun, Noid, Sumpter, & Merkle, 1996). A number of simulations conducted on liquid water transport through carbon nanotubes examined various parameters (Hummer et al., 2007; Thomas, McGaughey, & Kuter-Arnebeck, 2010). Simulations determined that hydrophobic surfaces in nanochannels have a unique impact on fluid/vapor interaction and that a vapor phase forms at the wall/liquid interface because of the "drying" transition (Lum, & Luzar, 1997). If this annular vapor region along the nanotube walls is modeled mathematically in terms of the vapor layer thickness and viscosity ratio of the gas to liquid, then a large amount of slip can be determined in the fluid flow profile (Myers, 2011). This fluid model was even accepted and used to account for variations in fluid density for molecular dynamics simulations on nanotubes with diameters ranging from 0.83 to 1.66 nanometers (Thomas, & McGaughey, 2009).

The formation of an annular region around the bulk water material allows for "easier" transport of water molecules through the nanochannel. Hydrogen bonds in the bulk water are disrupted as the water molecules enter the nanochannel and facilitate movement as a chain with relative ease through the nanochannel, because of the channel's hydrophobicity (Hummer, Rasaiah, & Noworyta, 2001). When a polar liquid, like water, encounters a hydrophobic surface, it is more attracted to another polar molecule than the hydrophobic surface since there is a stronger attraction

due to larger molecular binding energies (Mattia, & Calabro, 2012). This molecular interaction leads to higher than expected flow rates through a nanochannel.

Surface roughness dramatically inhibits fluid flow in nanochannels due to the small characteristic length scale creating a bottleneck. As the fluid flow approaches the free molecular flow regime, it is even more likely that the molecules will interact with the channel walls, thus slowing their movement. Soong, et al. (2007) found that not only does nanochannel surface roughness have a tremendous impact on nanofluidic flow, but so does crystallographic orientation. Surface orientation, flow orientation, wall and fluid densities, and molecular interaction parameters impact fluid slippage and channel flow rate , which interactively determine the flow rate and velocity profile (Soong, Yen, & Tzeng, 2007). However, while analytical models propose a comparative solution to the problems encountered with experimental analysis, they are still limited because of the difference in length scale between molecules large nanochannels/microchannels.

2.3.1 *Theory*

At the macroscale, channels follow Hagen-Poiseuille flow, which describes fluid flow through a long cylindrical pipe, see Figure 18. Hagen-Poiseuille Law, Equation 5, assumes the fluid is viscous and incompressible and flow is laminar through a pipe with constant cross-sectional area and a length much longer than the diameter. The law relates the mass flow rate ($\dot{m}_{HP}$) to the pipe diameter (d), pipe length (L), and pressure drop along the pipe (Δp), as well as, dynamic viscosity (μ) and density (ρ), which are material properties of the fluid. For continuum flow between two parallel plates, the velocity profile for Hagen-Poiseuille flow is fully developed and parabolic in nature Figure 18 (a).

$$\dot{m}_{HP} = \frac{\pi (d/2)^4}{8\mu} \frac{\rho \Delta p}{L} \qquad\qquad \text{Equation 5}$$

However, this macro-scale equation becomes invalid for micro and nanochannels. Figure 18 displays three flow regime approximations used for estimating the flow velocity profile in micro/nanochannels. The no-slip boundary condition for Hagen-Poiseuille assumes zero flow velocity at the wall of the channel, Figure 18(a). For some micro and nanochannels the no-slip boundary condition does not hold true and can no longer be assumed. Therefore, Equation 6 accounts for slip, observable in the extra terms not included in Equation 5: slip length (L_s), wall velocity (U_{wall}), and the velocity profile (dU/dr). Figure 18(c) illustrates the nonzero fluid velocity at the wall and the effect on the flow profile. The flow profile is similar to Hagen- Poiseuille flow, with the exception that the parabolic profile theoretically extends past the walls and the regions outside the walls do not contribute to the total volumetric flow. Instead, there exists a velocity at the wall.

$$\dot{m}_{slip} = \frac{\pi (d/2)^4 \rho \Delta p}{8\mu L} \left(1 + \frac{8L_s}{d}\right) \quad where \quad L_s = \frac{U_{wall}}{dU/dr} \qquad \text{Equation 6}$$
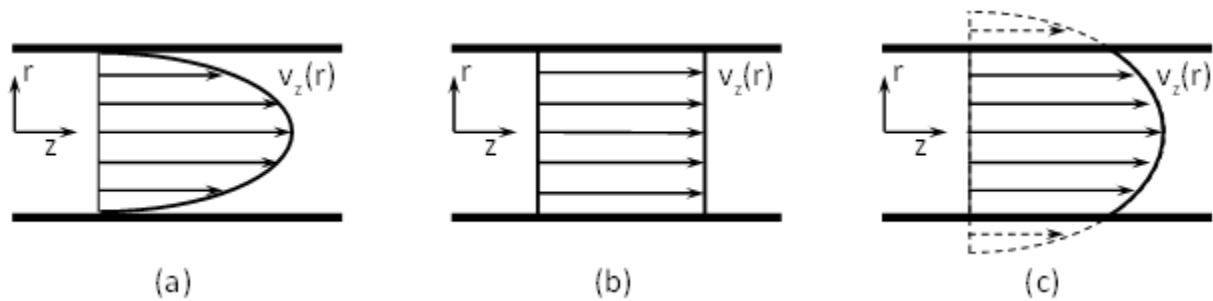
Figure 18: In continuum and slip flow, three different flow profiles simulate flow in a channel. (a) Hagen-Poiseuille flow exhibits a parabolic profile where flow at the wall is zero. (b) Plug flow has a constant flow velocity throughout the channel cross section. (c) Slip flow is similar to Hagen-Poiseuille with the caveat that flow velocity at the channel walls is non-zero.

Some micro/nanochannels experience plug flow, Figure 18(b). In plug flow, the velocity is constant along the entire cross section of the channel perpendicular to the flow direction. Due to geometry, the volumetric flow rate of plug flow is significantly easier to approximate by assuming a constant flow velocity across the flow profile. The plug flow model assumes there is no boundary layer adjacent to the channel wall and therefore, similar to the no-slip case, the flow velocity at the wall is nonzero. However, as the channel cross section decreases further, fluid flow transitions into the Knudsen diffusion regime.
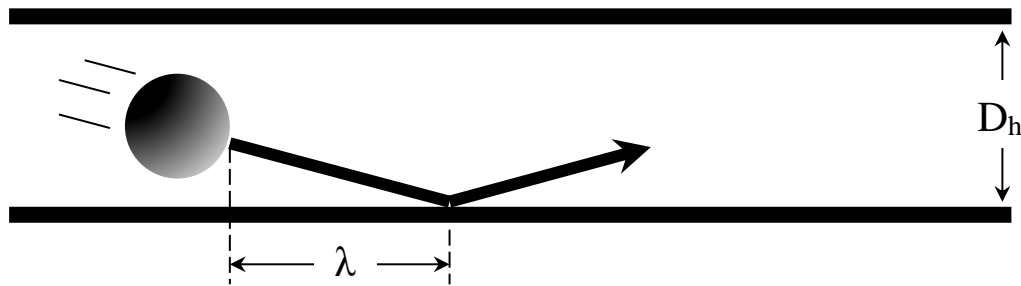
Figure 19: Knudsen diffusion in a channel where the hydraulic diameter approaches the mean free path of the molecule. In Knudsen diffusion, the molecules are much more likely to interact with channel walls than each other which affects the flow rate.

Knudsen diffusion occurs when the length scales of channels approach, equal, or are smaller than the mean free path of the particle(s). At this smaller scale, the fluid molecules are much more likely to interact with the channel walls than each other since the overall system dimensions are on a similar order to the mean-free path of the fluid. The Knudsen Number, Equation 7, is a standard metric used to determine the type of flow in a channel (Kandlikar, Satish, & Grande, 2003). Using Equation 7 and Equation 8 in conjunction with Table 3 it is possible to determine the type of flow that will be experienced which helps in determining mass flow rates in the system.

$$Kn = \frac{\lambda}{D_h}$$
Equation 7

$$\lambda = \frac{\mu\sqrt{\pi}}{\rho\sqrt{2RT}}$$

Equation 8

λ: mean free path
D_h: hydraulic diameter
μ: dynamic viscosity
ρ: density
R: gas constant
T: temperature

Table 3: The Knudsen number indicates the flow regime in a nanochannel (Harley, 1993).

Knudsen Numbers	Type of Flow
Kn<0.001	*Continuum Flow*: no rarefaction effects
0.001<Kn<0.1	*Slip Flow*: rarefaction effects that can be modeled with a modified continuum theory accounting for wall slip
0.1<Kn<10	*Transition Flow*: a type of flow between the slip flow and free molecular flow that is analyzed statistically; i.e. with Boltzman equation
Kn>10	*Free Molecular Flow*: Motion of individual molecules must be modeled and then treated statistically

Low Knudsen numbers indicate that the flow will likely follow the Hagen-Poiseuille flow regime, Figure 18(a). A Knudsen number between 0.001 and 0.1 is indicative that slip, Figure 18(c), is likely, which is commonly observed in carbon nanotubes. As the scale of the nanochannel decreases further, the flow through the channel evolves into the transitional flow regime. For Knudsen numbers much greater than one flow follows the Knudsen diffusion regime, Equation 9.

$$\dot{m} = \frac{2}{3} \sqrt{\frac{8\pi}{MRT}} \left(\frac{d}{2}\right)^3 V_m \frac{\Delta p}{L} \sigma A \rho \qquad\qquad \text{Equation 9}$$

M: molecular weight
R: universal gas constant
T: absolute temperature
d: pore diameter
V_m: molar volume
Δp: pressure drop
L: thickness of the membrane
σ: areal pore density
A: total area of the membrane
ρ: fluid density

Alternatively, with small channels liquid will typically condense and wet the channel due to the Kelvin pressure for capillaries being less than vapor pressure of a liquid. Condensation in a channel leads to the formation of a volume of water contained within the nanochannel, called a plug, disconnected for the main reservoir of water. Depending on the length scale, other factors restrict flow in addition to Hagen-Poiseuille type flow. For larger channels flow meniscus evaporation limits flow while for smaller channels the fluid plug tends to follow Hagen- Poiseuille flow. However, smaller channels tend to fill completely and became a focus of this research.
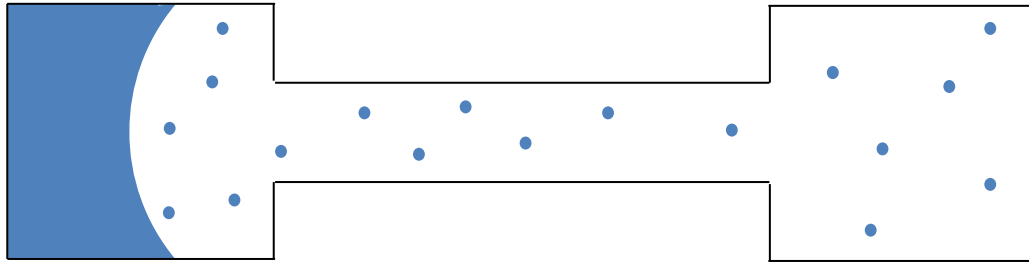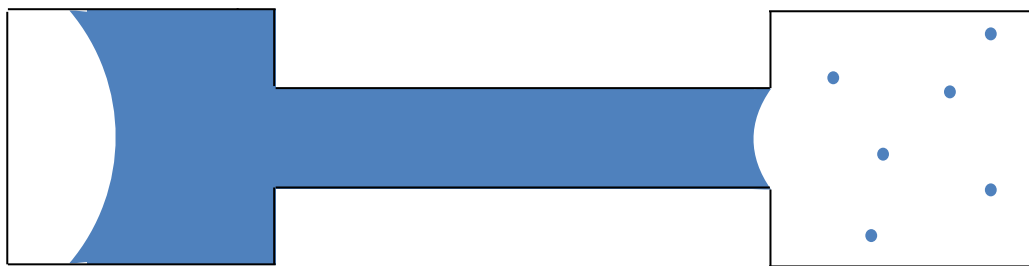
Figure 20: Nanochannel wetting determines the anticipated flow regime. The nanochannel fluid phase separator experiences Hagen-Poiseuille flow with water vapor if the liquid meniscus remains to the left of the nanochannel. If liquid wets the nanochannel, flow rates follow Washburn capillary filling.

Capillary filling restricts the flow rate in water-filled nanochannels connected to a water reservoir at the inlet and exposed to vacuum at the exit, Figure 20. Washburn's equation describes capillary flow for single and parallel tubes as well as porous media, Equation 10. The driving force for flow rate through the nanochannel is the Laplace pressure where the liquid meniscus meets vacuum. Vacuuming the channels prior to liquid filling eliminates any additional pressure on the fluid.

$$L^2 = \frac{\gamma D t \cos(\phi)}{4\eta}$$

Equation 10

L: length of capillary (m)
D: diameter (m)
γ: surface tension (N/m)
ϕ: water contact angle between liquid and surface (degree)
η: dynamic viscosity (Pa*s)
t: time to fill nanochannel (s)

Restructuring of Equation 10 yields the volumetric flow rate based on capillary filling, Equation 11. A nanochannel with a constant cross section and diameter D results in the maximum flow rate achievable based on the Washburn limit. Equation 10 does not consider slip, but empirical data indicates that slip (ζ) exists for fluid flow at the nanochannel scale. A slip of ζ=483.55 μm allowed for determination of the maximum possible flow rate in a nanochannel (Du et al., 2011). However, Qin et al. (2011) measured the flow rate through a single carbon nanotube and found that the slip length ranged between 53-58nm for a tube with diameter between .81-1.59nm. Thus, a slip of ζ =50μm established a conservative baseline for volumetric flow rate ($\dot{V}$) through a nanochannel with constant diameter, (D).

$$\dot{V} = \frac{\gamma * \cos(\phi) * \pi * (L + \zeta) * D^3}{16 * L^2 * \eta}$$

Equation 11

For planar nanochannels, a constant cross section with width (W) and depth (D) is assumed. Hydraulic diameter does not account for all fluid transport, as planar nanochannels have a low aspect ratio. Modification of Equation 11 to account for planar nanochannel geometry results in the formation of Equation 12, which includes a slip of ζ =50μm

$$\dot{V} = \frac{\gamma * \cos(\phi) * W * (L + \zeta) * D^2}{4 * L^2 * \eta}$$

Equation 12

2.3.2 Flow Measurements

With the dramatic rise in nanofluidic research, the minimal experimental verification of theory and molecular dynamics simulation is surprising. Of particular interest to nanofluids research for CubeSats is water vapor transport data through well-defined nanochannels. For use as a phase separator, it is imperative that water vapor transport through nanochannels is well established and predictable. Without experimental verification, the satellite propulsion system would be making a veritable "shot in the dark."

A few experiments successfully measured behavior within a nanochannel (Hamblin, 2011; Hanveld et al., 2008; Han et al., 2006; Sobolev et al., 2000; Oh, de Beer, & Mugele, 2010; Tas et al. 2004). A multitude of experiments used carbon nanotubes (CNT) specifically (Cao, et al., 2002; Holt et al., 2006; Qin 2011). Carbon nanotubes are tube-like structures composed of carbon with a diameter on the nanoscale and lengths up to hundreds of microns. With a high strength to weight ratio, CNT's are even stronger than steel, but they also possess amazing magnetic and electrical properties. Carbon nanotubes are single walled or multi walled and have a physical appearance similar to chicken wire. Figure 21 illustrate achievable dimensions for single walled carbon nanotube (Arnero, 2007). Because of CNT's interesting properties, they are frequently used with nanofluidics research.
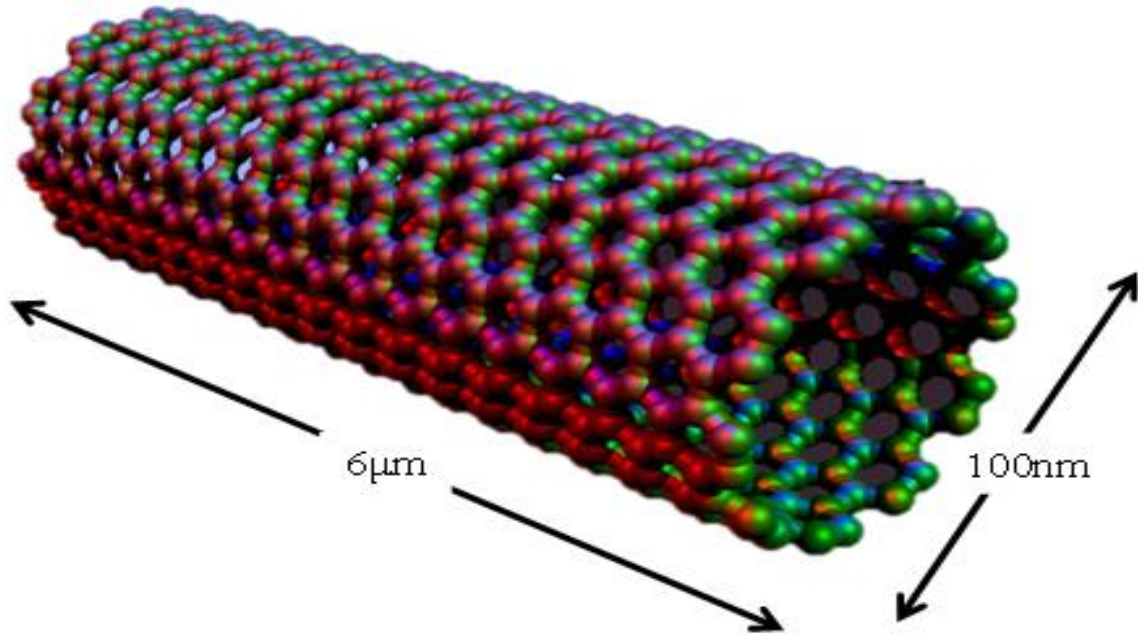
Figure 21: Carbon nanotubes are commonly used in nanofluidics due to their uniformity, size, and material properties. Carbon atoms bond in a hexagonal structure to form tubes like the one shown above. The nanochannel is an example of an armchair tube with a 100nm diameter (Arnero, 2007).

Hinds et al. (2004) were the first to publish experiments involving the transport of $Ru(NH_3)_6{}^{3+}$ in an aqueous solution through a membrane of nanotubes with diameter of 0.55 nanometers determining a slip length of 39-68μm. Holt et al. (2006) and Majumder et al. (2005) fabricated carbon nanotube membranes and measured water flow through the membranes. Rossi et al. (2004) used an environmental scanning electron microscope (ESEM) to study the evaporation/condensation of water in a carbon nanotube by controlling the temperature.

Majumder et al. (2005) continued the research conducted by Hinds et al. (2004) with true molecular nanotubes suspended in a polystyrene solution. Plasma etching exposed the nanotubes in the composite, creating a porous membrane (Majumder et al., 2005). Whitby and Quirke (2007) forced fluid through nanotubes using a simple pressure-driven flow apparatus and measured the mass transported at various intervals to determine the flow rate. Results from the Mattia and Gogotsi (2008) experiment showed a flow enhancement of around 10,000 times expectations based

on the Hagen-Poiseuille no-slip model. Slip lengths, derived from the measured fluid flow values, accounted for the flow enhancement experienced during experimentation.

Holt et al. (2006) fabricated a carbon nanotube membrane on a silicon substrate using chemical vapor deposition to grow a dense, vertically aligned array of dual wall carbon nanotubes (DWNT). Silicon nitride (Si_3N_4), used as filler material, supported the DWNT's and ion milling removed excess nitride, exposing the nanotubes (Holt et al., 2006). The meniscus level in the feed tube indicated the water flow rate due to the pressure-driven (0.82 atmosphere) flow through sub 2 nanometer carbon nanotubes (Whitby, & Quirke, 2007). Experimentally, DWNT's showed a flow enhancement ranging from 560 to 8400 times the expected results from the Hagen-Poiseuille no-slip model (Holt et al., 2006). Similar to Majumder et al. (2005), calculation of slip lengths explained the flow enhancement experienced during experiments.

Slip lengths calculated by Holt et al. (2006) and Whitby and Quirke (2007) ranged from 140 to 1400 nm while Majumder et al. (2005) found significantly larger values of 3 to 70 microns. The calculated values for slip were rather unexpected since, generally, the slip thickness is significantly smaller than the thickness of the bulk fluid flow (Myers, 2011). Thus, Myers (2011) proposed the extraordinarily large values for slip are a result of the vapor region along the wall and because of hydrophobic particle contamination.

Qin et al. (2011) effectively measured flow rates through 0.81-1.59nm diameter carbon nanotubes. Utilizing a series of field effect transistors, flow velocities ranging between 18.1 to 34.2 μm/s indicated a flow enhancement factor of 51-882. Slip lengths between 8-53nm were similar to values seen by Holt et al. (2006). Other similar experiments found water vapor flow rates of 2E-15 gm/s for a 20nm channel and 6E-18 gm/s for a 2nm channel (Tzevelekos et al., 1998; Lee, & Hwang, 1986).

2.4 MEMS AND NANOCHANNEL FABRICATION

Microelectromechanical systems (MEMS) and nanoelectromechanical systems (NEMS) generate ideas and techniques for creating new devices at the micro/nano scale. MEMS range in size from 1-1000 micrometers (µm) while NEMS are 1-1000 nanometers (nm). For space applications, MEMS/NEMS technology advances sensors, propulsion systems, and instruments making space flight more feasible. By reducing the size of the components and overall system, MEMS and NEMS decrease mass, power and ultimately cost. With the advancements and miniaturization in technology comes the ability to change the way data is collected. Whereas, before a single satellite collected one data point, it now becomes possible to change the measurement paradigm to facilitate a satellite array or matrix of data collection. Yet there exists a gap between science fiction and reality and MEMS/NEMS will bridge the gap. A nanochannel array plays a vital role in the cold-gas propulsion system (2.1.2) that makes the impossible, possible.

Nanochannels are often categorized as either 1D or 2D based on their dimensions and aspect ratio of their cross-sectional area. Figure 22 illustrates the dimensional difference between the categories of nanochannels. A two-dimensional nanochannel has characteristic dimensions (width and depth) that are both on the nanoscale, resulting in an aspect ratio near unity. If one dimension of the cross section is larger, micro to millimeter scale, then the nanochannel is one-dimensional with a low aspect ratio. This difference in the order of magnitude is a result of fabrication limitations where in general the width is much larger than the depth because of the larger tolerances in photolithography.
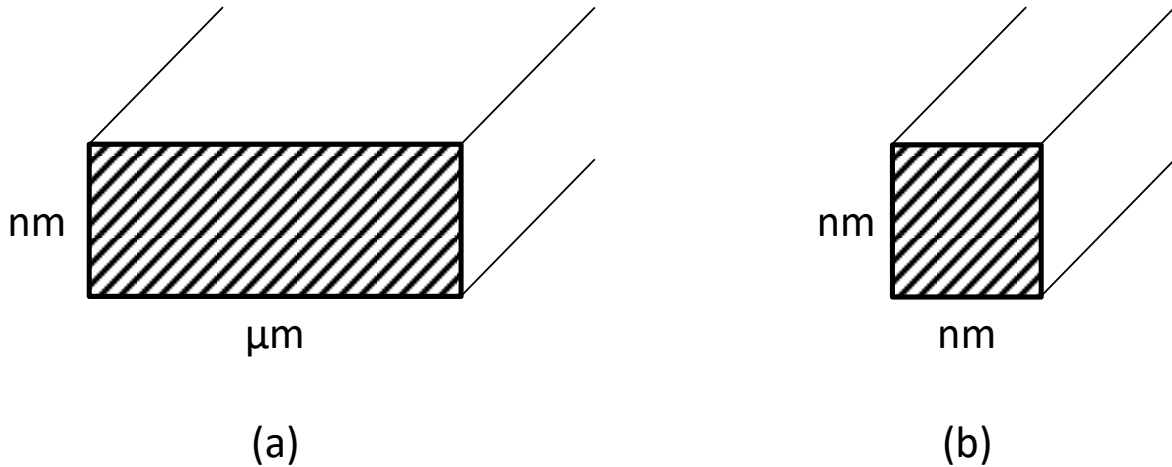
Figure 22: Nanochannels are categorized by their aspect ratio. A 1D planar nanochannel (a) has a width significantly larger than the depth, indicating a small aspect ratio. A 2D nanochannel (b) has a nanometer depth in addition to a nanometer width.

Various methods exist for fabrication of nanochannels. Examples of these techniques include micro-electro-mechanical-systems (MEMS) based surface and bulk micromachining, nanoimprinting, and direct nanolithography methods. The simplest form is the planar nanochannel, which has a low aspect ratio and a height in the nanometer range. A micrometer scale width allows for the use of standard photolithography techniques while the nanometer depth is achievable via tunable etching,

A few methods to achieve a planar nanochannel use bulk micromachining, a thin film spacer, or a sacrificial layer (Abgrall, & Nguyen, 2008). Bulk micromachining etches into the substrate material to form the nanochannels, capped by bonding to another wafer. The spacer method uses thin film deposition to form a patterned layer to form nanochannels with a characteristic depth equal to the thin film thickness. Research utilized amorphous silicon to fabricate nanometer deep by micrometer wide channels using both RIE and a lift off technique (Kutchoukov et al., 2004; Schoch, & Renaud, 2005). With the sacrificial technique, a patterned layer forms the inverse of the desired nanochannels. Deposition of a capping layer seals the nanochannels followed by the

removal of the sacrificial layer. Because of the relatively small scale of a nanochannel, the etching time of the sacrificial layer can be inordinately long, and in one instance required 80 hours for a 1.5mm long channel with cross section of 50nm by 1μm (Stern, Geis, & Curtin, 1997). All three of the listed methods have an inherent risk of collapse with the tremendous difference in the order of magnitude of the width vs height of the nanochannels.

Cao et al. (2002) used nanoimprint lithography and non-uniform deposition techniques to generate sealed nanochannels as small as 10nm X 50nm. Guo, Cheng, and Chou (2004) developed a method that presses a hard nanochannel template into a soft but curable polymer layer. The polymer layer thickness dictates the size of the nanochannel but this method achieved feature sizes down to 10nm X 10nm. A potential problem with the soft polymer layer is partial or complete sealing of the nanochannel if not properly controlled. Lee, Yang, Myung, and George (2003) developed a CMOS compatible method using multiple steps and selective etching, which resulted in 25nm X 100nm nanochannels. The actual dimensions of the nanochannel can be custom tailored based on the thermal oxidation, deposited film thickness, and photolithography.

Other common methods utilize electron beam lithography and laser machining which pattern high-resolution nanoscale trenches. However, e-beam lithography-based processes are relatively expensive and laser machining can only produce nanochannels with a minimum width of a few hundred nanometers. Tas et al. (2002) developed two methods, utilizing microfabrication techniques that produced nanochannels down to 90nm X 40nm with a potential to reduce the dimensions down to 10nm X 10nm using their technique. One method utilizes layering along with the deposition of a nanowire that is etched away to create a nanochannel while the other method uses a cantilever which is pulled down by capillary force and permanently adheres to the surface

46

(Tas et al., 2002). However, removal of the sacrificial material can be problematic and any fluid used can be difficult, if not impossible, to remove.

Another technique to fabricate nanochannels is Atomic Force Microscopy (AFM) nanolithography. This process uses the AFM probe tip to scribe a line in the material surface that is on the same order of magnitude of the scribing tool (Fang, Weng, & Chang, 2000). Particularly useful, an AFM can both pattern and characterize the nanoscale device. However, the resulting structure cross section is quite irregular because of the pyramidal tip that furrows the surface.

Fluid phase separators require channels at the length scale of 100's of nanometers to tens of micometers. Therefore, common microfabrication techniques were sufficient for this research. Both wet and dry etches used in conjunction with photolithography created channel depths on the nano-micro length scale.

2.4.1 *Wet Etching*

Buffered oxide etch (BOE) is a wet etch that is microfabrication process commonly used to etch silicon nitride and silicon dioxide. BOE is a mixture of ammonium fluoride (NH4F), the buffering agent, and hydrofluoric acid (HF). The buffering agent is necessary to control the etch rate because concentrated HF etches silicon dioxide too quickly and strips patterned photoresist (Wolf & Tauber, 1986). A polymer beaker is necessary as BOE etches glass. Buffered oxide etch 5:1 etched silicon oxide at room temperature for twenty-five minutes each step, Figure 23.

Figure 23: Buffered oxide (BOE) 5:1 was used to etch a 1000nm silicon oxide layer to expose the silicon wafer in a desired mask pattern.

Potassium hydroxide (KOH) is a wet etch that preferentially etches silicon on the {111} crystallographic plane, which for a 100 wafer is at a 54.7 degree angle from the surface (Kern, & Vossen, 1978). KOH requires a mask of silicon nitride or silicon dioxide since they etch at a much slower rate than silicon. A 35% w/v KOH, in metal pot, heated to 85°C etches silicon at approximately 100μm per hour. Temperature must be monitored periodically to maintain a consistent etch rate. Figure 24 shows the experimental procedure for KOH etching of silicon at an elevated temperature.

Figure 24: Potassium hydroxide (KOH) etches silicon on the {111} atomic plane. Silicon oxide formed the mask, leaving exposed silicon susceptible to KOH etching, which formed the micro/nanochannels.

2.4.2   Dry Etching

Reactive Ion Etching (RIE) is a dry etching process used in microfabrication. Inside a vacuum chamber, electrons are stripped from a gas creating a plasma. Electrons strike the surface of the substrate creating a negative charge while the plasma has a positive charge due to its ionic composition. This bias causes the ions to move toward the negatively charged substrate and react with the wafer chemically and mechanically. Due to the directionality, the etch profile is rather anisotropic when compared to wet etching. Etch depth in RIE are commonly limited to around 10 microns with an etch rate of 1 μm/min.

Deep Reactive Ion Etching (DRIE) is similar to the RIE process with the caveat that it is able to etch significantly deeper (600μm) at a faster rate (20 μm/min). Also known as the Bosch

Process, DRIE uses two steps: etch and passivation. Sulfur hexafluoride (SF_6) is highly reactive with silicon as an etchant while octafluorocyclobutane C_4F_8 passivates the surface preventing further etching. The two steps alternate with SF_6 etching the floor of etched areas (including the C_4F_8 layer) but because of the directionality leaves the sidewalls unaffected. Aspect ratios of 40:1 are achievable but the two-step process leaves the sidewalls scalloped.

3   DISSERTATION OBJECTIVES

The overall goal of this dissertation was to design a fluid phase separator using nanochannel arrays for a CubeSat propulsion system to be launched in the near future (ARKSAT-2). When water ejects to space it freezes, creating ice crystals that are detrimental to a propulsion system. Therefore, the phase separator will act as a vaporizer to inject water vapor into the propulsion system which is expelled into the vacuum of space in the form of thrust. The nanochannel array must be small enough to limit two phase flow, yet large enough to maximize mass flow. An optimal design/form factor exists to generate vapor for use in a CubeSat propulsion system to generate thrust enabling freedom of movement. The specific objectives of this work were to:

- Determine vapor viscosity for aqueous antifreeze solutions useful for thrust characterization and prediction. Antifreeze solution contained at atmospheric temperature and pressure in a vacuum chamber vaporizes as a mixture of antifreeze and water vapor to simulate a space environment. The viscosity of the evolved vapor is unknown, but necessary for flow estimation in space.

- Evaluate expansion characteristics of aqueous antifreeze solutions for use as a propellant on volume-limited cubesatellites. The intent of antifreeze, by nature, is remain in the liquid phase. Yet, CubeSat volume limitation and extreme temperatures of space necessitate a proper understanding of expansion during crystallization.

- Study nanofluidics of a fluid phase-separating nanochannel array. Flow across a nanochannel is usually pressure driven while in the novel propulsion system the fluid is at ambient pressure. Additionally, a binary component fluid, aqueous propylene glycol, is studied in a nanochannel where other tests examine a single component fluid, primarily water.

4   MESO-SCALE FLUID FLOW

4.1   HAGEN POISEUILLE FLOW IN A MICROCHANNEL

Initial approximations of flow through capillary tubes assumed Hagen-Poiseuille flow of aqueous propylene glycol vapor. Channel size determines flow regime, see 2.3.1, but for larger channels with vapor flow, Hagen-Poiseuille is valid. Capillary tubing procured from McMaster-Carr had inner diameters of 0.0325" (825.5μm), 0.0225" (571.5μm), 0.0125" (317.5μm), and 0.1" (254μm). Calculations assumed vapor pressure driven flow through the capillary tubing with no liquid flow. Capillary tube diameter and composition of propylene glycol varied to predict experimental flow rates regarding material properties, see Figure 25. Viscosity values for vapor phase aqueous antifreeze assumed a linear relationship between water vapor and propylene glycol vapor obtained from Kane et al. (1996). Density values for water vapor and vaporized propylene glycol assumed ideal gas behavior at standard ambient temperature and pressure.
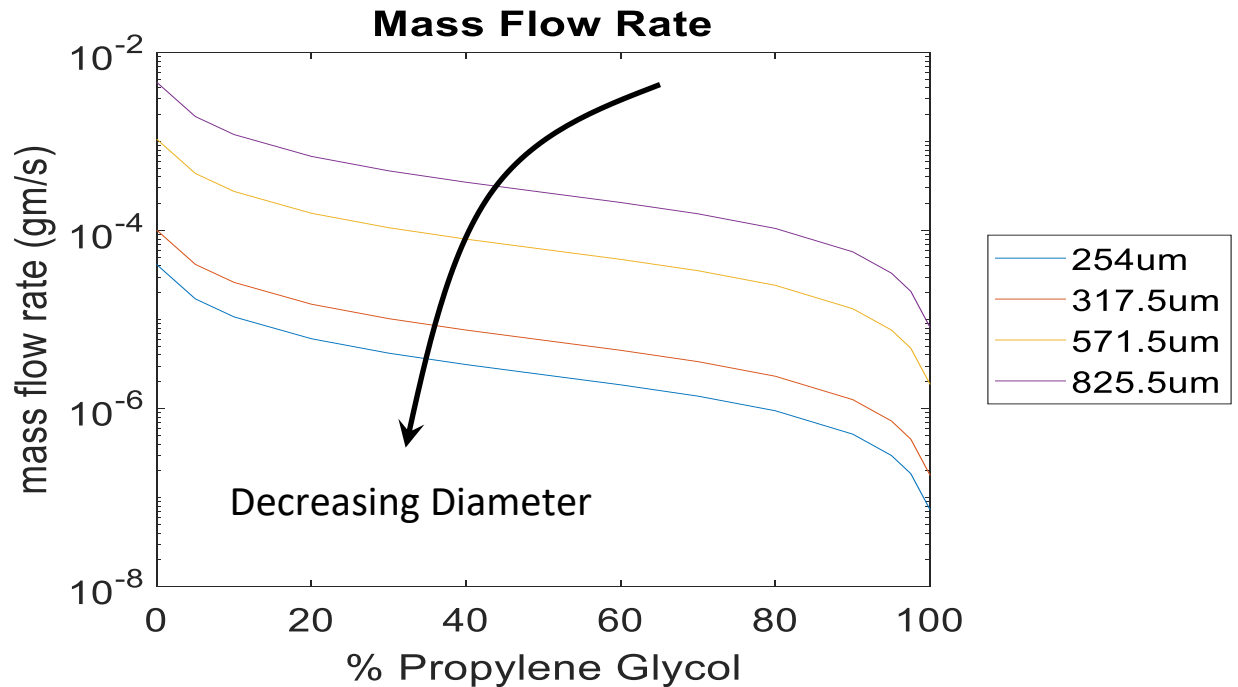
Figure 25: Using Hagen-Poiseuille law, Equation 5, theoretical flow of aqueous propylene glycol vapor was calculated for 254μm, 317.5 μm, 571.5 μm, and 825.5 μm diameter channels. Flow rate approximations aided in the design process and served as a sanity check for experimental data with known material properties.

4.2   EXPERIMENTAL SETUP
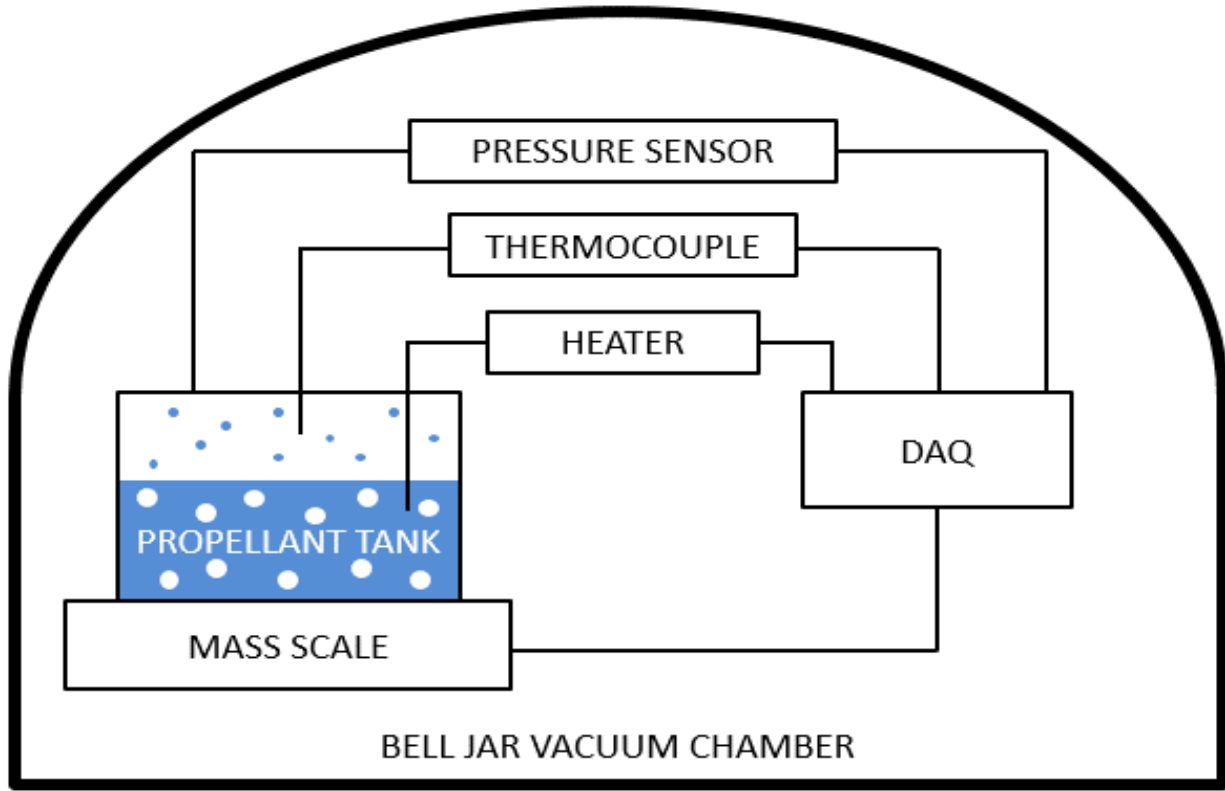
Figure 26: The general schematic of the mesoscale experimental setup schematic highlights the important equipment necessary to collect vaporization data.

Figure 26 displays an overview schematic of the mesoscale fluid flow experimental setup. Initially, a fabricated polycarbonate vacuum chamber (see Appendix 11.1) failed at maintaining the desirable space-like pressure conditions. The research necessitated a robust/dependable experimental setup. So, a Denton Vacuum DV-502, including the glass bell jar, served as the framework for the experimental vacuum chamber. The original configuration of the DV-502 pumped the bell jar to vacuum using mechanical pump and high vacuum by a diffusion pump. The setup, gutted entirely, utilized only the original glass bell jar and vacuum chamber, Figure 27(a). A new pump system schematic, Figure 27(b), utilized a roughing pump for low to medium vacuum and a turbo pump for high vacuum.
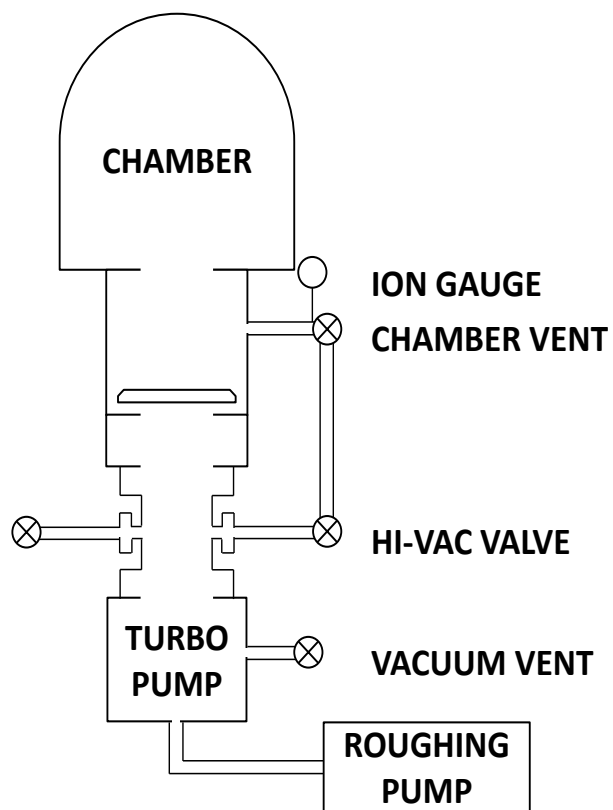
(a)   (b)

Figure 27: A DV-502 evaporator (a) was stripped and modified to allow for vacuum environment testing in a bell jar. The schematic (b) details modifications to the chamber, including the addition of rotary and turbo pumps.

A BOC Edwards rotary vacuum pump (E2M1.5 A371-32-902) and a BOC Edwards turbo pump (EXT75DX 63CF), Figure 28(b), maintained vacuum for experiments. A custom fabricated coupler adapted the turbo pump to the existing bolt pattern from the diffusion pump. Machined out of aluminum with a knife-edge groove, the ASA to 4.5" ConFlat flange adapter mated the turbo pump to the vacuum chamber. Clamping around a 4.5" copper gasket created an ultra-high vacuum seal.
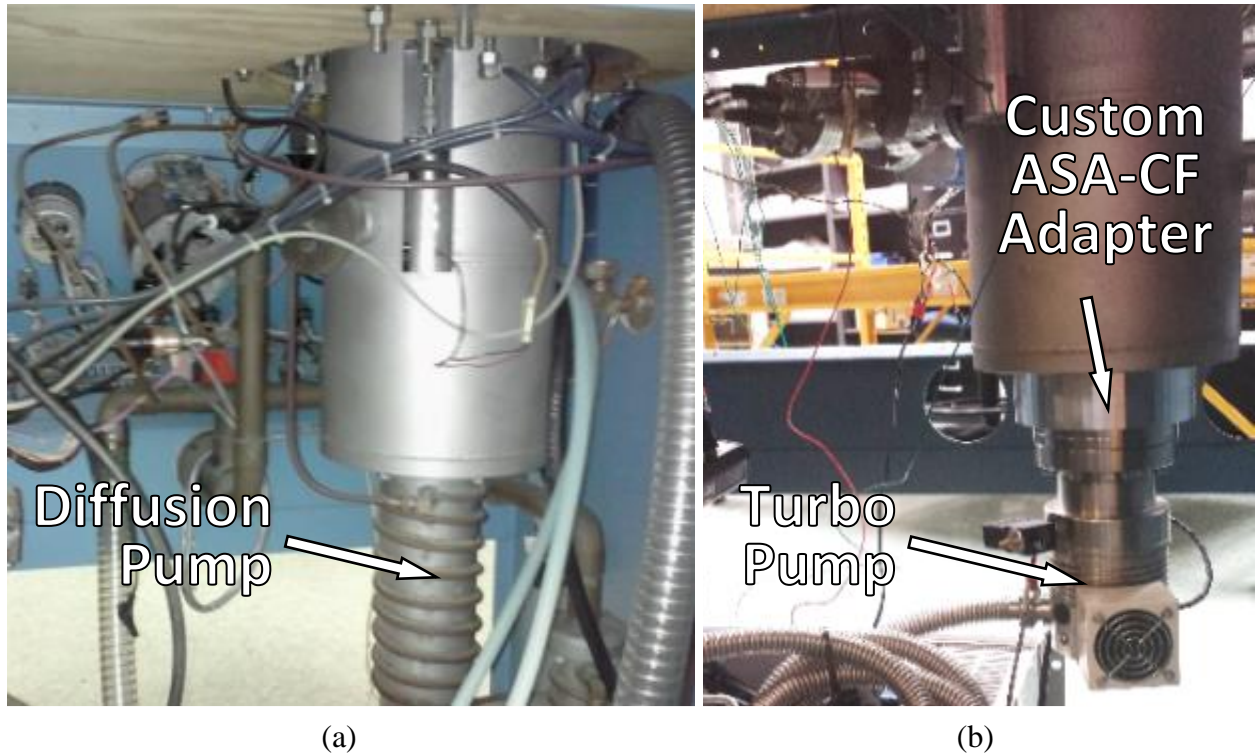
Figure 28: A diffusion pump (a) was removed and replaced with a turbo pump (b) to maintain a vacuum environment. The existing bolt hole pattern necessitated a custom-made adapter to mount the turbo pump to the vacuum chamber.

A series 275 Convectron Pirani vacuum gauge monitored the pressure inside the vacuum chamber. The Convectron has a pressure reading range of 760 Torr to 1×10^{-4} Torr, sufficient for experimental pressures in the chamber. A fast response time, in milliseconds, was beneficial for data collection. The NWKF16 flange on the Convectron allowed quick installation or changes to the setup. The 475 Convectron vacuum gauge controller output data via an RS232 in units of Torr. Overall, the bell jar setup maintained a high vacuum (~0.1 mTorr) for the mesoscale evaporation experiment.
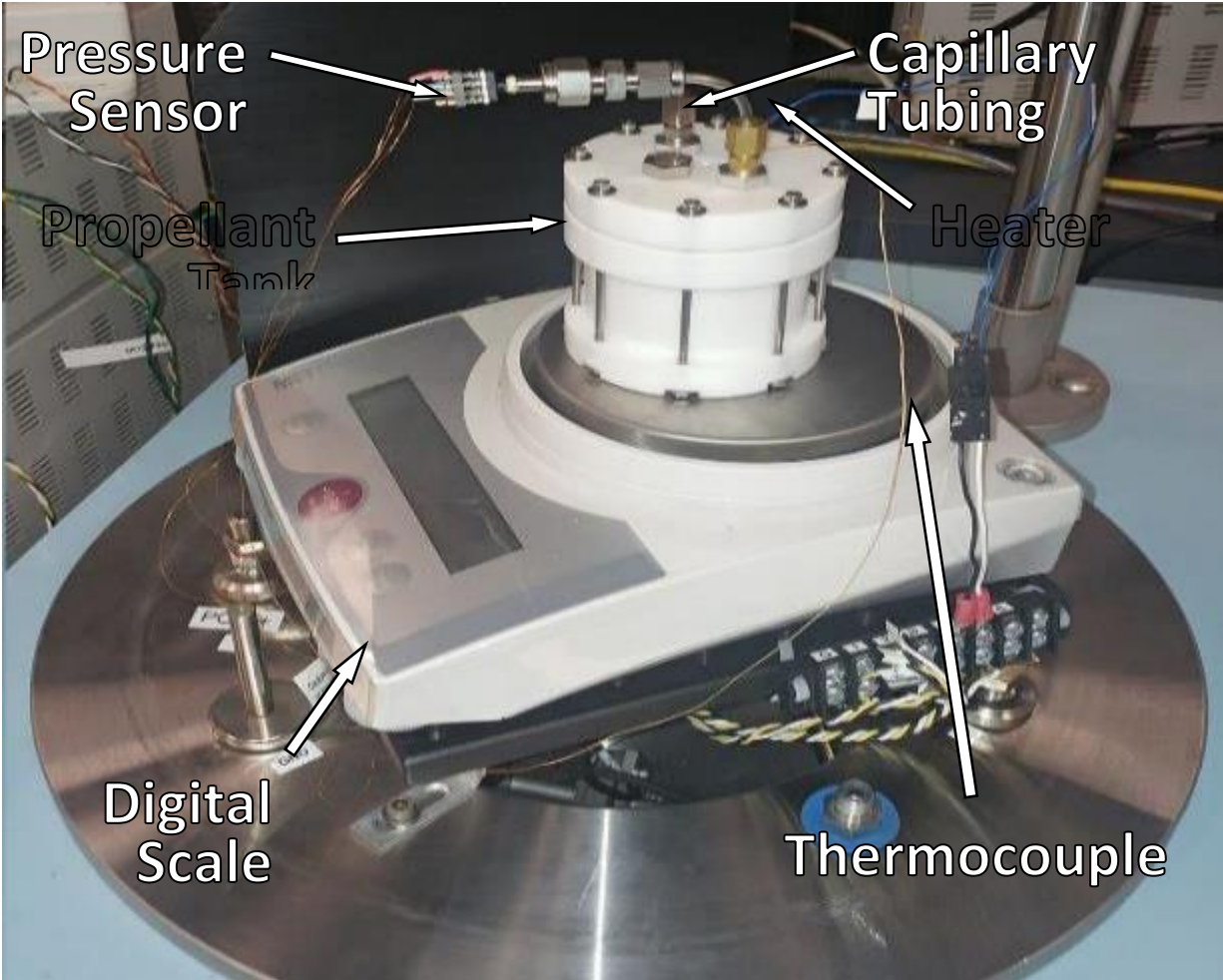
Figure 29: The mesoscale experiment used a Teflon propellant tank to restrict vaporization to the vacuum environment while limiting leaks and heat loss from the liquid. Propellant vaporization to vacuum is directly measured on the digital scale using the mass loss method.

Flow rates were calculated based on mass loss data collected by measuring the mass of an aqueous solution over time. A Mettler Toledo JL602-G/L scale, Figure 29, recorded all mass measurements with a readability of 0.01 grams. Typically used to measure gold and jewelry, the scale has a maximum loading capacity of 610 grams. Transmission via an RS232 enabled real-time recording of mass data. Calibration of the mass scale between 20 and 100 grams verified accuracy and linearity, Figure 30. Testing the scale in vacuum indicated a settling time during pump down of the chamber. This scale stabilization time necessitated omission of erroneous data during pump down and settling, Figure 31.
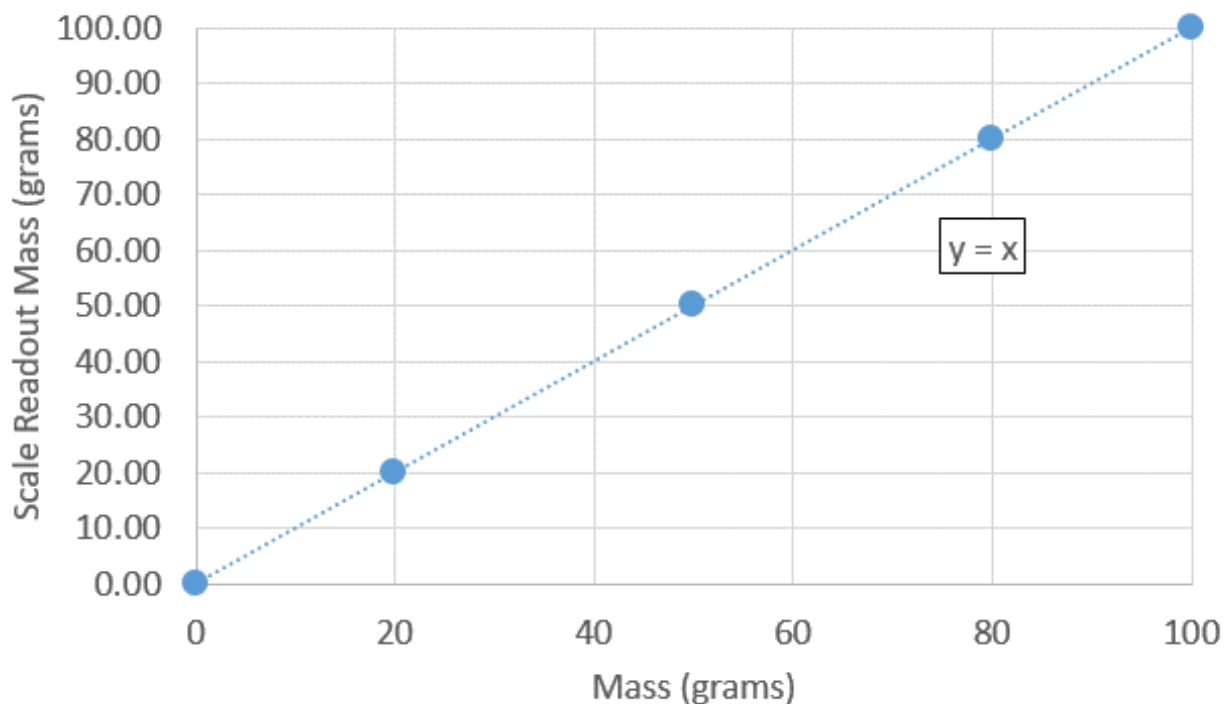
Figure 30: The mass scale was calibrated using calibration weights and indicated linearity and accuracy for measuring mass.

Water freezes in vacuum, so an immersion heater was necessary to control the temperature of fluid in the meso-scale evaporation experiment, see Appendix 11.1.2. A nichrome wire, 30 American wire gauge (AWG) bare nickel chromium (BNC), served as a resistive heater. A bang-bang thermostat program in Labview controlled the heater based on the high or low thermocouple reading of the fluid, see Appendix 11.5.3. A Honeywell TruStability board mount pressure sensor monitored vapor pressures of the aqueous solutions, see Appendix 11.5.2.
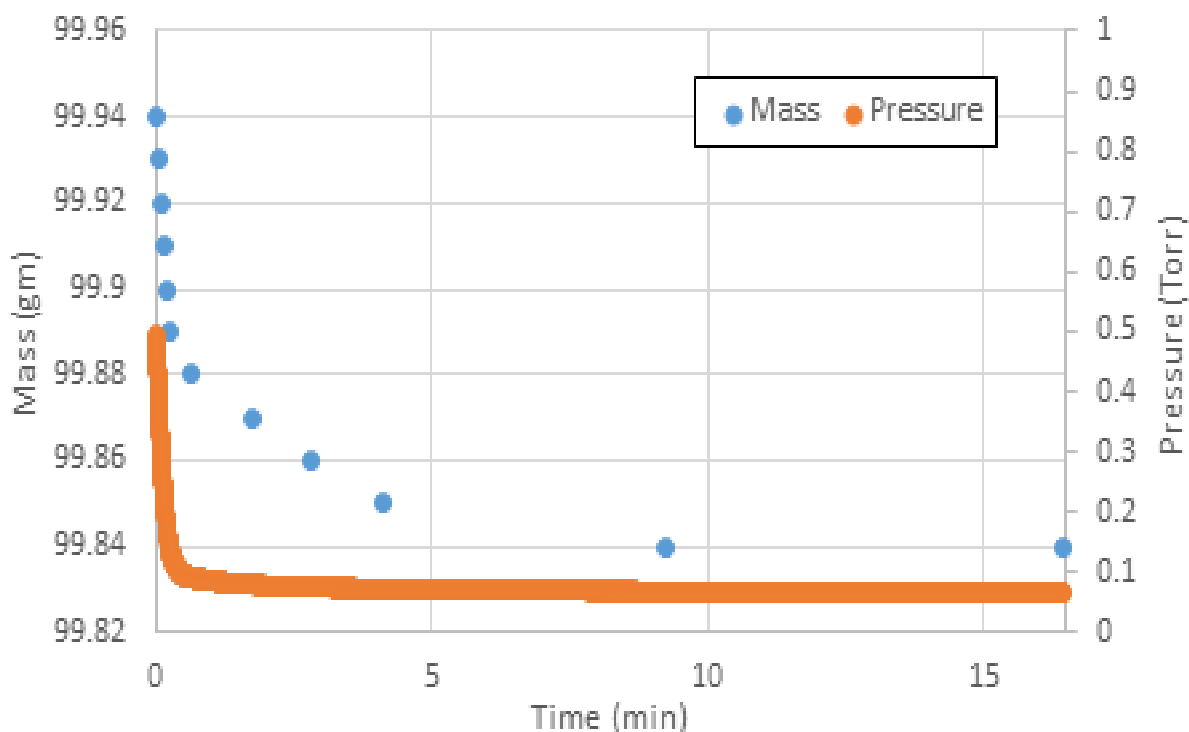
Figure 31: The mass scale stabilized in vacuum after approximately ten minutes. Data during pump down was omitted due to inconsistency of the reading.

4.2.1 Glass Chamber Viscometer

Mark 1 of the mesoscale evaporation experiment was simply a rubber stopper plugging a graduated cylinder. Visual inspection of the solution volume necessitated a clear container with volume demarcations. Leaks around the stopper and pressure build up quickly indicated the experimental setup was not robust enough for experimental trials. Yet, Mark 1 served as the first step in designing a more robust experimental setup, Figure 32. For more information and other problems encountered with Mark 1, refer to Appendix 11.1.2.
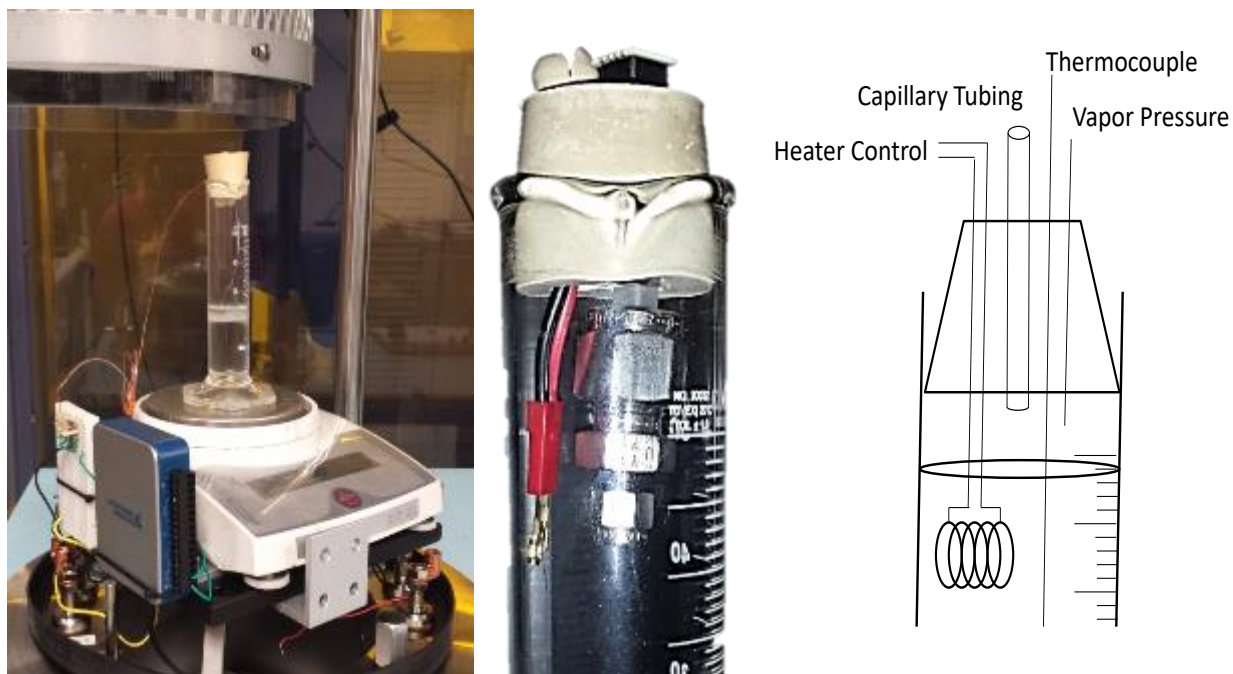
Figure 32: Mark 1 sealed the graduated cylinder with a rubber stopper. Over time, the rubber stopper leaked, but preliminary experimental ideas were determined from the crude setup.

Mark 2 aimed to reduce vapor leaks using o-ring seals and threaded fittings. A low form graduated cylinder with a custom fabricated stopper isolated the aqueous solution from the open vacuum environment. Figure 33 displays the design of the stopper with fittings for a heater, thermocouple, capillary tubing, and pressure sensor.
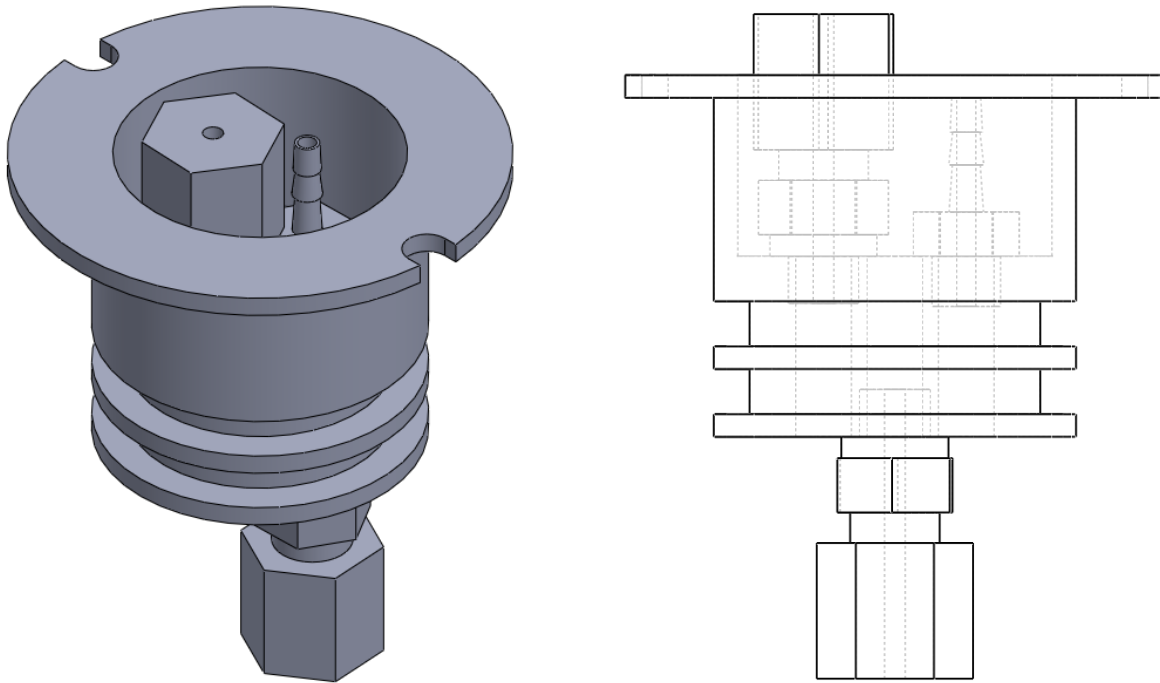
Figure 33: A custom-fabricated metal plug with double o-ring designed for a graduated cylinder maintained a tighter seal than Mark 1. Leaks were also decreased by using compression and threaded fittings.

Machined out of aluminum, Mark 2 established a tight seal with the graduated cylinder, seen in Figure 34. Different aqueous antifreeze solutions could be easily changed and tested with the improved stopper design. Testing of multiple capillary tubes, including different diameters and resulted in varying degrees of success. Data between trials was also very inconsistent. Additionally, heat transfer through the graduated cylinder affected the fluid flow rate and the research progressed with another experimental setup building upon information gathered from Mark 2.
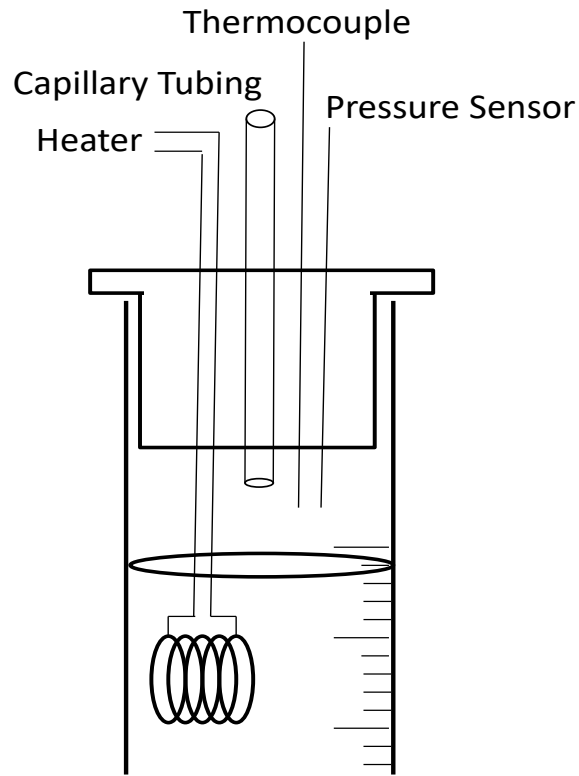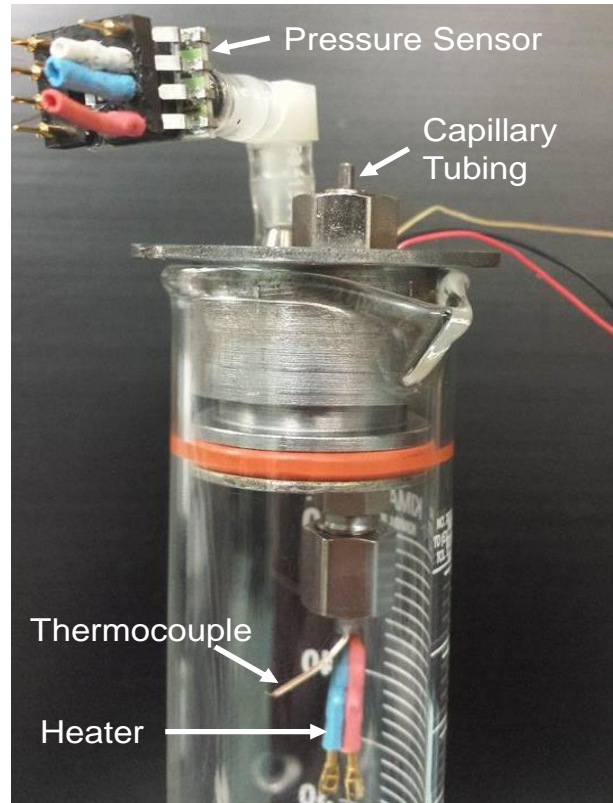
Figure 34: Mark 2 proved to be an adaptable experimental setup to control vapor evaporation. By measuring all necessary properties and using Equation 5, kinematic viscosity could be calculated for the vapor passing through the capillary tube.

4.2.2 Teflon Chamber Viscometer

Mark 3 aimed to provide an even tighter seal and isolate the fluid from the outside environment to minimize heat transfer through the chamber walls. Eight 4-40 machine screws compressed an o-ring between a Teflon disc and chamber creating a leak tight seal. Figure 35 shows the SolidWorks design and fabricated Teflon chamber. The standoffs minimized heat conduction from the chamber to the mass scale.
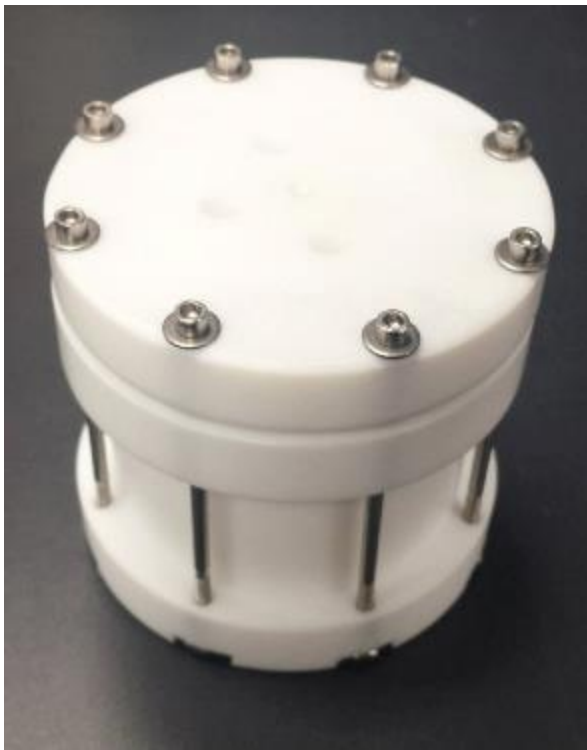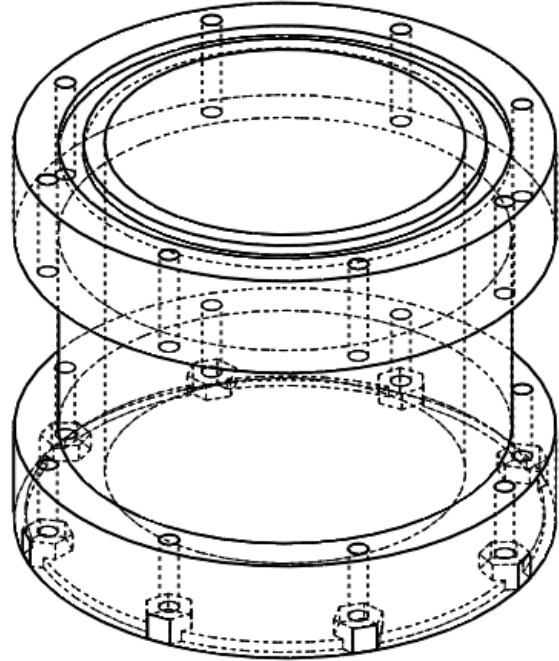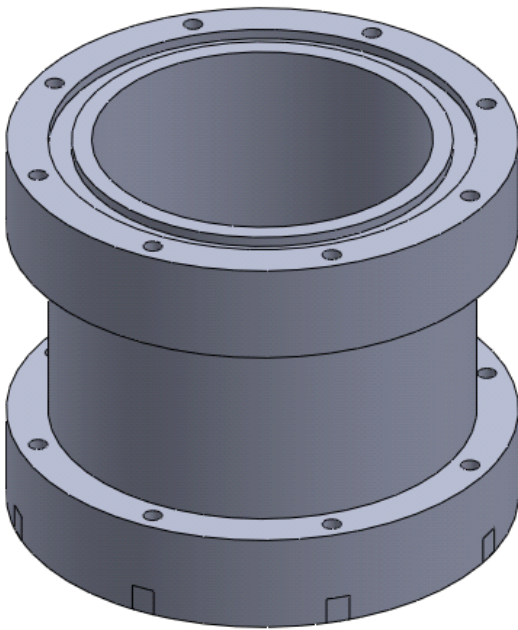
Figure 35: A Teflon propellant test chamber minimized error by limiting leaks and heat loss. Convection is minimal in a vacuum environment and conduction was limited by machining the bottom of the tank, leaving minimal stand-offs to conduct heat.

Teflon is a soft polymeric material with a low yield strength. Using small metal screw threads in Teflon is generally a bad idea due to thread pull out in soft material. Therefore, 5/16" aluminum bolts served as an intermediary between the smaller fittings and the Teflon, Figure 36. Drilled though holes and a machined surface provided access points for affixing the capillary tubing, pressure sensor, heater, and thermocouple while maintaining a leak tight test environment.
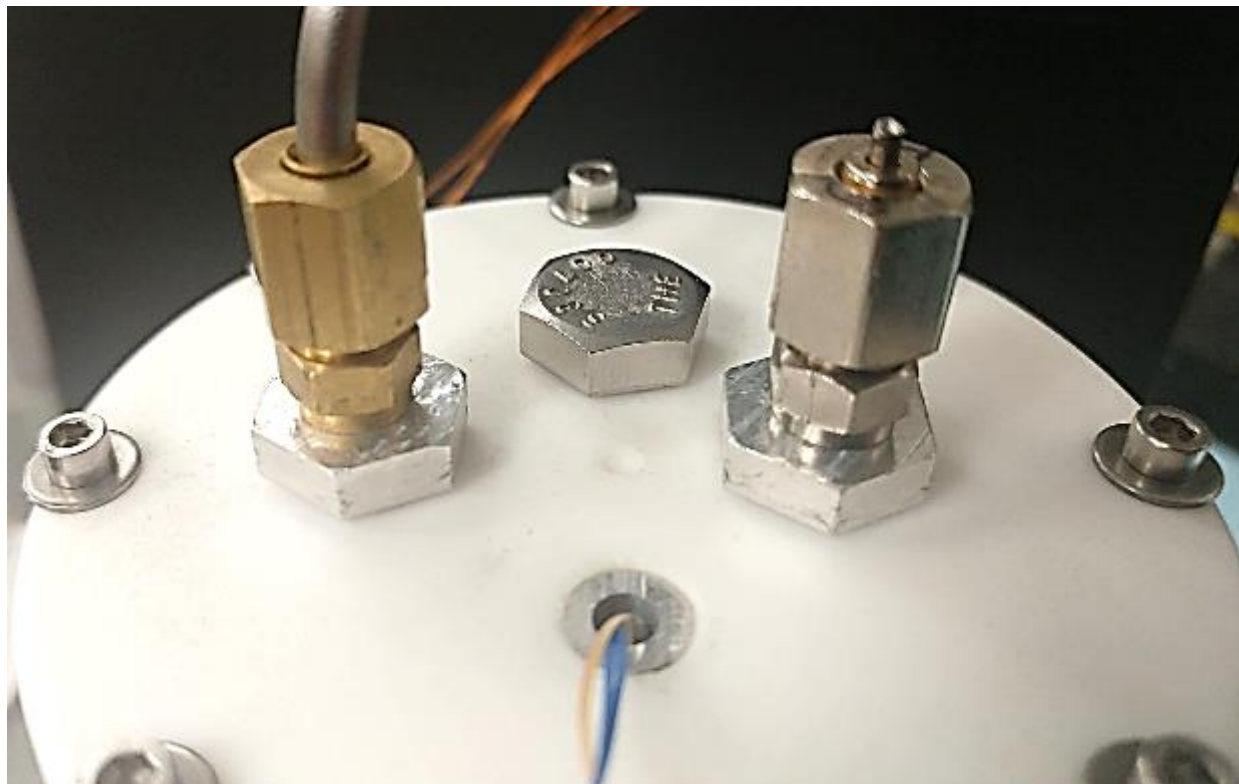
Figure 36: Sensor fittings were screwed into 5/16" aluminum bolts to minimize damage to the Teflon tank.

An immersion heater made of nichrome wire maintained fluid temperature in the experimental setup, Figure 37. Coiling the wire increased the exposed surface area resulting in quicker heating times and better temperature control. Heater and thermocouple wires passed into the Teflon chamber through a capillary tube, which was sealed with epoxy. Temperature regulation maintained 30°C +/- 0.5°C for the all Mark 3 experiments.

Figure 37: A coiled nichrome wire maintained constant aqueous antifreeze solution temperature during experimental trials.

4.3   RESULTS

Preliminary evaporation experiments using Mark 2 tested various concentrations of aqueous propylene glycol: 0%, 20%, 40%, 60%, 80%, and 100% propylene glycol (%w/w). Heating the solutions to 21°C and 30°C tested the effect of temperature on flow rate.   Three different capillary tubing diameters effectively restricted the flow rate: 0.0225" stainless, 0.0125" stainless, and 0.01" peak tubing. Aqueous antifreeze solution mass was recorded to monitor fluid mass lost through the capillary tubing. A linear regression applied to the mass loss data determined the mass flow rate to the vacuum environment. Figure 38 shows the results of this experimental trial over various solution concentrations where solid red indicates 30°C and outlined blue represents 21°C.

Glass Cylinder Viscometer
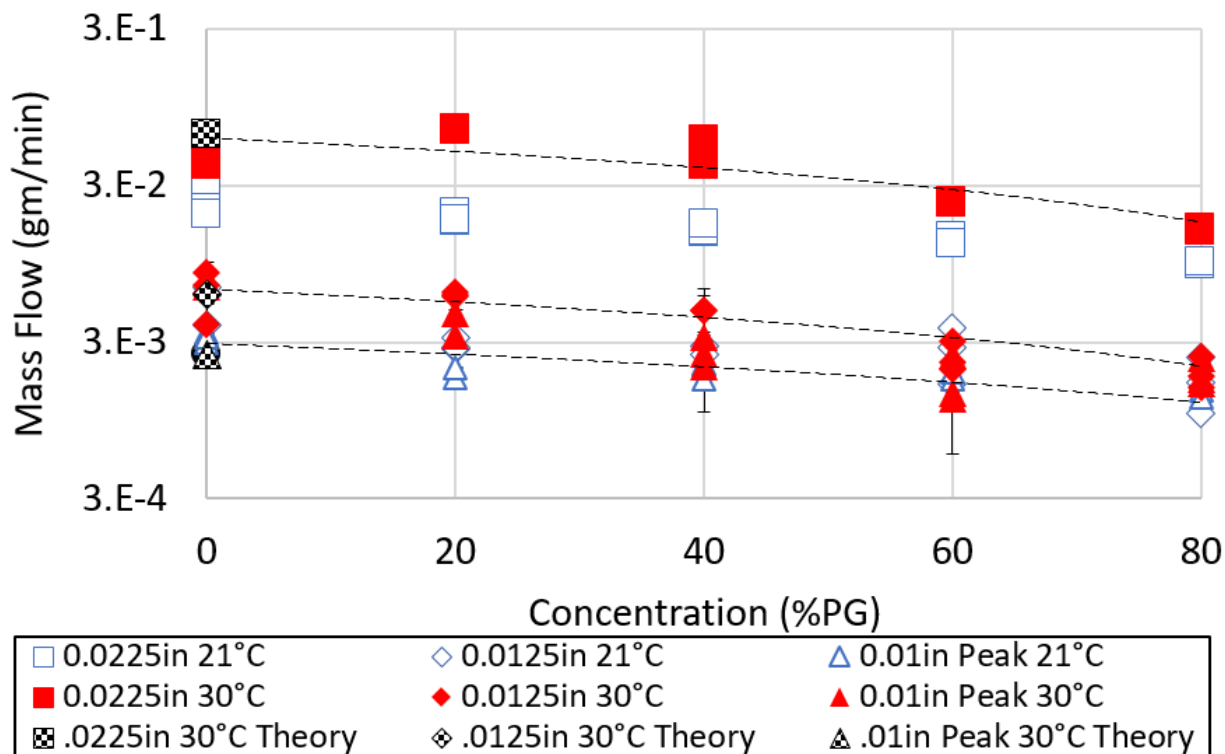
Figure 38: Mark 2 was used to measure mass flow rates through capillary tubes of various diameters. Data was collected using a mass loss method and applying a linear regression to the data. Uncertainty in the mass flow rate was determined using Logger Pro. Hashed data points represent theoretical Hagen-Poiseuille vapor phase flow for water vapor at 30°C since the kinematic viscosity is known at that state. Dashed lines were included to add clarity to the data and highlight trends. Uncertainty in the data is

Mark 2 experiments exposed important experimental setup guidelines. Larger diameter tubing resulted in excessive flow of liquid through, limiting the vacuum pressure achievable. Testing of capillary tubes with diameter 0.0325" resulted in droplets passing through the tube during fluid boiling, shown in Appendix 11.4.4.2. Liquid flow and not vapor passing through the capillary tube resulted in excessive flow rates when compared to Hagen-Poiseuille flow of vapor. Capillary tubing with 0.0225" diameters infrequently exhibited water phase leakage, but not as often as larger diameter capillary tubes. Therefore, future experiments used 0.0125" diameter capillary

65

tubes to eliminate water droplet transport while maintaining the highest possible vapor transport. Additionally, a heater controlled the temperature of the solution, but certain days the lab reached temperatures above 25°C. Without a means of cooling the solution, environment dictated a set experimental temperature of 30°C. Lastly, pure propylene glycol has a vapor pressure that is in the noise floor of the pressure sensor and the flow rate results in inordinately long trial times. Between those two factors, future experiments omitted 100% concentrations with immeasurable vapor pressures.

From Figure 39, it makes logical sense that the evaporation rate would be higher with a higher vapor pressure since it is a key factor in Hagen-Poiseuille Law. Similarly, increasing the solution temperature increases the energy of the system and atomic movement leading to a higher evaporation rate. However, the data is non-linear, indicating there are other important factors (i.e. variable material properties studied further) affecting the mass flow rate. This assumption is reaffirmed by the difference between experimental data and theoretical approximation for flow rate, shown in Figure 38. By comparing the expected curve from Figure 25 with Figure 38 and Figure 39 it is obvious viscosity is non-linear between pure PG and water.
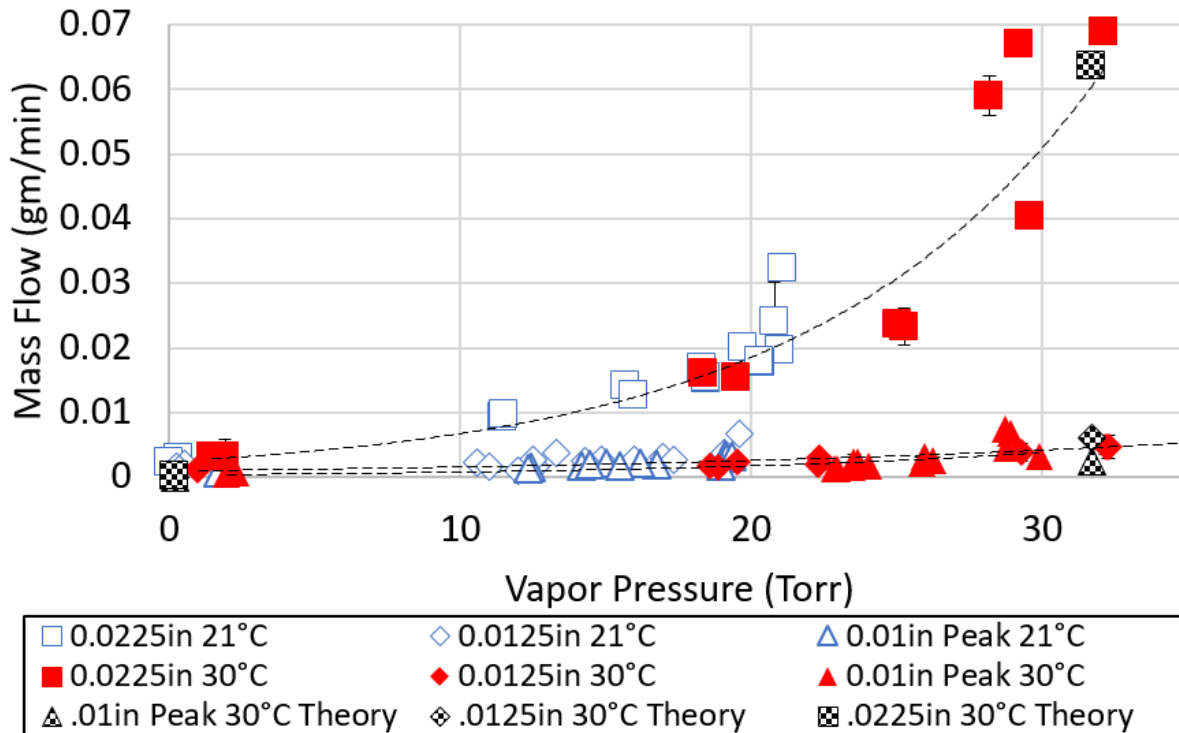
Figure 39: Vapor pressure of aqueous propylene glycol solutions directly affects flow rate. Nonlinearity of the mass flow rate with respect to vapor pressure indicates kinematic viscosity is nonlinear between water and propylene glycol. Uncertainty in the mass flow rate was determined using Logger Pro. Hashed data points show theoretical Hagen-Poiseuille vapor phase flow for water vapor at 30°C while the trend line adds clarity to the data trend.

Mark 3 reduced leaks with a tighter seal and heat loss by using Teflon. Applying lessons learned from Mark 2, Mark 3 tested aqueous antifreeze solutions at 30°C with the following concentrations: 20%, 40%, 60%, 80%, 90% w/w antifreeze. Measured vapor pressure compared favorably with theoretical values, as seen in Figure 40. Single data points for all concentrations represent experimental data and antifreezes test while the solid line is theoretical from Raoult's law for ideal mixtures. Additionally, Curme & Johnston (1952) measured vapor pressure for aqueous propylene glycol, represented by '-', and reported similar accuracy in measurements.
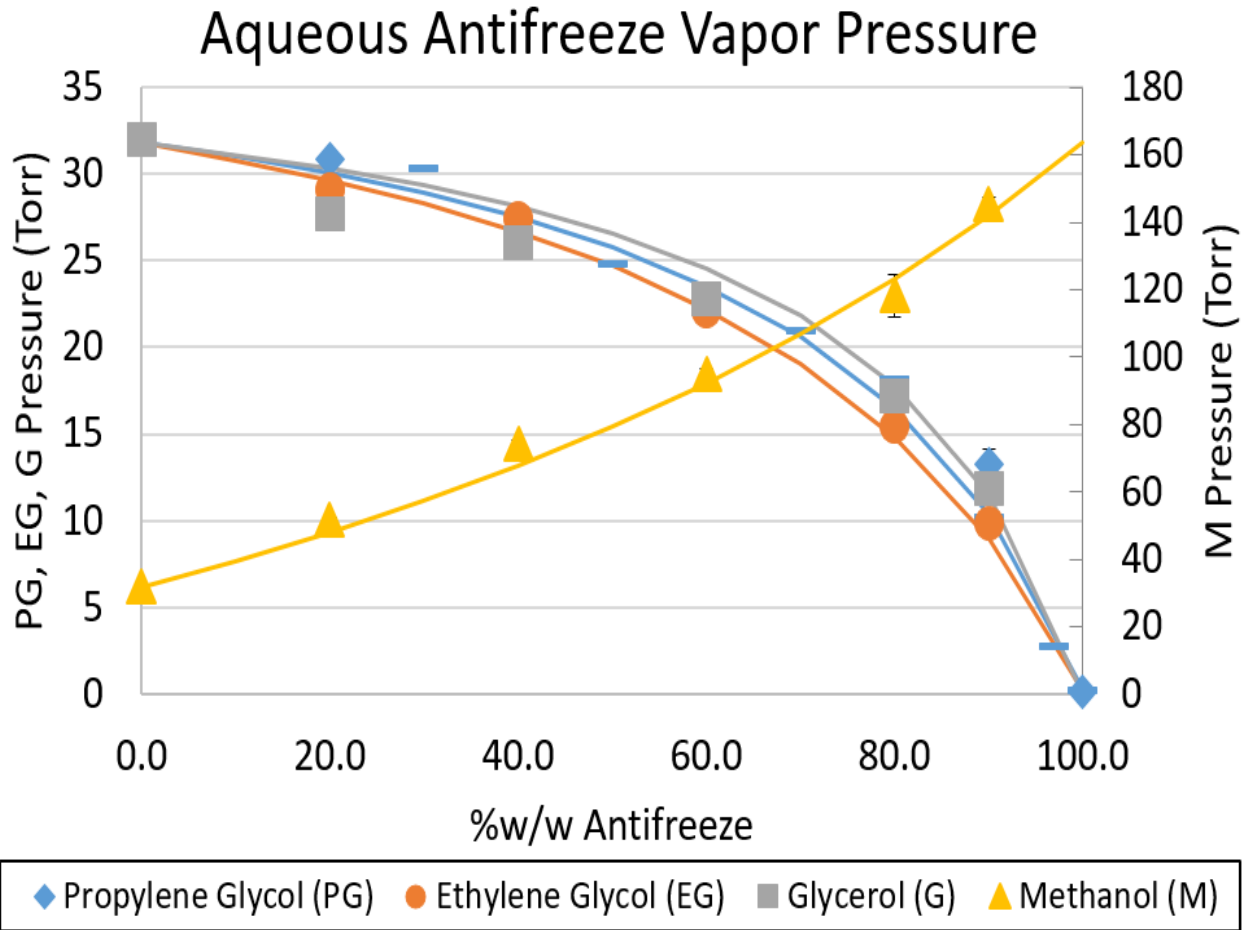
Figure 40: Vapor pressure was recorded during vaporization experimental trials and the mean of the data is displayed by individual data points. Uncertainty in the data is based on the standard deviation of pressure data during experimentation. Solid lines signify theoretical vapor pressure derived from Raoult's Law for ideal mixtures. Aqueous propylene glycol vapor pressure was also recorded by Curme & Johnston (1952) and are represented by (-).

Mark 3 used stainless capillary tubing 0.0125" in diameter with a length of 1.2", longer than the entrance length to ensure fully developed flow. Aqueous solutions of propylene glycol, ethylene glycol, and glycerol have similar vapor pressures, as noted in Figure 40, so it makes sense that the mass flow rates would follow a similar trend as well, Figure 41. With increasing antifreeze concentration, the flow rate declines in a similar manner to vapor pressure. Methanol has a distinctly different vapor pressure trend which increases with increasing concentration when mixed with water. Similarly, the mass flow rate increases as methanol concentration increases.
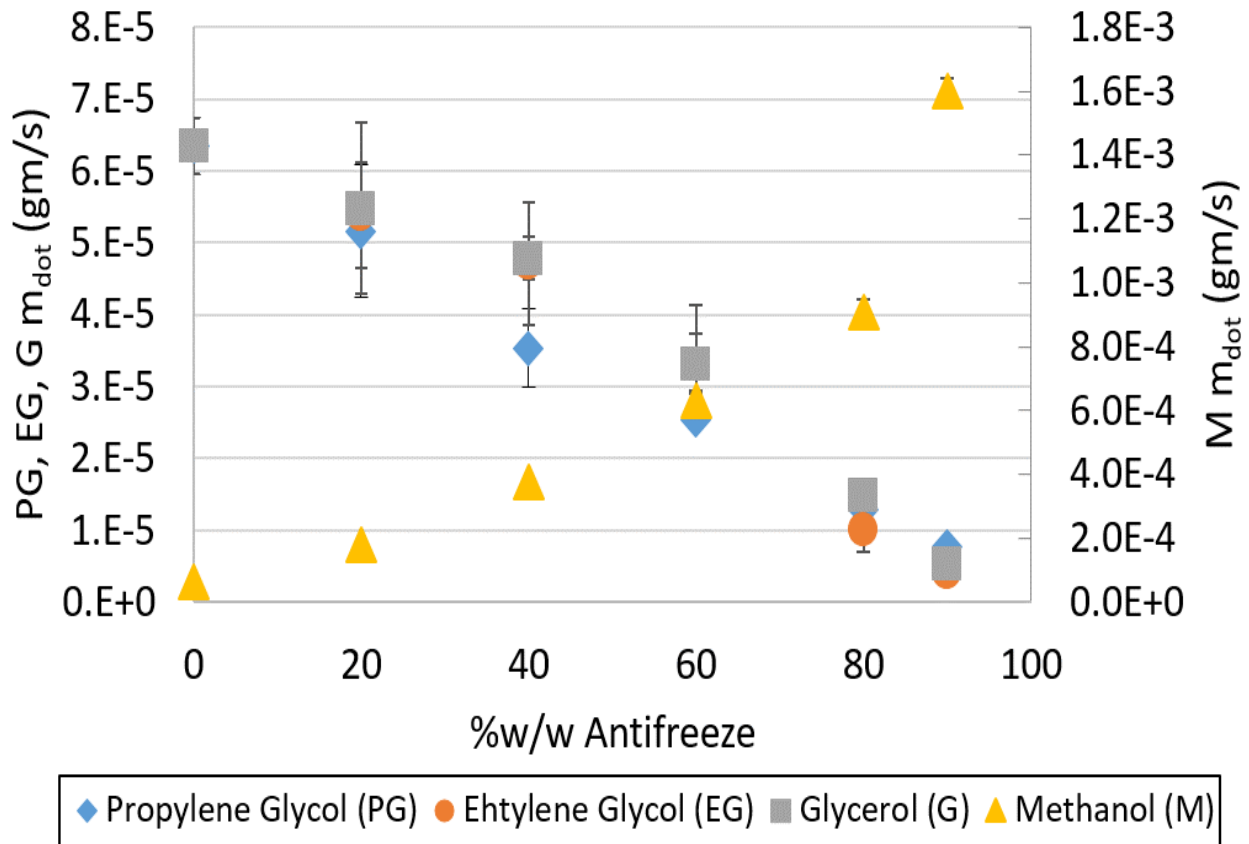
Figure 41: Aqueous antifreeze mass loss was recorded over time using the Mark 3 experimental setup. A linear fit applied to the data determined a mass flow rate and the systematic uncertainty was determined using the method outlined in Figure 42. Evaporation to vacuum was restricted by 0.0125" diameter capillary tubing.

A linear regression to the mass vs time data determination of the mass flow rate. The mass scale resolution of 0.01 grams lead to discretization, shown in Figure 42 as steps in the mass loss data. This discretization is even more evident during short trials. For evaluating linearity, a unique binning method determined uncertainty in mass flow measurements. Breaking up the mass loss data into two equal lengths, a linear regression determined the slope of each section of data. Figure 42: Uncertainty shows the standard deviation of the calculated slopes plotted against the length of the sections. Iteration of this process broke the data into 2^n segments for standard deviation

69

comparison for n values of 1 to 50. Compiling the composite data into Figure 42: Uncertainty

enabled determination of the point at which standard deviation increased with decreasing bin size.

Uncertainty reported in Figure 41 for each data point was extracted from the point at which the

standard deviation increased in Figure 42. The bin size corresponding to the uncertainty point

determined the minimum time necessary to obtain the desired level of uncertainty in the data. A

longer recording, assuming continued linearity, results in a lower uncertainty in the data.
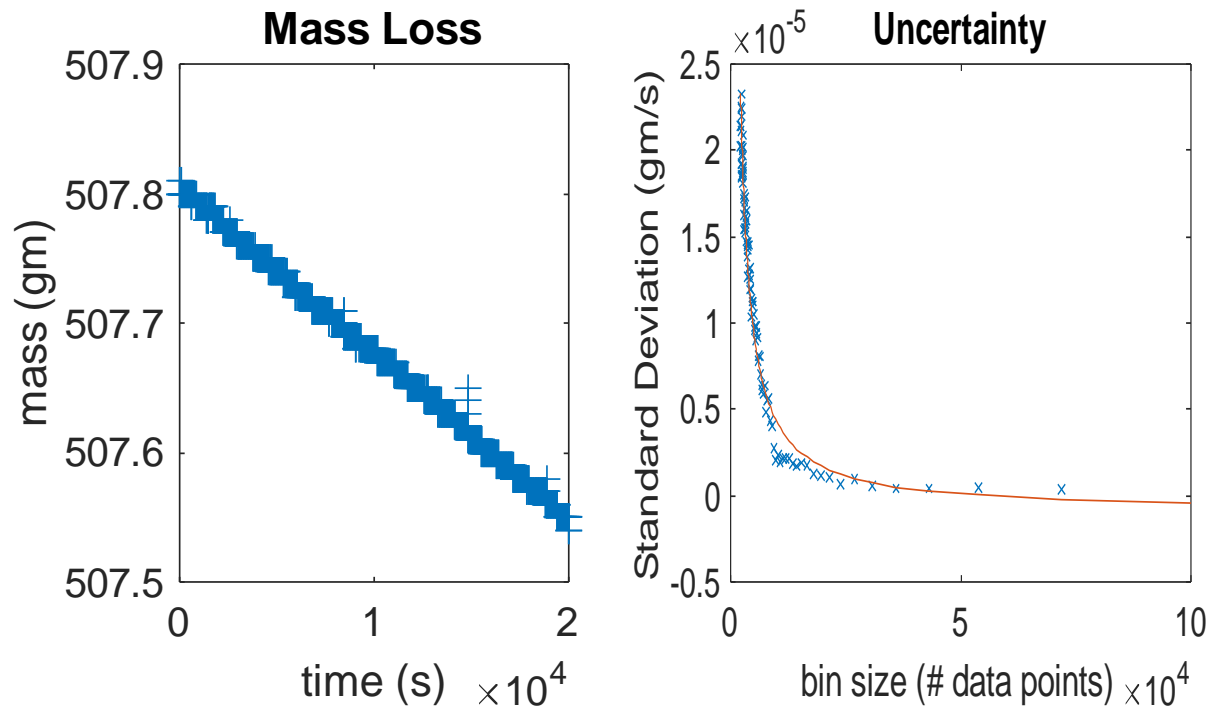
Figure 42: A linear regression applied to the raw mass data over time determined the mass flow rate. The trend, while relatively linear, was discretized due to the 0.01gram resolution of the mass scale. Binning the data into smaller line segments, applying a linear regression to each segment, and calculating a standard deviation from the regressions generated a single data point in the figure to the right. Iteratively repeating the process generated a trend with increasing standard deviation with decreasing bin size. From this trend, a linear uncertainty was determined when the standard deviation began to increase, and the corresponding bin size was reported.

Kinematic viscosity values for vapor evolving from aqueous antifreeze solutions derived from

Equation 5. Experimental kinematic viscosity for water vapor (3.358E-4 m^2/s) agree with

published values (3.3029E-4 m^2/s). Uncertainty values followed Equation 13 for combined

uncertainties from multiplication and division. Primarily dominated by mass flow rate, kinematic viscosity uncertainty also considered pressure and length in the overall value. Omission of diameter from uncertainty calculations was a result of no published tolerance for the capillary tubes.
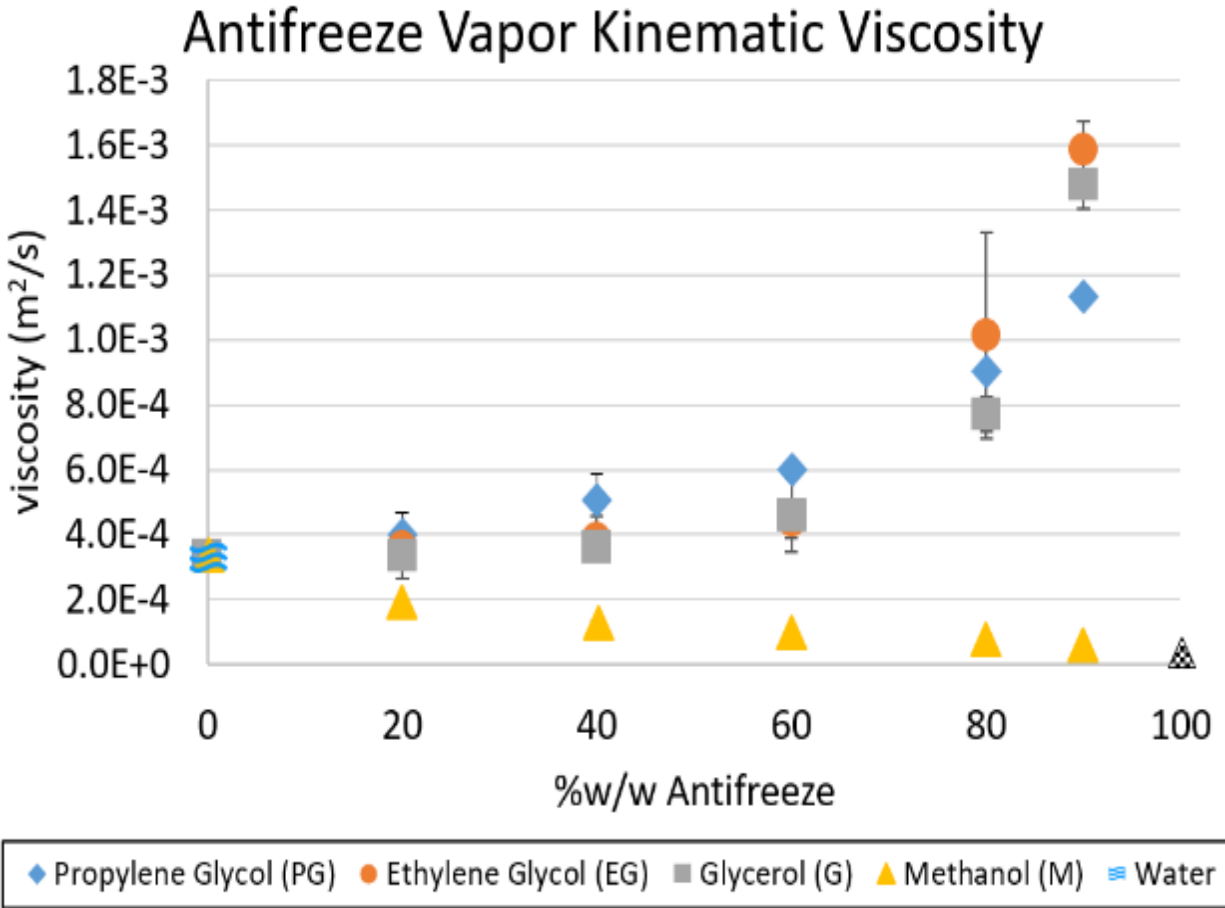
Figure 43: Kinematic viscosities of aqueous PG, EG, methanol, and glycerol vapor were calculated using Equation 5 and the mass flow data shown in Figure 42. Systematic uncertainties were calculated using Equation 13. A cross hatched triangle signifies pure methanol vapor while waves represent pure water vapor kinematic viscosity. Omission of Pure PG, EG, and G kinetic viscosities is a result of values not fitting in the scale of the graph.

$$\eta_{uncertainty} = \eta * \sqrt{\left(\frac{\Delta L}{L}\right)^2 + \left(\frac{\Delta P}{P_{vap}}\right)^2 + \left(\frac{\Delta \dot{m}}{\dot{m}}\right)^2} \qquad \text{Equation 13}$$

71

4.4   DISCUSSION

Initial design of the fluid phase separator assumed vapor phase flow through the nanochannel. Viscosity values are necessary when predicting flow through channels and vapor phase data is lacking for aqueous antifreeze mixtures. Experimental results successfully determined kinematic viscosity for evolving vapor from aqueous solutions of known concentration. The measured value for water vapor kinematic viscosity was 3.358E-4 m^2/s which nearly matched the published value of 3.3029E-4 m^2/s. Kinematic viscosity values of aqueous antifreeze vapor trended toward published values for pure antifreeze vapor. Published antifreeze kinematic values are 9.75E-3, 1.8E-2, 4.67E-3, and 3.53E-5 m^2/s for propylene glycol, ethylene glycol, glycerol, and methanol respectively. Viscosity values are also beneficial when determining thrust values and flow through a nozzle. Data determined from experiments furthered the understanding of aqueous antifreeze vapor.

Vapor pressure monitoring successfully matched the concentration of the aqueous antifreeze solution. Validation of this principle indicates vapor pressure monitoring is a viable method for in-situ concentration determination for predicting fluid properties. On-board monitoring of the propellant would offset non-linear evaporation rates of the binary fluid. Only aqueous methanol exhibited an appreciable trend during evaporation with a decreasing vapor pressure during every trial. For methanol, a decreasing vapor pressure is consistent with methanol evaporating at a faster rate than water. This concept is similar to distillation methods to separate methanol from water, as it will evaporate first under vacuum. However, as there is no method to trap the water into condensate, water is free to evolve to vacuum, albeit at a lower rate than methanol. The other three antifreeze solutions exhibited no noticeable trend over the experimental trials.

5 SOLUTION PHASE CHANGE EXPANSION

5.1 EXPERIMENTAL SETUP
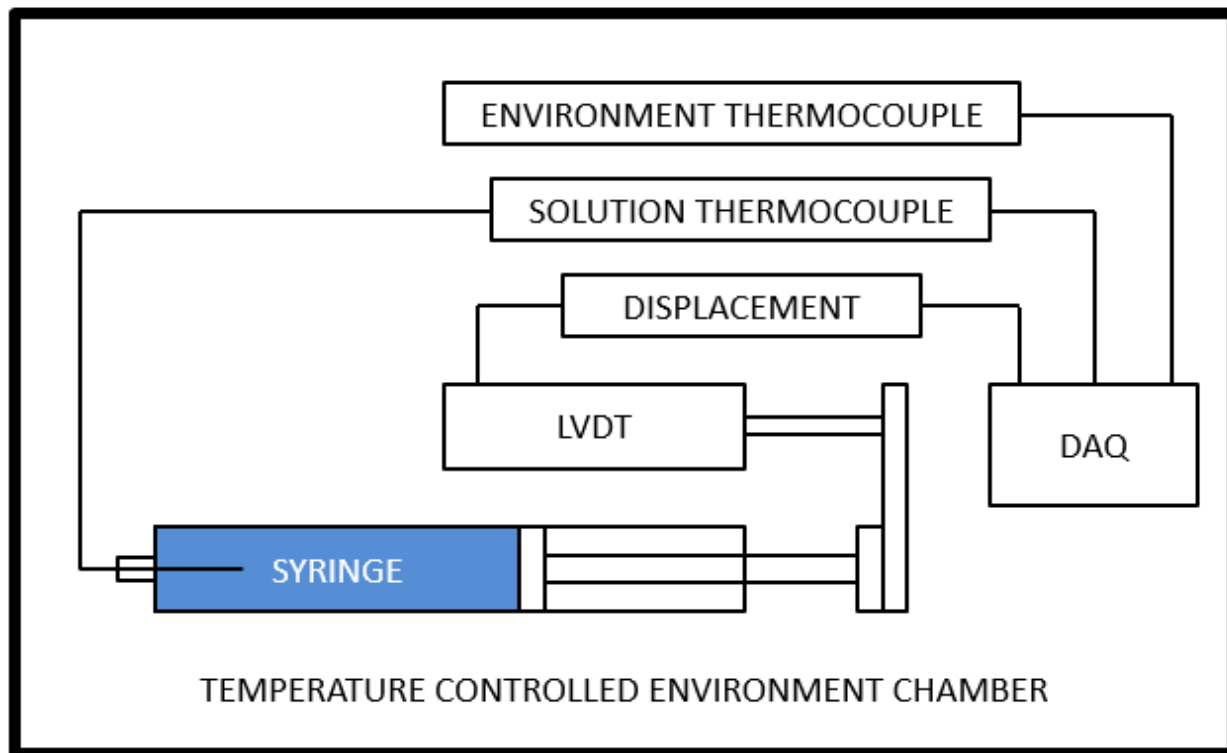
Figure 44: The general schematic of the solution phase change experimental setup schematic highlights the important equipment necessary to collect crystallization data.

Figure 44 displays an overview schematic of the entire experimental setup. Crystallization of water is a well-documented area of research, but the phase change of aqueous antifreeze has been neglected. Constraining an antifreeze solution in a syringe forced all expansion to occur in an axial direction. This research utilized a linear variable differential transformer (LVDT) to monitor the linear expansion of liquid during phase change to solid. An LVDT converts rectilinear motion to a corresponding electrical signal. An LVM110 signal conditioner controlled the voltage supplied to the LVDT and conditioned the electrical response from the LVDT. Designed in SolidWorks and shown in blue, Figure 45, are parts to couple the LVDT with the syringe enabling direct measurement of expansion during phase change.

73
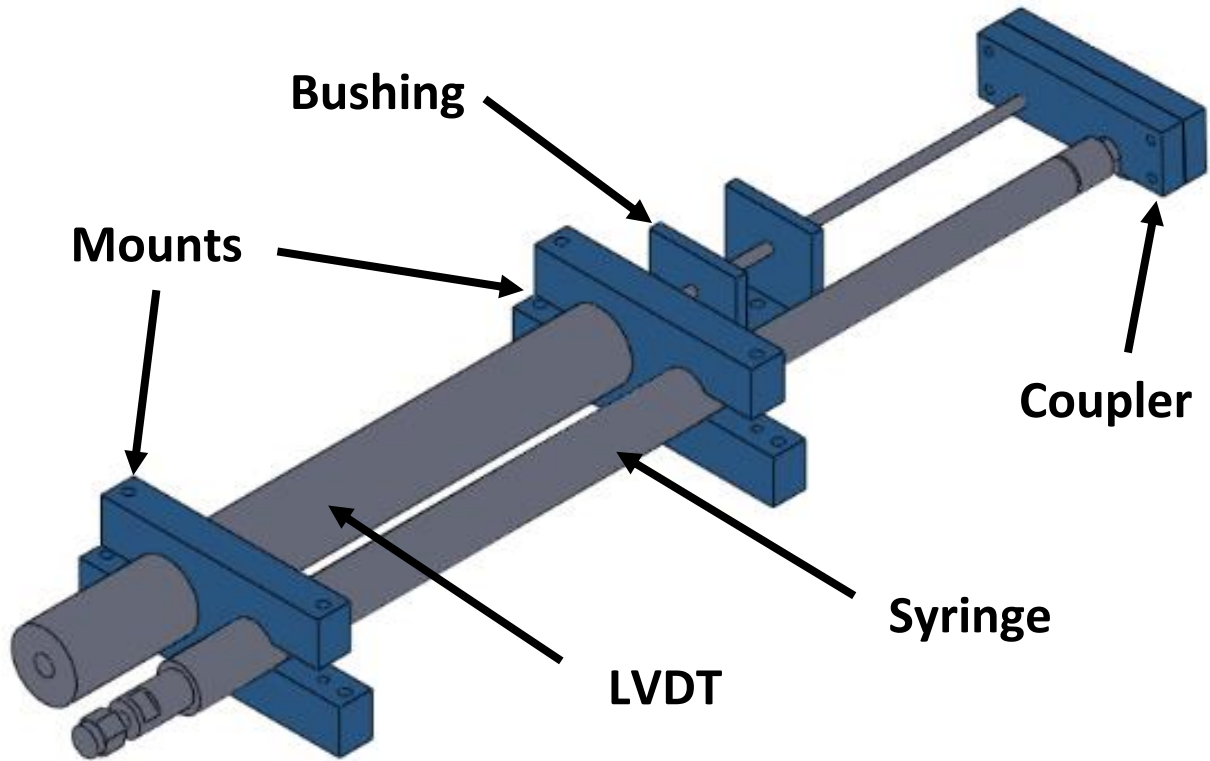
Figure 45: The LVDT coupled directly with the syringe to monitor movement of the syringe plunger. Custom-fabricated parts are shown in blue.

Machining the mounting hardware out of aluminum created a rigid and robust structure, reducing error in measurements. A Cincinnati Sub-Zero MicroClimate chamber (Model No. MCBH-1.2-.33-.33-H/AC) controlled the testing environment for heat transfer in aqueous samples during phase change. Real time recording of both rectilinear motion and solution temperature yields expansion curves. Appendix 11.5.4 shows the electrical diagrams for the LVDT and thermocouple.
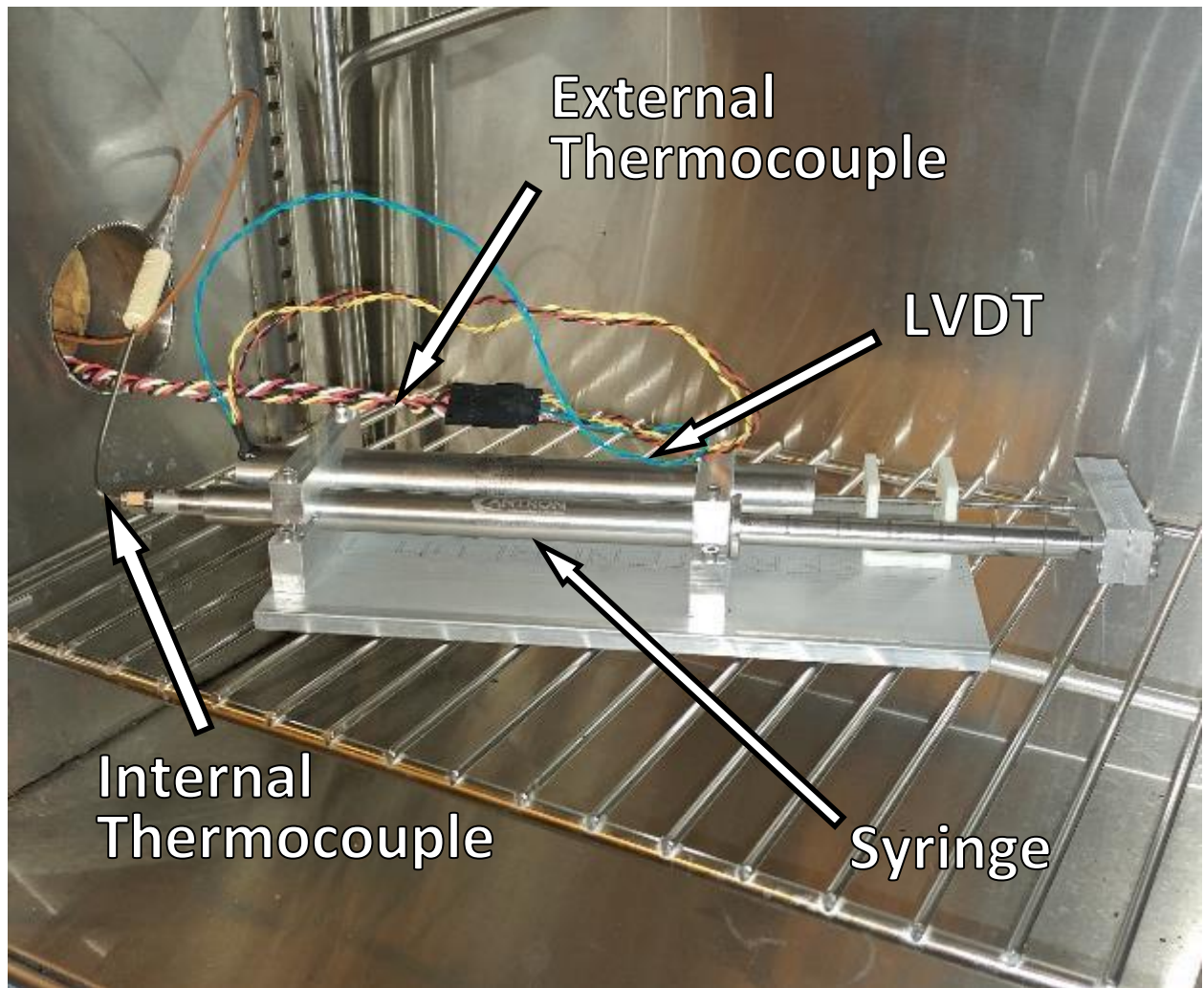
Figure 46: The phase change expansion was constrained to progress in the axial direction of the syringe. The LVDT generated a voltage corresponding to the syringe movement, indicating a volumetric expansion during crystallization. A microclimate chamber controlled the environmental temperature for testing. The aluminum fixture established a rigid experimental setup to minimize error in the direct strain measurements.

Sample preparation included mixing the aqueous antifreeze solutions to the specified test concentrations. Drawing the solution into the syringe introduced air bubbles, especially in the viscous fluids. A vacuum system with a condensation trap pulled air out of the fluid, removing dead space, and increased measurement accuracy. Cycling the high vacuum on and off for 5 minutes removed air without drawing water from the syringe.

Microclimate chamber temperatures cycled between 35°C and -65°C, working within equipment limitations, see Appendix 11.6.4. Upon completion of each trial the syringe did not contract during the heating stage, as there was no force on the plunger. Each melt and refreeze saw the plunger progress further and further in the axial direction. Thus, resetting the syringe to its null position was paramount to the accuracy of the phase change data.

In general, the testing procedure heated the sample up to slightly above room temperature (30°C) for a consistent starting point of each measurement. The chamber then rapidly cooled to -65°C only limited by the equipment capabilities. Upon reaching the -65°C, the temperature maintained for thirty minutes allowing the test fluid to cool. At that point, the temperature returned to 35°C to melt the crystallized antifreeze solution. Table 4 outlines the MicroClimate chamber control program for the aqueous antifreeze phase-change experiment.

Table 4: Sample temperature control program with CSZ Microclimate chamber

Step #	Step Type	Wait for Step	Time	Set Point
1	Ramp Time		1 sec	30C
2	Soak	1	1 sec	30C
3	Soak		10 min	
4	Ramp Time		1 sec	-65C
5	Soak	4	1 sec	-65C
6	Soak		30 min	
7	Ramp Time		1 sec	35C
8	Soak	7	1 sec	35C
9	Soak		10 min	
10	End			

Inserting a 1/16-inch diameter thermocouple enabled direct measurement of the solution temperature during phase change. As a side effect, inserting the thermocouple skewed the volumetric reading of the syringe. To account for the thermocouple volume, measurements of both the liquid and solid phase omitted the volume occupied by the thermocouple for an accurate reading. Figure 47 is a rendering of the thermocouple inserted into the syringe and the resulting occupied volume.
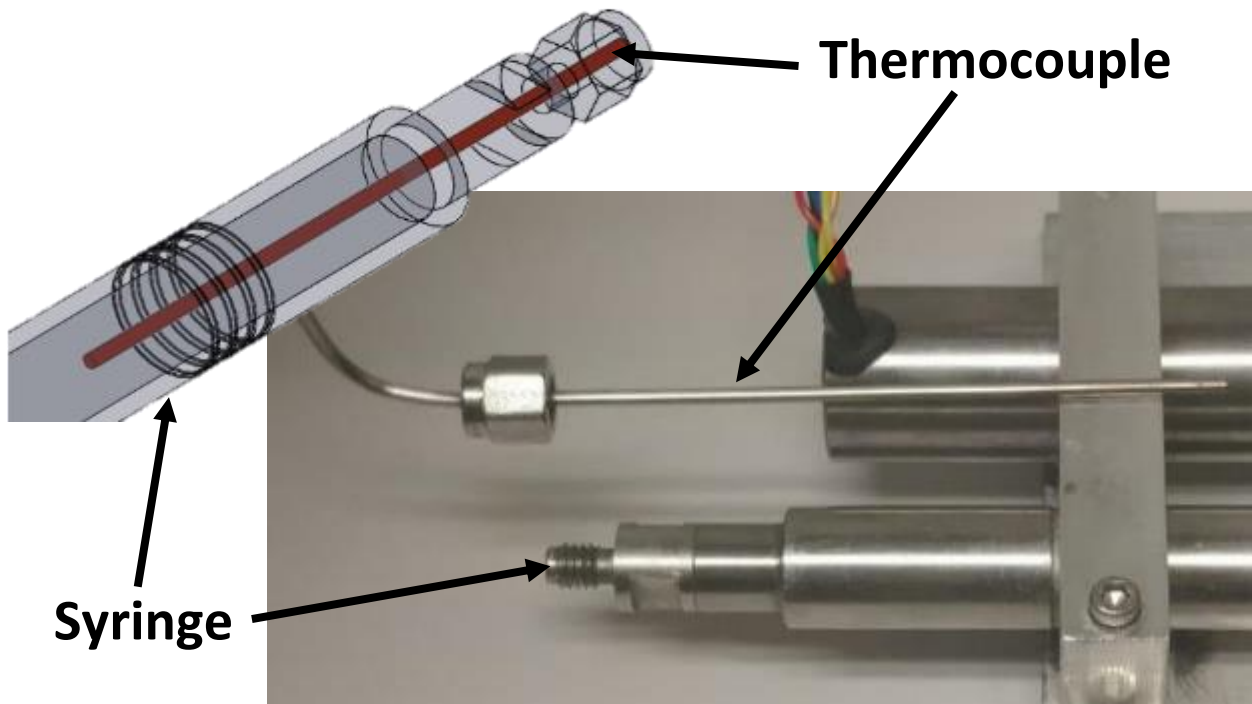
Figure 47: A thermocouple was inserted into the syringe to monitor solution temperature during cooldown and phase change. The thermocouple occupied a portion of the internal volume of the syringe and resulted in a measurement offset.

To start each experiment, the syringe drew seven milliliters of aqueous solution. 7mL of water should expand to approximately 7.6mL. This expansion was under the total syringe volume of 8mL and allowed for a small safety volume. Beginning each experiment with 7mL also established consistency between experiments while increasing accuracy by maximizing the translation of the LVDT. Adjusting the zero-potentiometer set zero output voltage at the null syringe position.

Coupling the syringe and the LVDT so the null position equated to 7.6116 mL allowed for a high accuracy reading. Adjusting the gain potentiometer scaled the output to -10V at -1inch and +10V at 1in, maximizing utilization of the full span of the LVDT. Figure 48 shows the calibration for converting the LVDT output voltage to syringe displacement volume.
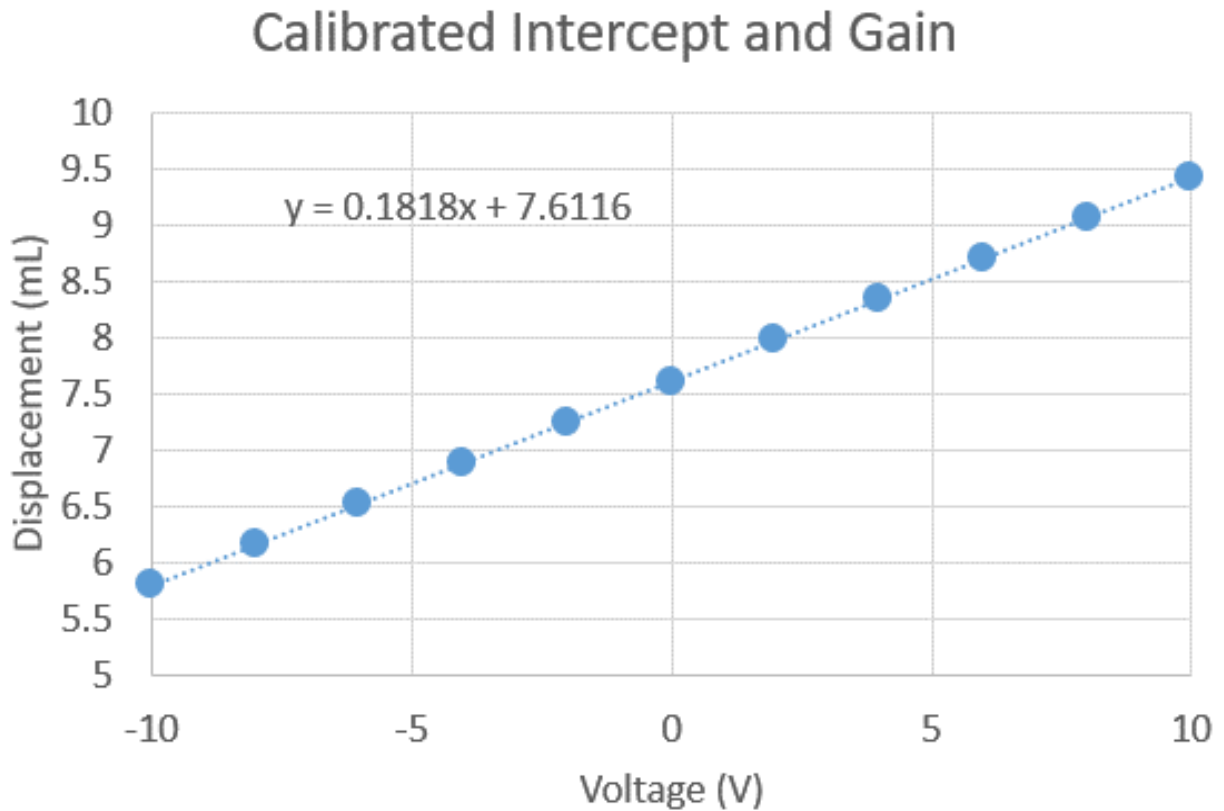
Figure 48: The LVDT was with the null position around 7mL to capture the syringe movement in the +/-1" region, maximizing measurement accuracy.

5.2 RESULTS

Experiments characterized the expansion of four antifreeze liquids: propylene glycol, ethylene glycol, glycerol, and methanol. Mixed with water, testing concentrations of 0%, 2%, 4%, 10%, 15%, 20%, 25%, 30%, 35%, 40% across all four fluids enabled comparative analysis regarding expansion. Higher antifreeze concentrations were tested if the freezing point was above -35°C.

However, the microclimate chamber could only achieve -65°C, limiting solution temperature minimum to approximately -35C. Therefore, inclusion of aqueous antifreeze solutions with a freezing point lower than -35 resulted in redundant data.

Expansion tests of distilled water consistently expanded to around 8% across numerous trials. The reported number of approximately 9% is a well-known and commonly accepted value, yet experimental verification is somewhat outdated and difficult to procure. Regardless, Figure 49 through Figure 52 illustrate the percent expansion of the various concentrations of aqueous antifreeze solutions. For the full data sets, refer to Appendix 11.2.1.
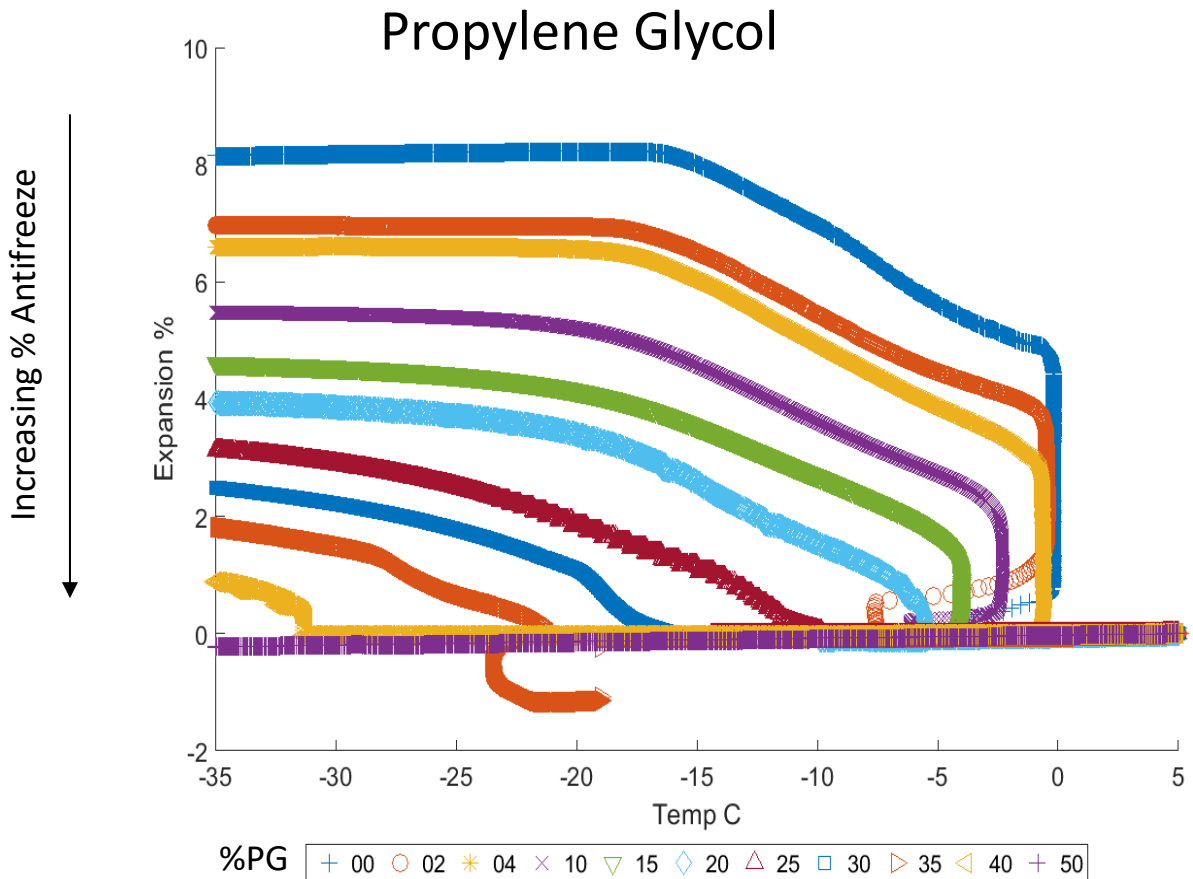
Figure 49: Pure water expanded around 8% during crystallization and solidified at 0°C. Adding propylene glycol depressed the freezing point, but also decreased the overall expansion of the solution.

79
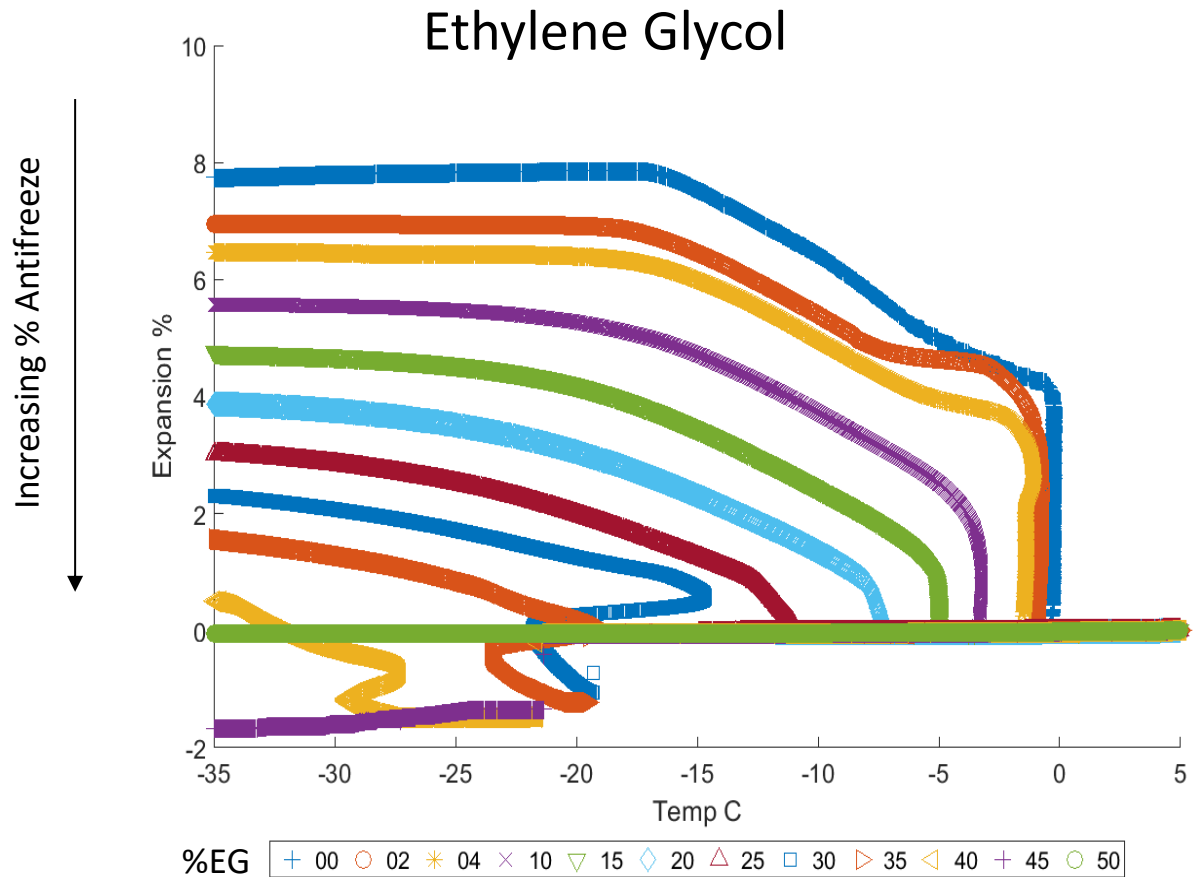
Figure 50: Pure water expanded around 8% during crystallization and solidified at 0°C. Adding ethylene glycol depressed the freezing point, but also decreased the overall expansion of the solution.
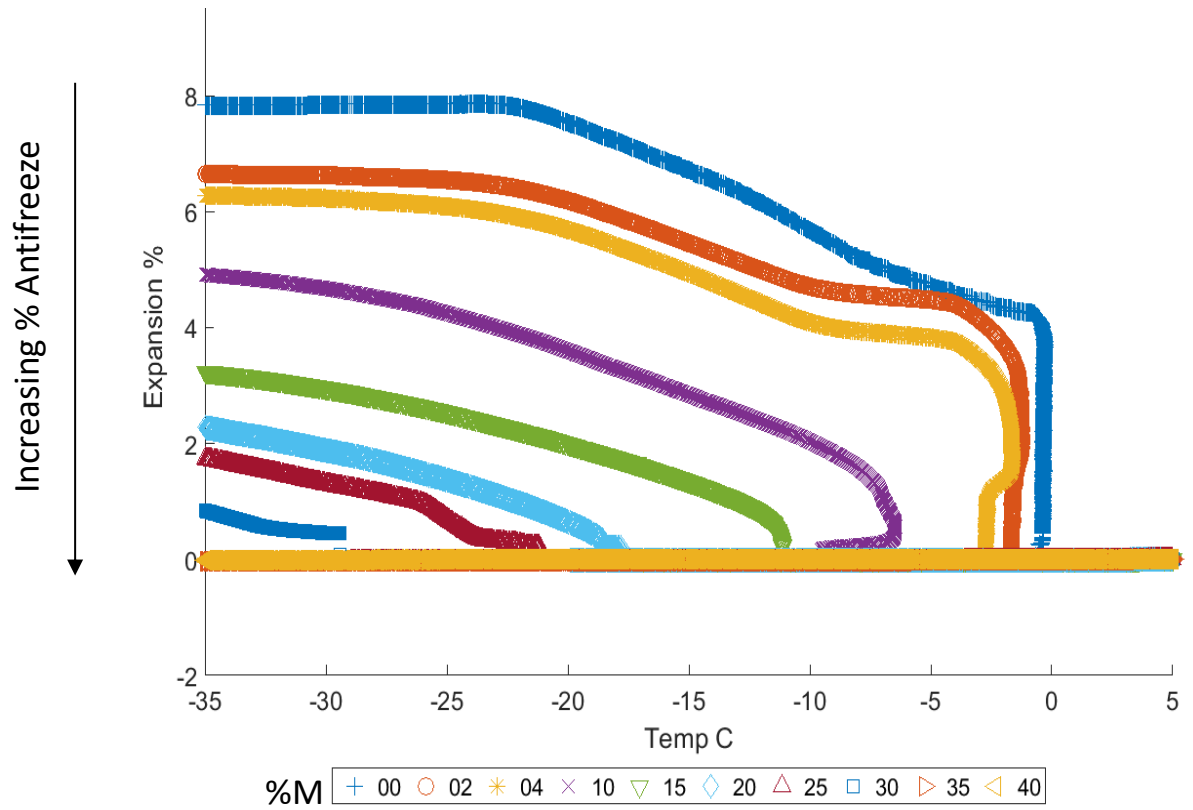
Figure 51: Pure water expanded around 8% during crystallization and solidified at 0°C. Adding methanol depressed the freezing point, but also decreased the overall expansion of the solution. Of the four antifreeze solutions, methanol had the greatest impact on freezing point and expansion.
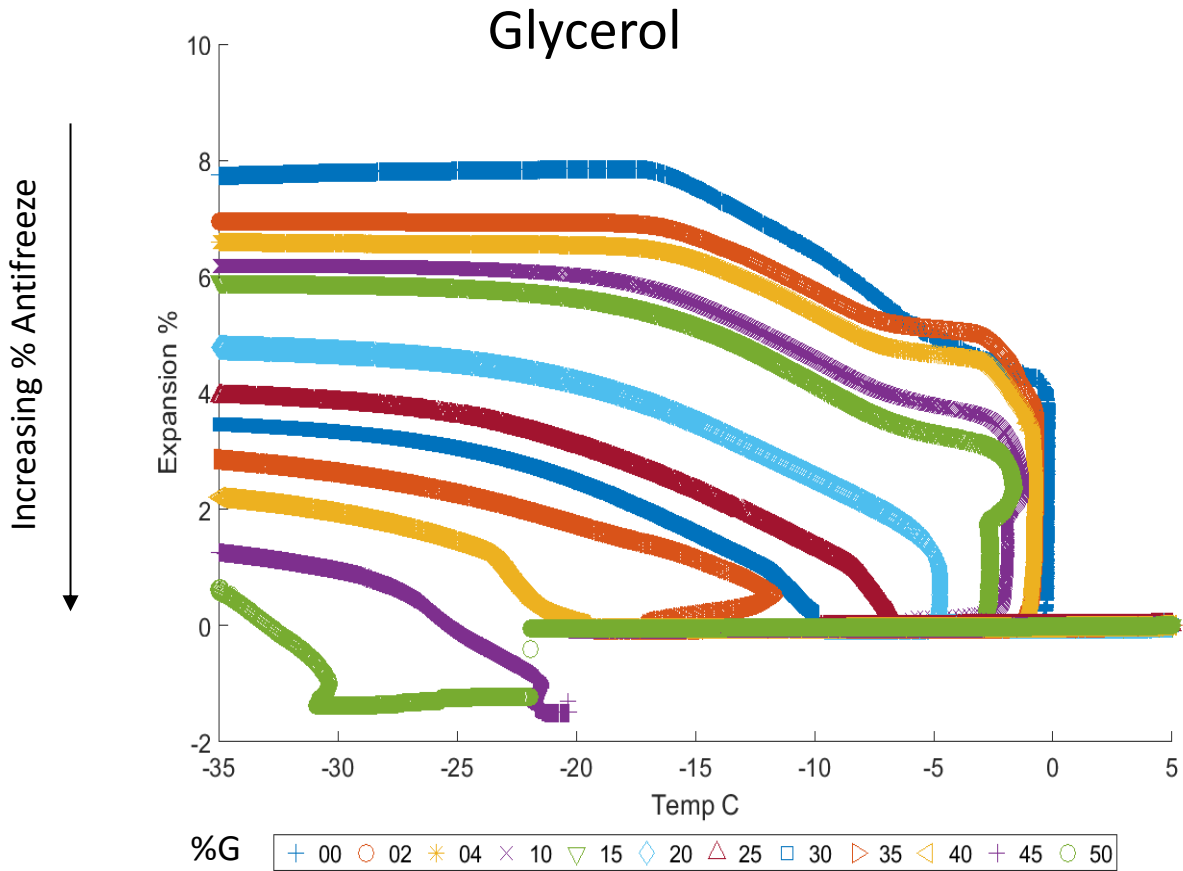
Figure 52: Pure water expanded around 8% during crystallization and solidified at 0°C. Adding glycerol depressed the freezing point, but also decreased the overall expansion of the solution.

As expected, increasing the antifreeze solution depresses the freezing point. From Figure 49 to Figure 52, a sudden increase in percent expansion corresponds to the freezing point of the solution. An increase in expansion signifies nucleation in the bulk solution and crystal growth, which for water causes a decrease in density. Higher concentrations of antifreeze did not exhibit the sudden expansion observed at lower concentrations. Rapid expansion occurs during nucleation and crystallization which progresses across the entire volume of liquid. Vertical lines in the expansion curves are indicative of the crystallization. A less obvious onset of expansion resulted in an ambiguous (at a lower temperature than documented) freezing point determination at higher concentrations of antifreeze. Non-equilibrium cooling also led to freezing points appearing lower

than published values because solutions do not have enough time to completely expand and begin

to cool before identifiable expansion occurs. Therefore, experimental freezing points at higher

concentrations of antifreeze are lower than reported values.
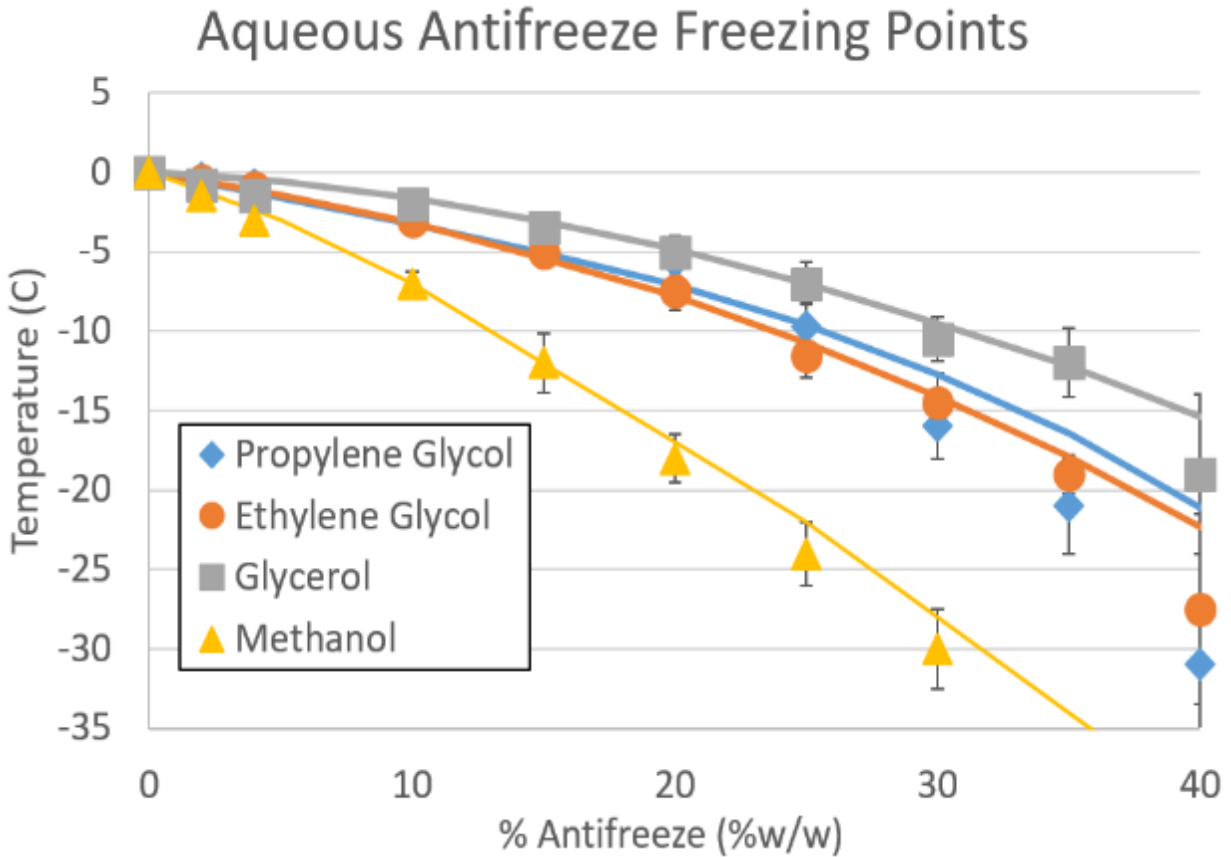
Figure 53: Freezing points were determined by observing the temperature when the expansion curve formed a vertical line. An increase in expansion signifies nucleation in the bulk solution and crystal growth. Solid lines designate documented freezing points for the aqueous antifreeze solutions. Uncertainty is indicated by the standard deviation of the 1000 data points after freezing.

Expansion of aqueous antifreeze solutions during freezing exhibited an exponentially declining

relationship with concentration of antifreeze, Figure 54. Propylene glycol and ethylene glycol

followed a similar path, glycerol expanded the most, and methanol expanded the least. Antifreeze

concentrations above 30% did not expand completely because of the limited temperature

achievable in the microclimate chamber.
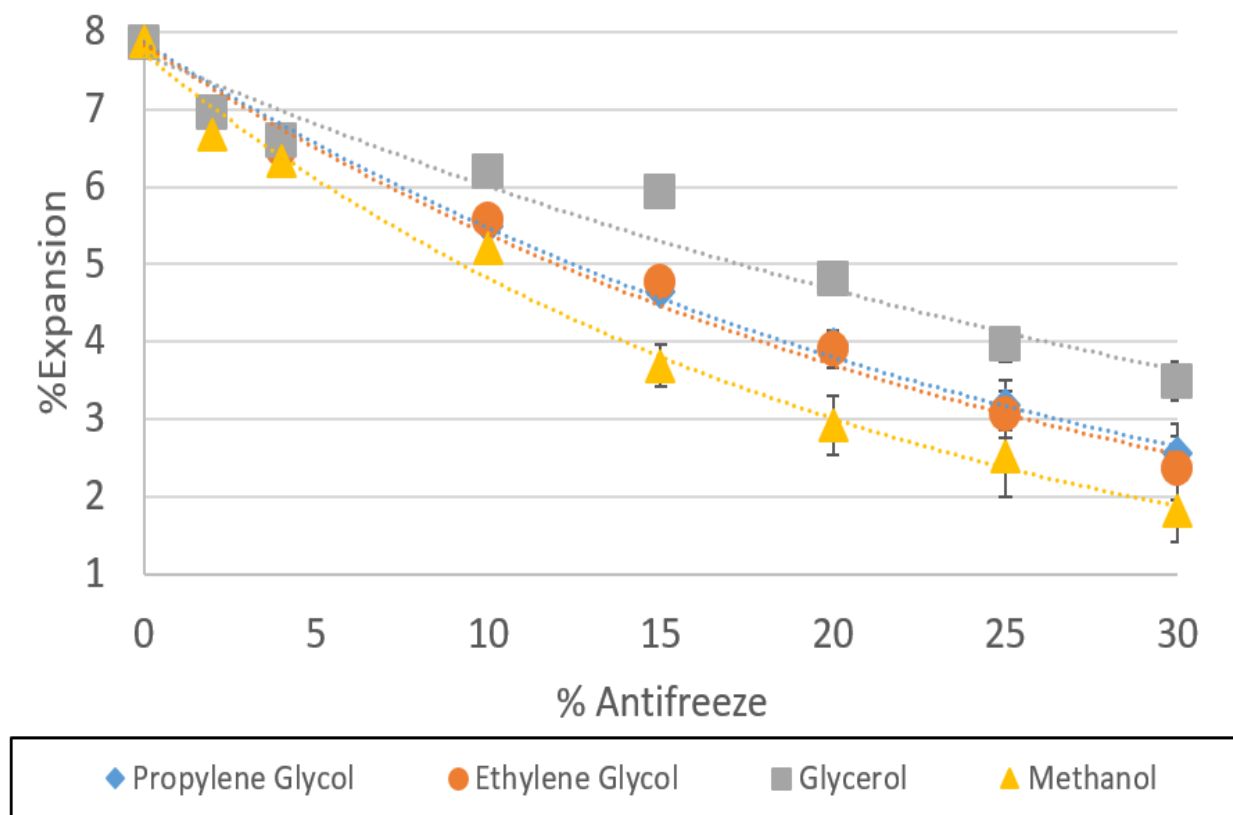
Figure 54: Maximum expansion was determined form the expansion curves. Expansion decreased nonlinearly with increasing composition of antifreeze. Curve fits indicate an exponentially declining trend. Uncertainty in the expansion was determined by the standard deviation of 1000 data points after completion of the thermal arrest.

5.3   DISCUSSION

As expected, hydrogen bond disruption due to antifreeze played a significant role in the phase change by reducing the freezing point but also reducing the expansion of the fluid. Crystallization still occurred during phase change, but interspersed antifreeze molecules limited crystallization of water molecules from processing across the entire fluid volume. Hydrogen bond disruption was quantifiable through observation of expansion reduction with increasing antifreeze concentration.

Figure 49 through Figure 52 do not follow commonly accepted expansion curves. The reason for the discrepancy is the solutions cooled in a non-equilibrium manner. Non-equilibrium cooling forces the antifreeze solution to cool below the freezing point completely crystallizing. In Figure 55, four separate trials all conducted with distilled water yielded distinctly different expansion curves as temperature decreased. Sample "-65" indicates a sample rapidly cooled to -65°C at the maximum capability of the microclimate chamber. Sample "-05" cooled until nucleation occurred, at which point the temperature adjusted to -5°C for a period, allowing solidification to occur, after which the temperature dropped to -65°C. Similarly, "-02' set at -2°C after nucleation for a period until it dropped to -65°C. Sample "-00" exemplifies the traditional expansion curve for the water/ice transition. To achieve the figure the temperature slowly dropped until nucleation occurred at which point the temperature returned to 0°C. The temperature remained at 0°C for an hour, allowing for the entire volume of water in the syringe to crystallize. After complete solidification, the temperature again dropped to -65°C to complete the cooling process. Notable is the fact that the parcel of water did not continue to expand after complete solidification, unlike the other three curves. Instead, the expansion began to decline with cooler temperatures, relative to how ice becomes denser as it cools. Therefore, equilibrium cooling added no accuracy in expansion measurements over the quicker non-equilibrium cooled fluid.
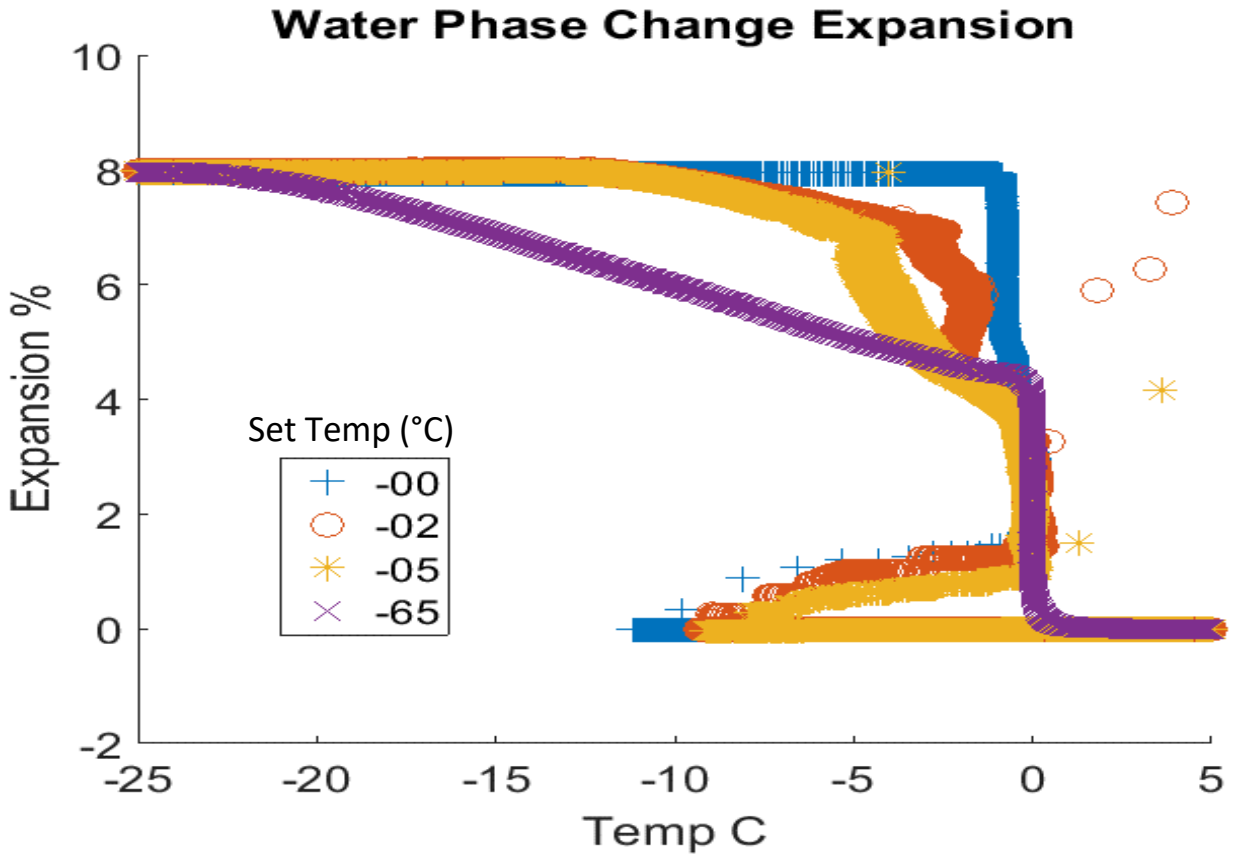
Figure 55: Cooling rates of the solution were varied to determine the effect on expansion. Faster cooling of water resulted in a "-65" curve where the temperature is ramped down as quickly as possible and the water is forced to cool. This forced cooling resulted in a definitive "elbow" in the expansion curve. Maintaining the water temperature at 0°C resulted in the "-00" curve where the expansion reached 8% at 0°C before the temperature was decreased further. Varying levels of non-equilibrium cooling affect the expansion profile. Intermediate cooling rates where the temperature was set at -2°C and -5°C resulted in "-02" and "-5" expansion profiles, respectively.

Equilibrium vs non-equilibrium cooling is particularly evident when observing Figure 56. The equilibrium cooling curve relates to "-00" data where the volume of water has sufficient time for complete solidification before the environmental temperature reduces further. This period of thermal arrest is evident in the flat portion of the cooling curve, which remains at 0°C for approximately 75 minutes until the exterior temperature reduces. Non-equilibrium cooling increases the rate of heat transfer causing the section of thermal arrest to be significantly shorter, approximately 3 minutes.
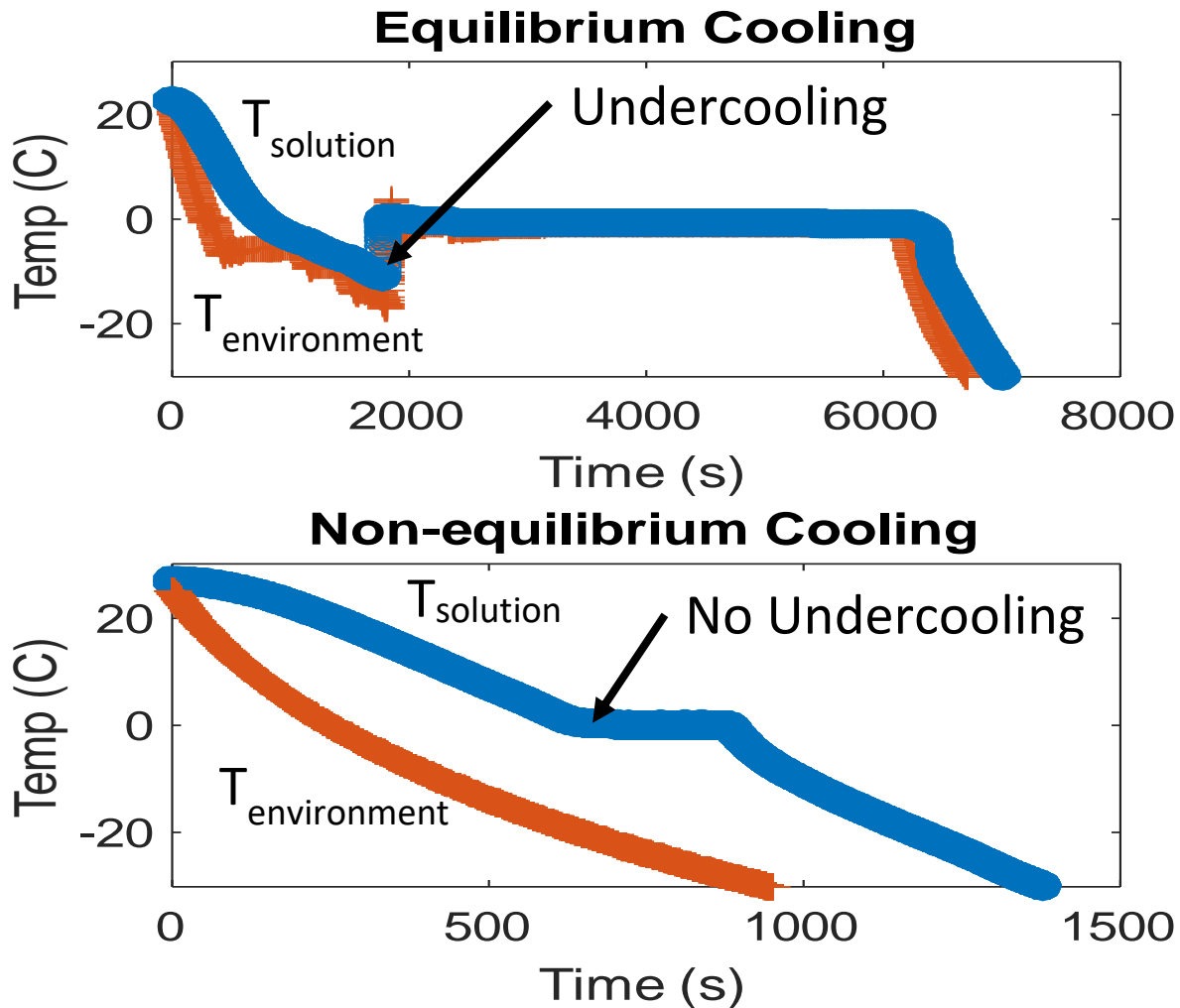
Figure 56: Cooling curves for water demonstrated the difference between equilibrium and non-equilibrium cooling. Non-equilibrium cooling exposes the experimental setup to an environment colder than the water, drawing heat out of the liquid at a faster rate. Equilibrium cooling matches the environment and water temperature, minimizing heat transfer and allowing crystallization to occur fully across the entire volume of liquid.

Undercooling in the equilibrium-cooled fluid is also notable. Undercooling occurs when liquid temperature reaches below the freezing point and is statistically more likely to occur in filtered liquids. Filtering removes impurities decreasing potential nucleation sites and increasing the likelihood of homogeneous nucleation in the bulk fluid. Homogeneous nucleation is more likely to occur in equilibrium-cooled fluids while non-homogeneous nucleation generally has an extraneous stimulus that induces nucleation. A particle acts as a nucleation site, external stimulus

increases molecule movement, or forced heat transfer adds the activation energy necessary for nucleation to occur which all reduce the likelihood of undercooling. Undercooling is a statistical process, varying between trials, but is more likely to occur in (quasi) equilibrium-cooled fluids as shown in Figure 55 and Figure 56.

The expansion profiles versus time also look different for equilibrium and non-equilibrium cooled liquids. Both modes resulted in a full 8% expansion during phase change. Non-equilibrium cooling achieved full expansion in ten minutes while equilibrium cooling required an hour for complete solidification. However, the immediate expansion after nucleation is particularly interesting. Undercooling significantly affects nucleation and the energy in the expansion process. With undercooling, water expanded 2% in volume in under ten seconds while without undercooling the same water expanded 0.002% in the same amount of time. For undercooled fluids, that indicates a large amount of energy over a short period.
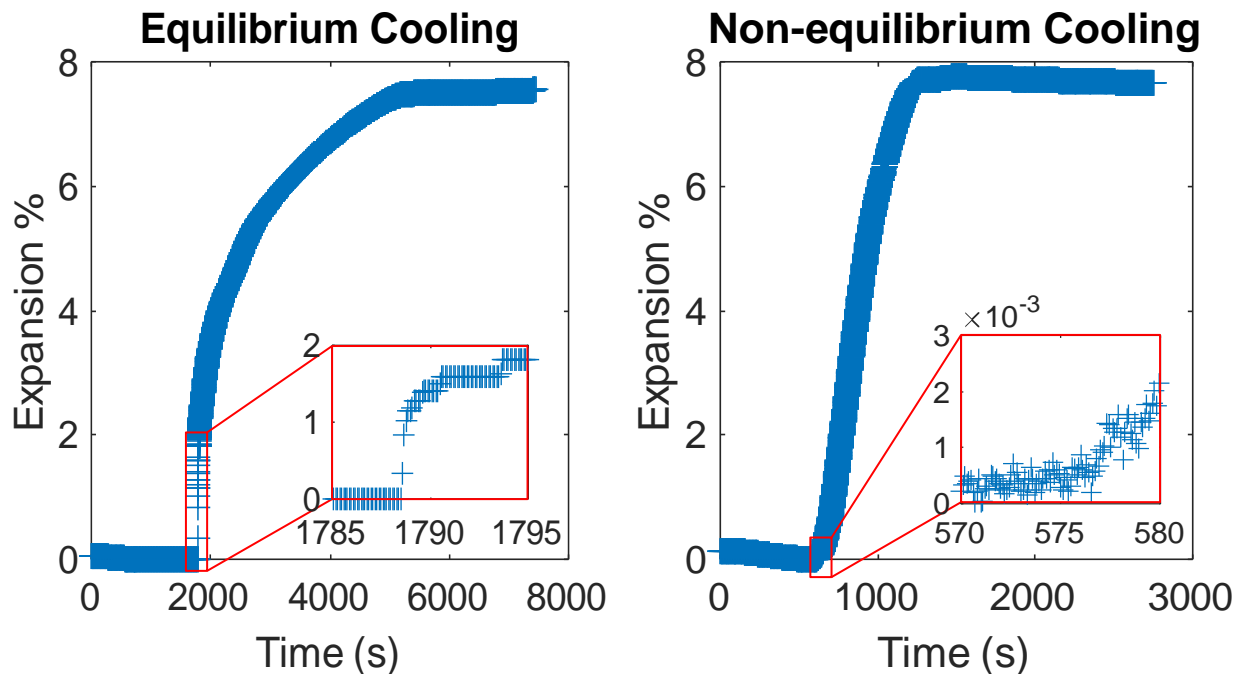
Figure 57: With undercooling, nucleation results in sudden expansion, 2% over ten seconds. During non-equilibrium cooling, undercooling wasn't as common and nucleation occurred at a much slower rate, 0.002% over ten seconds.

Propylene glycol, ethylene glycol, and glycerol exhibited an interesting behavior not displayed by methanol. The experimental setup, designed specifically for expansion, detected rapid contraction just prior to freezing at various concentrations. Glycerol exhibited the behavior from 45-50% concentration at 20-22°C. For ethylene glycol, the range was 30-40% concentration between 18-22°C. Propylene glycol exhibited a smaller range around 35% PG at 18°C. The behavior was repeatable with various trials over the range of concentrations, shown in Appendix 11.2.1.

6   NANOCHANNEL PHASE SEPARATION

6.1   NANOCHANNEL FLOW THEORY

From Figure 20, the two types of expected channel wetting result in two distinct flow regimes. When the channel is "dry," Hagen-Poiseuille flow describes evolving vapor flowing through the channel to vacuum. When the channel is wet, Washburn capillary filling restricts flow through the channel to vacuum.

Initial approximations of flow through nanochannel assumed Hagen-Poiseuille (Equation 5) flow of aqueous propylene glycol vapor. Calculations assumed vapor pressure driven flow through a single nanochannel. Expected nanochannel depths are 500nm and 1000nm, but evaluation of a range of values established a backdrop for design of experimentation.   Viscosity values for vapor phase aqueous antifreeze assumed a linear relationship between water vapor and propylene glycol vapor obtained from Kane et al. (1996). Density values for water vapor and vaporized propylene glycol assumed ideal gas behavior at standard ambient temperature and pressure. Diameter and composition of propylene glycol varied to predict experimental flow rates based on material properties see Figure 58.
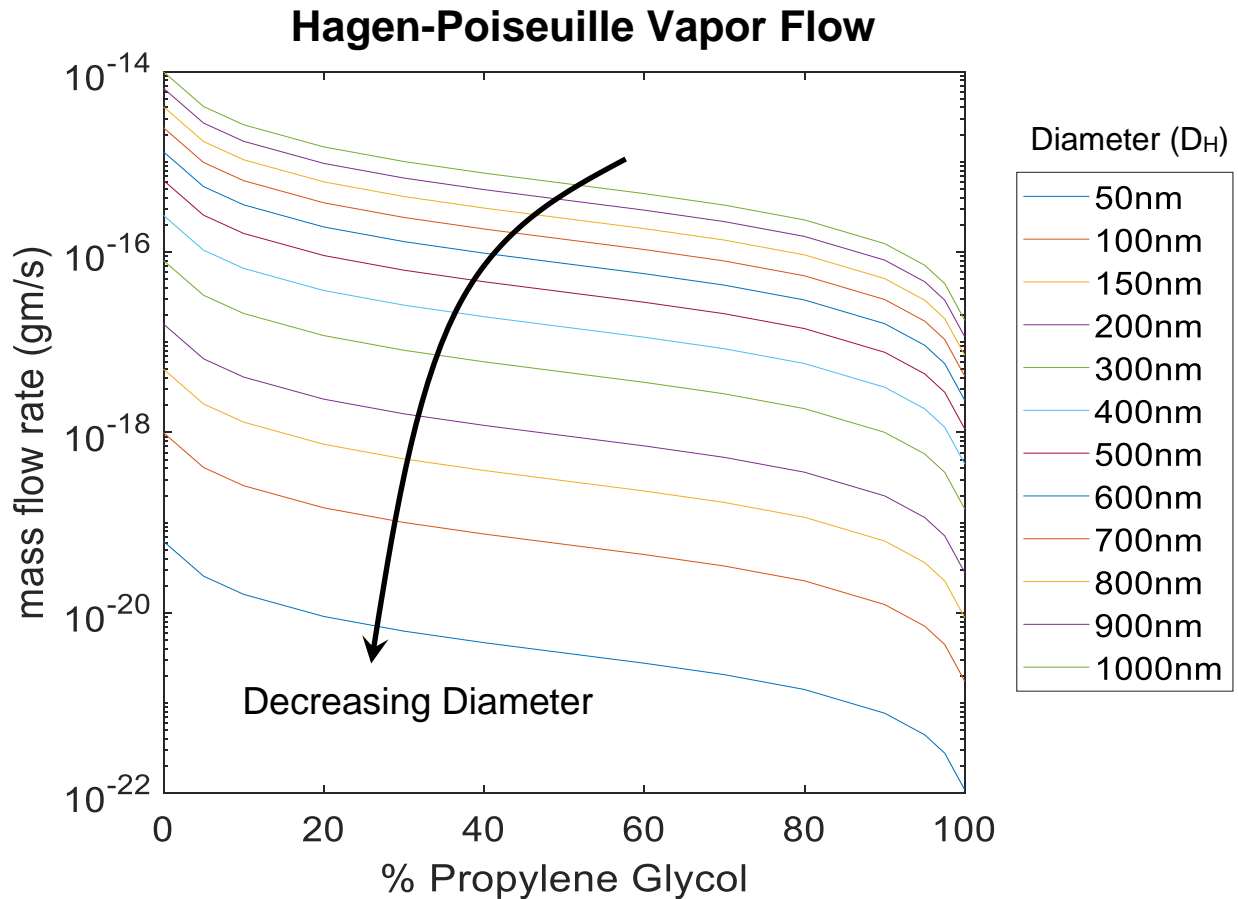
Figure 58: Using Hagen-Poiseuille law, Equation 5, theoretical flow of aqueous propylene glycol vapor was calculated for 50nm to 1000nm diameter channels. Flow rate approximations aided in the design process and served as a sanity check for experimental data with known material properties.

The second determination of theoretical flow through a nanochannel assumed Washburn capillary filling (Equation 12) of liquid aqueous propylene glycol. Calculations assumed capillary driven flow through a single nanochannel. Expected nanochannel depths are 500nm and 1000nm, but evaluation of a range of values established a backdrop for design of experimentation. Viscosity and surface tension values for liquid phase aqueous propylene used data from Curme and Johnston. (1952). Calculations assumed a channel length of 1mm, channel width of 50μm, contact angle of 82°, and a slip length of 50nm. Channel depth and composition of propylene glycol were varied to predict experimental flow rates based on material properties see Figure 58.
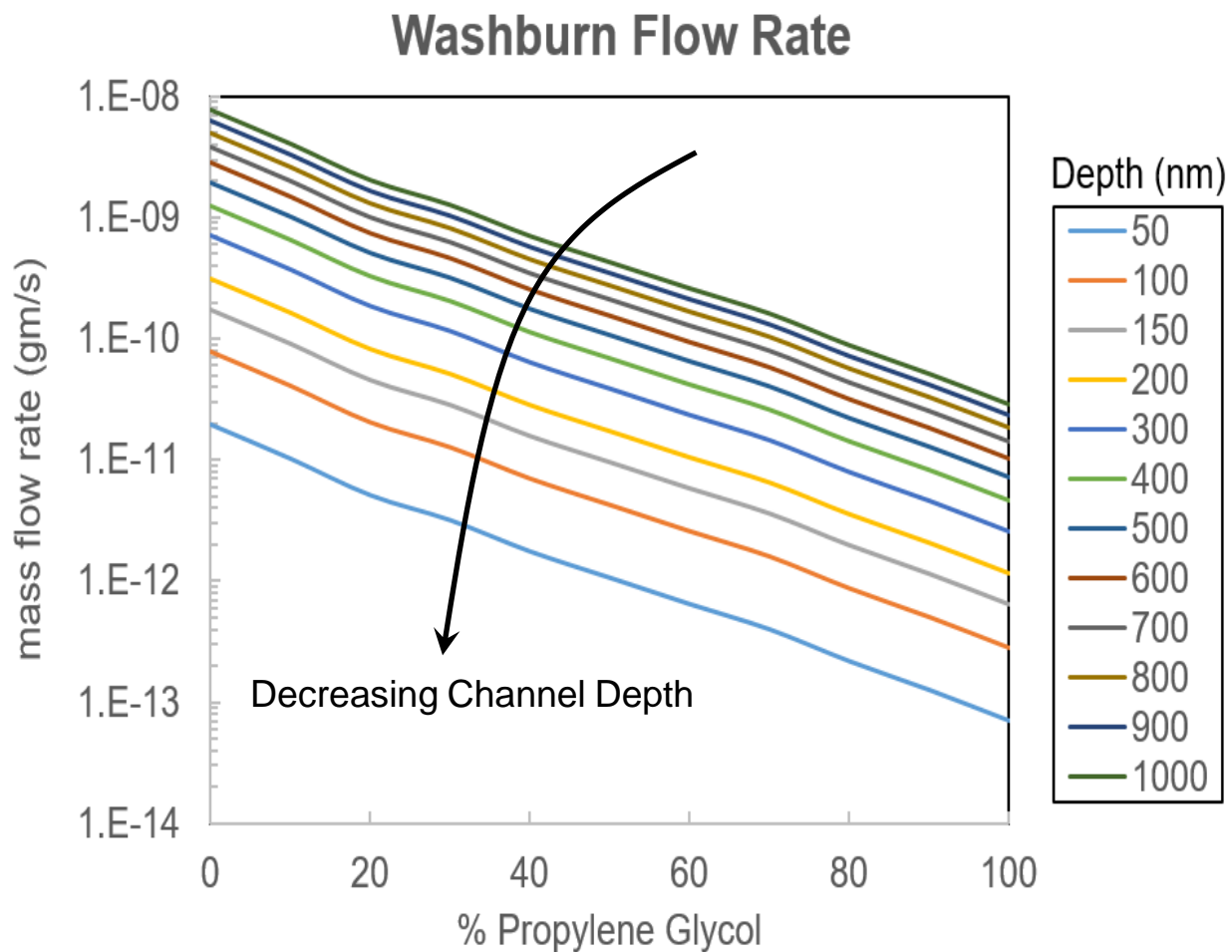
Figure 59: Using Washburn flow, Equation 12, theoretical capillary flow of aqueous propylene glycol liquid was calculated for 50nm to 1000nm deep channels with a width of 50µm. Flow rate approximations aided in the design process and served as a sanity check for experimental data with known material properties.

6.2 EXPERIMENTAL SETUP

6.2.1 Test Apparatus
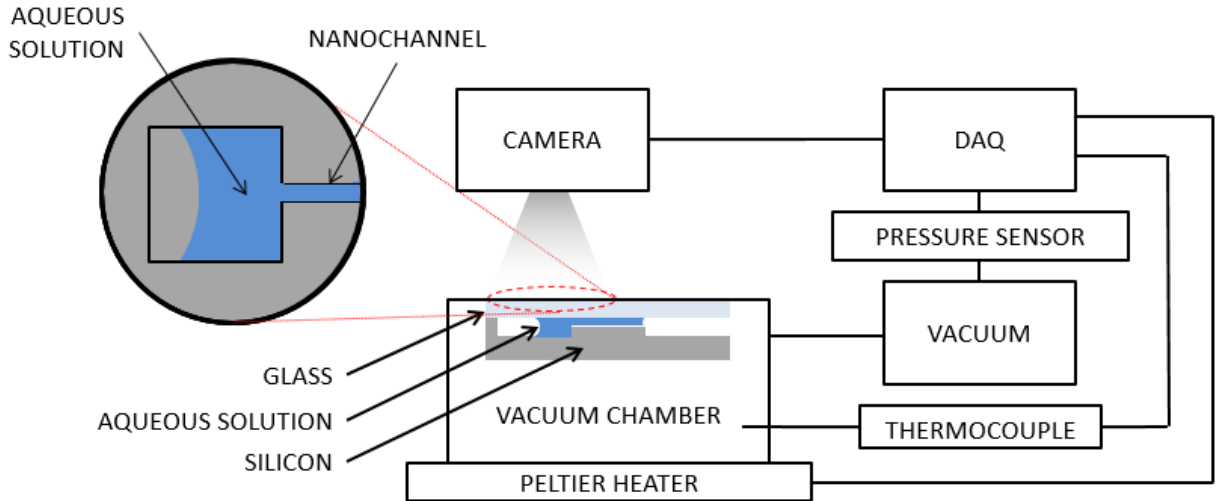
Figure 60: The general schematic of the nanochannel fluid phase separator experimental setup schematic highlights the important equipment necessary to collect vaporization data.

Figure 60 displays an overview schematic of the entire experimental setup. Machined out of aluminum, the vacuum chamber cavity was big enough to contain a 0.35-inch X 1-inch silicon chip. Design of the setup allowed for overhead inspection of the chip for volumetric fluid analysis. When pumped down to vacuum, an o-ring interfaced with the glass slide to seal the device. Figure 61 shows the design of the machined experimental setup.
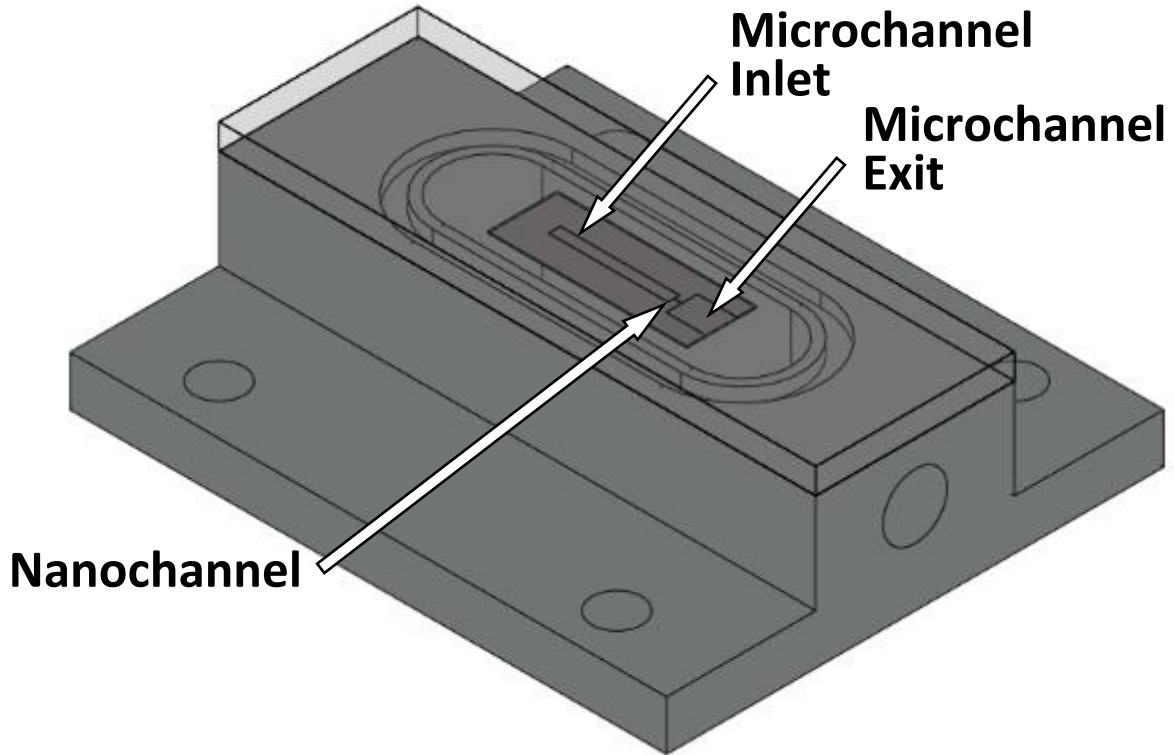
Figure 61: Test pieces consisted of a 0.35" X 1" silicon chip bonded to a borosilicate glass slide. A custom fabricated mini vacuum chamber sealed the nanochannel device by drawing it against an o-ring with vacuum. The nanochannel experimental setup allowed for overhead visual inspection of fluid flow through he nanochannel.

Finite element analysis conducted in SolidWorks verified stresses on the glass would not exceed the yield strength of Pyrex, Figure 62.   Assuming a fixed boundary condition at the o-ring and a pressure of one atmosphere on the glass slide, maximum stresses observed only reached 1.632 mega Pascal. Stress values were approximately twenty times less than the tensile strength of Pyrex, 35 mega Pascal.
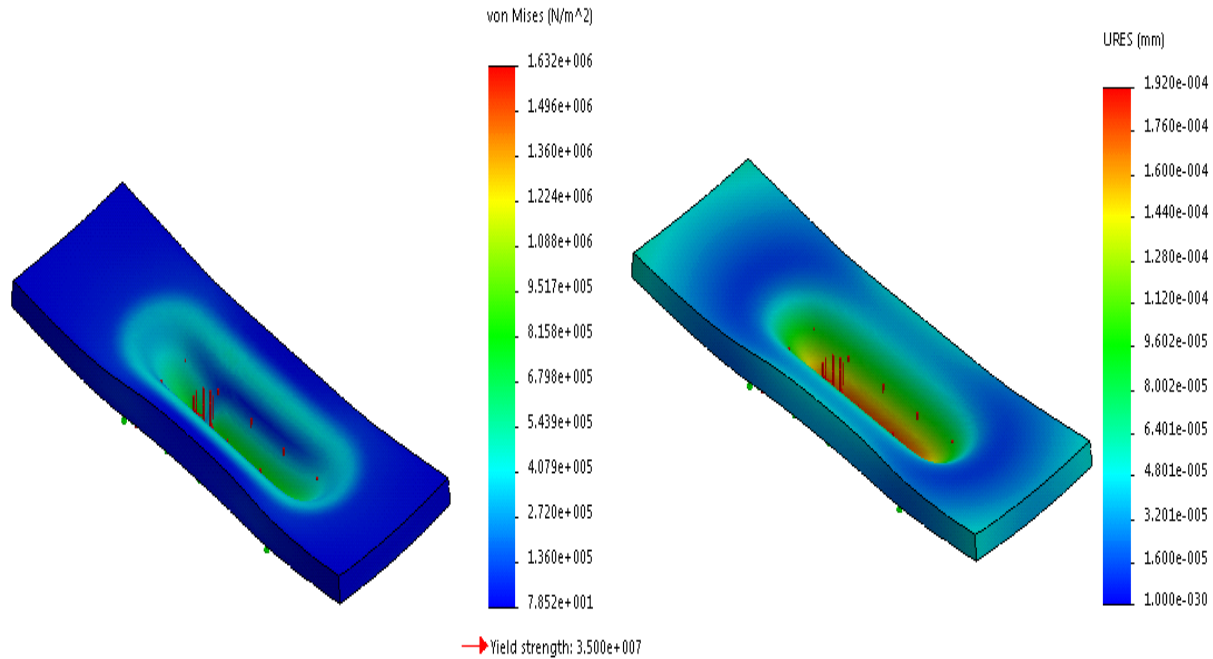
Borosilicate Glass

Modulus = 65 Gpa   Tensile Strength = 35 Mpa   Poisson's Ratio = 0.2

Figure 62: To ensure safety and robustness of the glass slide, a finite element analysis was conducted in SolidWorks on a 1X3" glass slide under an atmosphere of pressure. Stresses on the glass slide were an order of magnitude less than the yield strength of borosilicate glass.

A Basler Scout camera performed the visual inspection of the nanochannel restricted fluid flow. The Zeiss SteREO Discovery.V8 microscope has magnifications ranging from 1X to 8X increasing accuracy and speed of flow measurements. A LabVIEW data acquisition system recorded/controlled the pressure sensor, thermocouple, and Peltier stage, see Appendix 11.5 for more information. Orientation of the sample relative to the camera minimized error in measurements while the translational stage and bellow hose allowed for fine x/y adjustment of the sample, see Figure 63.
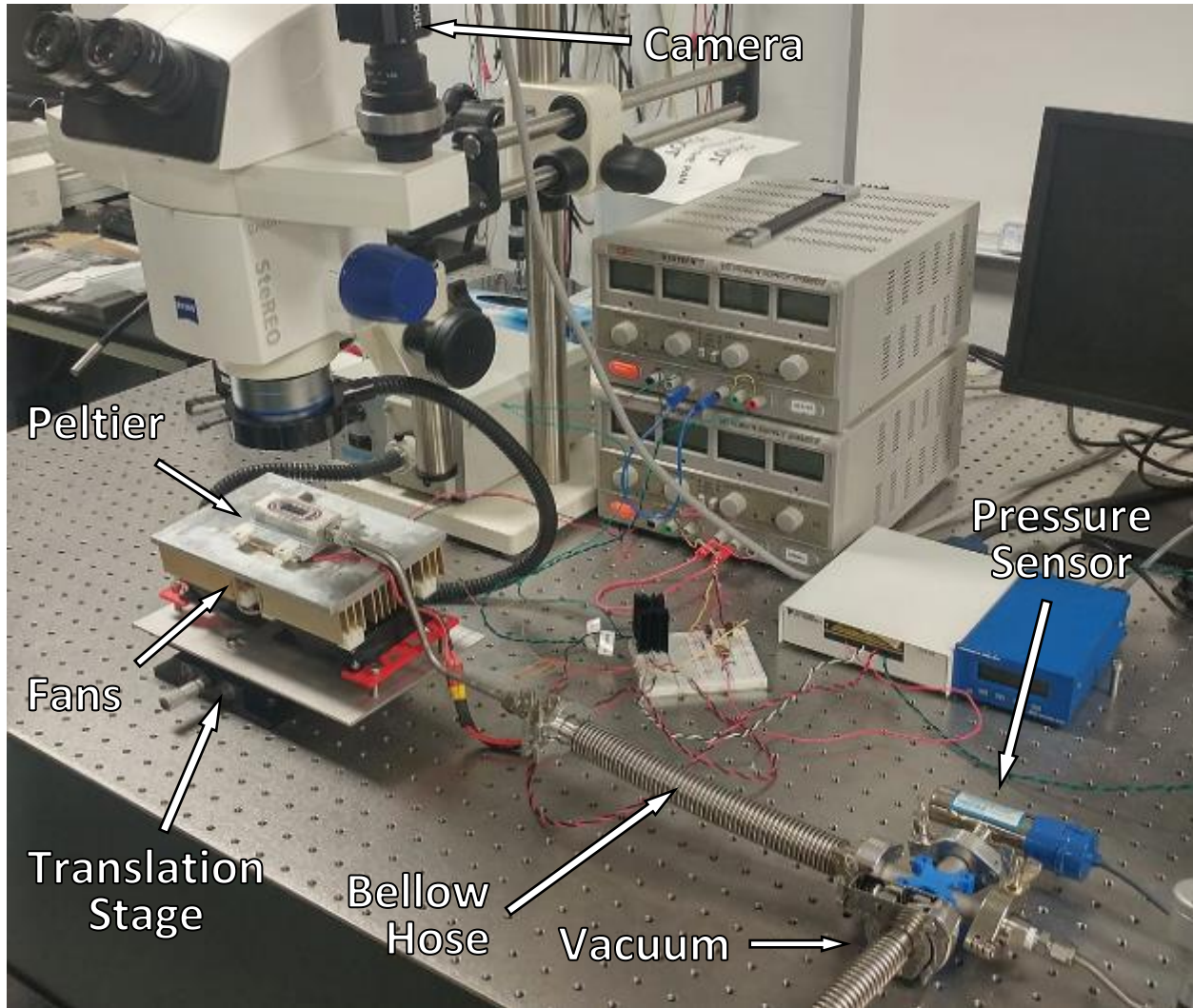
Figure 63: A camera/microscope system monitored the fluid in the microchannel inlet. A flexible bellow hose facilitated minor X-Y adjustments with the translation stage.

Under vacuum, an o-ring created a seal with the glass slide enabling testing of multiple samples in series. Addition of an aluminum heater block internal to the cavity, resting flush against the silicon nanochannel device maintained a constant temperature during experimentation, Figure 64. A thermocouple fed through a vacuum tight compression fitting monitored the internal temperature to ensure a constant temperature environment. Without a thermal mass regulating local temperature, evaporation across the liquid meniscus to vacuum resulted in freezing which restricted fluid flow. For further information, refer to Appendix 11.3.1.
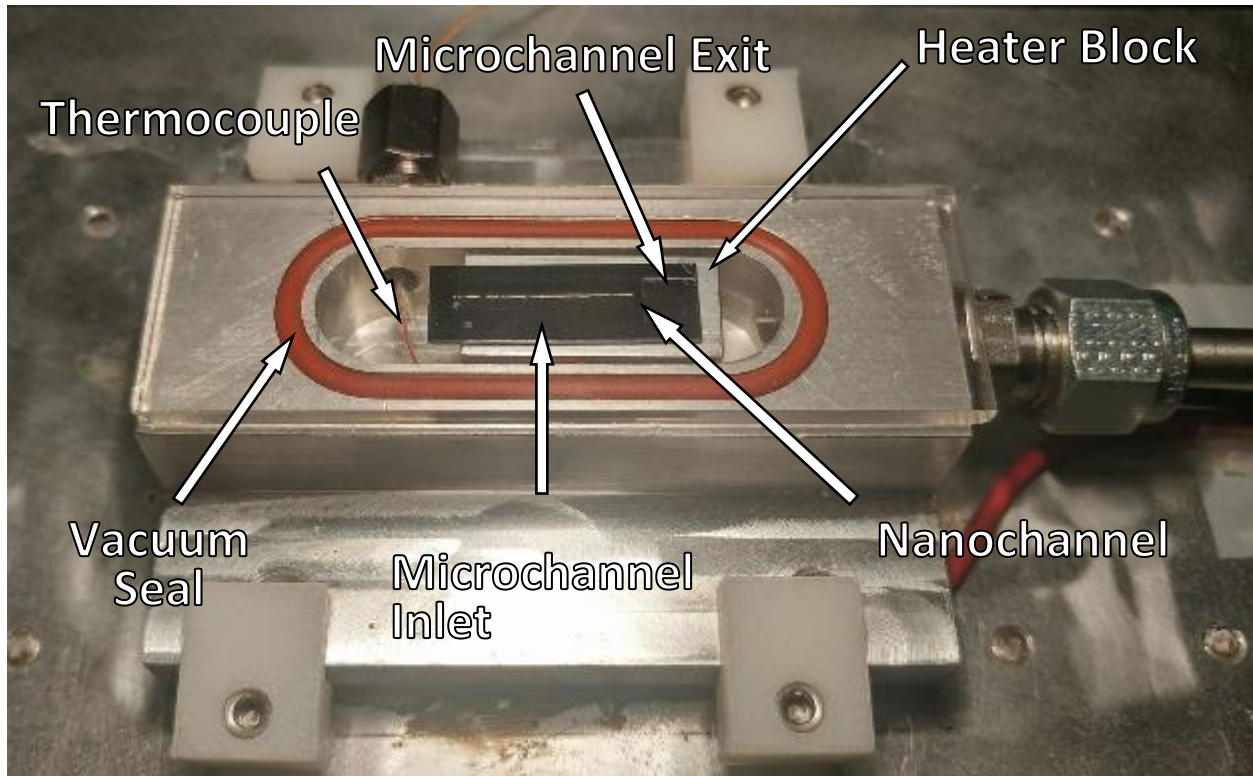
Figure 64: Liquid at atmospheric pressure in the microchannel inlet was separated from vacuum by the nanochannel(s). In the current configuration, liquid wet the nanochannel, indicating Washburn capillary limits on the flow rate.

The weight of the microscope and large moment arm caused the camera to rest at a non-90-degree angle causing reflection and shadows around the meniscus. To alleviate the sagging issue, 3D printed brackets tilted the stage until optical artifacts were minimal. Figure 65 illustrates the angle matching between the experiment stage and the microscope. Additionally, fins and computer fans removed excess heat from the experimental setup.
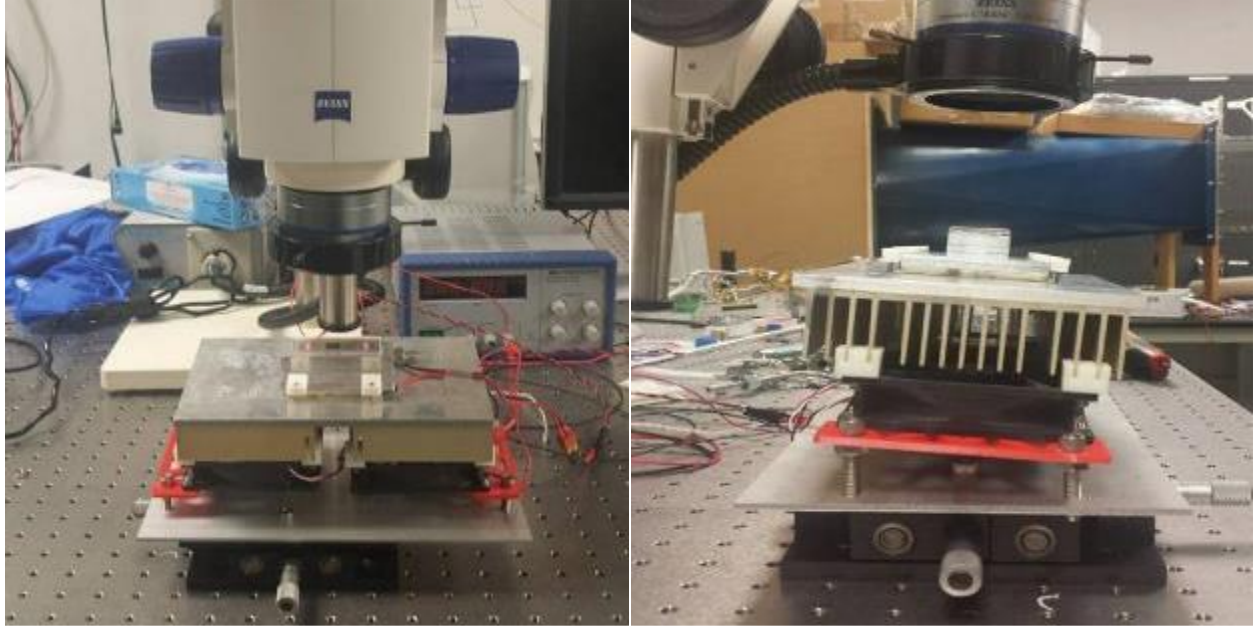
Figure 65: 3D printed brackets tilted the setup for proper viewing alignment.

Images of fiducials of known width and height were captured at various magnifications with the experimental setup. The pixel height and width were calibrated to microns using the known fiducial dimensions. Pixels for the Basler Scout camera were determined to be square in shape and exhibited a calibration profile shown in Figure 66.
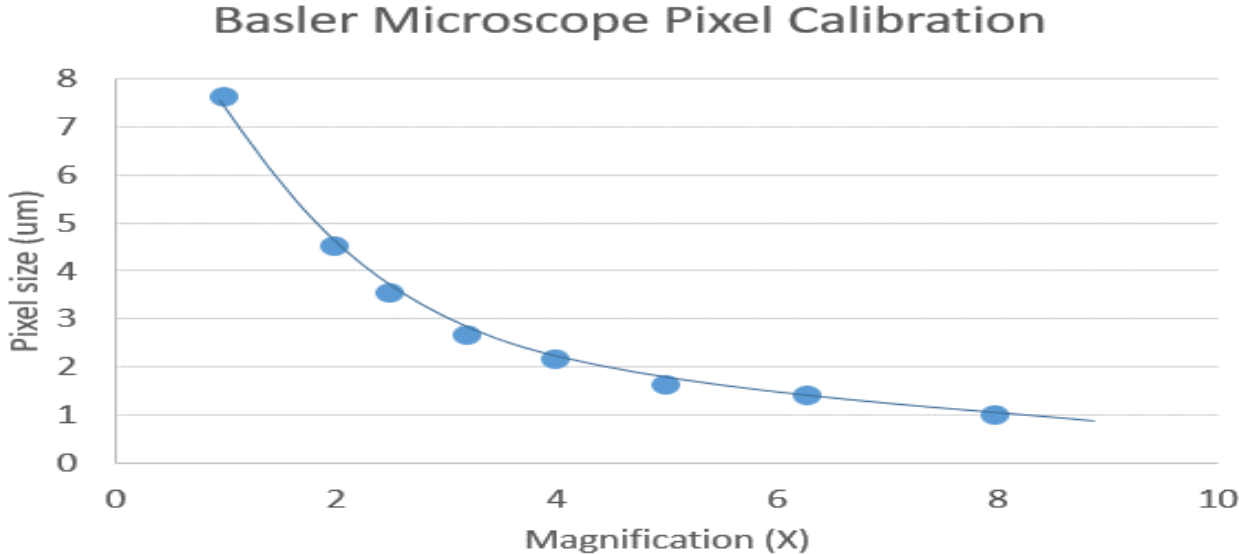
Figure 66: Microscope calibration established the pixel to μm conversion between ratios.

6.2.2   Chip Design and Fabrication

The entire nanochannel fabrication process utilized only common microfabrication techniques, outlined in Figure 67. The process shown is not to scale but represents the overall design and fabrication flow. A Karl Suss aligner patterns a spun-on layer of photoresist, forming the microchannel mask (a). A twenty-minute buffered oxide etch strips the oxide layer, exposing the bare silicon wafer (b). A thirty minute 35% KOH etch at 85°C forms the microchannel portion of the device (c). With careful alignment using the exterior fiducials, a second patterning of photoresist exposes the nanochannel mask (d). A 20-minute BOE removes the oxide over the desired nanochannel, connecting the microchannel inlet and exit, and again exposing the silicon wafer (e). Another KOH etch step forms the nanochannel(s) portion of the separator (f). 35% KOH at 45°C etches silicon at a rate of 2nm/s. Channels with depths of 500nm, 1µm, and 10µm require wet etches of 3.5, 7, and 70 minutes respectively. A twenty-minute BOE removes all remaining oxide from the wafer, leaving a clean silicon wafer surface (g). Prior to bonding, a clean wafer surface is essential, so an HCl and H_2O_2 bath decontaminated the substrate. With careful alignment, anodic bonding affixes the glass to the silicon fluidic device creating a sealed nanochannel (h). For more information about the anodic bonding process used, refer to Appendix 11.7.4.3.

Top View		Cross Section View
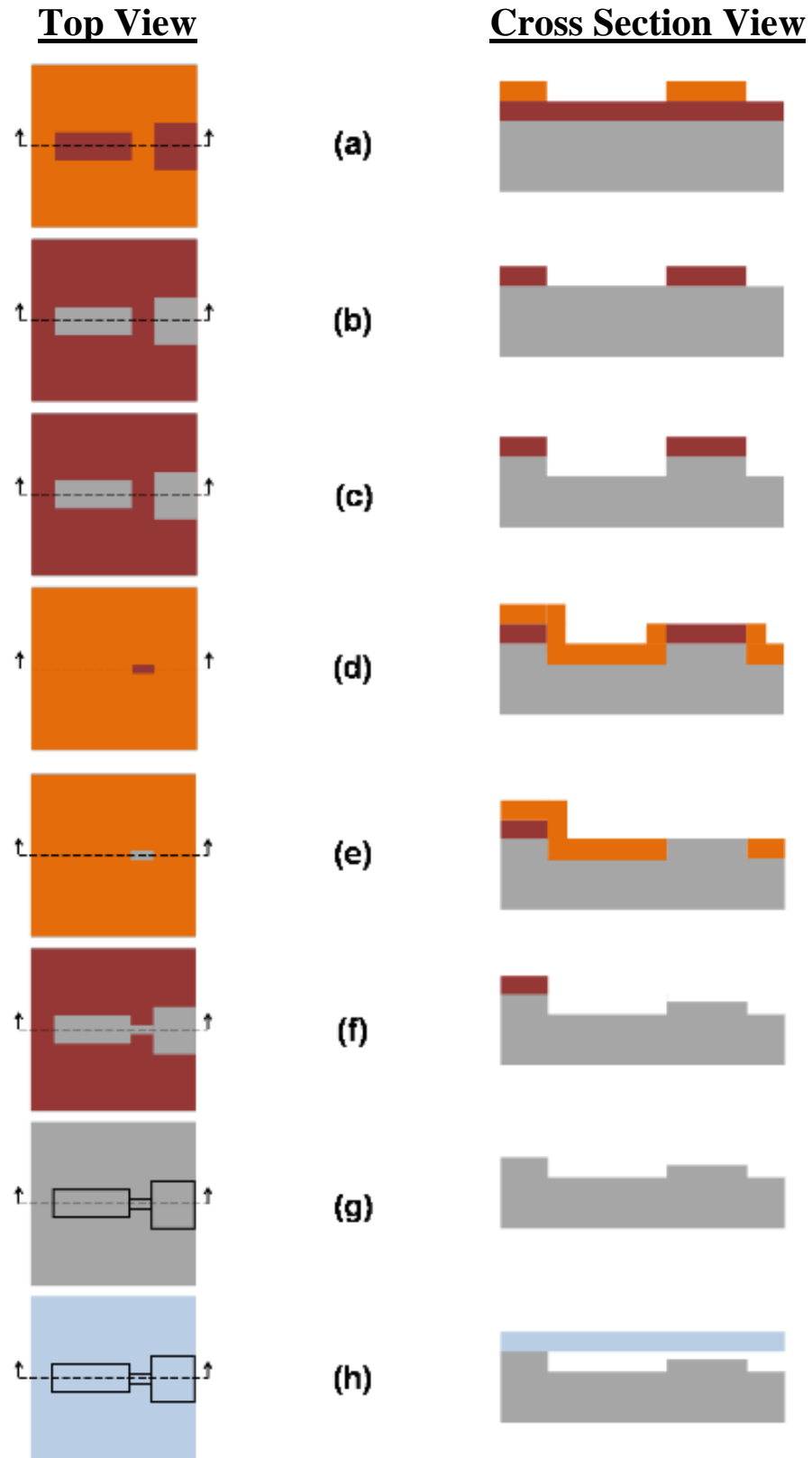
Figure 67: Micro/nanochannel fabrication utilized common lithography techniques.

6.2.2.1   Gen 1

After abandonment of the AFM nanolithography method, see Appendix 11.7.3, initial device fabrication utilized deep reactive ion etching techniques.   Various designs focused on fluid trapping in an observable field of view. Figure 68 shows different designs of microchannels to trap fluid for visual tracking of the meniscus. Unfortunately, the DRIE in HiDEC was no longer operational and altering the fabrication method became necessary.
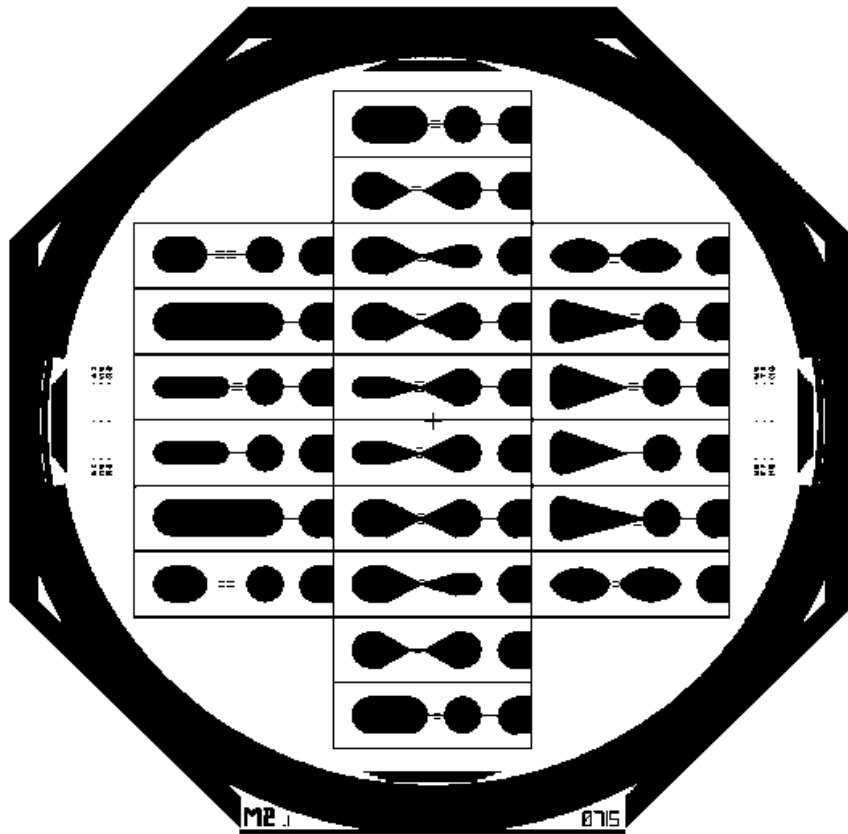
Figure 68: Gen 1 tested various microchannel fluid trapping geometries. Liquid trapping was tested to obtain Hagen-Poiseuille vapor phase flow through the nanochannels by preventing wetting of the nanochannel. Refer to Appendices 11.3.2.1 and 11.4.4.3 for fluid trapping examples.

6.2.2.2   Gen 2

Gen 2 utilized KOH etching for fabrication of the microchannels. Because of the anisotropic etch; all shapes had no curved surfaces and primarily ninety-degree corners. Liquid trapping tests indicated that regardless of design, fluid fills the smallest cavity, which was always the nanochannel. Therefore, simplification of the overall design was desirable.
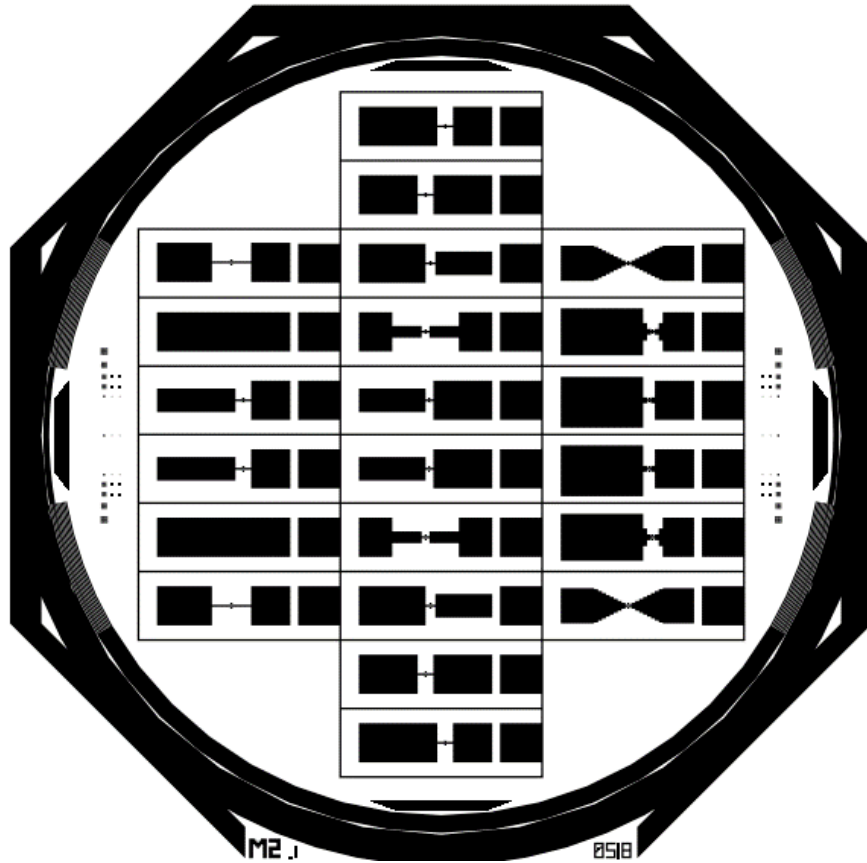
Figure 69: After the DRIE was inoperable, Gen 1 was adapted for KOH etching by removing curves and angled geometries. Gen 2 attempted to trap liquid away from the nanochannels. Ultimately, it was discovered that the fluid will wet the smallest volume encountered which was always the nanochannel.

6.2.2.3   Gen 3

Gen 3 was designed with a 1.5 mm wide microchannel inlet for observation of meniscus progression with a 4 mm wide exit microchannel. Chips were 0.35" wide by 1" long with two different modes of operation based on dicing location. Cut on the solid line, chips form a fully enclosed microchannel while cutting on the dashed line opens the microchannel exit to vacuum. Nanochannels were all 50 μm wide with lengths of 250, 500, 750 and 1000 μm based on the chip designation I, II, III, IV respectively. Fiducials on the left and right side of the mask served as marks for aligning multiple masks and ensuring nanochannels connected the two microchannels regions.
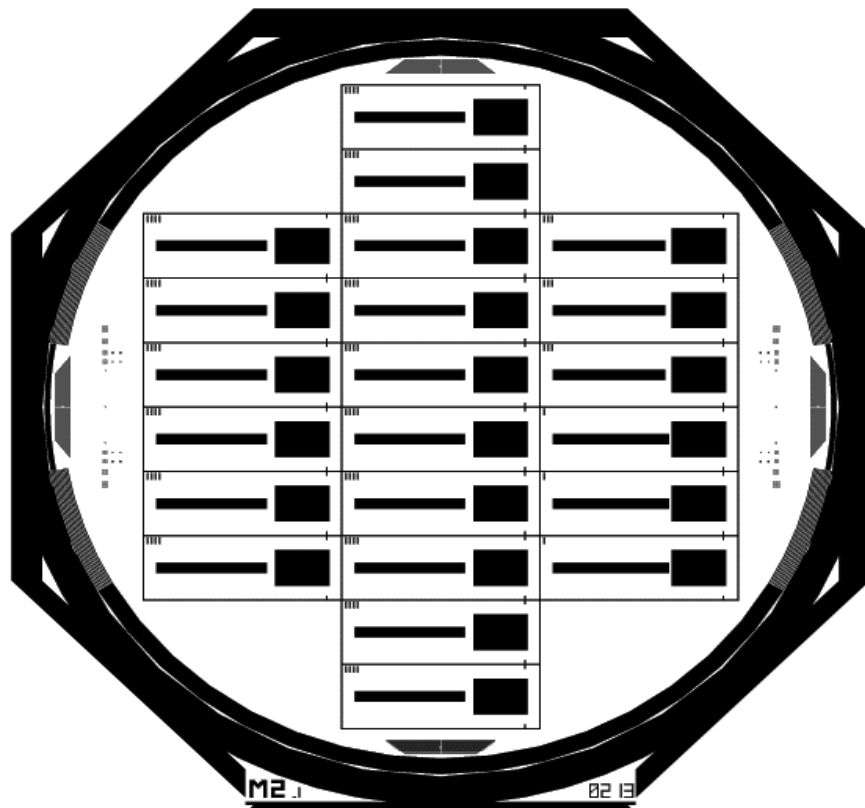
Figure 70: A photolithography mask was created for fabrication of multiple test chips. KOH is used for channel etching, so the mask profile only used 90° corners.

6.2.3 Nanochannel Profile Characterization

A Keyence VK-X200K laser profilometer measured the surface of all channels to determine width and depth. The Keyence uses confocal laser optics to scan a surface creating a 2D (X-Y) pixelated image. Each individual pixel is a Z-height, which is the point when the received laser intensity is maximized, indicating the system is in focus at the given depth. Height resolution is 0.5nm and the X-Y resolution is 1nm. Recording the X-Y scan optics in conjunction with the maximum intensity reading Z-height renders a high-accuracy 3D image of the scanned surface.

Figure 71: A Keyence X200 laser profilometer measured the channels in three dimensions. The laser scanned individual pixels and based on intensity readings determined a Z-height. Entire channels are scanned at once to visualize any defect that might inhibit flow in the nanochannel.

Imaging the entire channel profile enabled visual inspection to ensure constant cross-section and with no irregularities restricting fluid flow. Figure 72 illustrates a 12 μm channel with constant cross section and a smooth floor. The smaller channel connects the microchannel inlet with the microchannel exit, both etched to a depth of 79 μm.
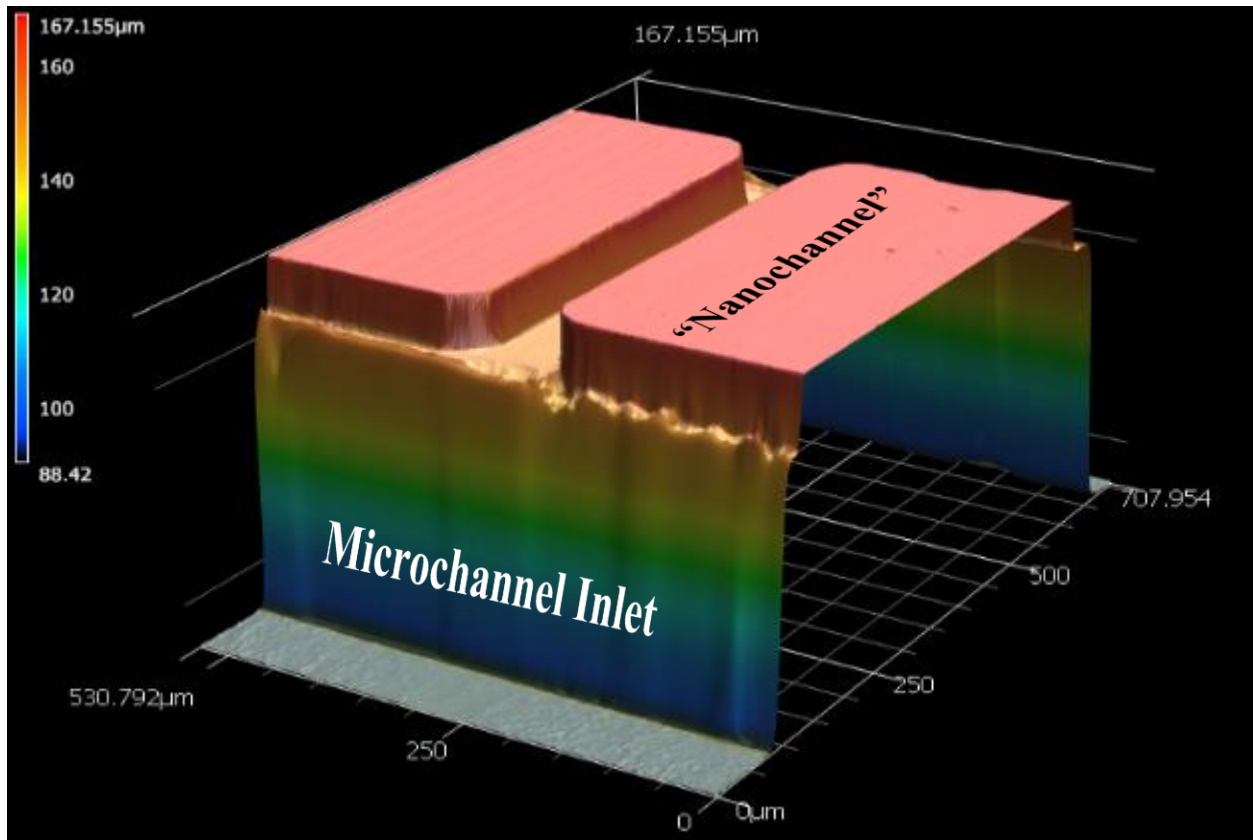
Figure 72: KOH etched a well-defined 12μm channel. The top surface is the bare silicon wafer. The microchannel was etched first, followed by the "nanochannel" for better tolerance of the "nanochannel."
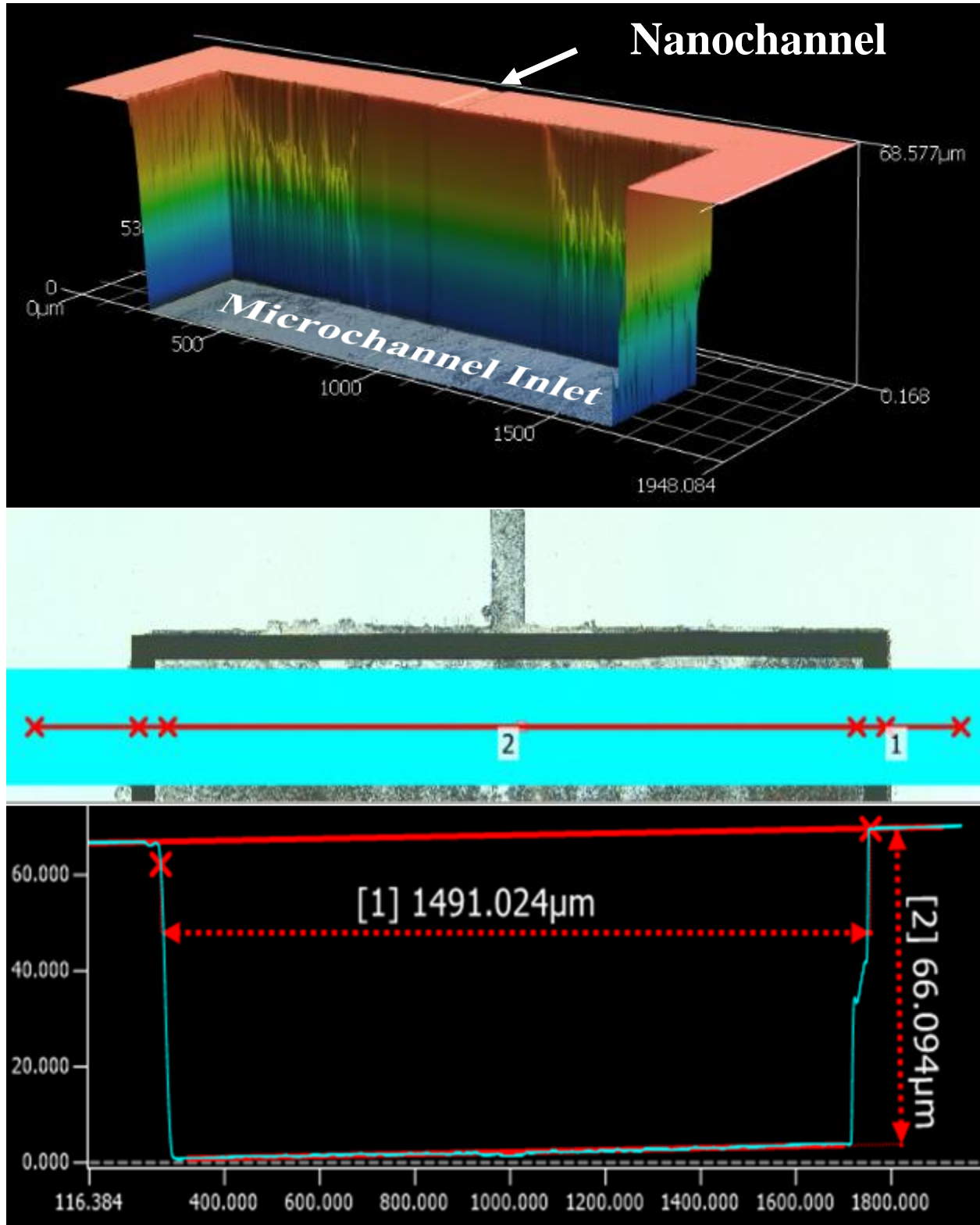
Figure 73: Many scan lines were averaged to determine the channel width and depth. For example, averaging 150 lines, the microchannel inlet width was approximately 1.5mm and the depth was 66.094μm. The number of scan lines was dictated by the allowable space recorded by the Keyence.

Profiling the microchannel inlet established key parameters for the flow rate determination; see Figure 73. While the microchannel inlet was designed with a 1.5mm width, the Keyence measured widths consistently around 1.49mm relatively independent of etching time, temperature, and concentration. Microchannel inlet depths varied depending on the length and temperature of the two KOH etch steps combined. Nanochannels with deeper etches resulted in slightly deeper microchannels, but primarily depth was dictated by the first KOH etch step. A shallower etch results in a more accurate flow rate measurement via meniscus tracking. However, the visibility of the meniscus diminishes as the channel decreases in depth, establishing a lower limit for etch depth. For readability purposes, 40μm was the lower limit for the microchannel inlet.
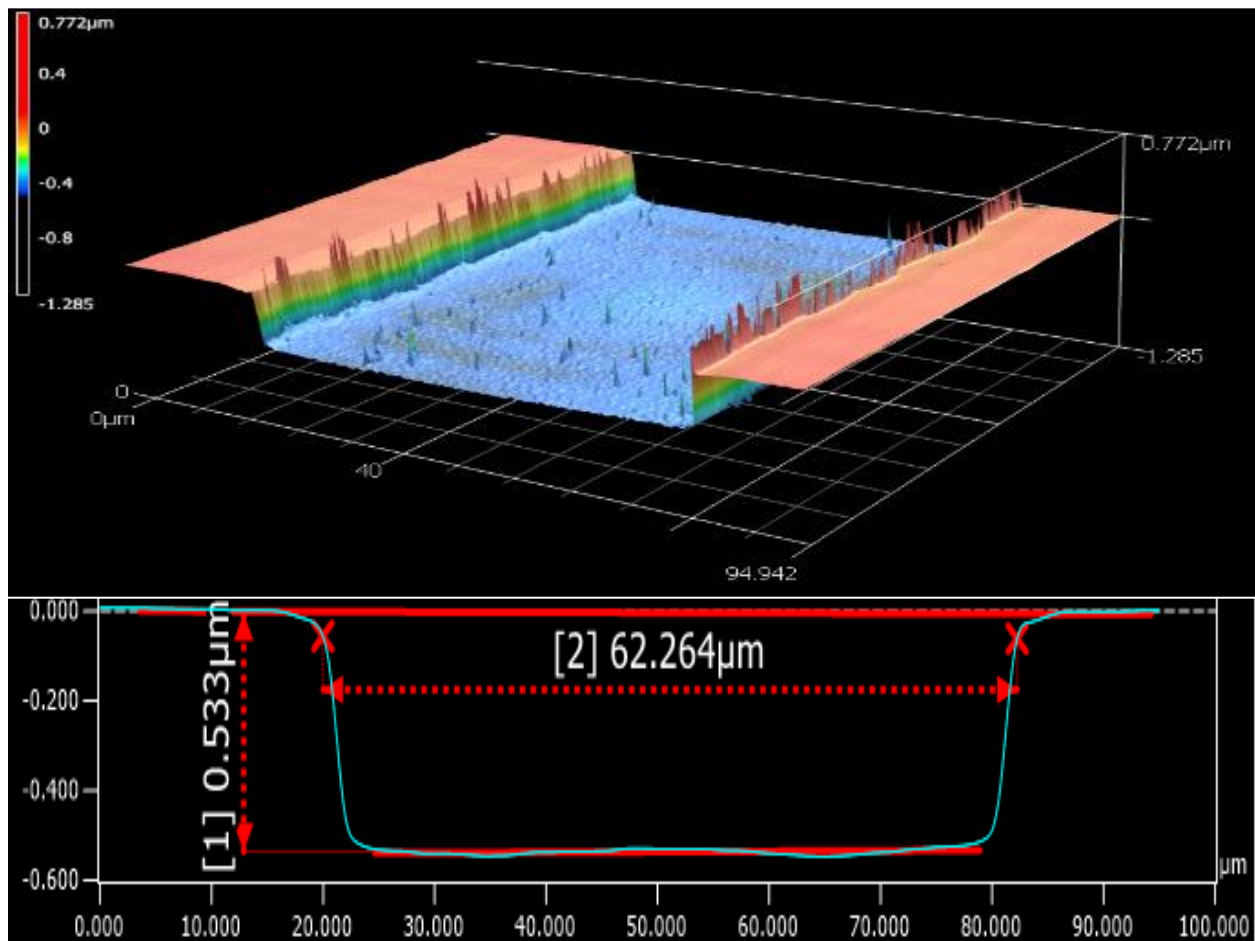
Figure 74: As channels approached the nanoscale, noise in the measurement was noticeable. Visual inspection for nanochannel uniformity increased the potential for consistent measurement.

The Keyence profiled both single nanochannels and nanochannel arrays etched in silicon. Figure 74 illustrates a single nanochannel scan where the upper surface (red) is the original silicon wafer surface. The floor of the channel (blue) is the result of bulk micromachining using KOH to etch into silicon. A three-minute KOH etch achieved a depth of 533μm with a smooth floor and consistent cross sectional area. The upper surface, protected by an oxide layer, was pristine for anodic bonding.
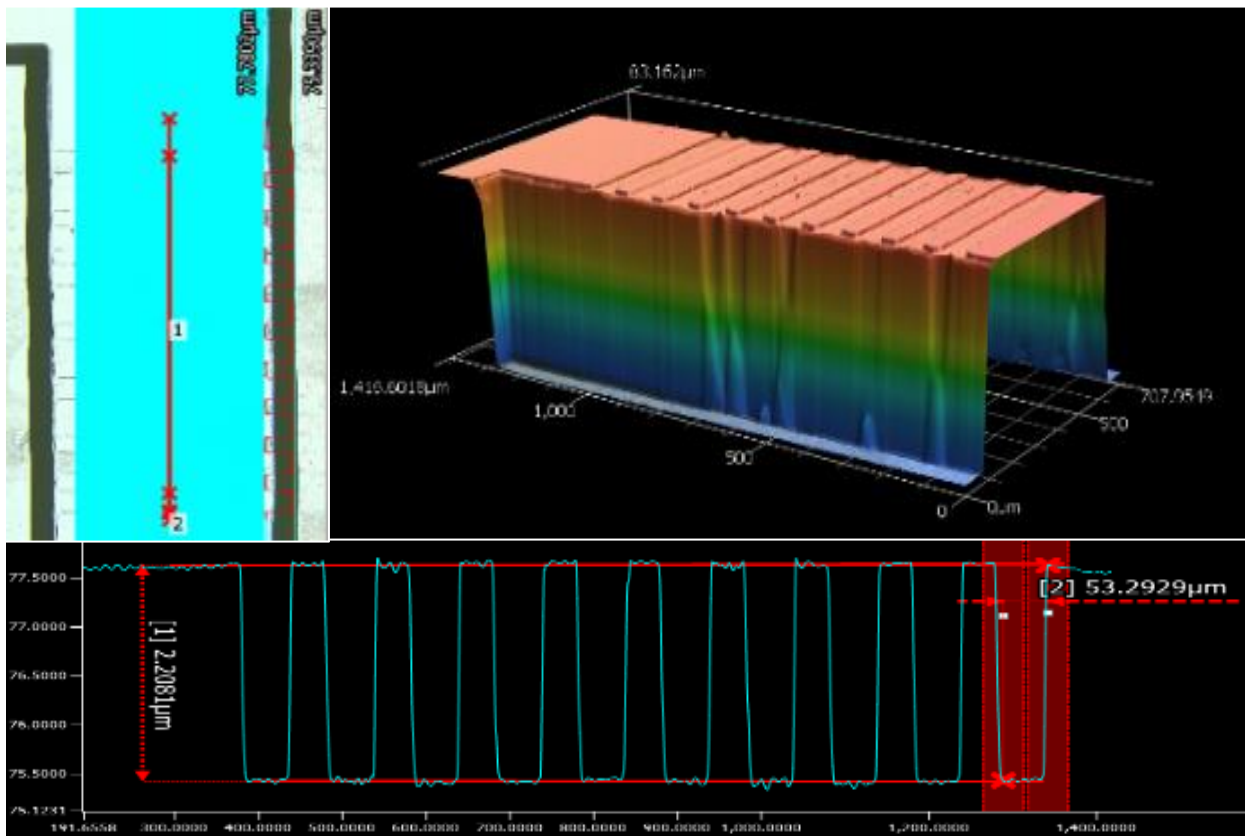
Figure 75: Nanochannel arrays were a pattern of 8-10 parallel channels. Channels exhibited some variation in width and depth when scanned in an array.

Similar in fabrication process to single nanochannels, Figure 75 depicts an array of ten microchannels etched into silicon. KOH etching for twelve minutes achieved a depth of 2.2μm, consistent across all nanochannels and along the entire length of the array. Refer to Appendix 11.3.3 for a complete table of profiled channel dimensions.

6.2.4 Microchannel Priming

Multiple methods tested to fill the microchannel inlet produced mixed results; see Appendix 11.3.1.3. The most effective method, an acrylic filling chamber, evacuated to sub Torr pressures removing all vapor and air from the micro/nanochannel, Figure 76. A laser cutter etched a cavity in acrylic and a CNC milled o-ring gland creating a tight seal. A 3D printed syringe pump pressurized fluid, filled the cavity, and maintained a constant pressure.
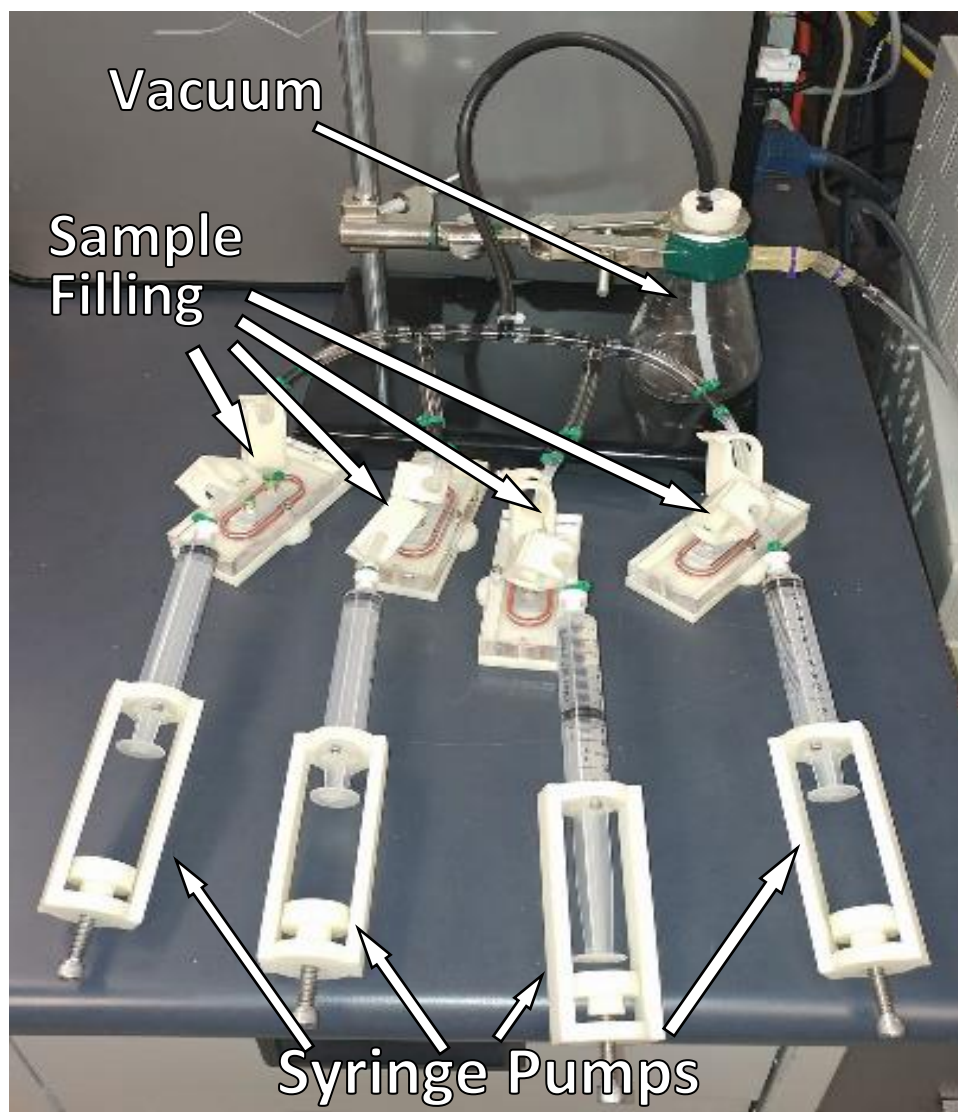
Figure 76: The sample filling chambers were vacuumed to remove all air and liquid from the nanochannel and microchannel inlet. A syringe pump pressurized pushed liquid into the nanochannel-filling apparatus after evacuation.

Aqueous solutions flowed through the nanochannel into the microchannel inlet forming a visible meniscus. Pressurizing the fluid significantly decreased filling time necessary for sample preparation, although strength of the glass slide limited the applicable pressure. Over-pressurization of the glass slide results in catastrophic cracking of the glass, rendering samples unusable. Figure 77 shows the filling progression of the meniscus in the microchannel inlet.
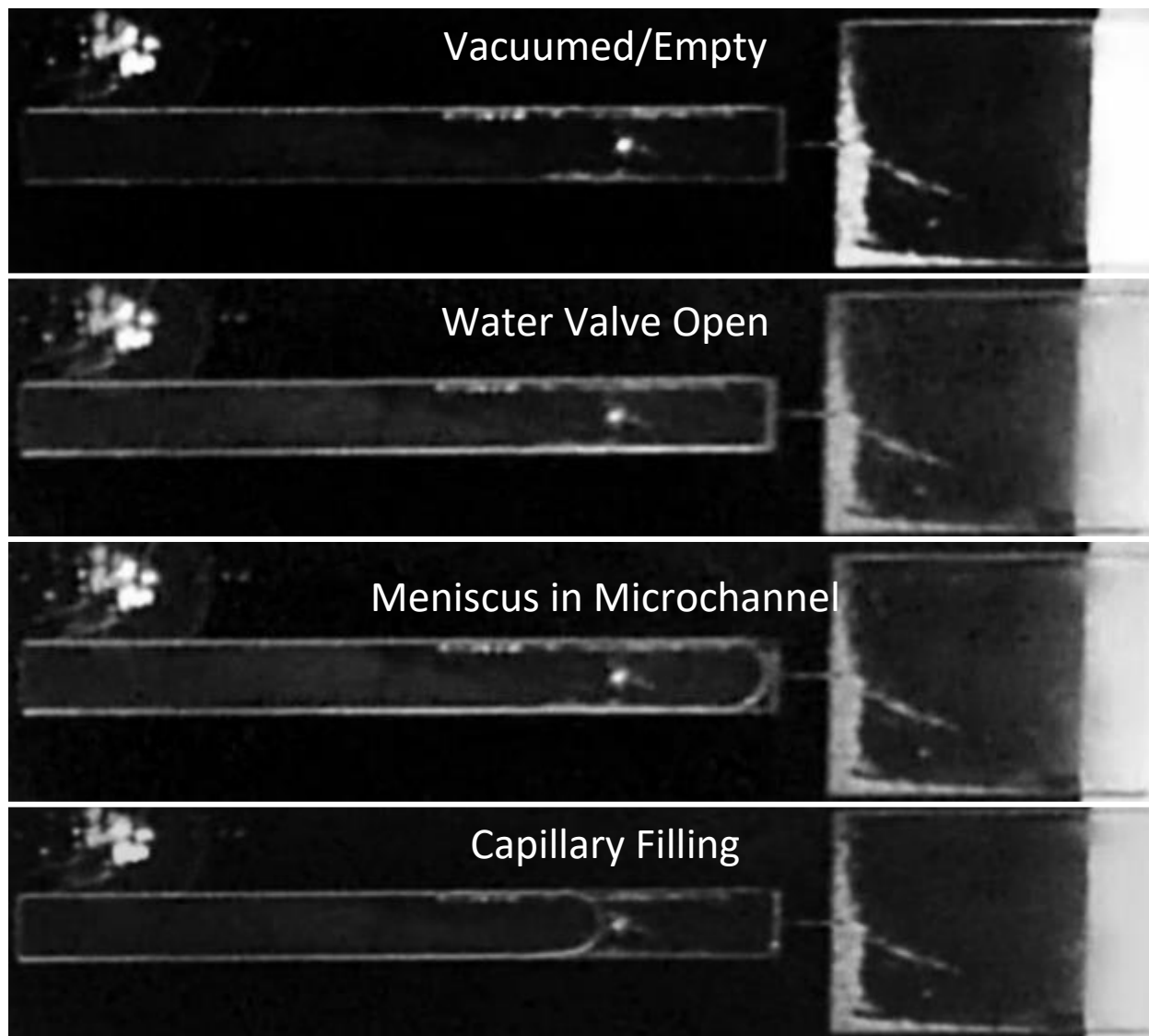
Figure 77: During filling, water flowed through the nanochannel and formed a meniscus in the microchannel inlet. With continued pressure, the meniscus progressed further into the microchannel inlet. During filling, the liquid in the nanochannel was ideally in contact with the nanochannel section, eliminating other liquid sources to be tracked.

6.3 RESULTS

After liquid priming the nanochannel device, a visible meniscus formed in the microchannel inlet. Initially, the exit channel contained fluid that evolved rapidly when pumped to high vacuum as shown in Figure 78. On the vacuum side in Figure 78 no liquid or meniscus is visible in contact with the nanochannel array. Additionally, no liquid is visible in the nanochannels despite fluid flowing through to vacuum across a meniscus at the exit. This visibility issue with liquid in shallow channels illustrates the necessity for a microchannel for meniscus observation and fluid tracking. Additional undesirable scenarios for accurate measurements include bubbling, condensation, trapped air, and fluid freezing. All three issues affect clarity of the meniscus and/or flow rate. For more information, refer to Appendix 11.3.1.
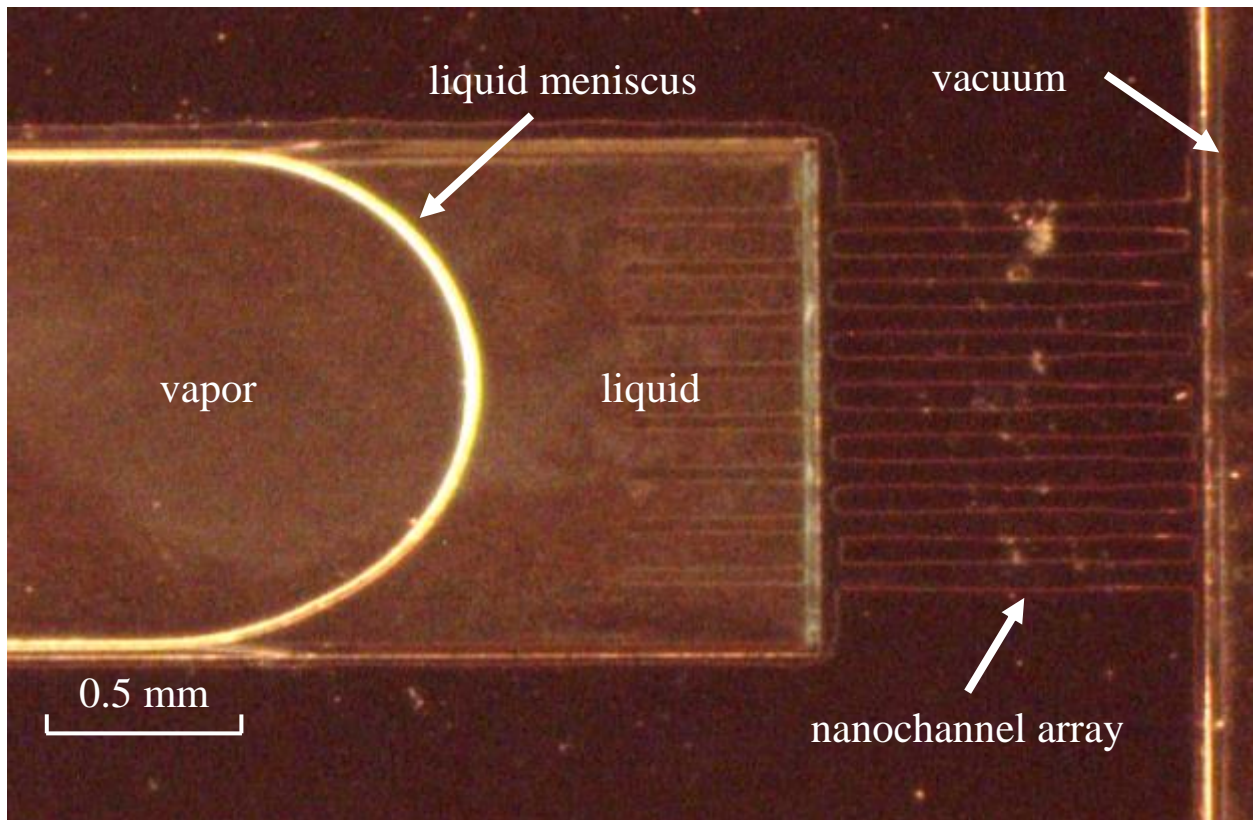
Figure 78: When the chip is exposed to vacuum, the liquid meniscus progresses from left to right at a rate regulated by the nanochannel(s). Although difficult to see by eye, water fills the nanochannels, but vaporizes to vacuum to the right.

While under vacuum, the meniscus progressed from the left to the right at a rate regulated by the nanochannel(s) and influenced by the microchannel inlet depth. The meniscus progresses slower in a deeper channel and faster in a shallow channel. Meniscus movement follows the limit set by Washburn flow for planar channels, Equation 12. Figure 79 shows the distinctive meniscus progression under 8X magnification. Processing images in LabVIEW generated pixel data for meniscus location, yielding a laminar flow velocity. Data manipulation determined a corresponding volumetric flow rate based on channel dimensions.
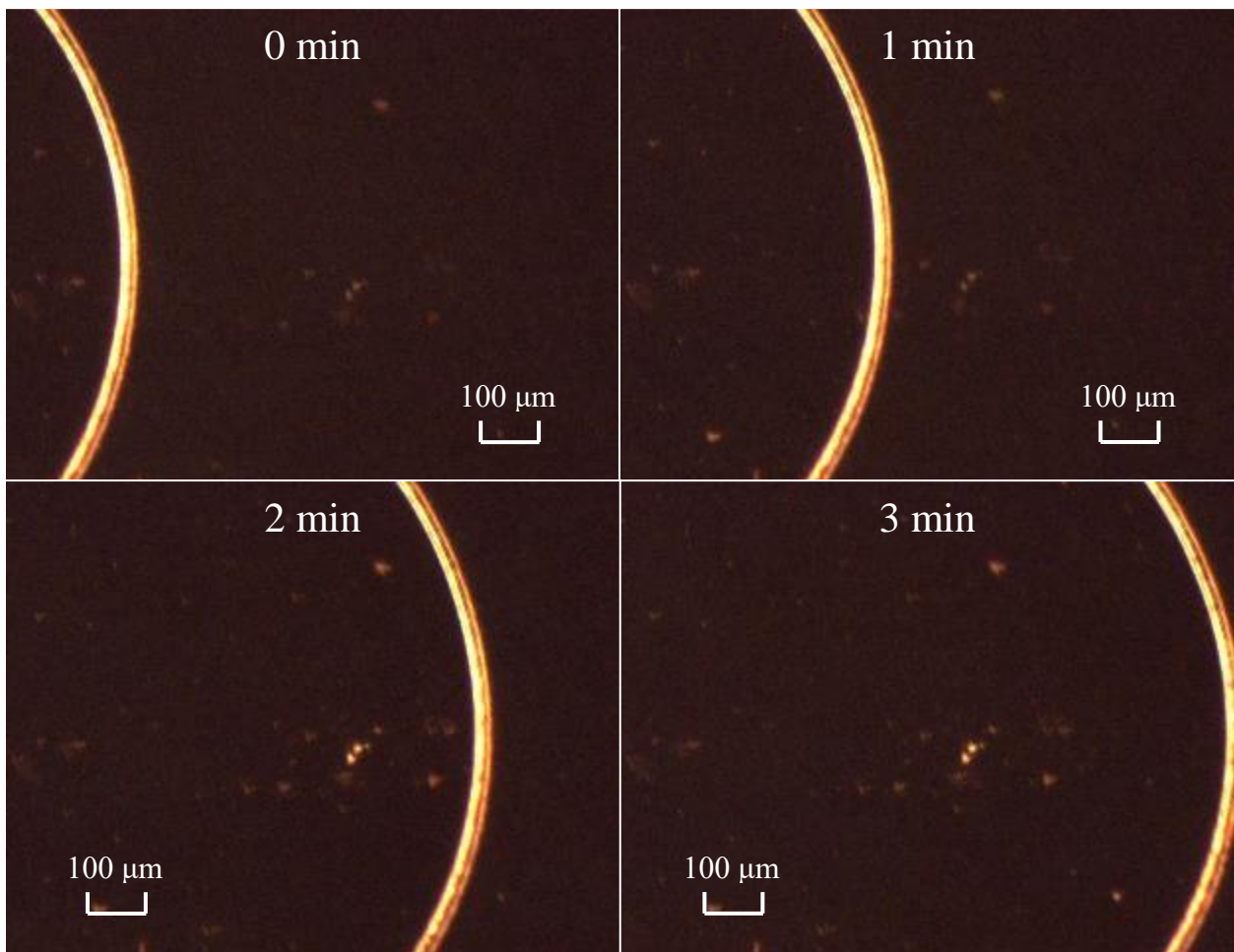
Figure 79: While under vacuum the meniscus progresses towards the nanochannels. The meniscus progression indicated a volumetric flow rate based on liquid properties and microchannel inlet geometry.
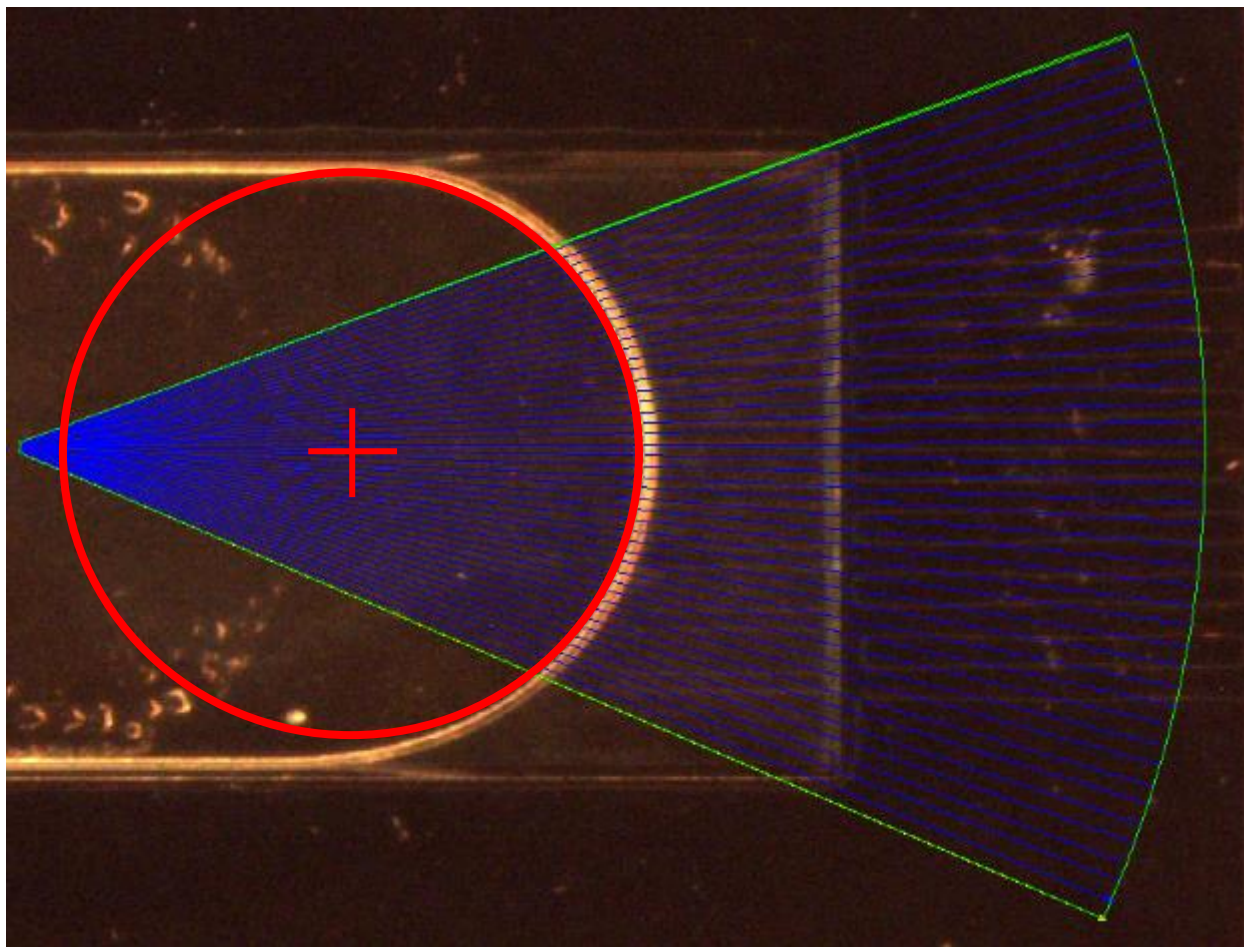
Figure 80: Labview tracking of the meniscus assigned an (x,y) center location of a circle as fluid progressed to vacuum. The circle was determined based on the intensity of the meniscus and a best fit circle was assigned.

Labview Vision assigned a location of the meniscus by fitting a circle to the curve in the designated field of view. Recording the center x and y pixel coordinates established a coordinate system for meniscus movement. As the meniscus progressed to the right of the image, recorded pixel values indicated a trend in the x-direction. A linear fit applied to the x pixel data, converted to micrometers using Figure 66, determined a fluid flow velocity, see Figure 81. Based on geometric parameters of the microchannel inlet and material properties of the fluid, mass and molar flow rate were derived from fluid flow velocity. Uncertainty in the flow rate was calculated using Logger Pro.
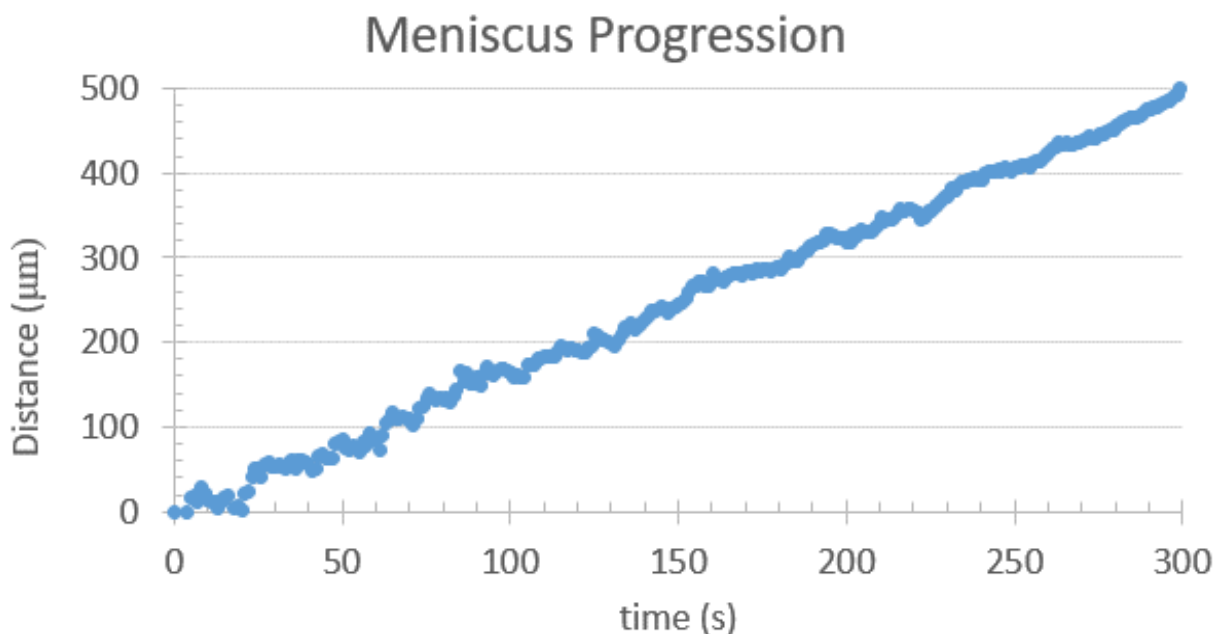
Figure 81: Sequential images were processed using Labview to determine the center x-coordinate of a circle fitted to the meniscus. Progression of the meniscus to the right corresponded to an x-coordinate movement. A linear regression applied to the meniscus x-coordinate movement indicated the fluid flow velocity which was converted to mass flow rate and molar flow rate. Uncertainty in the slope was determined using Logger Pro.

Lei et al. (2015) published data for nanochannels of similar magnitude for water "leak" to vacuum. Figure 82 plots experimental nanochannel evaporation data from Lei et al, represented as a blue square. The data followed Washburn capillary filling rates with slip for pipes with circular cross-section. Converting all data to a flow rate of mols of fluid per second maintains consistency between multiple experiments and improves comparability. Experimental data for single planar nanochannels, represented by orange diamonds in Figure 82, are in agreement with Washburn capillary flow for planar nanochannels, with one notable exception. Higher flow rates are for pure water and decreased accordingly with increasing concentration of propylene glycol. Array data is an order of magnitude faster due to the multiple channels, but for comparison Figure 82 plots array data as a composite average per channel. Flow rates for nanochannel arrays, shown in Figure 82 as green triangles, also agreed with Washburn limits.

114
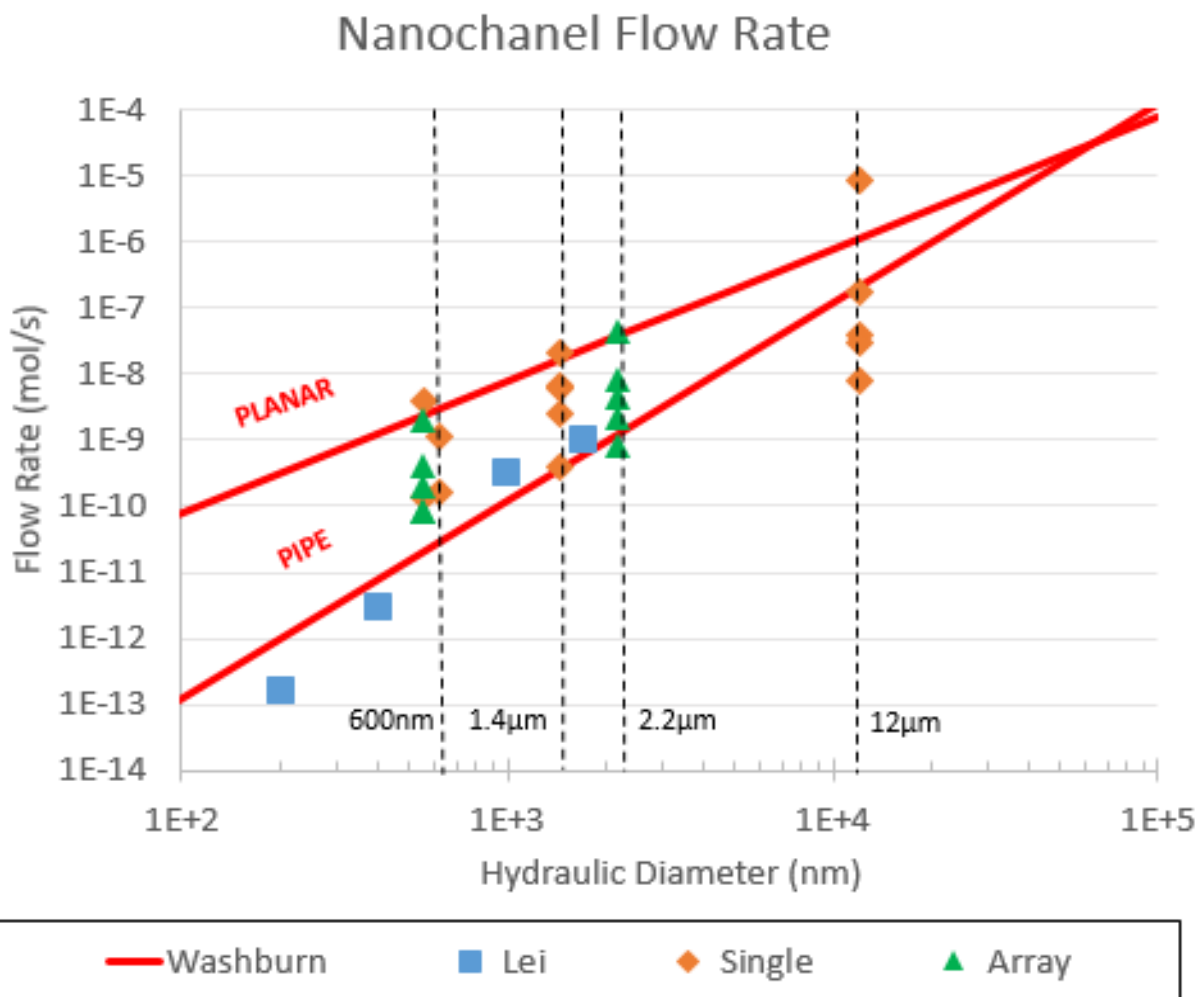
Figure 82: Flow rates were measured for planar channels with varying depth and antifreeze concentration. Theoretical Washburn capillary filling rates are designated by red lines for both planar and pipe channels. Single channels are designated with a diamond. Array data, diamond, was normalized to a per channel value for comparison on the same figure. A similar experiment using nanochannels with circular cross sections was conducted by Lei et al. (2015) and is represented by squares. Uncertainties were omitted for clarity, but can be seen in Figure 84 through Figure 86 for the individual data sets.

For the three channel sizes, the trend was an exponentially declining flow rate with increasing propylene glycol concentration. Water flowed faster than propylene glycol through the nanochannels due to its lower viscosity and higher vapor pressure. Additionally, surface tension for water (79.2 dyne/cm) increases capillary flow when compared to the surface tension for propylene glycol (39.1 dyne/cm).
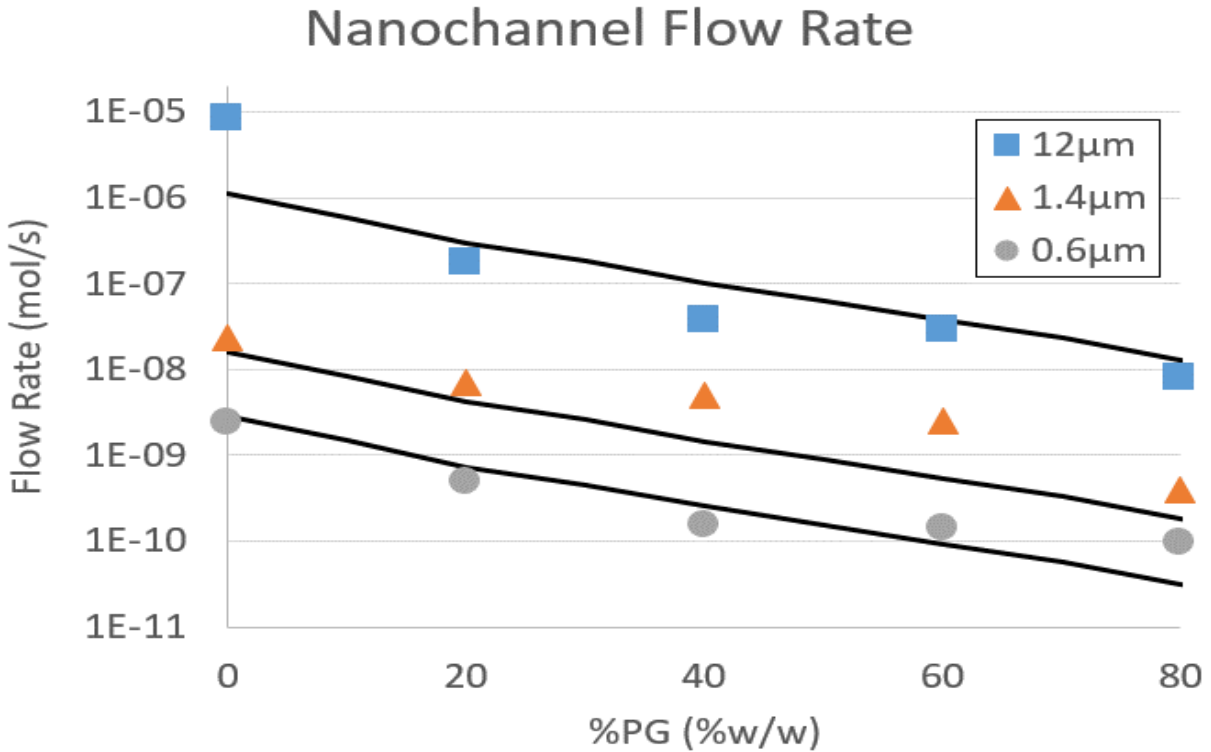
Figure 83: Fluid vaporization experiments evaluated channels of three different depths: 12µm, 1.4µm, and 0.6µm. Liquid filled the nanochannel(s) but flow from the microchannel inlet to the microchannel exit was restricted by the nanochannel(s). Solid lines represent theoretical Washburn capillary filling rates. Uncertainties were omitted for clarity, but can be seen in Figure 84 through Figure 86 for the individual data sets.

For the 12µm channel, flow rates scaled appropriately according to theory, except for pure water. When exposed to vacuum water flowed through the channel exceeding Washburn limits, as the channel was too large to restrict the flow by capillary action. Unlike other trials, no meniscus formed at the "nanochannel" exit and water flowed in the Hagen-Poiseuille regime. As antifreeze concentration increased, fluid flow resumed Washburn type flow at flow rates two orders of magnitude lower.
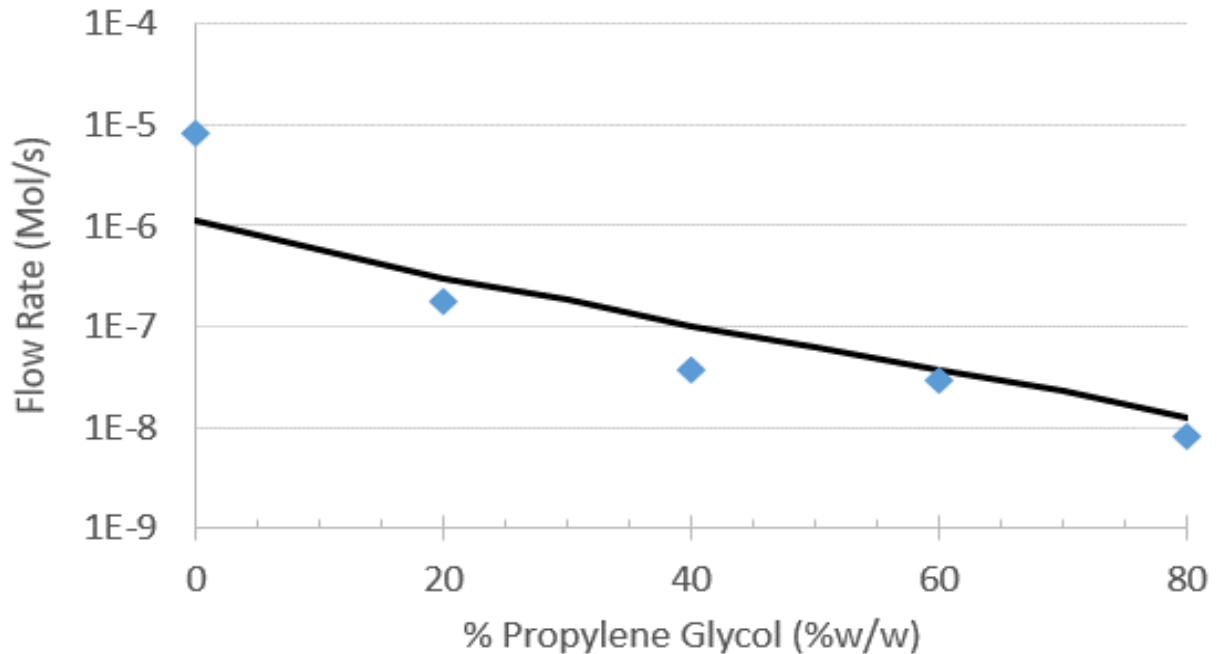
Figure 84: Liquid filled the nanochannel(s) but flow from the microchannel inlet to the microchannel exit was restricted by the nanochannel(s). The solid line represents theoretical Washburn capillary filling rates for a single 50µm wide by 12µm deep channel. Liquid water flowed through the 12µm channel at a higher rate than expected with theory. Linear fit uncertainties are displayed, but are smaller than the individual data markers.

Figure 85 shows flow through single 1.442µm channels as blue diamonds and an array of ten 2.19µm channels as orange circles. The 8-channel array increased the overall flow rate, but not at 1:1 scaling. Normalizing the data relative to the depth of the channel, the flow rate for each channel in the array was assumed to be 100% of the single channel flow rate. However, the flow rate per channel was determined to be only 94%, 54%, 32%, 40%, and 91% for 0%, 20%, 40%, 60%, and 80% propylene glycol concentration respectively. Ideally, the array would scale 100% for each addition channel, but variability in channel array dimensions influences the overall flow rate. However, considering noise in the measurement and flow irregularities the flow rate exhibited an increase across the full range of concentrations for channel arrays.

117
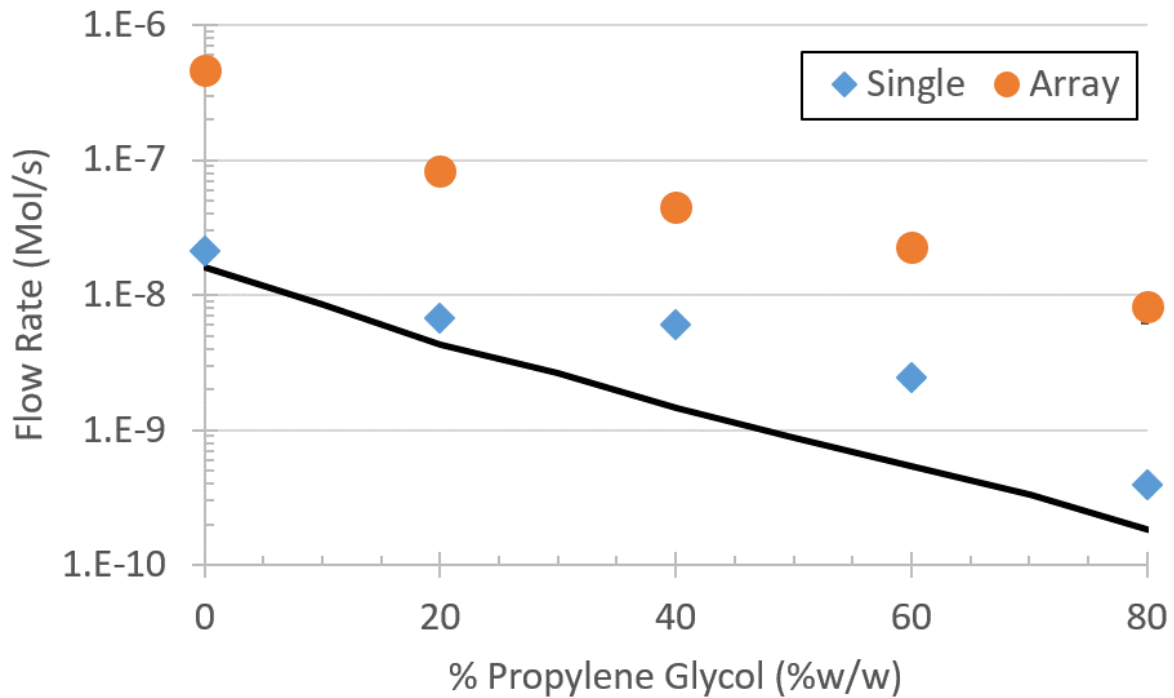
Figure 85: Liquid filled the nanochannel(s) but flow from the microchannel inlet to the microchannel exit was restricted by the nanochannel(s). Ten-channel arrays exhibited a higher flow rate than single nanochannels but did not increase at a 1:1 rate. The solid line represents theoretical Washburn capillary filling rates for single planar microchannels 50µm wide by 1.442µm deep. Linear fit uncertainties are displayed, but are smaller than the individual data markers.

Figure 86 shows flow through single 550-600nm channels as blue diamonds and an array of ten 550nm channels as orange circles. The 10-channel array increased the overall flow rate, but not at 1:1 scaling. Normalizing the data relative to the depth of the channel, the flow rate for each channel in the array was assumed to be 100% of the single channel flow rate. However, the flow rate per channel was determined to be only 55%, 30%, 98%, 56%, and 79% for 0%, 20%, 40%, 60%, and 80% propylene glycol concentration respectively. The flow rate exhibited an increase across the full range of concentrations for channel arrays.
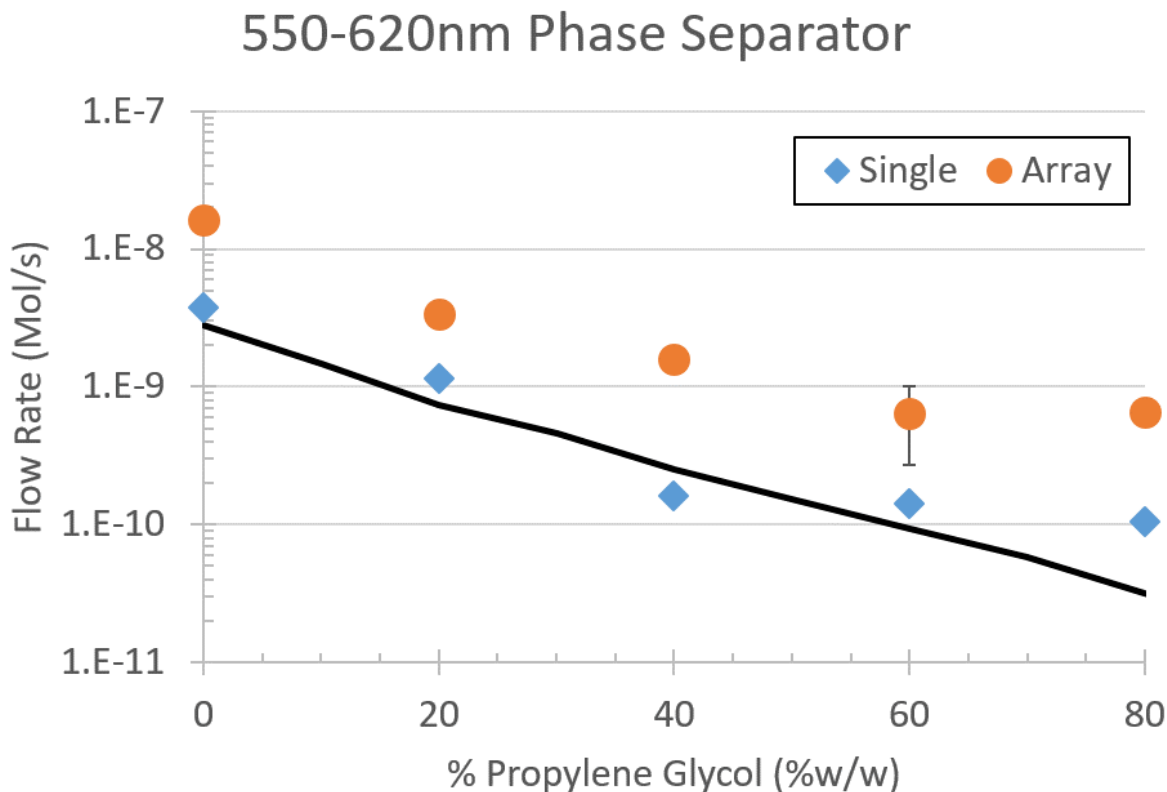
Figure 86: Liquid filled the nanochannel(s) but flow from the microchannel inlet to the microchannel exit was restricted by the nanochannel(s). Eight-channel arrays exhibited a higher flow rate than single nanochannels but did not increase at a 1:1 rate. At higher concentrations of propylene glycol, the improvement in flow rate was even less. The solid line represents theoretical Washburn capillary filling rates for single planar nanochannels 50μm wide by 550nm deep. Linear fit uncertainties are displayed, but are smaller than the individual data markers, except for the 60% propylene glycol channel array.

6.4   DISCUSSION

Experimental verification of nanochannel fluid flow is still in very early stages. This work advanced the field with successful measurement and a novel method for measuring fluid flow at the nanoscale. Research offered the first flow measurements of aqueous antifreeze mixtures through planar nanochannels with no external pressure.

Referencing the 12μm water data in Figure 82 and Figure 83, the flow rate is one to two orders of magnitude higher than the rest of the data. This abnormality indicates the Washburn capillary filling effect is not restricting fluid flow. At that point, water is no longer evaporating across the meniscus, as desired, but rather liquid water is flowing through the channel into the vacuum environment. In the propulsion system, such an effect leads to decreased thrust due to crystallization of the liquid water droplets. Between 1.4μm-12μm, the fluid rate transitions from an evaporative mode to a liquid transport mode, the upper limit to phase separation channel design.

Prior to this research, flow rates in the picoliter (pL) per hour range were anticipated based on Hagen-Poiseuille flow limits. However, the minimum flow rate observed during experimentation was for a 500nm channel with 80% propylene glycol was still 23,760 picoliter per hour, an encouraging 4 orders of magnitude faster. In fact, the flow rate was so fast the minimum value registered at 6.6 pL per second. For 600 nm channels flow rates ranged from 6.6 pL/s for 80% propylene glycol to 59.5 pL/s for pure water. 1.4 μm channels experienced flow rates of 25 pL/s for 80% propylene glycol to 416 pL/s for water. 12 μm channels, excluding water, saw flow rates between 5200 pL/s for 20% propylene glycol and 501 pL/s for 80% propylene glycol.

Channel array flow rates were even more productive. A 600 nm 8-channel array generated flow rates of 320 pL/s for water to 9 pL/s for 80% PG. A 2.2 μm 10-channel array experienced flow rates of 8610 pL/s for water down to 545 pL/s for 80% PG. All flow rates are orders of magnitude better than anticipated values, indicating appreciably better potential thrust values for CubeSats.

As expected, surface quality of the channels played a significant role in flow rate. Channels required a consistent etch floor for optimal production. Defects in the channel floor protruding into the channel volume resulted in decreased flow rates despite an otherwise consistent etch

pattern, Figure 87 and Figure 88. Additionally, poor etching of sections of silicon resulted in large

structures restricting flow through otherwise pristine channels, Figure 89. Channels like Figure 87

measured in the μm scale but because of the additional restriction, performed at a rate consistent

with the nm range or lower. Out of ten channels fabricated at the 1-2 μm scale, three experienced

this effect. Two out of the three would not even fill for testing due to restricted flow. The third

channel filled once, but experienced flow rated consistent with a 200-300nm channel.
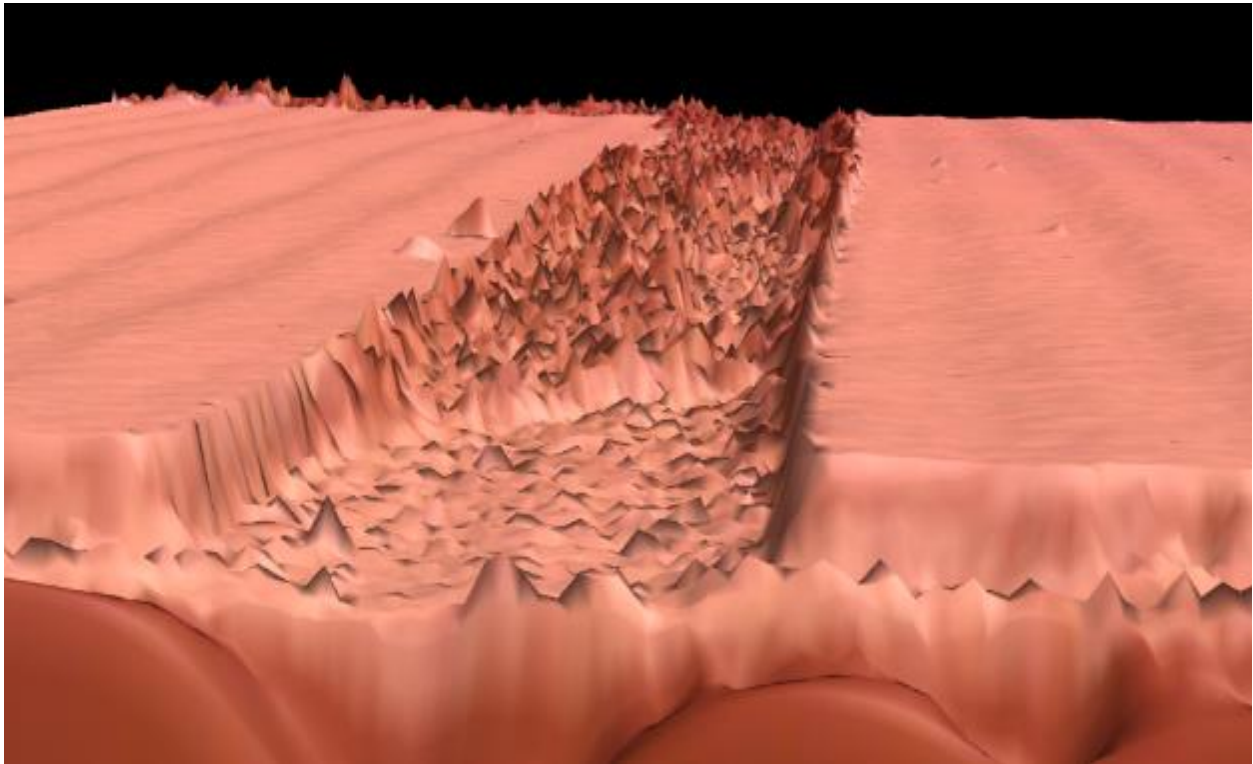
Figure 87: Uneven potassium hydroxide etching resulted in stalagmite-like structures which restrict flow rate. Buffered oxide etching of the oxide layer is critical for formation of a mask to prevent uneven KOH etching of silicon.
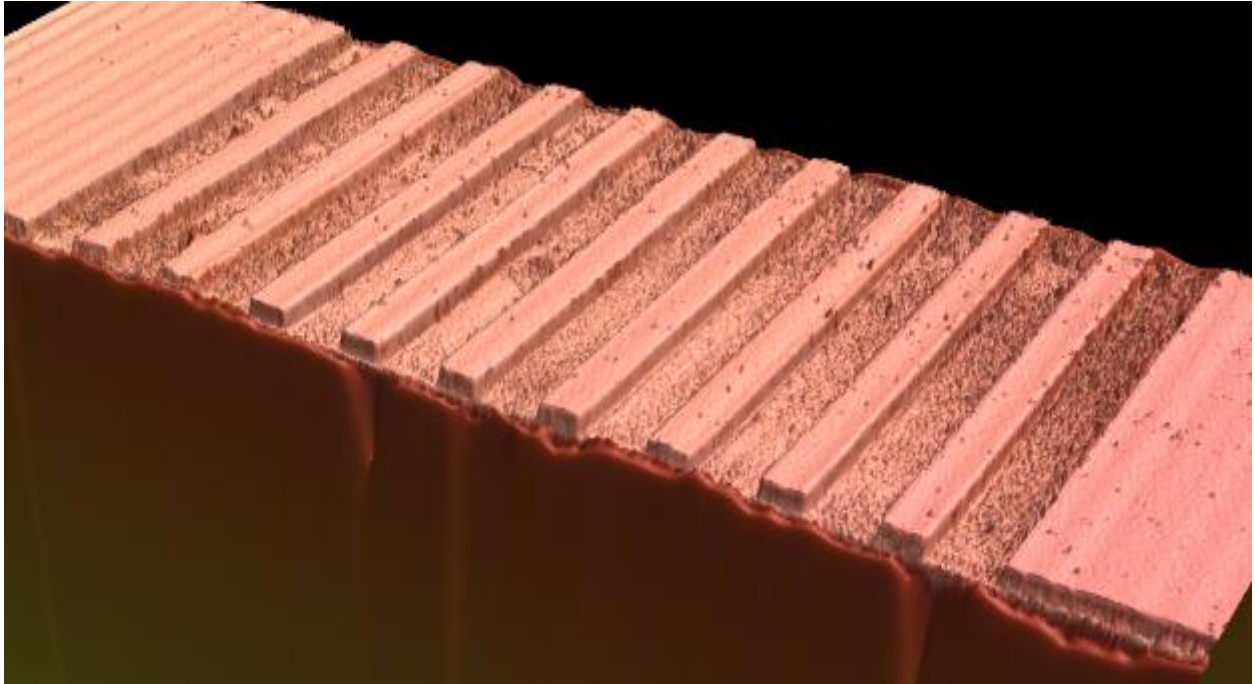
Figure 88: Uneven potassium hydroxide etching results in varying channel surface roughness across the channel array. A few channels exhibit near ideal surface roughness, while other channels will not achieve theoretical flow rates. The composite flow rate will be lower than 1:1 scaling.
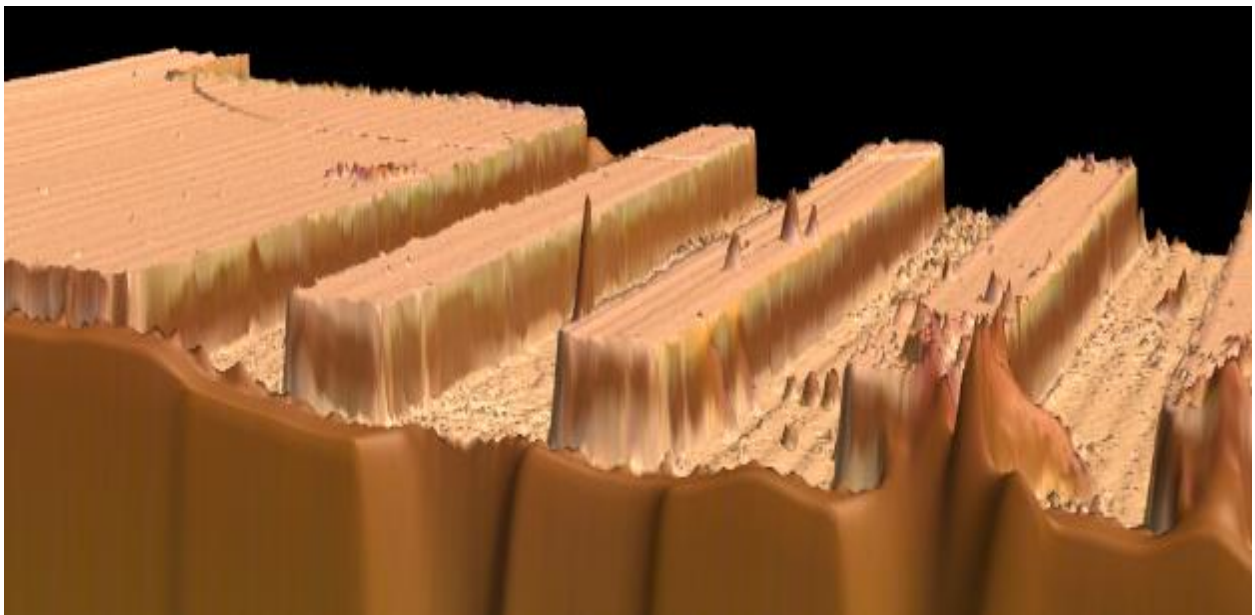
Figure 89: Even when channel etch is relatively uniform across the channel array, poorly etched sections block channels, restricting flow. Tight control of the fabrication process and cleanliness limits the occurrence of these defects but will not eliminate them completely.

Channels represented in Figure 87 through Figure 89 also have a larger exposed surface area, increasing the chance of fouling. Surface roughness, especially at the nanochannel length scale causes material build up and restricts flow. Even with filtered and chemical grade liquids nanochannels experience fouling at a higher rate. The 500nm channels experienced a much higher rate of failure/repeatability. Ten channels fabricated at the 500-600nm range reported a current failure rate of 50%. Failed channels completed at least one trial that either resulted in liquid trapped in the microchannel inlet or similar flow rates were not repeatable. Failed channels remained in a vacuum chamber for a day at high vacuum before assigning a "failed" designation.

7   A "GREEN" COLD-GAS PROPULSION SYSTEM FOR CUBESATELLITES

All three separate experiments combine to play a vital role in designing a propulsion system for cubesatellites. Aqueous antifreeze vapor values assist in prediction of achievable thrust values, which is an important mission design parameter. Understanding expansion principles of aqueous antifreeze liquids establishes quantifiable limits on the volume limited cubesatellite. In addition, understanding nanofluidics is integral for the propulsion system to calibrate propellant delivery to the thruster.

Accurate and timely prediction of propellant concentration (demonstrated in the mesoscale experiment) in the tank is essential to predicting the system limits for fluid freezing and expansion. On board monitoring of concentration determines the required temperature in the tank to prevent freezing. Moreover, if the propellant were to freeze, system design could anticipate and account for expansion, minimizing stress to the satellite.

Using experimental mass flow rates from Figure 82, an approximation for the potential thrust is calculable. Before determining thrust, the specific impulse of aqueous antifreeze vapor is needed. Kane et al. (1996) published the specific heat ratios for vapor phase propylene glycol, ethylene glycol, and glycerol. Theoretical specific impulses for aqueous antifreeze vapor are calculated using Equation 14. The vapor mixture is assumed to behave as an ideal gas and specific heat ratio was linearly interpolated between pure water vapor and pure antifreeze vapor. Theoretical specific impulse for aqueous vapor mixtures of ethylene glycol, propylene glycol, and glycerol are shown in Figure 90.

$$I_{sp} = \frac{\sqrt{\gamma R T}}{\gamma \left(\frac{2}{\gamma+1}\right)^{\frac{\gamma+1}{2\gamma-2}}} \gamma \sqrt{\left(\frac{2}{\gamma-1}\right)\left(\frac{2}{\gamma+1}\right)^{\frac{\gamma+1}{\gamma-1}}}$$

Equation 14

γ: specific heat ratio (J/(gm*K))
T: temperature (K)
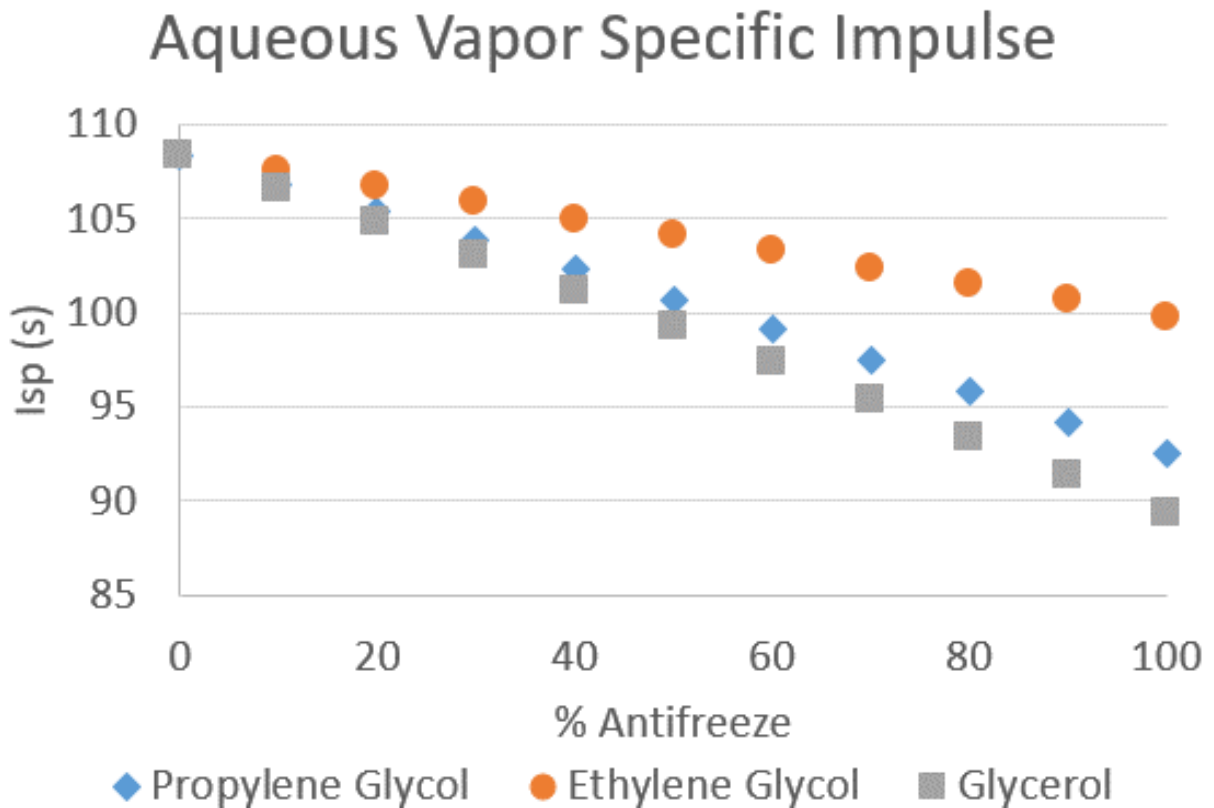
Figure 90: Theoretical specific impulse of aqueous antifreeze vapor is calculable using Equation 14. Assuming a linear relationship between water and pure antifreeze for the specific heat ratio, the specific impulse decreased linearly from 108s for pure water.

Since efficiency of a propellant is proportional to specific impulse, the ideal propellant would be pure water. Yet, water expands upon freezing at 0°C, which is problematic when considering the limited volume of the small satellite. The satellite design may incorporate results from Figure 54 and account for expansion preventing potential damage to the satellite. As an added bonus,

decreasing the required temperature lowers the power requirement of the satellite. A CubeSat has limited on board power, which is necessary to maintain fluid temperature or even locally heating. As a rule of thumb, the design parameters for a small satellite require that the core temperature remain ±20°C. The energy necessary to maintain fluid temperatures results in heat, increasing the core temperature of the satellite. Heat transfer of the small satellite is a complex analysis and likely requires heat sinks to maintain a reasonable satellite temperature. Therefore, the mission specific ideal water/PG ratio limits expansion/crystallization of water, yet is vaporizable at lower temperature, while maintaining a high level of efficiency.

Overall, the future goal of the research is development of a propulsion system utilizing a nanochannel array, as a phase separator, to deliver the PG/water solution as a propellant. Using Equation 2 the thrust generated by one nanochannel is calculable by rearranging the equation, where F equals thrust. The experimental mass flow rates, from Figure 82, multiplied by the propylene glycol specific impulse, shown in Figure 90, and multiplied by gravity yields the thrust approximation shown in Figure 91.
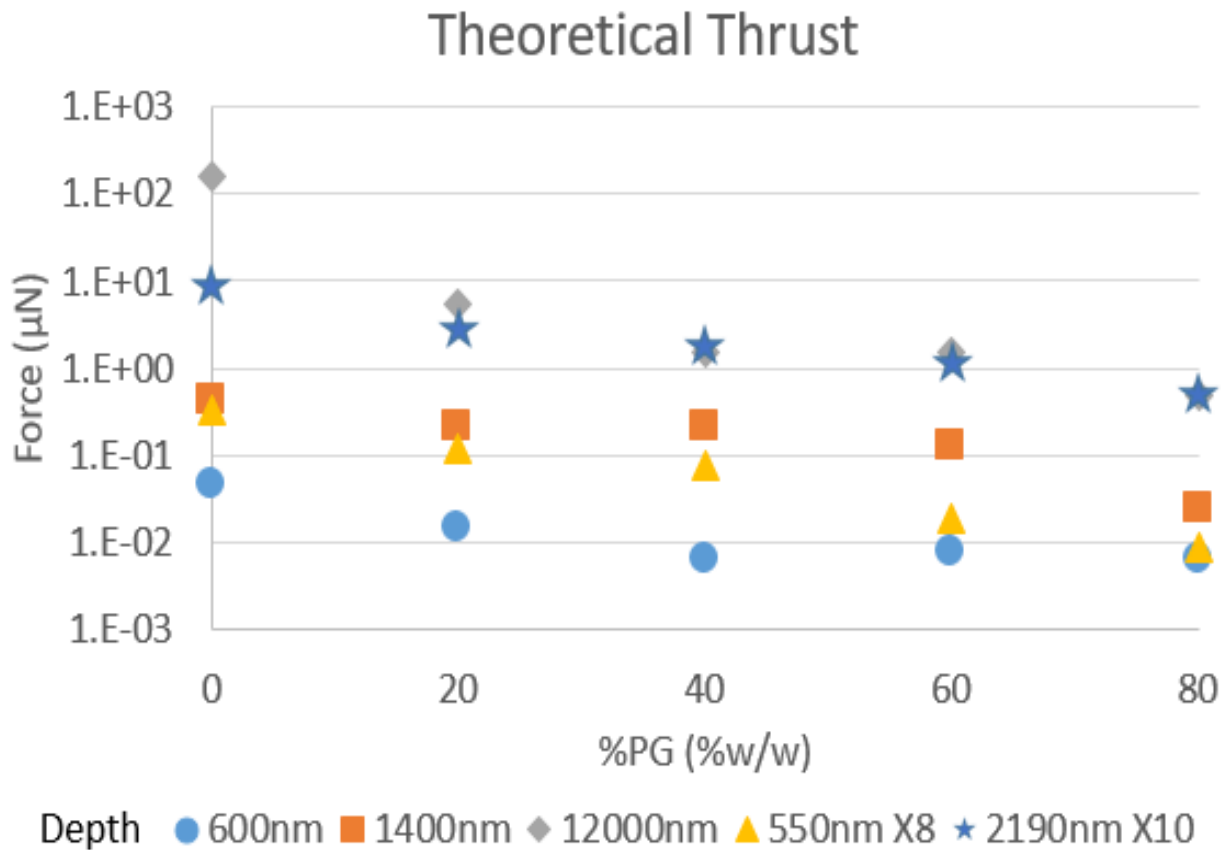
Figure 91: Using flow rate data from Figure 82, theoretical cold-gas thrust from the single channels and arrays was calculated. For planar channels with a depth on the microscale range the thrust achievable is in the micronewton range.

Interestingly, all single nanochannels tested theoretically can produce 0.01 to 1µN levels of thrust with propellants ranging from pure water to 80% propylene glycol. Nanochannel arrays performed even better with a 2.19µm ten-channel array performing as well as the 12µm single channel. Moreover, the 2.19µm array restricted the flow of water indicating Washburn flow while still maintaining thrust levels. Both cases are essential for scalability of nanochannels for use as a phase separator. Based on its performance, scaling up the 2.19µm array enabled evaluation of potential thrust values and the corresponding number of channels required.
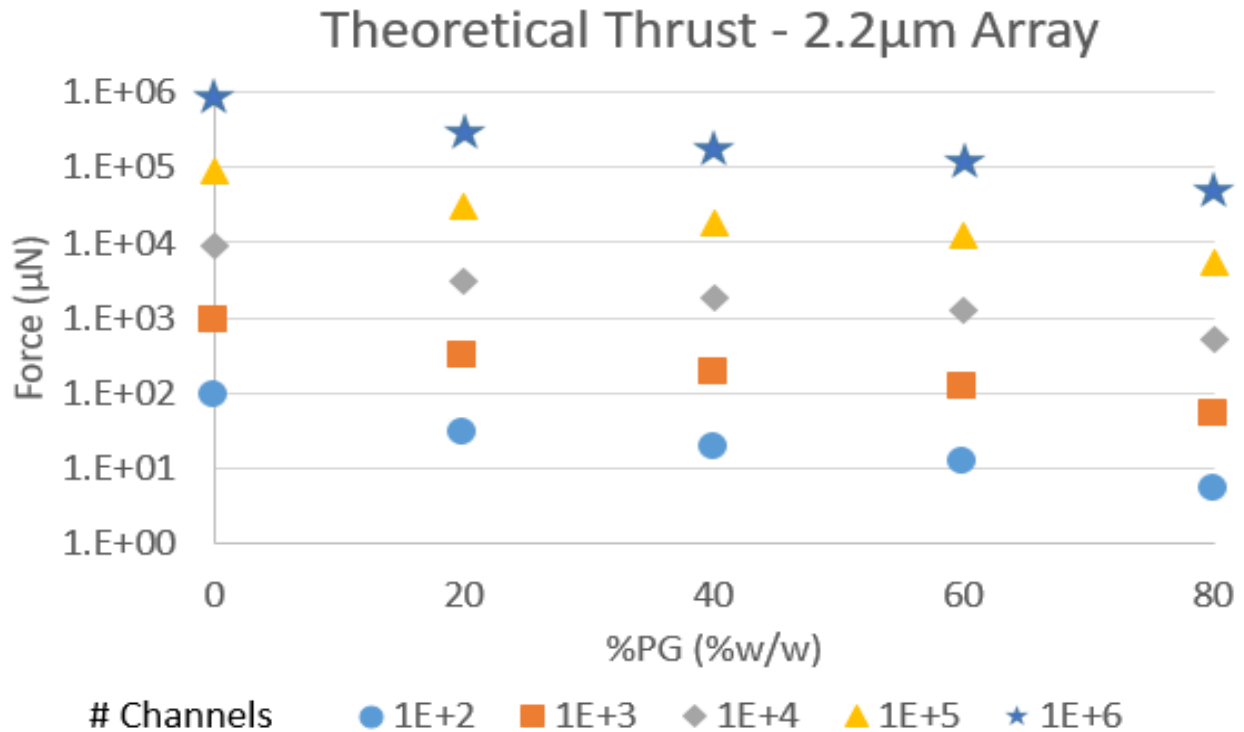
Figure 92: Thrust generated by a 2.2µm deep 10-channel array was used to predict the thrust of larger channel arrays. The thrust was divided by 10 to achieve a "single channel thrust output" and then multiplied to determine potential thrust.

From Figure 92, millinewton levels of thrust are achievable with 1,000-10,000 2.2µm channel arrays, which is easily in the realm of possibility. Borderline Newton levels of thrust are still possible but require one million channels. A stacked array or even porous membrane controlled to channel diameter make such a high number an even greater possibility. Based on physical requirements outlined in Figure 7, the channel array theoretical thrust derived from experimental mass flow data is sufficient for any level of orbital maneuver. Based on the results presented, a micro/nanochannel array is a viable option as a phase separator for use in a CubeSat propulsion system.

8   CONCLUSIONS

Experiments established that a nanochannel array is a viable option as a phase separator for a CubeSat propulsion system when using a propylene glycol-water mixture. Experimental mass flow rates exceeded anticipated values since the channels are planar and not pipe. Planar nanochannels experience higher flow rates than typical macroscale flow approximations using hydraulic diameter due to the mode of fluid transport. At the 100nm-10µm length scale, Washburn capillary filling regulates fluid flow instead of traditional Hagen-Poiseuille flow. Single channel flow rates had magnitudes of 1E-10 mol/s for a 600nm channel, 1E-9 mol/s for a 1.4µm channel, and 1E-8 mol/s for a 12µm channel. Channel arrays increased flow rates to 10E-9 mol/s for a 550nm 8-channel array and 10E-7 mol/s for a 2.19µm 10-channel array. While channel arrays increased the overall flow rate, it was not at 1:1 scaling. Flow rates for each channel in the array were assumed to be 100% of the single channel flow rate. However, the flow rate per channel was determined to be, on average, only 65% of the single channel flow rates.

Experiments successfully determined expansion maximums for aqueous antifreeze solutions during phase change. All aqueous antifreeze solutions demonstrated an exponential decline in expansion percentage with increasing concentration of antifreeze. Pure water expands approximately 9% during freezing. A 7.5 %w/w propylene glycol-water reduces the overall expansion by 2% while 20 %w/w PG reduces the expansion 4%. Similar trends resulted from other antifreeze experiments with ethylene glycol behaving similarly to PG, methanol experiencing the greatest reduction in expansion percentage, and glycerol seeing slightly less impact when mixed with water. Freezing point depression agreed with material property data with ethylene and propylene glycol displaying similar trends, glycerol exhibiting the least reduction in

freezing point, and methanol having the strongest effect on freezing point depression. All results establish important design guidelines for satellites.

Viscosity values are necessary when evaluating flow downstream after evaporation and for predicting vapor phase flow through nanochannels. Understanding kinematic viscosity for evolving gas at various concentrations of aqueous antifreeze enables determination and prediction of fluid flow through nanochannels and nozzles. A viscometer, developed expressly for this study, measured kinematic viscosity values between 1E-2 and 1E-4 m^2/s for water solutions mixed with propylene glycol, ethylene glycol, methanol, and glycerol. Measured kinematic viscosity values agree with pure water and methanol. Intermediate concentration trends approached values consistent with pure materials. Experiments conducted not only delivered viscosity values for evolving vapor, but also developed an in-situ propellant concentration monitoring system. Concentration in the propellant chamber directly relates to vapor pressure and temperature. Monitoring temperature and pressure enables accurate prediction of mass flow, specific impulse, and thrust improving Cubesatellite mission capabilities and accuracy.

9   FUTURE WORK

9.1   CHANNEL LEAK/FLOW REGIME CROSSOVER AND NANOCHANNEL ARRAY SCALABILITY

Future research needs to test aqueous propylene glycol solutions using microchannels with depths between 2.1μm and 10μm deep. A flow regime transition in the micrometer length scale transitions from Washburn capillary flow to liquid Hagen-Poiseuille. The flow-regime transition is the limit for capillary restricted flow and the maximum mass flow allowable from the phase separator.   The dimensional limit may be material specific and surface engineering (hydrophobicity/hydrophilicity) can influence the flow rate.   In addition, Washburn capillary action limits planar channels, but can manipulation of channel width further increase flow rate? Scalability of the channel array must be extended and researched. Ten channels scale from one but scaling to one thousand to one million is necessary for desired thrust values.

9.2   PROPYLENE   GLYCOL   FREEZING   ANOMOLY,   NUCLEATION,   AND UNDERCOOLING

The contraction observed during phase change for propylene glycol, ethylene glycol, and glycerol at 30-50%w/w is particularly interesting as it was unexpected. The experimental setup design focused on accurate measurement of fluid expansion during phase change, not contraction, since water expands when forming. However, significant and repeatable contraction occurred at specific concentrations and temperatures during the cooling process.   Experimentation and isolation of this anomaly is a potential research topic.

Undercooling and nucleation are statistical processes that vary based on the purity of the fluid and cooling rate.   A significant amount of energy releases during the phase change with undercooling, over a very short time. This process could have various potential applications

including heat transfer, a thermal engine, or thermal actuator. Initially, study of the nucleation kinetics and undercooling in a bulk antifreeze fluid would lay the groundwork for utilization of a commonly used material, albeit in a different way.

9.3   KUNDT TUBE

It is possible to use a modified Kundt Tube to measure the density and specific heat ratios of aqueous antifreeze vapor phase (Garland, Nibler, & Shoemaker, 2009), Figure 93. The experiment uses a speaker to generate a range of frequencies recorded at the other end of the tube at a fixed distance away. When the phase shift of the wave is 0 or 180, it is possible to determine the wavelength of the longitudinal plane waves propagating through the vapor mixture. Using Equation 15 - Equation 17, it is then possible to determine the specific heat ratio of the vapor assuming that it behaves as an ideal gas. Equation 15 derives from the Newton-Laplace equation for speed of sound with the assumption that the medium is an ideal gas. Equation 16 describes the speed of acoustic wave propagation through a medium with respect to the wavelength and frequency of the wave. By combining Equation 15and Equation 16, and solving for the gamma, it is possible to determine the specific heat ratio for a gas mixture assuming that it is an ideal gas. Additionally, the Kundt tube allows for the recording of the density of the gas mixture in parallel. Recording the pressure in the chamber as well allowed for use of the ideal gas equation, Equation 18, to determine the density.

$$c = \sqrt{\gamma RT}$$

Equation 15

$$c = \lambda f$$

Equation 16

$$\gamma = \frac{(\lambda f)^2}{RT}$$

Equation 17

$$\rho = \frac{p}{RT} \qquad\qquad \text{Equation 18}$$

c: speed of sound in the gas mixture
γ: specific heat ratio of the gas mixture
R: specific gas constant
T: temperature inside the Kundt tube
λ: wavelength of the longitudinal plane waves
f: frequency of the longitudinal plane waves
p: pressure inside the Kundt tube
ρ: density of the gas mixture
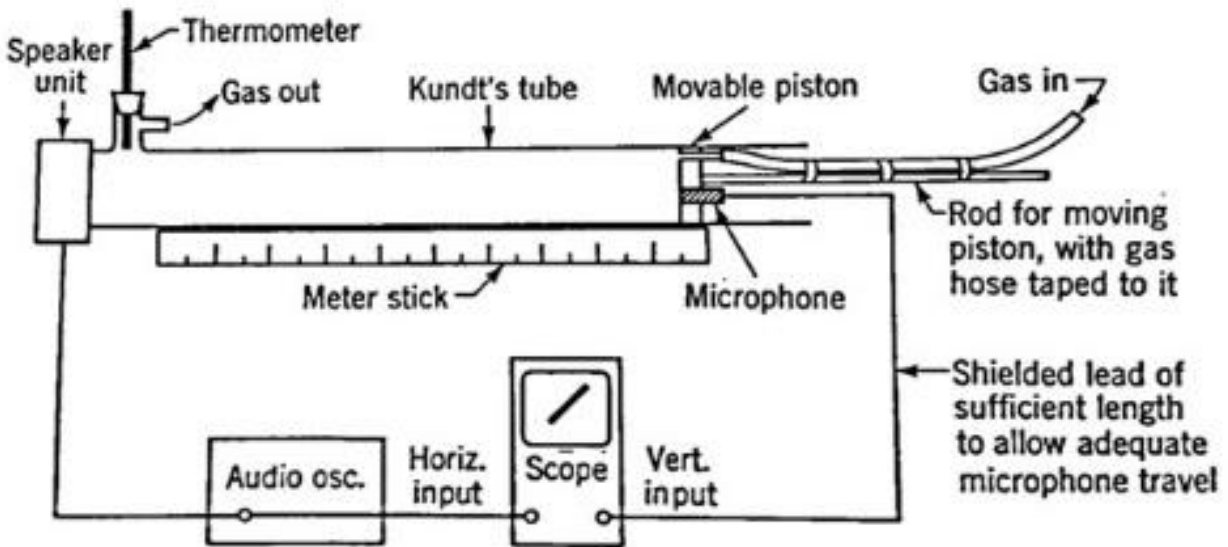
Figure 93: A modified Kundt Tube has been designed to measure density and specific heat of antifreeze vapor (Garland, Nibler, & Shoemaker, 2009). A Kundt tube is an acoustical apparatus usually used to visually demonstrate standing waves, but originally it was designed to measure the speed of sound of a gas.

9.4   THRUST MEASUREMENT AND INTEGRATION ON ARKSAT-2

The highest priority future research is integration of the fluid phase separator into the propulsion system on ARKSAT-2. Technology readiness levels (TRL) are currently around TRL 3-4 but quickly need to progress to TRL 6-7 prior to launch. Establishing the TRL 3-4, phase separation using a nanochannel array has proven viable as a mass flow regulator to vacuum. Development of the technology will transition the system into TRL 4-5 while thrust measurement pushes the system into TRL 5-6. A thrust stand developed during past research could potentially serve as the experimental setup, but NASA Marshall has a more accurate micro-Newton level thrust stand that is available for use. Lastly, integration into ARKSAT-2 moves to TRL 6-8 where the ultimate goal is system test, launch, & operations capping at TRL 8-9.

10 REFERENCES

1.   AAU CubeSat [Internet].; 2003. Available from: http://www.space.aau.dk/CubeSat/.

2.   Abgrall, P., Nguyen N. T. Nanofluidic Devices and Their Applications. Analytical Chemistry. 2008, 80 (7), 2326 -2341.

3.   Arnero., Carbon nanotube armchair. 2007. Wikimedia Commons:

4.   Boeing successfully completes CubeSat mission to advance nano-satellite technology [Internet].; 2007. Available from: http://www.boeing.com/news/releases/2007/q3/070816a_nr.html.

5.   Boquet L., Tabling P., Physics and technological aspects of nanofluidics. Lab on a Chip. 2014. 17, 3143-3158.

6.   Boresi AP, Schmidt RJ. Advanced mechanics of materials. New York: John Wiley & Sons; 2003.

7.   Brooks Automation. Micro-ion® plus module instruction manual. Rev 4 ed.; 2008.

8.   Burton R. L., Turchi P. J. "Pulsed Plasma Thruster", Journal of Propulsion and Power, Vol. 14, No. 5. 1998, pp. 716-735.

9.   Cao, H., Yu, Z., Wang, J., Tegenfeldt, J., Austin, R., Chen, E., Chou, S. (2002). Fabrication of 10 nm enclosed nanofluidic channels. Applied Physics Letters, 81(1), 174-176.

10.   Chen, X, et al. "Nanoscale fluid transport: Size and rate effects." NANO LETTERS, v. 8 issue 9, 2008, p. 2988-2992.

11.   Chobotov V., Orbital Mechanics. 3rd ed. AIAA; 2002.

12.   CubeSat ELaNa III launch on NPP mission [Internet].; 2011. Available from: http://www.nasa.gov/pdf/627975main_65121-2011-CA000-NPP_CubeSat_Factsheet_FINAL.pdf.

13.   CubeSat launch initiative (CSLI) [Internet].; 2012. Available from: http://www.nasa.gov/directorates/heo/home/CubeSats_initiative.html.

14.   Curme GO, Johnston F. Glycols. New York: Reinhold; 1952.

15.   Dow Chemical Company. DOWFROST™. [Internet] 2018. Available from: http://msdssearch.dow.com/PublishedLiteratureDOWCOM/dh_098b/0901b8038098b3ac.pdf?filepath=/heattrans/pdfs/noreg/180-01314.pdf&fromPage=GetDoc

16. Dow Chemical Company. DOWTHERM^{TM} SR-1 Fluid. [Internet] 2018. Available from:http://msdssearch.dow.com/PublishedLiteratureDOWCOM/dh_098b/0901b803 8098b3a6.pdf?filepath=/heattrans/pdfs/noreg/180-01312.pdf&fromPage=GetDoc

17. Du F., Qu L., Xia Z., Feng L., Dai L. Membranes of vertically aligned superlong carbon nanotubes. Langmuir 2011, 27, 8437−8443.

18. Eijkel J, van den Berg A. Nanofluidics: What is it and what can we expect from it? Microfluid Nanofluid. 2005 JUL;1(3):249-67.

19. Fang T, Weng C, Chang J. Machining characterization of the nano-lithography process using atomic force microscopy. Nanotechnology. 2000 SEP;11(3):181-7.

20. Funase, R., Takei, E., Nakamura, Y., Nagai, M., Enokuchi, A., Yuliang, C., Nakada, K., Nojiri, Y., Sasaki, F., Funane, T., Eishima, T., Nakasuka, S., "Technology Demonstration on University of Tokyo's Picosatellite `XI-V' and its effective Operations Result using Ground Station Network," Proceedings of the 56th IAC 2005, Fukuoda, Japan, Oct. 17-21, 2005

21. Garland C.W., Nibler J.W., Shoemaker D.P. Experiments in Physical Chemistry. Boston: McGraw-Hill Higher Education, 2009.

22. GeneSat-1 [Internet].; 2007. Available from: http://www.nasa.gov/centers/ames/missions/2007/genesat1.html.

23. Guarducci, F., M. Coletti, and S. B. Gabriel. "Design and testing of a micro pulsed plasma thruster for CubeSat application." 32nd International Electric Propulsion Conference. 2011.

24. Guo L, Cheng X, Chou C. Fabrication of size-controllable nanofluidic channels by nanoimprinting and its application for DNA stretching. Nano Lett. 2004 JAN;4(1):69-73.

25. Hamblin, M. N. et al. Capillary flow in sacrificially etched nanochannels. Biomicrofluidics 5, 021103 (2011).

26. Han, M. "Thermally-driven nanoscale pump by molecular dynamics simulation." JOURNAL OF MECHANICAL SCIENCE AND TECHNOLOGY, v. 22 issue 1, 2008, p. 157-165.

27. Haneveld, J., Tas, N. R., Brunets, N., Jansen, H. V. & Elwenspoek, M. Capillary filling of sub-10 nm nanochannels. J. Appl. Phys. 104, 014309 (2008).

28. Hardbake of Photoresist Structures. Microchemicals, 7 Nov. 2013.

29. Harley, J. C., Compressible Gas Flows in Microchannels and Microjets, Ph.D. Thesis, University of Pennsylvania, Philadelphia, PA, 1993.

30. Haywood D.G., Saha-Shah A, Baker L.A., and Jacobson S.C., Fundamental Studies of Nanofluidics: Nanopores, Nanochannels, and Nanopipets. Analytical Chemistry. 2015; 87 (1): 172-187

31. Hinds BJ, Chopra N, Rantell T, Andrews R, Gavalas V, Bachas LG. Aligned multiwalled carbon nanotube membranes. Science. 2004 JAN 2 2004;303(5654):62-5.

32. Hoke B, Patton E. Surface tensions of propylene-glycol plus water. J Chem Eng Data. 1992 JUL;37(3):331-3.

33. Holt J, Park H, Wang Y, Stadermann M, Artyukhin A, Grigoropoulos C, et al. Fast mass transport through sub-2-nanometer carbon nanotubes. Science. 2006 MAY 19;312(5776):1034-7.

34. Huang, A., Wilson, E., & Chan, Y.Development of critical technologies for formation and proximity flight with nano-satellites. Paper presented at the 22nd Arkansas Space Grant Consortium Symposium, Hot Springs, AR. April 7, 2014.

35. Hubble essentials [Internet].: NASA. Available from: http://hubblesite.org/the_telescope/hubble_essentials/.

36. Hummer G, Rasaiah J, Noworyta J. Water conduction through the hydrophobic channel of a carbon nanotube. Nature. 2001 NOV 8;414(6860):188-90.

37. Ike Y, Seshimo Y, Kojima S. Crystallization and vitrification of cryoprotectants studied by raman scattering, brillouin scattering and THz-TDS. J Mol Struct. 2009 APR 30;924-26:127-30.

38. Janson SW, Helvajian H, Hansen WW, Lodmell J., Microthrusters for nanosatellites. Proc. of the second international conference on integrated micro nanotechnology for space applications; Pasadena, Ca. Aerospace Corporation; 1999.

39. Kandlikar, Satish G., and William J. Grande. Evolution of Microchannel Flow Passages - Thermohydraulic Performance and Fabrication Technology. Heat Transfer Engineering 24.1 (2003): 3-17.

40. Kane D., El-Shall M. S. Condensation of supersaturated vapors of hydrogen bonding molecules: Ethylene glycol, propylene glycol, trimethylene glycol, and glycerol. The Journal of Chemical Physics, 1996, 105(17), 7617-7631.

41. Kern W., Vossen J., Thin Film Processes, Academic Press: New York, 1978, Ch V-1

42. Killgore J.P., Geiss R.H., Hurley, D.C., Continuous measurement of AFM tip wear by contact resonance force microscopy. Small. Published March 15, 2011.

43. Kutchoukov V. G., Laugere F., van der Vlist, W., Pakula, L.; Garini, Y., Bossche, A., Fabrication of nanofluidic devices using glass-to-glass anodic bonding. Sensors and Actuators A-Physical 2004, 114, 521-527.

44. Larsson A, Wingborg N. Green propellants based on ammonium dinitramide (ADN). In: Hall J, editor. InTech; 2011. p. 139; 139,156; 156.

45. Lee C, Yang E, Myung N, George T. A nanochannel fabrication technique without nanolithography. Nano Lett. 2003 OCT;3(10):1339-40.

46. Lee J, Huang A. Microthruster knife-edge thrust stand. Proc. of 2009 ASME international mechanical engineering congress and exposition; Nov. 13-19; Lake Buena Vista, Florida. ; 2009.

47. Lee, John and Huang, Adam, "A "Green Cold-Gas" Propulsion System for CubeSats." 31st Annual AIAA/USU Conference on Small Satellites, Logan, UT, Aug. 8, 2017.

48. Lee K.-H., Hwang Sun-Tak. The Transport of Condensible Vapors through a Microporous Vycor Glass Membrane. J. Colloid Interface Sci. 1986, 110, 544−555.

49. Lei W., Fong N., Yin Y., Svehla M., McKenzie D.R., Science of Water Leaks: Validated Theory for Moisture Flow in Microchannels and Nanochannels. Langmuir 2015 31 (42), 11740-11747

50. Lokcu E, Ash RL. A de-orbit system design for CubeSat payloads. Proceedings of the 2011 5th International Conference on Recent Advances in Space Technologies (RAST). 2011 2011:470; 470,474; 474.

51. Lum K, Luzar A. Pathway to surface-induced phase transition of a confined fluid. Physical Review E. 1997 DEC 1997;56(6):R6283-6.

52. Majumder M, Chopra N, Andrews R, Hinds BJ. Nanoscale hydrodynamics - enhanced flow in carbon nanotubes. Nature. 2005 NOV 3 2005;438(7064):44-.

53. Mao P, Han J. Fabrication and characterization of 20 nm planar nanofluidic channels by glass-glass and glass-silicon bonding. Lab Chip. 2005;5(8):837-44.

54. Mattia D, Calabro F. Explaining high flow rate of water in carbon nanotubes via solid-liquid molecular interactions. Microfluidics and Nanofluidics. 2012 JUL 2012;13(1):125-130.

55. Mason L., Jankovsky R., and Manzella D. "1000 hours of testing on a 10 kilowatt Hall effect thruster", 37th Joint Propulsion Conference and Exhibit, Joint Propulsion Conferences. 2001.

56. Mattia D, Gogotsi Y. Review: Static and dynamic behavior of liquids inside carbon nanotubes. Microfluidics and Nanofluidics. 2008 SEP 2008; 5 (3): 289-305.

57.   Mawatari K, Kazoe Y, Shimizu H, Pihosh Y, and Kitamori T, Extended-Nanofluidics: Fundamental Technologies, Unique Liquid Properties, and Application in Chemical and Bio Analysis Methods and Devices. Analytical Chemistry. 2014; 86 (9): 4068-4077.

58.   Micci MM, Ketsdever AD. Micropropulsion for small aircraft. AIAA; 2000.

59.   Miller, K. A rocky road to outer space but one year later, student satellite still flying high. 2001. Stanford Report.

60.   Mueller J, Ziemer J. A survey of micro-thrust propulsion options for microspacecraft and formation flying missions. Proc. of 5th annual CubeSat developers workshop; 2008; San Luis Obispo, CA. Jet Propulsion Laboratory

61.   Mukhopadhyay R., What Does Nanofluidics Have to Offer? Analytical Chemistry. 2006; 78 (21): 7379-7382.

62.   Myers TG. Why are slip lengths so large in carbon nanotubes? Microfluidics and Nanofluidics. 2011 MAY 2011;10(5):1141-5.

63.   Nano-satellite systems [Internet]. Available from: http://tyvak.com/.

64.   NRL launches nano-satellite experimental platforms [Internet].; 2010. Available from: http://www.nrl.navy.mil/media/news-releases/2010/nrl-launches-nanosatellite-experimental-platforms.

65.   Nugent, Ryan, Munakata, Riki, Chin, Alexander, Coelho, Roland, & Puig-suari, Prof. CubeSat: The Pico-Satellite Standard for Research and Education. 2008.

66.   Oh, J. M., Faez, T., de Beer, S. & Mugele, F. Capillarity-driven dynamics of water–alcohol mixtures in nanofluidic channels. Microfluid. Nanofluid. 9, 123–129 (2010).

67.   Pappalardo, J., How small can satellites get and still be functional? from nanosats to femtosats. 2006. Air and Space Magazine,

68.   Pietropaolo A., Senesi R., Andreani C., Botti A., Ricci M. A., Bruni F., Excess of proton mean kinetic energy in supercooled water. Physical Review Letters. 2008. 100 (12) 127802

69.   Platt D. A monopropellant milli - newton thruster system for attitude control of nanosatellites. 16th annual USU conference on small satellites; Logan, Utah. ; 2002.

70.   Polzin K.A. "Iodine Hall Thruster Propellant Feed System for a CubeSat", 50th AIAA/ASME/SAE/ASEE Joint Propulsion Conference, AIAA Propulsion and Energy Forum, (AIAA 2014-3915). 2014.

71.   Product safety assessment: Propylene glycol [Internet]. Available from: http://www.dow.com/productsafety/finder/prog.htm.

72.   Proving high-tech rocket systems, vega soars to space [Internet].; 2012. Available from: http://spaceflightnow.com/vega/vv01/120213launch/.

73.   Pumpkin price list [Internet]. Available from: http://www.pumpkininc.com/content/doc/forms/pricelist.pdf.

74.   Qin X. Yuan Q., Zhao Y., Xie S., Liu Z. Measurement of the rate of water translocation through carbon nanotubes. Nano Lett. 2011, 11, 2173−2177.

75.   Rossi M, Ye H, Gogotsi Y, Babu S, Ndungu P, Bradley J. Environmental scanning electron microscopy study of water in carbon nanopipes. Nano Lett. 2004 MAY;4(5):989-93.

76.   Satellite classification [Internet]. Available from: http://centaur.sstl.co.uk/SSHP/sshp_classify.html.

77.   Schoch, R. B., Renaud, P. Ion transport through nanoslits dominated by the effective surface charge. Applied Physics Letters 2005, 86

78.   Silicon AFM tapping mode probes: Tap 190DLC [Internet]. Available from: http://www.tedpella.com/probes_html/budgetsensors-1.htm.

79.   Sobolev, V., Churaev, N., Velarde, M. & Zorin, Z. Surface tension and dynamic contact angle of water in thin quartz capillaries. J. Colloid Interface Sci. 222, 51–54 (2000).

80.   Softbake of Photoresist Films. Microchemicals, 7 Nov. 2013.

81.   Soong CY, Yen TH, Tzeng PY. Molecular dynamics simulation of nanochannel flows with effects of wall lattice-fluid interactions. Phys Rev E. 2007 SEP;76(3):036303.

82.   Space electronics [Internet]. Available from: http://www.spacemicro.com/.

83.   Spacecraft power management [Internet]. Available from: http://www.clyde-space.com/.

84.   Sparreboom W., van den Berg A., Eijkel J. C. T., Principles and applications of nanofluidic transport. Nature Nanotechnology. 2009, 4, 713-720.

85.   2009, 4, 713.

86.   Steitz DE. NASA goes green: NASA selects green propellant technology demonstration mission. NASA. 2012.

87.   Stern M. B., Geis M. W., Curtin J. E. Nanochannel fabrication for chemical sensors. Journal of Vacuum Science & Technology B, Nanotechnology and Microelectronics: Materials, Processing, Measurement, and Phenomena. 1997, 15, 2887-2891.

88.   Szabo J., Pote B., Paintal S., Robin M., Hillier A., Branam R.D., Huffmann R.E. "Performance Evaluation of an Iodine-Vapor Hall Thruster", Journal of Propulsion and Power, Vol. 28, No. 4 (2012), pp. 848-857.

89.   Tang, W; Advani, S. "Drag on a nanotube in uniform liquid argon flow." The Journal of Chemical Physics, v. 125 issue 17, 2006, p. 174706.

90.   Tas N, Berenschot J, Mela P, Jansen H, Elwenspoek M, van den Berg A. 2D-confined nanochannels fabricated by conventional micromachining. Nano Lett. 2002 SEP;2(9):1031-2.

91.   Tas, N., Haneveld, J., Jansen, H., Elwenspoek, M. & Van Den Berg, A. Capillary filling speed of water in nanochannels. Appl. Phys. Lett. 85, 3274–3276 (2004).

92.   Tuzun, R; Noid, D; Sumpter, B; Merkle, R. "Dynamics of fluid flow inside carbon nanotubes." NANOTECHNOLOGY, v. 7 issue 3, 1996, p. 241-246.

93.   The james webb space telescope [Internet].: NASA. Available from: http://www.jwst.nasa.gov/.

94.   Thomas JA, McGaughey AJH, Kuter-Arnebeck O. Pressure-driven water flow through carbon nanotubes: Insights from molecular dynamics simulation. International Journal of Thermal Sciences. 2010 FEB 2010;49(2):281-9.

95.   Thomas JA, McGaughey AJH. Water flow in carbon nanotubes: Transition to subcontinuum transport. Phys Rev Lett. 2009 MAY 8;102(18):184502.

96.   To the stars: NASA selects small spacecraft technology demonstration missions [Internet].; 2012. Available from: http://www.nasa.gov/home/hqnews/2012/aug/HQ_12-274_Small_Tech_Demo_Missions.html.

97.   Tzevelekos K. P., Kikkinides E. S., Stubos A. K., Kainourgiakis M. E., Kanellopoulos, N. K. On the possibility of characterising mesoporous materials by permeability measurements of condensable vapours theory and experiments. Adv. Colloid Interface Sci. 1998, 76− 77, 373−388. (33) Li, Y.; X

98.   ULA atlas V finally launches with NROL-36 [Internet].; 2012. Available from: http://www.nasaspaceflight.com/2012/09/uatlas-v-launch-nrol-36-vandenberg/.

99.   Varshneya, A., Fundamentals of Inorganic Glasses. Academic Press; 1993.

100.   Vernon H. M., XLV. On the maximum density of water, The London, Edinburgh, and Dublin Philosophical Magazine and Journal of Science. 1891; 31:192, 387-392

101.   Ward TA. Aerospace propulsion systems. 1st ed. John Wiley & Sons; 2010.

102. Wells, G.J., Stras, L., Jeans, T., "Canada's Smallest Satellite:- The Canadian Advanced Nanospace eXperiment (CanX-1)," AIAA/USU Conference on Small Satellites, Logan, UT, Aug. 12-15, 2002, SSC02-VI-2

103. Whitby M, Quirke N. Fluid flow in carbon nanotubes and nanopipes. Nature Nanotechnology. 2007 FEB 2007;2(2):87-94.

104. Wolf S., Tauber R.N., Silicon Processing for the VLSI Era: Volume 1 - Process Technology. 1986. pp. 532–533.

105. XSAS microgravity project [Internet].; 2010. Available from: http://xsasmicrogravity.blogspot.com/2010/01/welcome-to-xsas-blog.html.

106. Xu, J; Zhou, Z; Xu, X. "Molecular dynamics simulation of micro-Poiseuille flow the liquid argon in nanoscale." INTERNATIONAL JOURNAL OF NUMERICAL METHODS FOR HEAT & FLUID FLOW, v. 14 issue 5-6, 2004, p. 664-688.

107. Xu, Yan. "Nanofluidics: A New Arena for Materials Science." Advanced Materials 30.3 (2018)

108. Zhou, Y., Hu, K., Shen, J., Wu, X., & Cheng, G. Microstructure variations with concentration of propylene glycol-water solution probed by NMR. Journal of Molecular Structure, 2009. 921(1-3), 150-155.

11 APPENDIX

11.1 ADDITIONAL MESO-SCALE

11.1.1 Vacuum Chamber Box

A vacuum chamber designed in SolidWorks and fabricated out of Polycarbonate. Polycarbonate is a translucent, high strength polymer that is relatively easy to machine. The clear material would enable visual inspection of the propellant during testing under vacuum. Liquid gasket sealed all interfaces and o-ring sealed the top removable face.
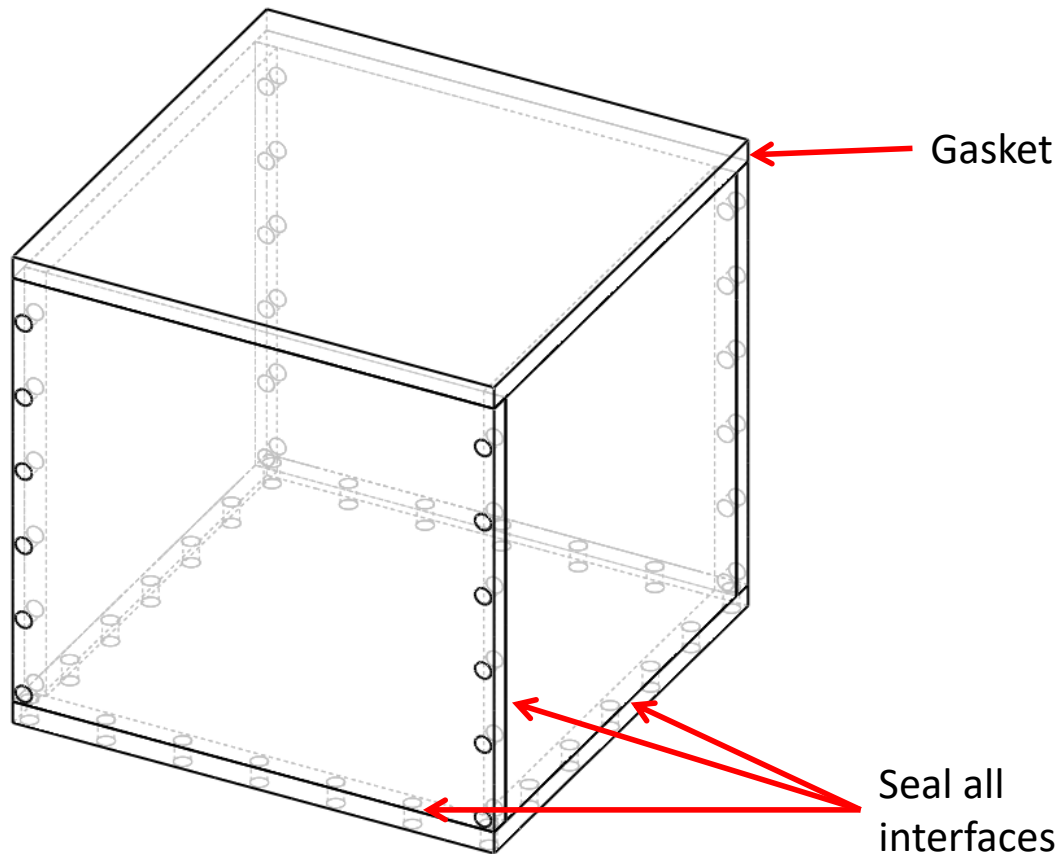
Figure 94: A polycarbonate box establishes a space environment with external observation.

The box consisted of five fixed plates with a removable top plate to allowing access to the chamber. The top section of the box also included a spacer with an o-ring groove machined into

the top surface, upon which the top plate rested. An o-ring seated in the spacer creates a seal between the spacer and the top plate. Silicone sealed the rest of the box at and between every interface. A valve on the turbopump allows the vacuum box to safely return to atmosphereic pressure. The polycarbonate box was large enough to accommodate a mass scale and the experimental setup while also being mounted to a plate affixed to a turbo pump. An l-bracket skeleton support structure made of 1/8" thick angled aluminum prevented flexing and increased strength and rigidity of the experimental setup. A webcam mounted to the top of the box for monitored the scale mass and on the side for measuring fluid volume.

| (a) | (b) | (c) |
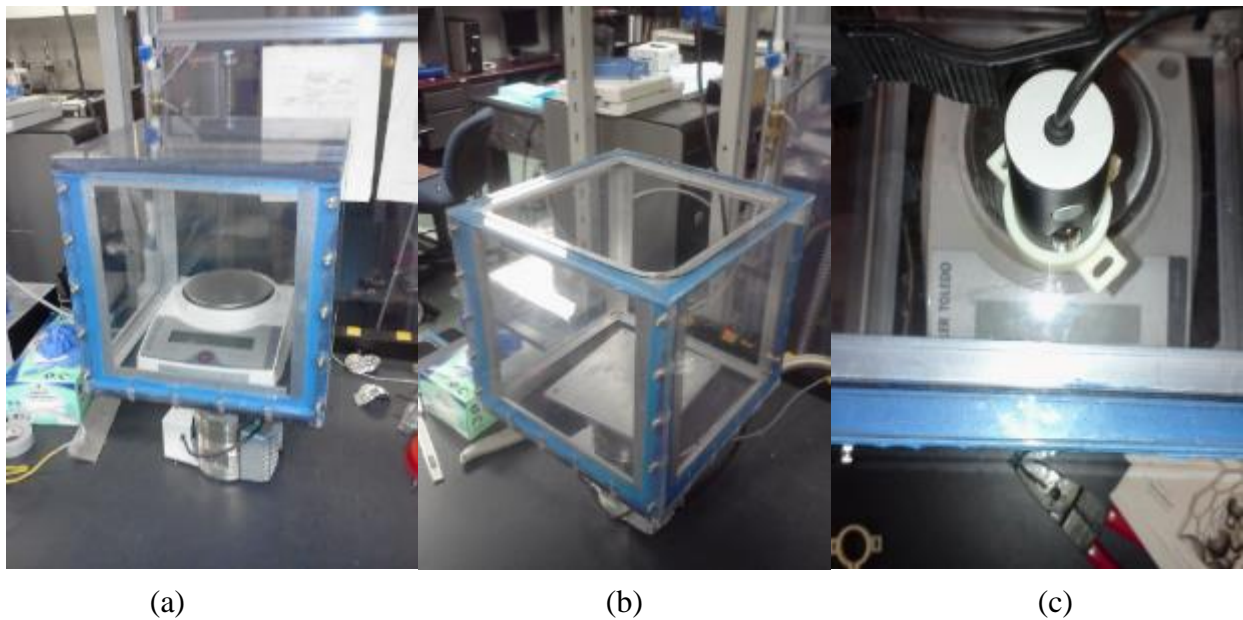
Figure 95: The polycarbonate box allowed for visual inspection of mass and volume data.

A national pipe thread port drilled into the side of the vacuum box allowed for pressure monitoring of the chamber. The O-ring groove cut in the top plate of polycarbonate would not seal completely since the box would flex under vacuum.

<div align="center">(a)   (b)   (c)</div>
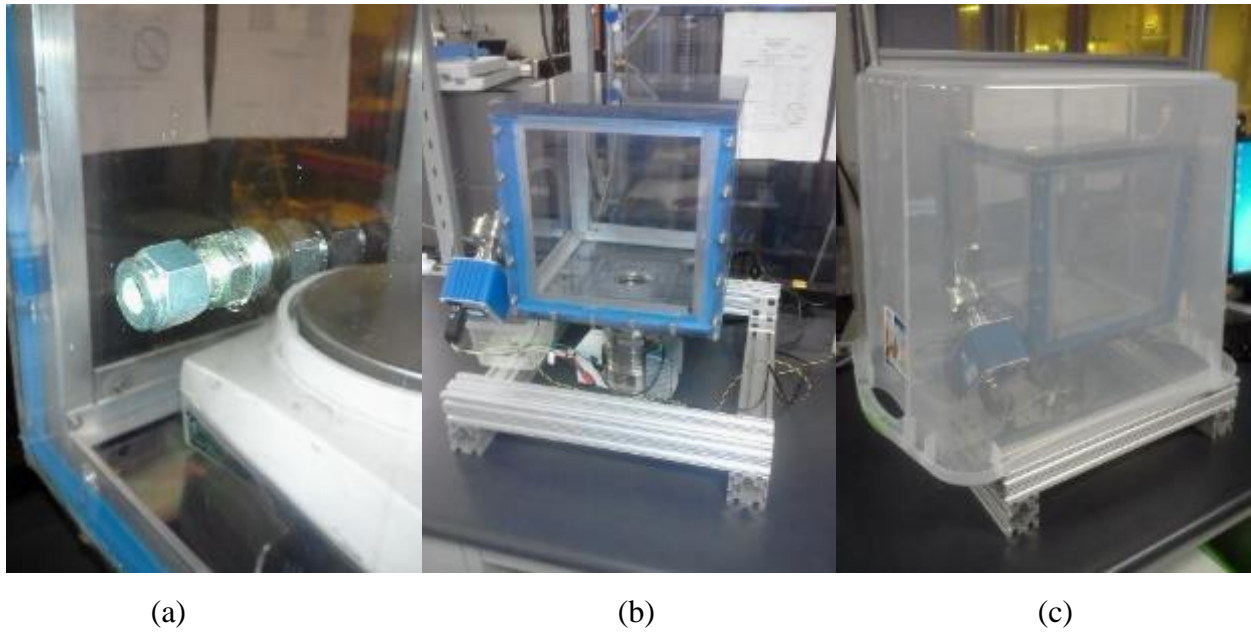
Figure 96: Access points located at the points of lowest stress enabled data collection.

Maximum stress values on the polycarbonate plate were calculated analytically using equations derived by Boresi & Schmidt **(2003)**. It was assumed that one side of the box would act as a 10 inch square plate with clamped boundary conditions and a uniform pressure distribution over the entire plate of 1 atmosphere (14.7 psi or 101.3 kPa). A pressure of 1 atmosphere was used since the vacuum box can pump down from standard atmospheric pressure to between 10^{-2} to 10^{-5} Torr (1.33 Pa to 1.33^{-3}Pa). Using the information described a maximum stress expected on the plate was calculated to be 9.7 MPa. The yield strength of polycarbonate is MPa, therefore the initial stress calculation was promising for use of polycarbonate as the vacuum box material.

Initial stress calculations assumed a very simple geometry and boundary conditions, while the actual box was much more complex in design and mounting. The plate, modeled as a 10 inch square, included the 3.8-millimeter diameter screw holes. A pressure load of one atmosphere applied across the entire plate simulated the pressure difference between atmosphere and vacuum.

<div align="center">145</div>

Instead of assuming clamped-edge boundary condition, the plate modeled as fixed only at the screw holes. With the given parameters, the maximum stress was 30 MPa, significantly higher than initial calculations. The jump in maximum stress in the SolidWorks® simulation is a result of the stress concentration caused by the screw holes towards the outer edges of the plate.

Stress levels are greatest towards the edge of the plate, which is where the screw holes are located. Dark blue regions in Figure 97(b) indicate a low level of stress while the light blue regions represent a slightly higher stress level. Localized high stress levels around the screw holes are unnoticeable in Figure 97(b). A hole is shown in the center of the plate in Figure 97 was the location of the pressure sensor and it was assumed that particular plate would experience the lowest stress levels in the entire box. Maximum stress values in the simulation were still lower than the yield strength of which indicated polycarbonate was still an acceptable material for the vacuum box. Figure 97(a) shows the displacement of the plate under the same loading parameters. A maximum anticipated displacement of approximately 2 millimeters occurs in the center of the plate. Fixed at the screw locations, the edges of the plate experience little to no displacement.
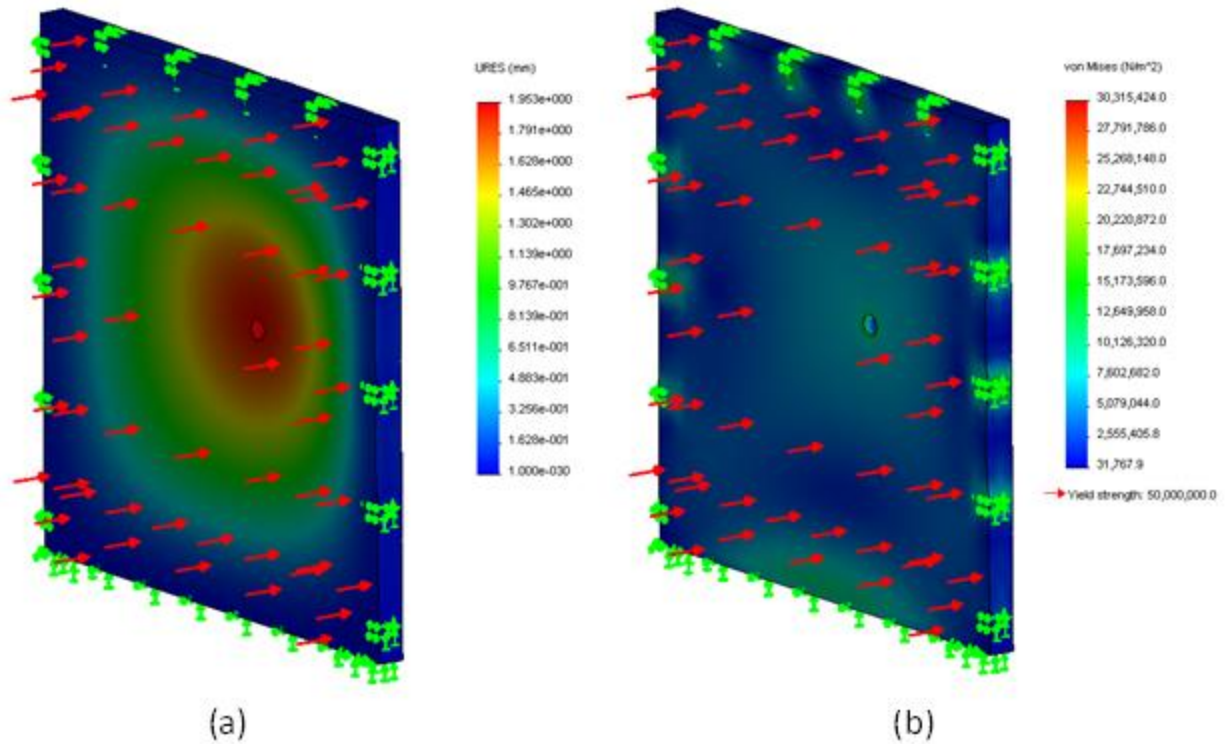
Figure 97: Finite element analysis indicated stress levels would not exceed material strength

The assembled box, Figure 98, successfully pumped to a pressure of 160 Torr, and maintained for 30 minutes without structural failure of the vacuum box. After shutting off the BOC Edwards vacuum system, the box maintained a seal for over 10 minutes, indicating a slight leak. However, stress levels in the box were approximately 80% of the expected maximum stress when a pressure of 10^{-2} to 10^{-5} Torr will be achieved.
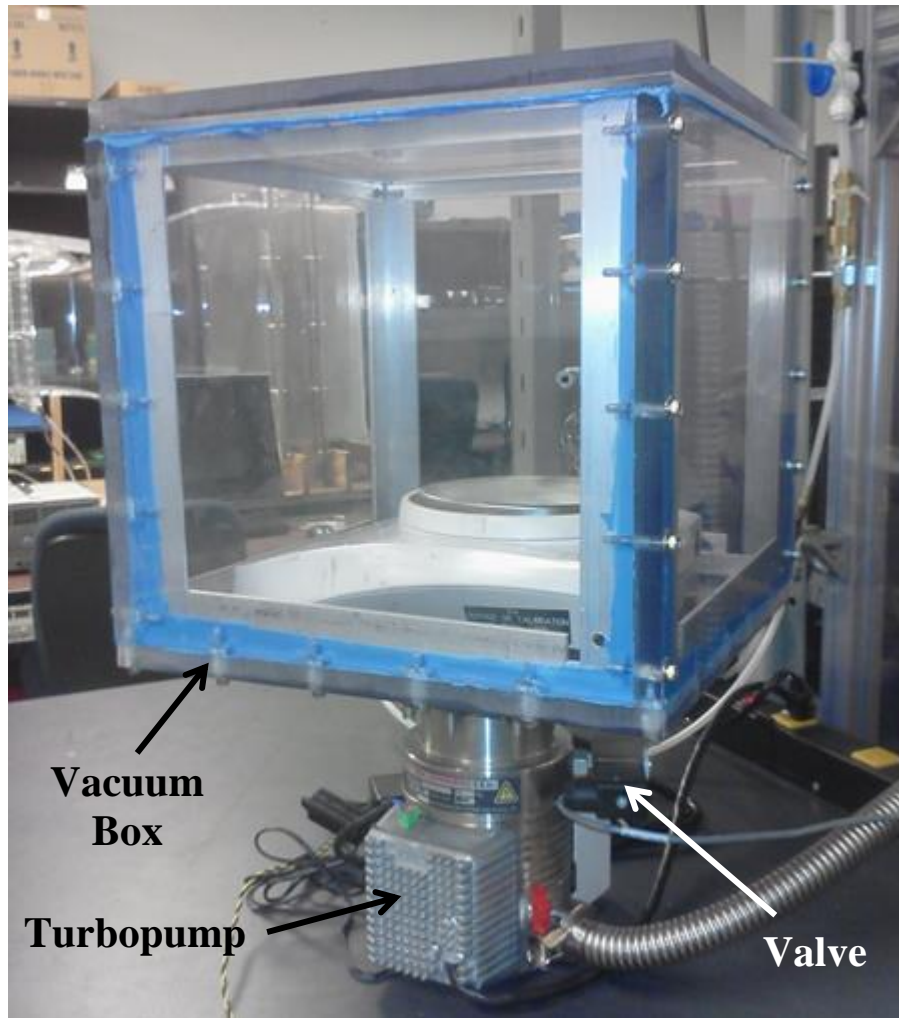
Figure 98: The polycarbonate box pumped down to 49 Torr, but flexed under vacuum.

The chamber pumped down for 30 min and maintained a vacuum for 30 min, indicating a leak. During pump down the chamber achieved a pressure of 49 Torr and leaks were noticeable at the seals, bolts, and o-ring. First signs of failure exhibited around the tapped screw holes where the polycarbonate was weakest, resulting in the highest values of stress, see Figure 99. Additionally, the O-ring groove in the top plate of polycarbonate would not seal completely since the box would flex under vacuum. Unfortunately, after repeatedly cycling between atmospheric pressure and vacuum, the top edge of the chamber was able to deflect enough to break the seal and cause a

catastrophic leak in the vacuum box. After replacing the silicone seals multiple times, it was determined to be an impractical solution to the problem. Upon further consideration, it was determined to set aside the polycarbonate vacuum box in favor of another recently available piece of equipment, the Denton Vacuum DV-502.

(a)   (b)
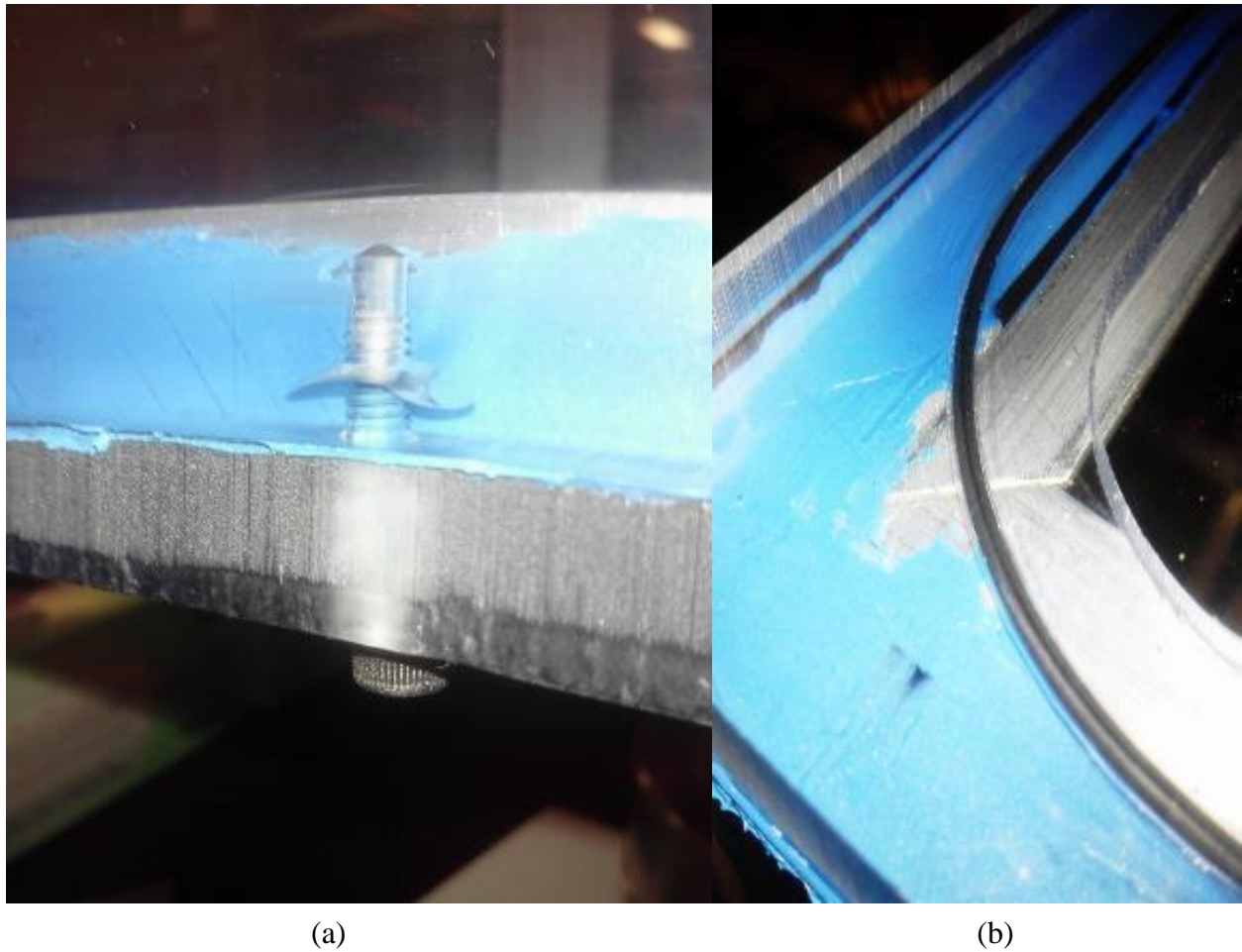
Figure 99: Cracks formed at the threaded bolt holes resulting in catastrophic leaks.

11.1.2 Mark 1

Issues encountered with Mark 1 include water freezing and capillary tube blockage. Installing an immersion heater in the setup quickly resolved the water freezing issue, Figure 100. The

capillary blockage issue proved to be much more problematic. Fluid bubbling and surface tension resulted in water blocking the capillary tubing and restricting flow of vapor. Liquid collection around the capillary tubing, Figure 101, caused fluid flow rates to drastically drop and even stop entirely. Filters over the capillary inlet aimed to prevent collection and restriction of vapor flow to vacuum.   Multiple iterations attempted to solve the problem, but all failed, while some exacerbated the problem, Figure 102 .
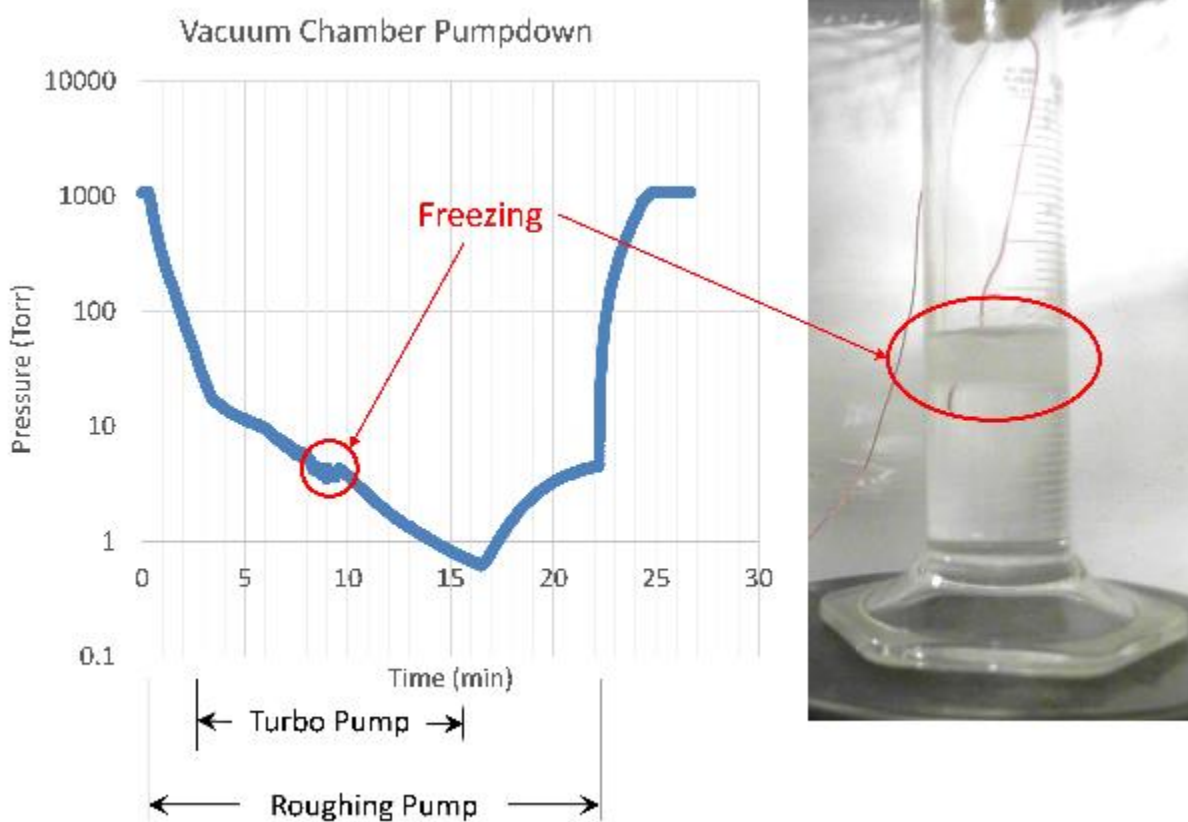
Figure 100: Freezing of water in vacuum
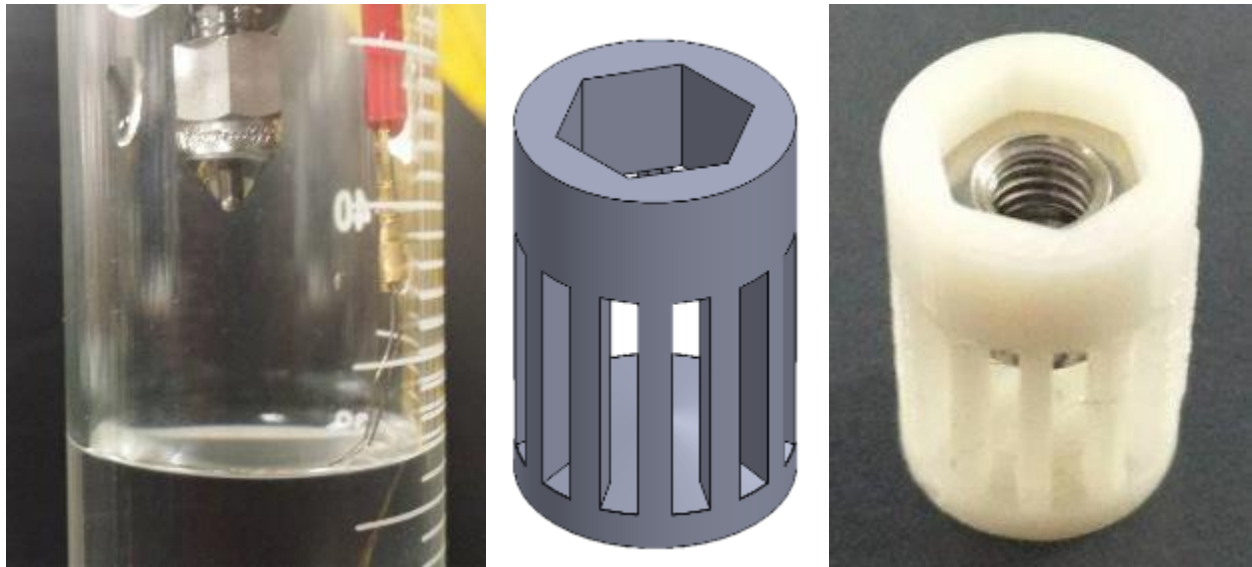
Figure 101: Filters designed to prevent fluid collection aimed to prevent water blockage
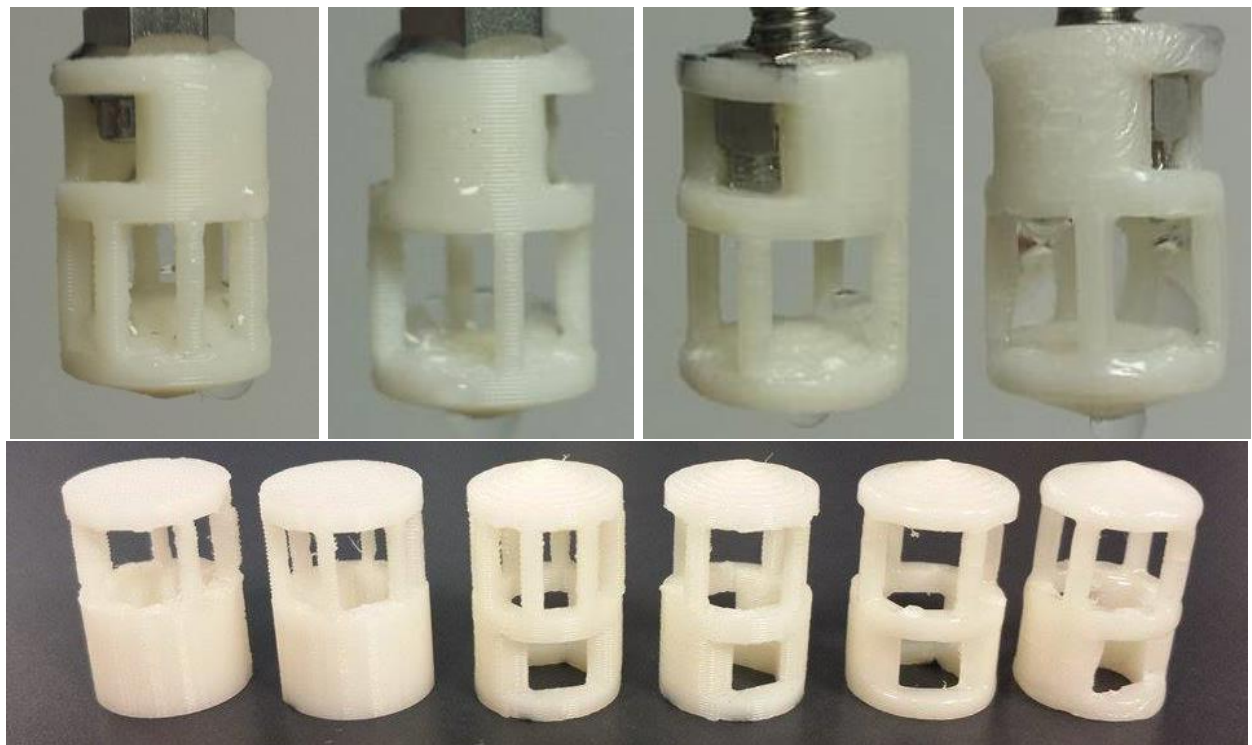
Figure 102: Various filters designed all failed to prevent fluid collection

11.2 ADDITIONAL SOLUTION PHASE CHANGE EXPANSION

11.2.1 Composite Graphs (All Data)
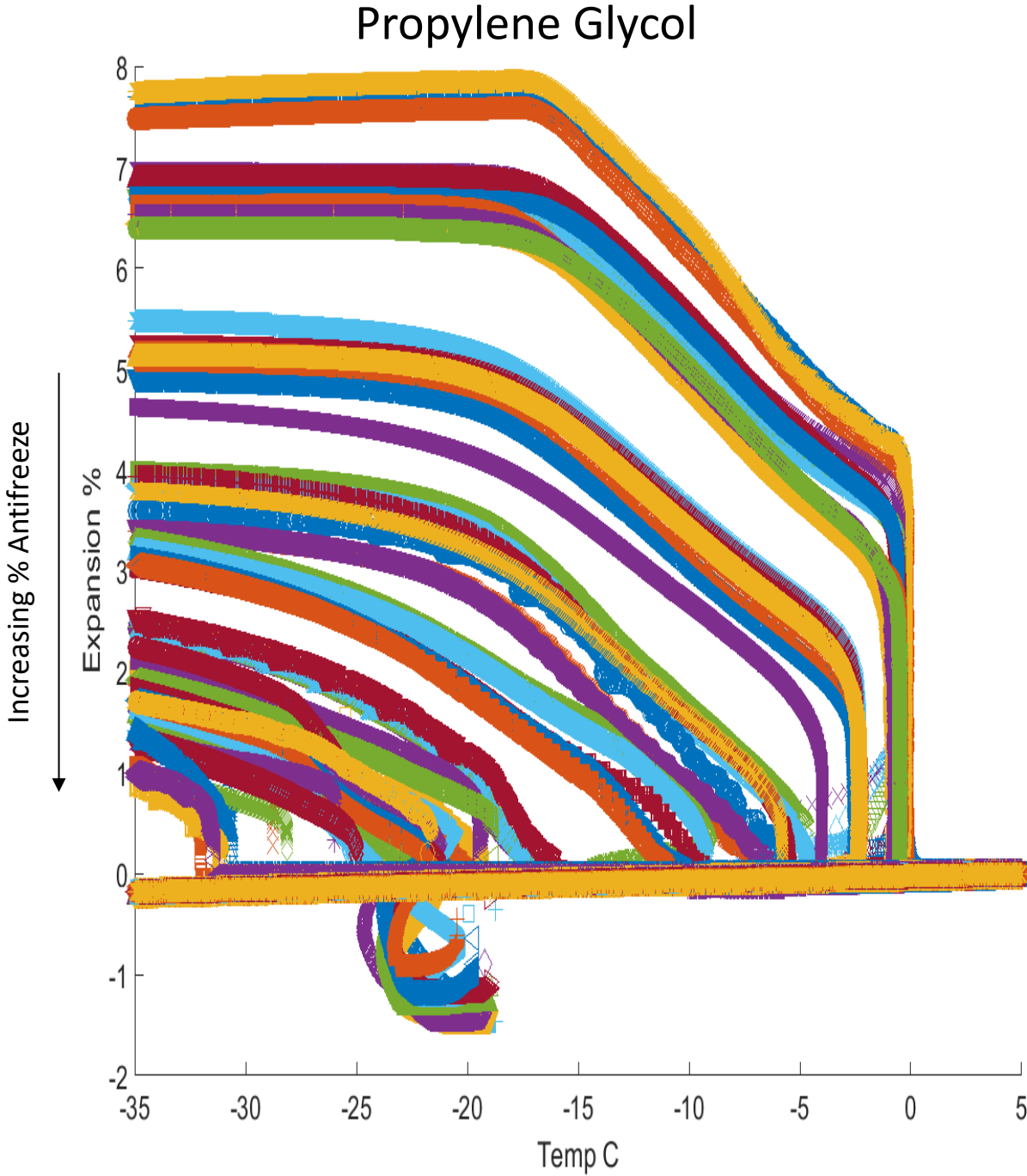
Figure 103: Propylene glycol expansion data (full set)
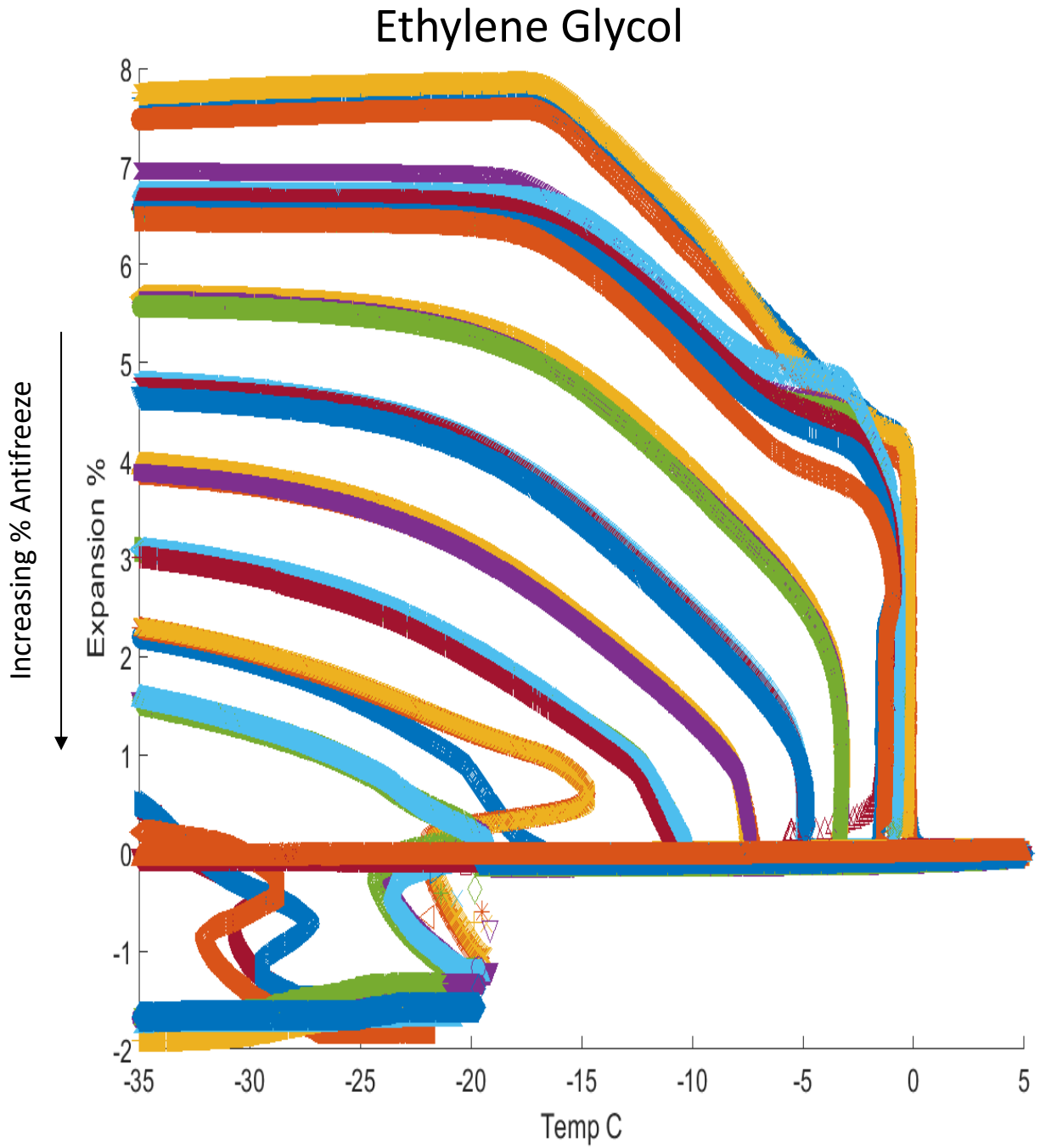
Figure 104: Ethylene glycol expansion data (full set)
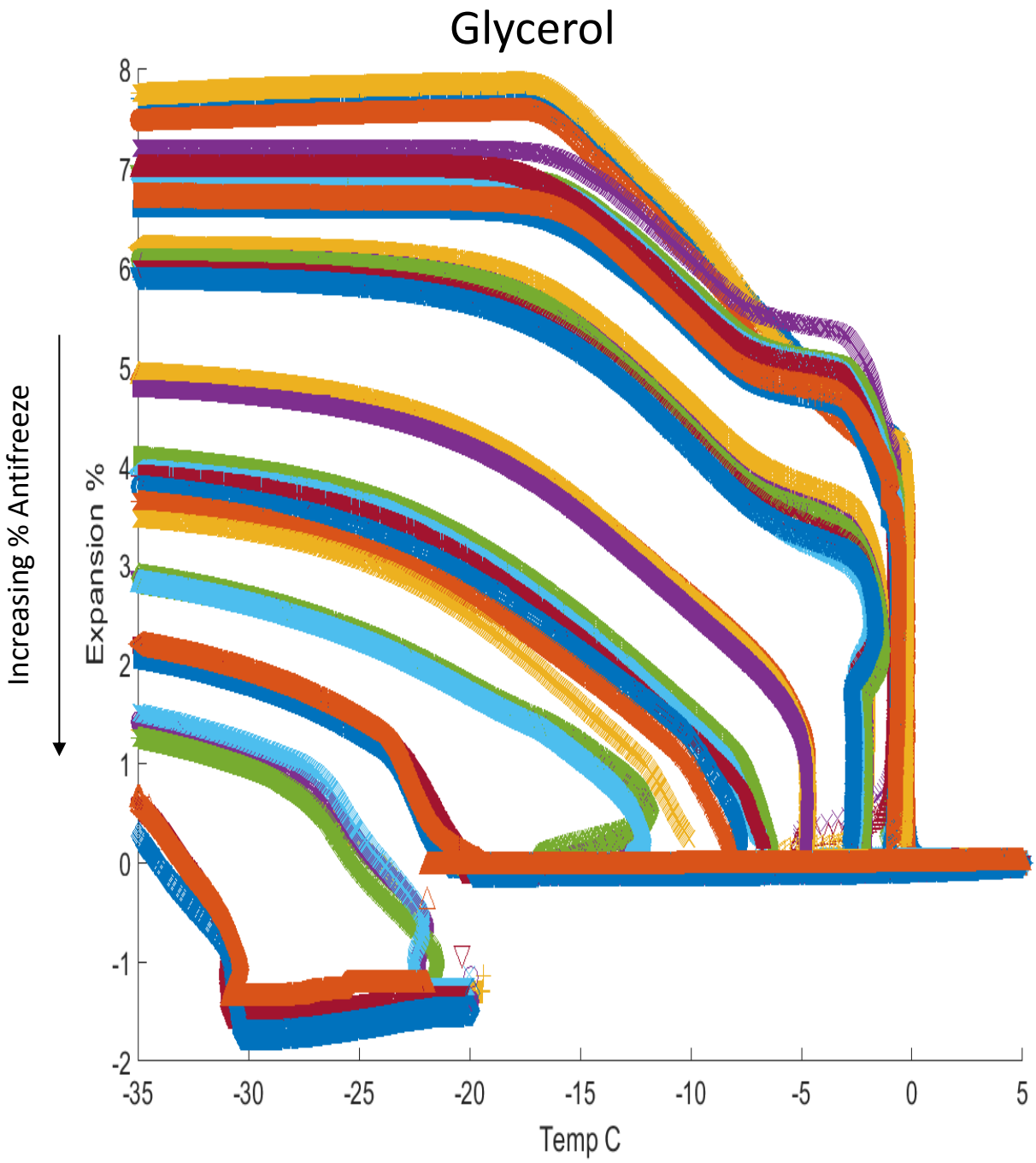
Figure 105: Glycerol expansion data (full set)
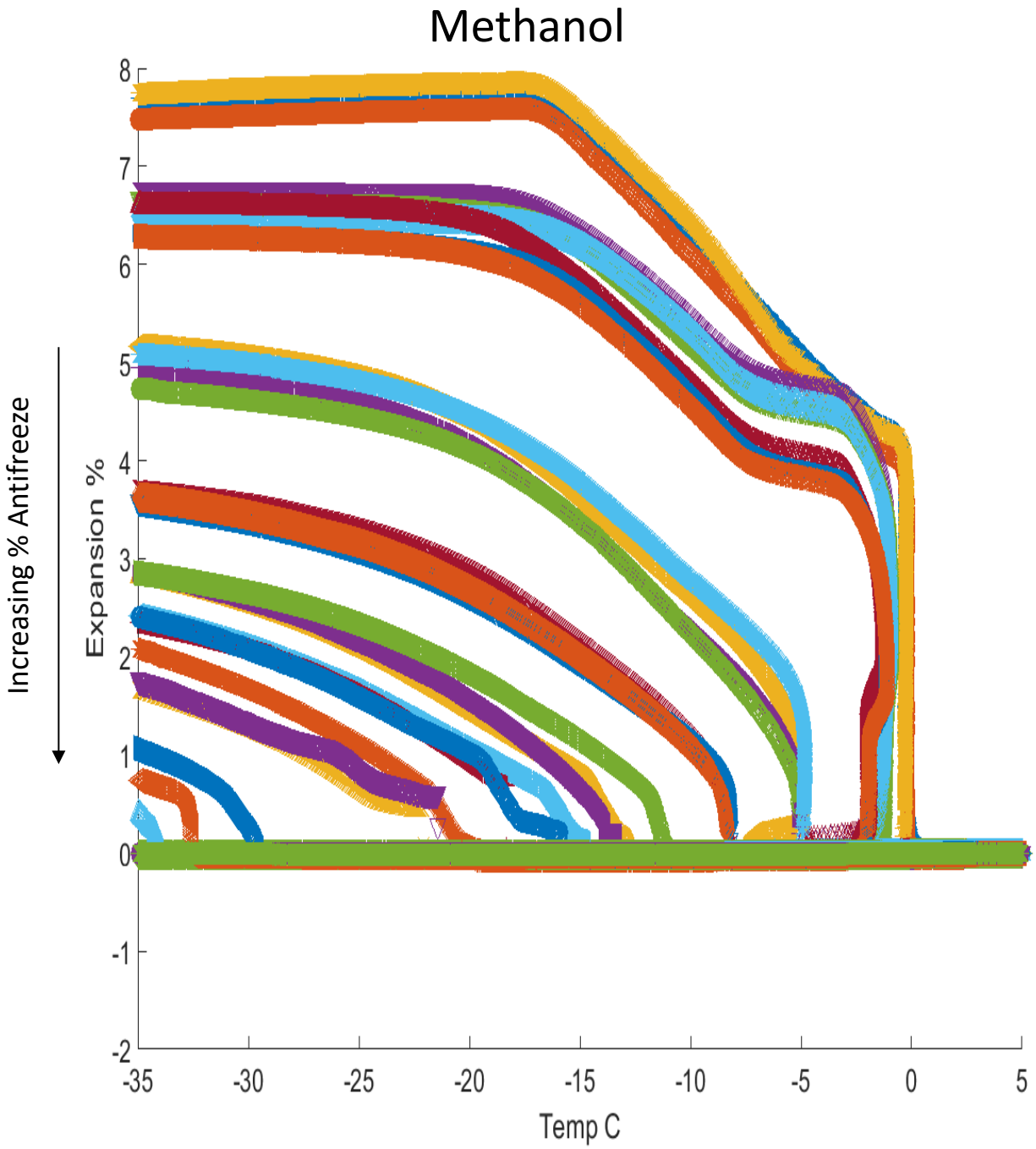
Figure 106: Methanol expansion data (full set)

11.3 ADDITIONAL NANOCHANNEL PHASE SEPARATION

11.3.1 Visual Inspection Issues

11.3.1.1 Bubbles
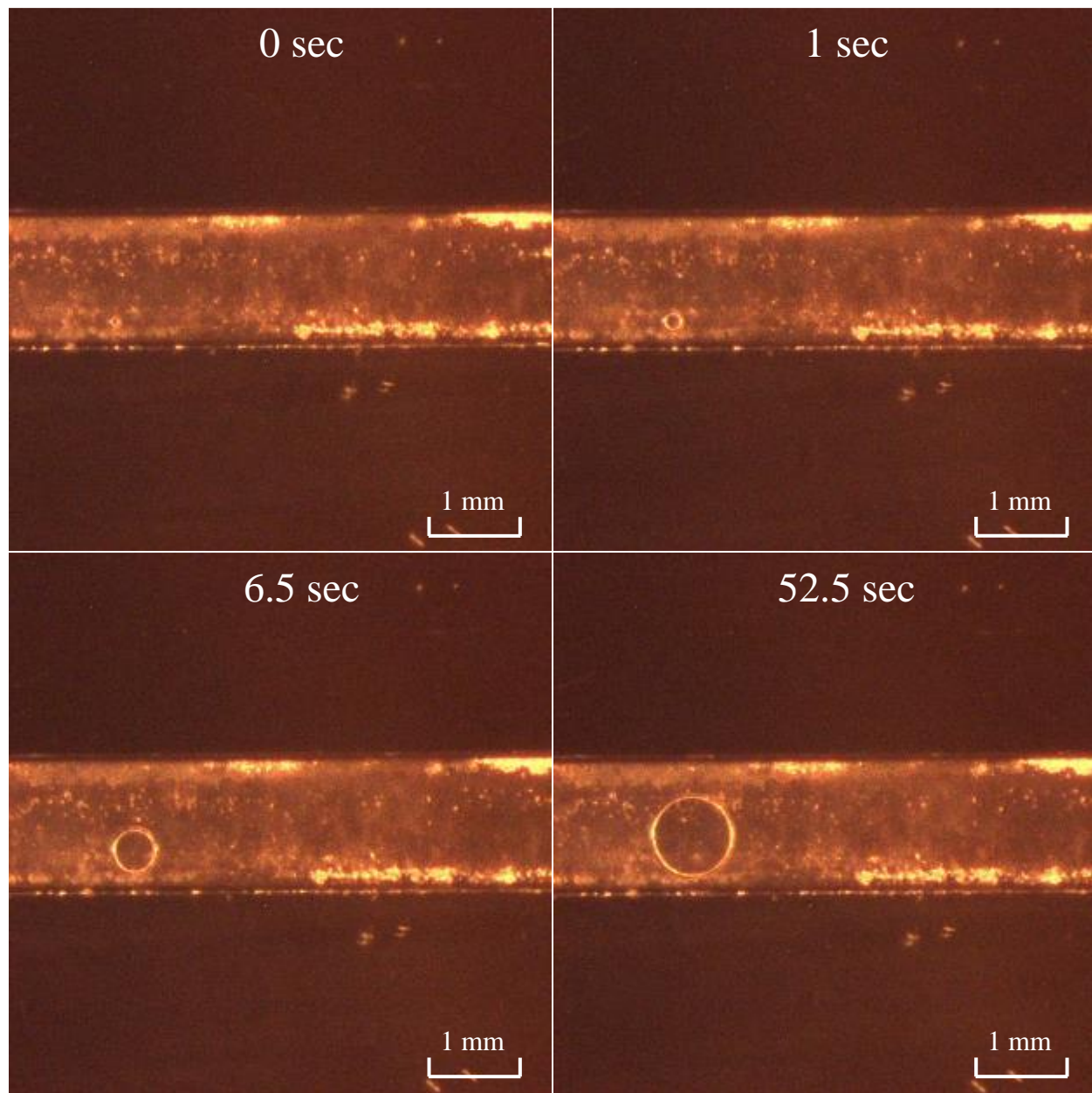
Figure 107: Data collection avoided bubbles caused by trapped air

11.3.1.2 Nanochannel Freezing
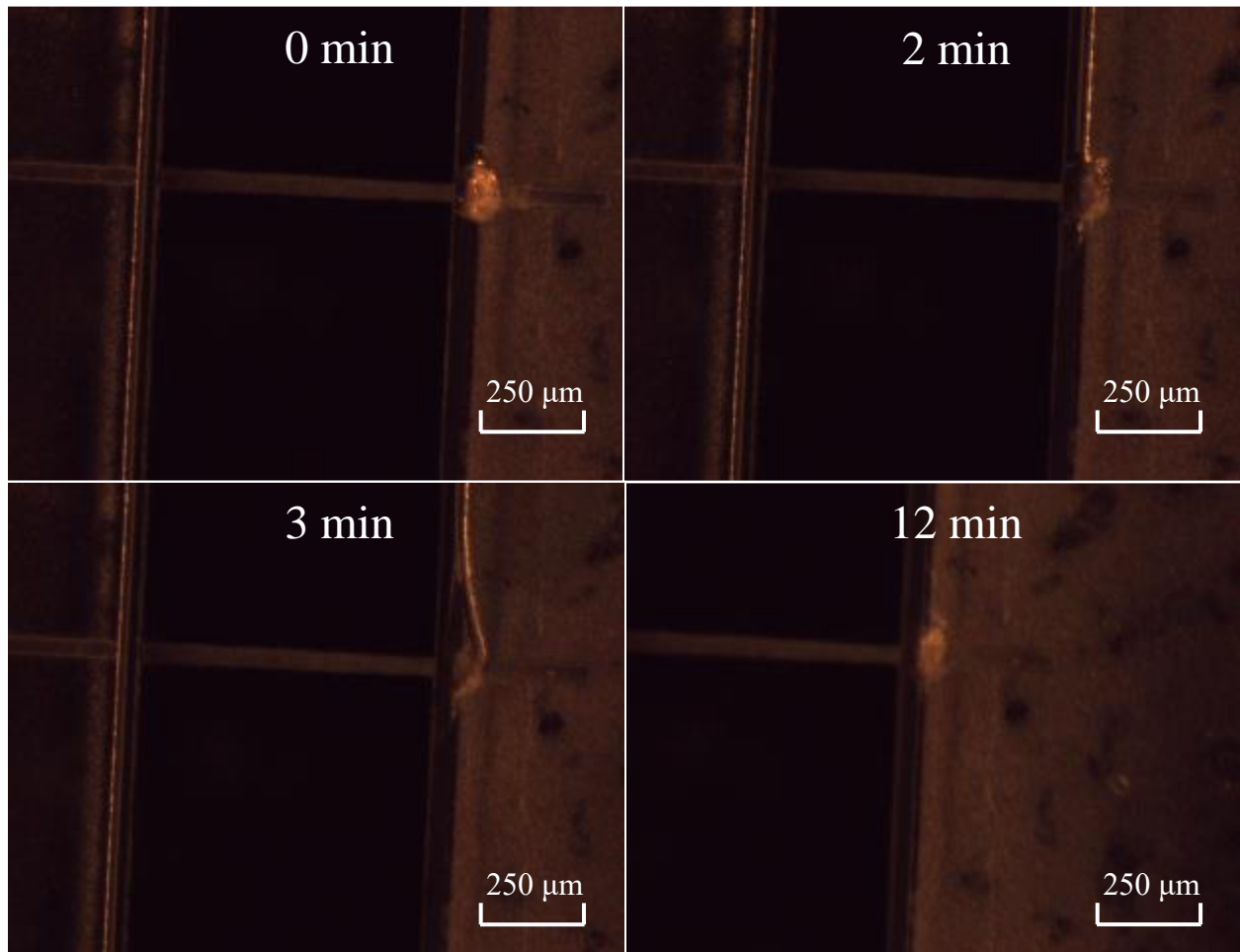
Figure 108: Ice formed at the liquid meniscus under vacuum

11.3.1.3 Boiling/Condensation
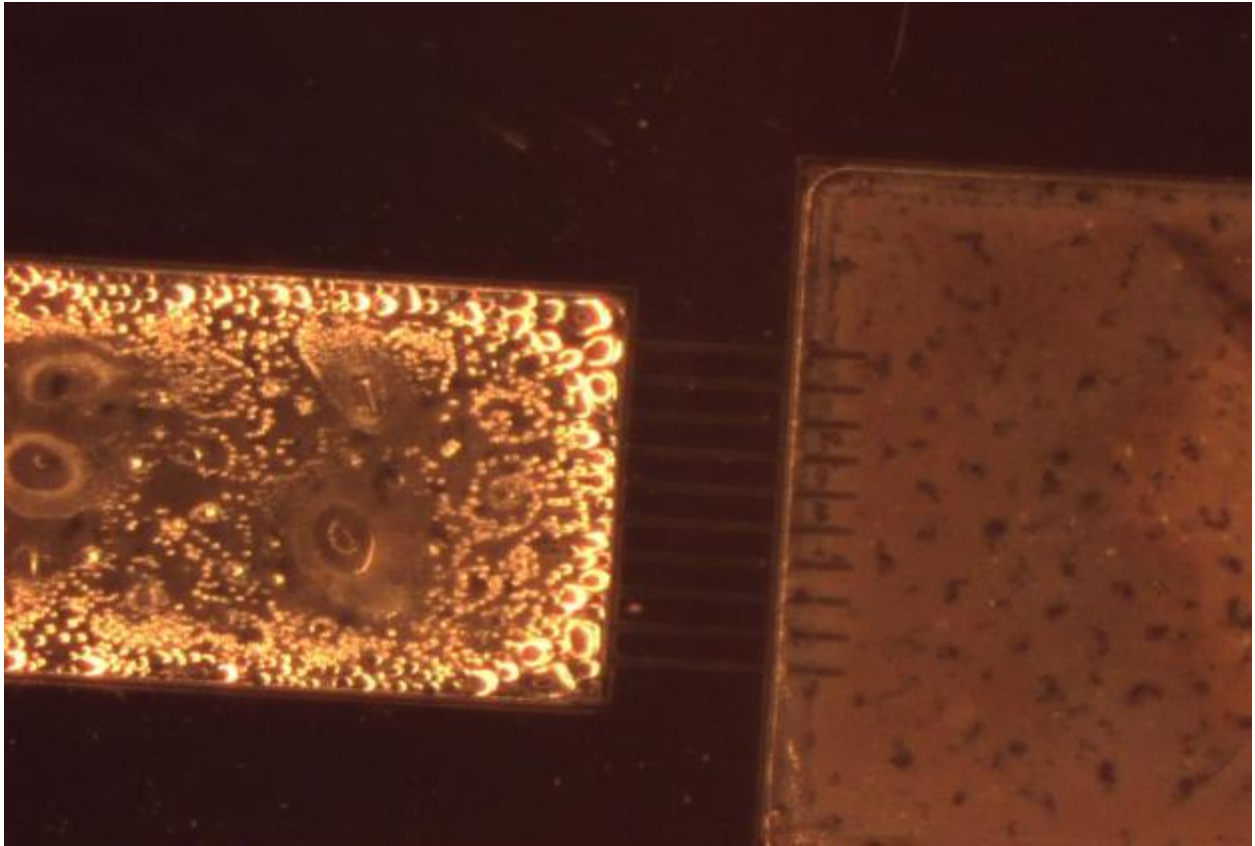
Figure 109: Bubbles formed during heating and droplets during cooling
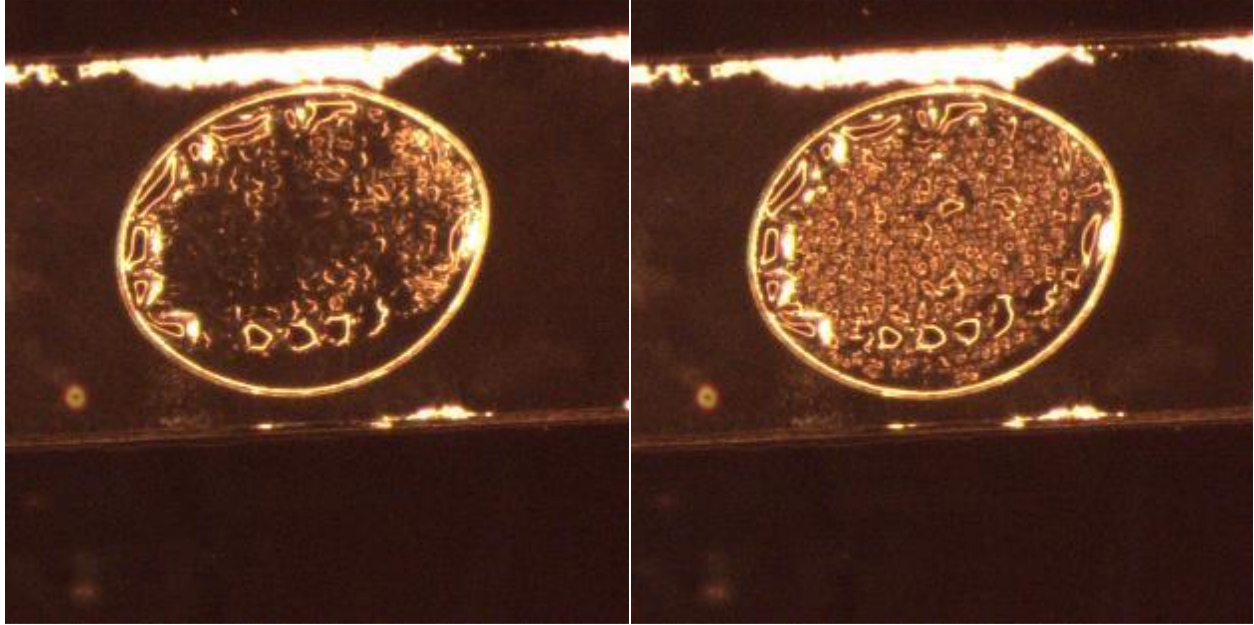
Figure 110: Heating above the boiling point caused localized bubbling and condensation

11.3.2 Microchannel Priming

11.3.2.1 Pipette

Initially a VWR Signature™ Ergonomic High Performance Single-Channel Variable Volume Pipette pushed fluid into the microchannel exit and the fluid wicked into the nanochannel. Vias etched through the silicon chip and holes drilled through glass allowed for filling of the channels with a pipette. Figure 111 shows a nozzle chip, filled using a pipette, and indicated wetting at the throat with a perceivable meniscus. Once exposed the vacuum the meniscus progressed as shown in the figure above. This method resulted in uneven wetting of the microchannel inlet and trapped air, causing difficulty with the fluid volume tracking. Additionally, the volume of fluid in the glass inlet hole was significantly larger than the volume of fluid in the microchannel, which caused trial setup times to be inordinately long.
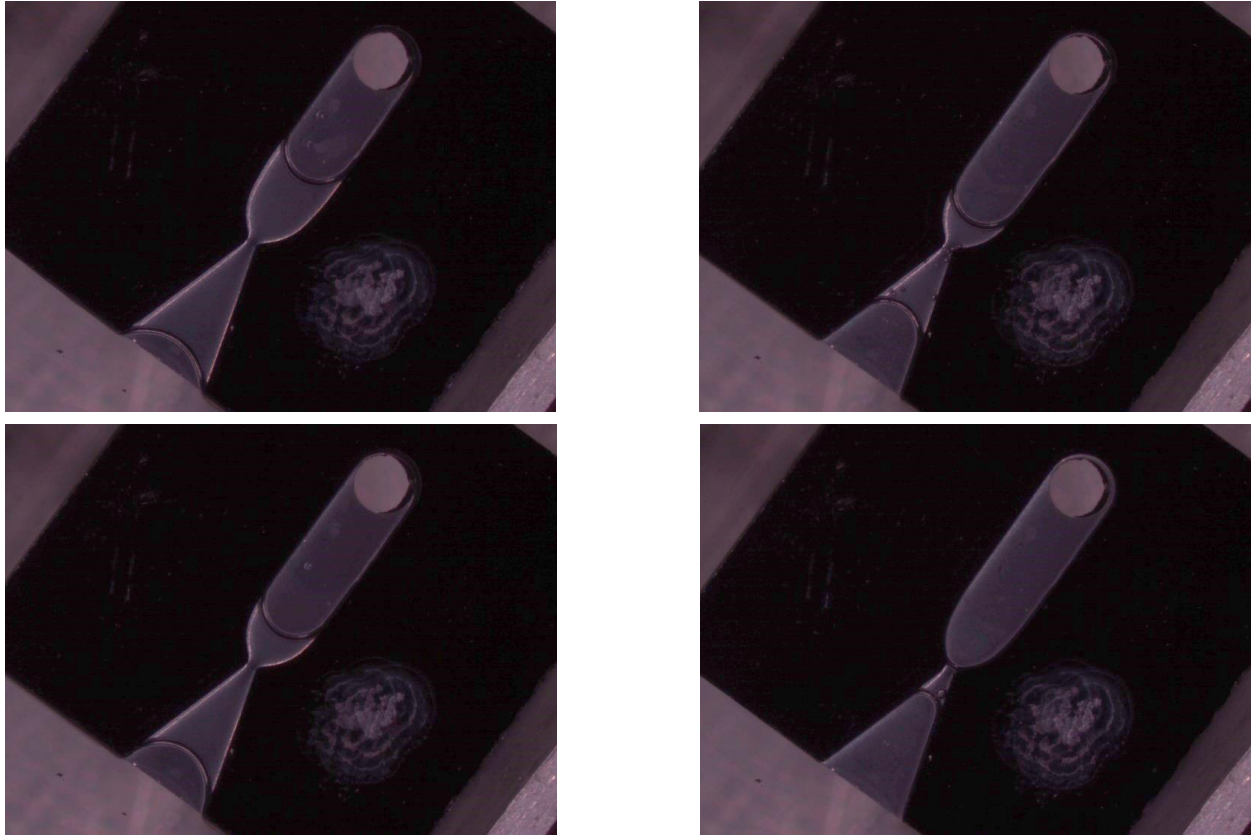
Figure 111: Meniscus progression during fluid evaporation under vacuum

11.3.2.2 Vacuum Filling

To fill the microchannel, a vacuum attached to the inlet hole drew fluid into the microchannel through the nanochannel. Since this method was essentially the desired end experiment in reverse, it relied on the vapor pressure of the solution to drive flow across the nanochannel. Along with being somewhat unreliable, this method resulted in excessive priming time.

11.3.2.3 Pressurized Filling Chamber

An acrylic chamber evacuated to sub Torr pressures to remove all vapor and air from the micro/nanochannel. A 3D printed syringe pump pushed fluids, filling the cavity until it pressurized. The pressurized fluid flowed across the nanochannel into the microchannel forming

a visible meniscus. Pressurizing the fluid significantly decreased the filling time necessary for preparing samples and the limiting factor for pressure was the strength of the glass slide. Over pressurization of the glass slide resulted in catastrophic cracking of the glass and rendered the sample useless.

11.3.3 Keyence Channel Profile Measurements

.5µm		NanoDepth	Nano Width	MicroDepth
Single	2.1.1	0.650	59.085	65.722
	2.2.5	0.773	62.675	68.549
	4.1.1	0.585	61.629	82.102
	4.1.2	0.587	60.589	82.137
	4.1.3	0.620	60.383	82.639
	4.1.4	0.556	109.674	45.923
	4.1.5	0.551	98.321	46.983
	4.1.6	0.516	52.642	44.097
	4.1.7	0.580	78.515	45.000
	4.1.8	0.791	63.034	81.7
Array	2.2.6	0.662	60.836	75.616
	4.3.1	0.553	59.802	46.649
	4.3.2	0.544	66.989	44.045
	4.3.3	0.532	65.963	44.887
	4.3.4	0.554	63.301	45.965

1µm		NanoDepth	Nano Width	MicroDepth
Single	2.1.1	1.248	67.388	66.124
	2.1.2	1.007	60.868	66.526
	4.1.1	0.832	62.720	82.580
	4.1.6	1.405	70.041	82.186
	4.1.7	1.442	62.313	82.553
	4.1.8	1.211	63.303	81.997
Array	2.3.1	2.190	59.694	76.848
	2.3.2	2.358	63.380	76.833
	2.3.3	2.263	58.457	76.377
	2.3.4	2.278	59.836	77.718

10µm		NanoDepth	Nano Width	MicroDepth
Single	2.1.1	12.305	73.179	77.948
	2.1.2	11.949	76.159	76.906
	4.1.1	12.012	65.159	95.236
	4.1.2	12.043	62.379	94.347
Array	2.2.1	12.407	59.667	85.790
	2.2.2	12.093	59.544	87.160
	4.2.1	11.542	65.861	85.999
	4.2.2	12.129	63.645	86.253

Figure 112: Nanochannel width/depth and microchannel inlet depth (all units in µm)

11.4 SOFTWARE

11.4.1 SolidWorks

This research utilized SolidWorks for design, modelling, and fabrication and for basic finite element analysis. 3D drawings, part files, and assemblies of drawings, assembly files, serve as useful virtual prototypes and working models. Dassault Systems generously provides the software to the University of Arkansas. SolidWorks 2017 is the latest version of the software used. Parts fabricated using 3D printing, laser cutting, computer numerical controlled milling, as well as conventional milling fabrication methods all utilized models generated in SolidWorks. SolidWorks served a vital role in essentially every single aspect of this research.

11.4.2 Mastercam

Mastercam is a computer-aided design and manufacturing software used to generate machining codes for computer numerical controlled milling machines. Importing a part, exported from SolidWorks as an .xt file, into Mastercam creates a systematic toolpath based on input milling parameters. The choices for toolpath are predefined but include, contour, pocket, drill, face, etc. Mastercam outputs the toolpath in the form of G-code native to the milling machine. G-code is the most widely used numerical control programming language. Mastercam X9 generated toolpaths for this research.

11.4.3 National Instruments (NI) Labview

Labview is a graphical programming language utilizing pre-programmed blocks of code. The nature of the program allows for visualization of every application, including configuration, data measurement and manipulation, and debugging. Program-subroutines created using Labview save in the form of a virtual instrument, or .vi for short. Used in conjunction with a data acquisition unit (DAQ) the software controls or measures virtually any hardware enabling a completely custom user interface. This research used NI Labview 2016 (64bit).

11.4.4 National Instruments (NI) Vision Assistant

NI Vision is a tool for prototyping a testing image processing applications. The software allows for testing a single image with different tools on the image for a variety of applications. One at a time, multiple images run through the processing algorithm, testing the robustness and viability for large-scale tests.   Upon completion of the systematic programming, generation of a script allows for use of the program in Labview. This research utilized Vision Assistant version 2016.

162

11.4.4.1 Fluid Volume (Height Measurement)

Using Labview Vision, recorded mages of fluid in a graduated cylinder indicate the volume of liquid. Figure 113 outlines the process for rotating an image relative to the graduated cylinder, finding a reference edge, and detecting the meniscus level of the fluid. Interpolating the meniscus pixel values, referenced between two known volumetric graduation marks yields the fluid volume in milliliters. Tracking the progression of the liquid volume produces a volumetric flow rate.

Original Image   Rotated + Threshold + Edge Finder
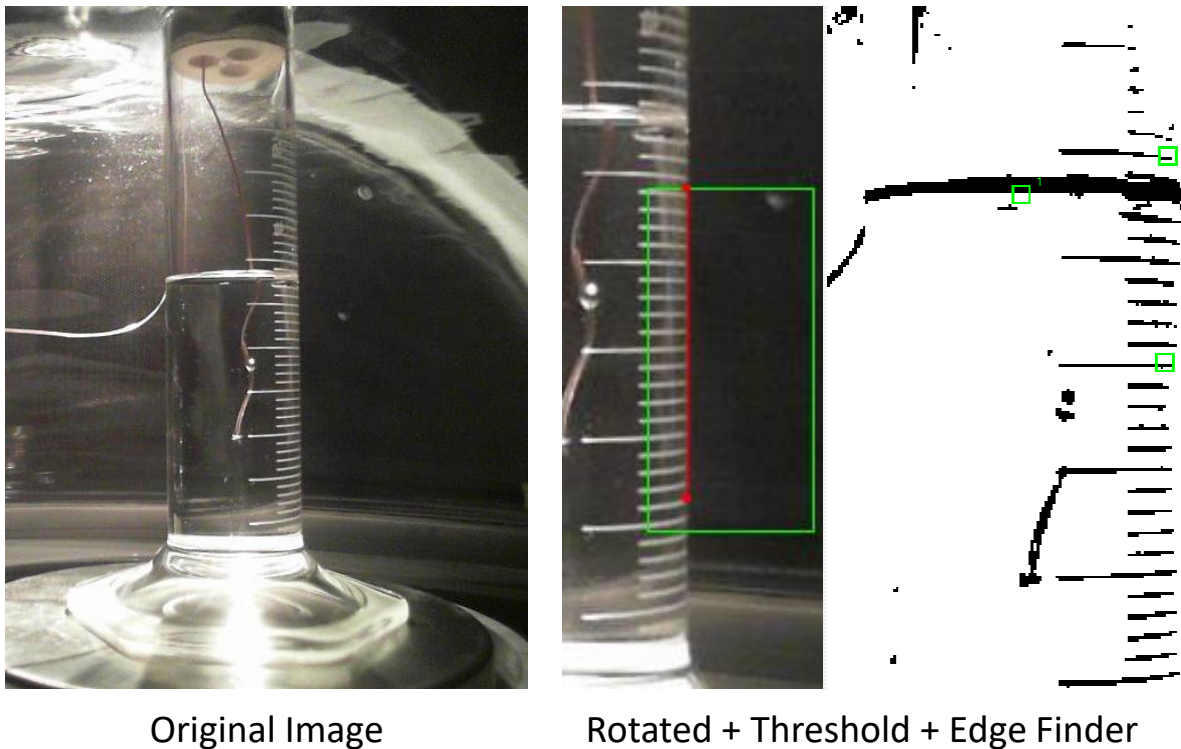
Figure 113: Vision recording liquid volume in a graduated cylinder.

Preliminary attempts at measuring fluid volume resulted in extremely noisy volume data, Figure 114. Upon reaching vacuum, the fluid began to boil resulting in an unstable meniscus reading. This boiling effect did not decrease or stabilize since the vacuum maintained the fluid at its vapor pressure. Additionally, the fluid temperature dropped during pump down due to evaporation, indicating the need for a heating device to maintain a constant temperature.
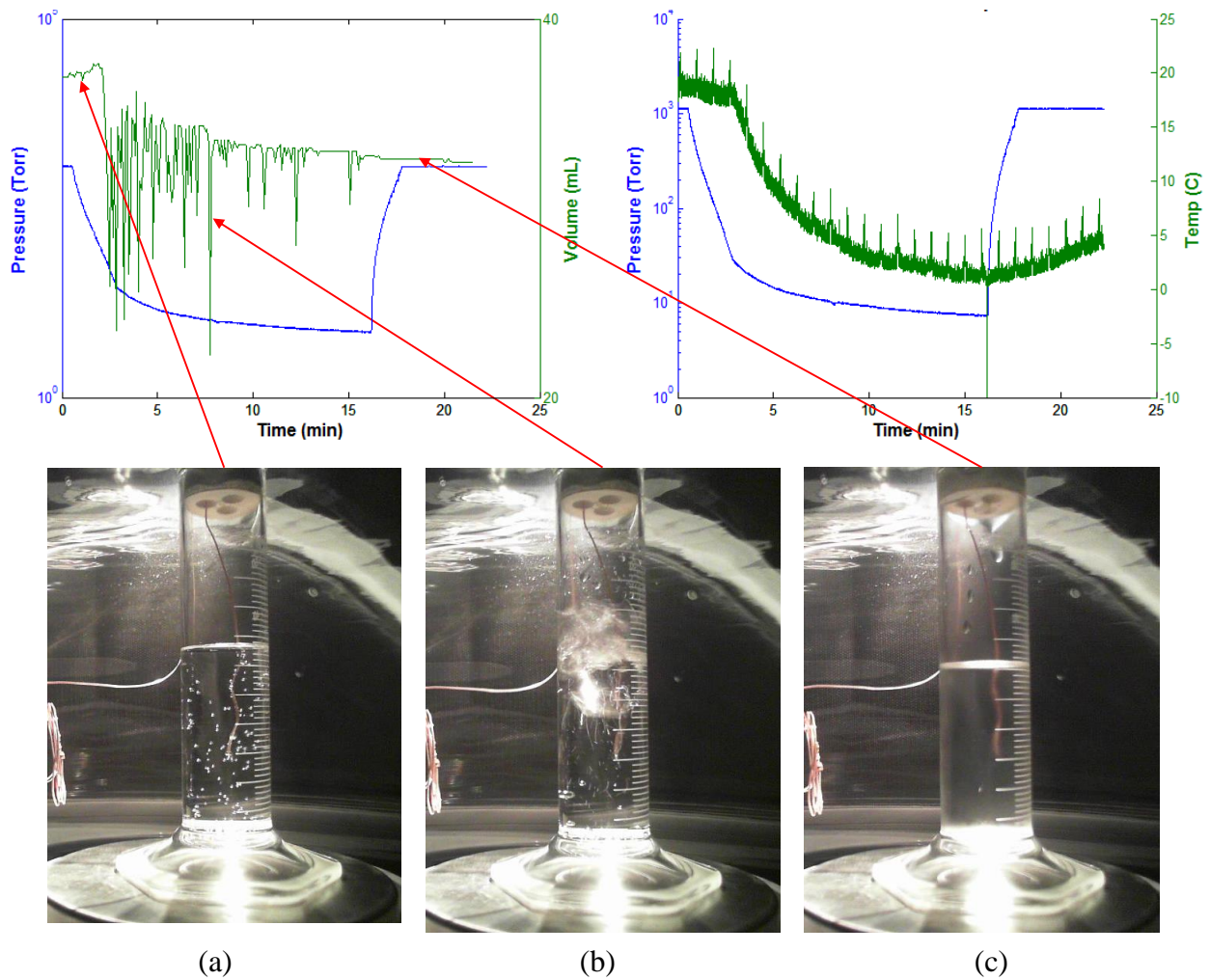
Figure 114: Boiling liquid under vacuum

Volumetric noise overshadowed the noticeable volumetric trend. Bubbling of fluid yields a low volume reading, while incomplete image processing yields a high value, Figure 115. Applying a threshold reduces the error in the measurement, but is an extreme manipulation of the data. Based on the noise and lighting difficulty, the research proceeded with a different approach for obtaining the flow rate.
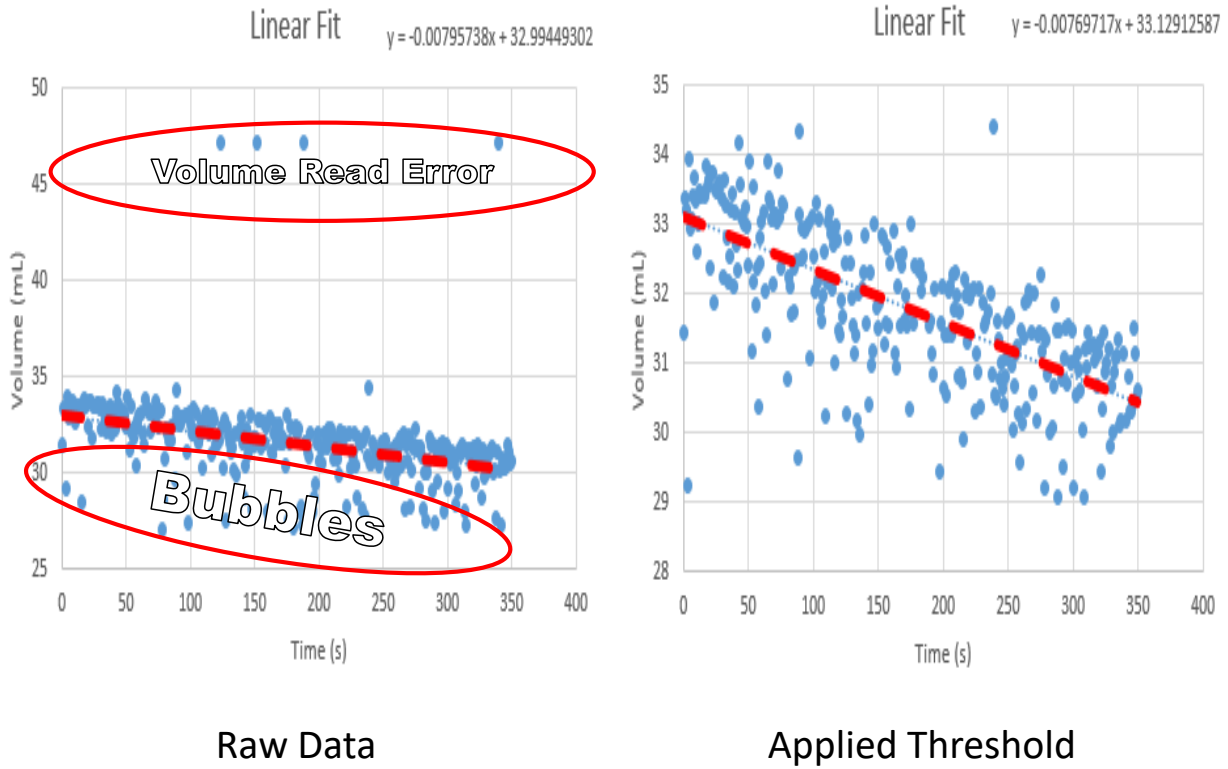
Figure 115: Bubbling fluid volumetric data

11.4.4.2 Optical Character Recognition

Optical character recognition is a powerful tool for identification of characters using a camera and computer software, in this case Labview Vision. Figure 116 outlines the basic process for converting an image into usable string data. Pattern matching locates the face of the scale (a) and thresholding highlights numbers (b). Image reverse creates a binary image (b) and with character training, optical character recognition converts the image into a string.
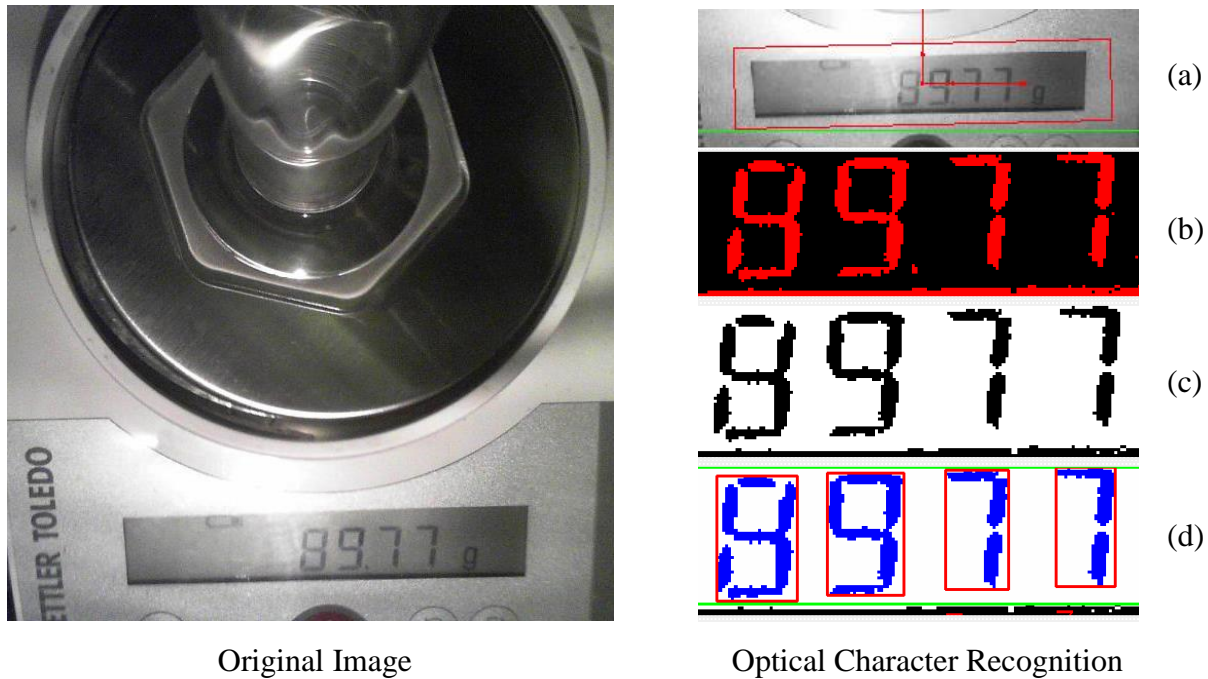
Figure 116: Optical character recognition with Labview Vision

Unfortunately, readability issues (including glare, water droplets, character learning, etc) led using a digital readout scale for a reduction in measurement complication and increased accuracy. Figure 117 illustrates measurement difficulties as a result of both glare and water droplets. While the water droplet issue resolved by restricting the flow with capillary tubes, lighting remained a constant source of difficulty and the research progressed with another method to obtain flow rate.

Begin t=0min   End t=3.126min

Figure 117: Visual disruption of scale readout

11.4.4.3 Fluid Volume (Areal Monitoring)

For the nanochannel fluid phase separation experiment, Labview Vision monitored fluid movement using image manipulation. An example of the algorithm created with NI Vision Assistant outlines the steps necessary to analyze the volume of water from an image of area covered by fluid. Initially, fluid volume
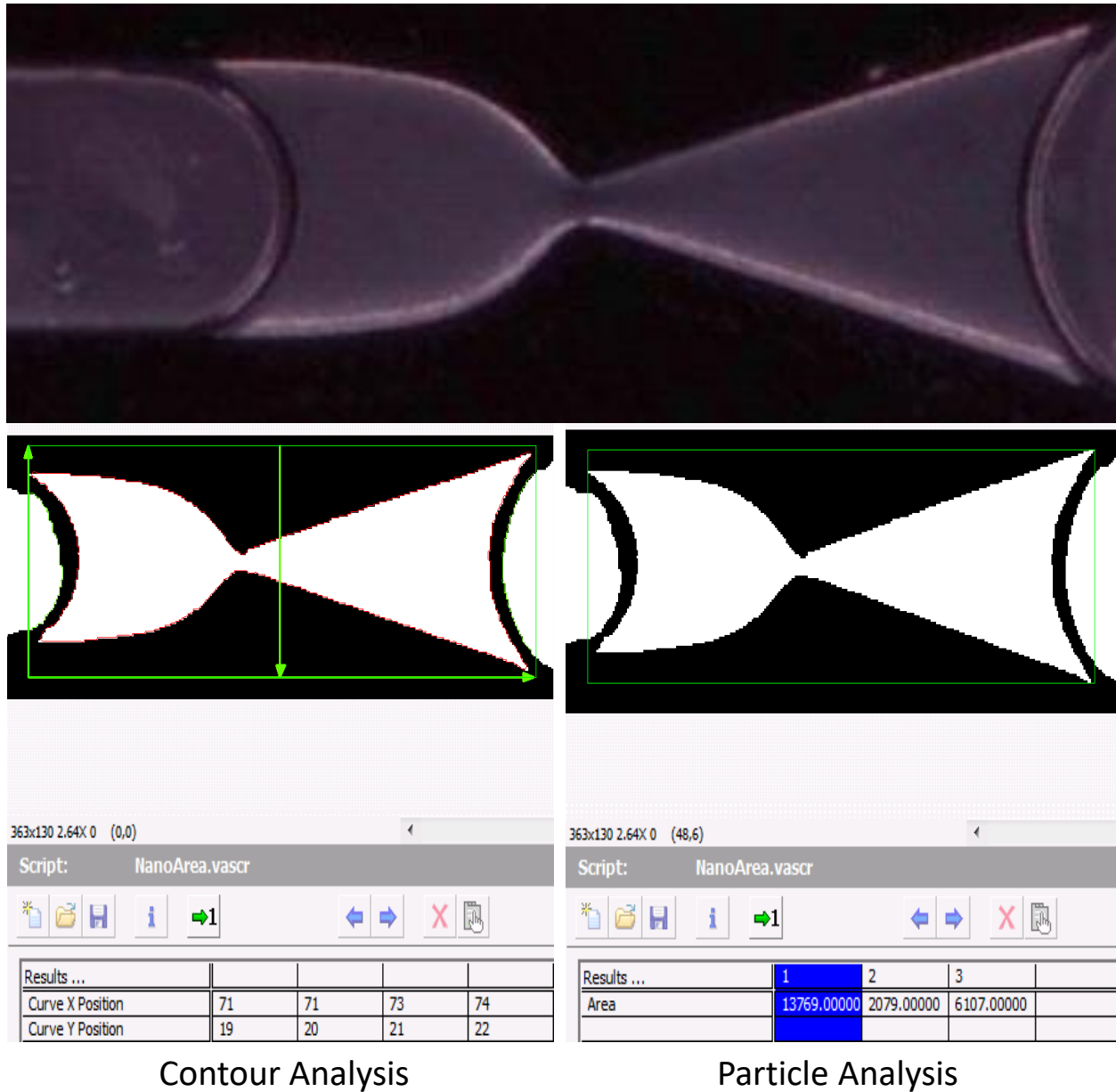
Figure 118: Contour and particle analysis, yielded similar liquid coverage results.

168

11.4.5 Excel

Microsoft Excel is a spreadsheet software used for calculation, graphing, and programming in visual basic for applications. Preliminary analysis generally used excel for quick calculations and visualization of data. However, large sets of data caused the program to lag and at times even exceeded the 1048576-row limit. This research used Microsoft Excel 2016 for analysis purposes.

11.4.6 MATLAB

Large and numerous data sets necessitated a more powerful program to handle the data post processing. MATLAB R2017a fit the bill. MATLAB is a numerical computer environment with its own proprietary programming language (.m). The program allows for matrix manipulations, function and plotting, and even interfacing with other programs and hardware. Multiple scripts generated using MATLAB processed the large quantity of data produced from experiments for this research.

11.5 ELECTRONIC COMPONENTS

11.5.1 Thermocouple

An Analog Devices monolithic thermocouple amplifier with cold junction compensation (AD595) in combination with an omega thermocouple (part number 5TC-TT-K-40-36) measured the temperature in both the meso-scale evaporation and nanochannel experiments. Insulated with perfluoroalkoxy alkane (PFA, the type K thermocouples were 36 inches long and 40 gauge wire. National Semiconductor 7815 and 7915 voltage regulators controlled the output voltage to +/- 15V for the AD595.
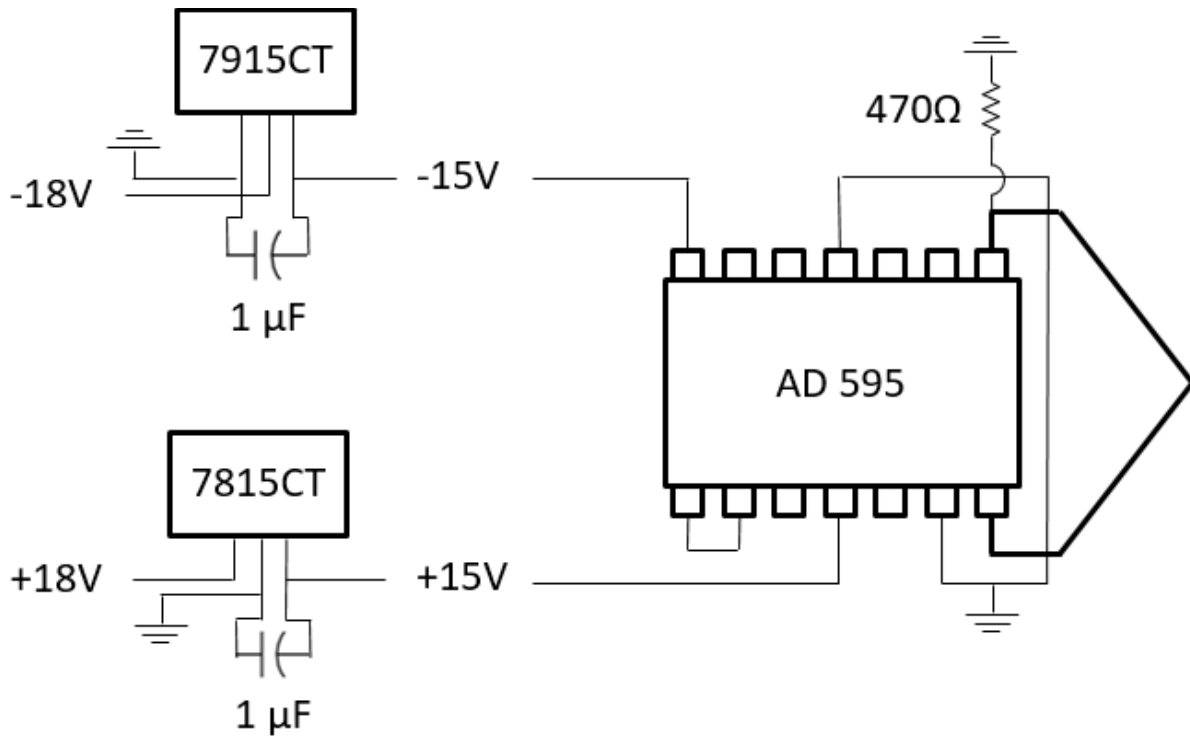
Figure 119: Thermocouple electrical diagram to monitor temperatures in experiments.

11.5.2 Pressure Sensor

A Honeywell TruStability board mount pressure sensor recorded the vapor pressure in the meso-scale evaporation experiment. The model number, HSCDANT030PAAA5, indicates a device with high accuracy, compensated/amplifier (HSC), dual inline pin (D), single axial barbed port (AN), liquid media compatible (T), an absolute pressure range of 0-30psi (030PA), analog output (A), a transfer function with 10-90% of the supply voltage (A), and a supply voltage of 5 volts (5). An Analog Devices pin programmable precision voltage reference supplied the 5V supply voltage to the pressure sensor. A National Semiconductor 7915 voltage regulator controlled the output voltage to + 15V for the AD584.
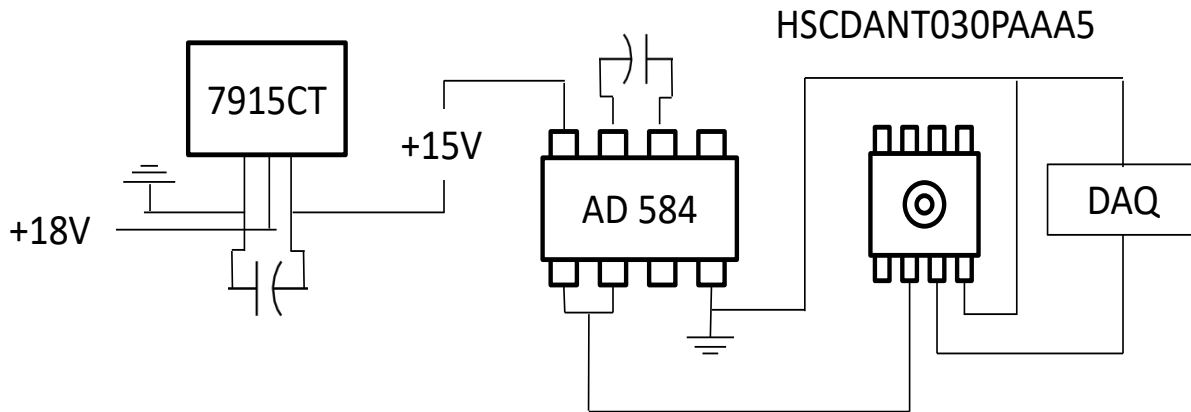
Figure 120: Pressure sensor electrical diagram for the meso-scale evaporation experiment.

11.5.3 Nichrome Wire Heater

An immersion heater was necessary to control the temperature of fluid in the meso-scale evaporation experiment. A nichrome wire heater, 30 American wire gauge (AWG) bare nickel chromium (BNC), satisfied this requirement. The wire, from Consolidated Electronic Wire & Cable, is composed of 60% nickel, 16% chromium, and 24% iron, has a temperature limit of 982°C, and has a resistance of 6.75 ohms per foot. Wire gauge, length, and voltage all influence the heater temperature. For example, a 36-gauge wire, eight inch long, with 17.2 Volts quickly heated 200mL of water up to 35.7°C, Figure 121.

(a)   (b)
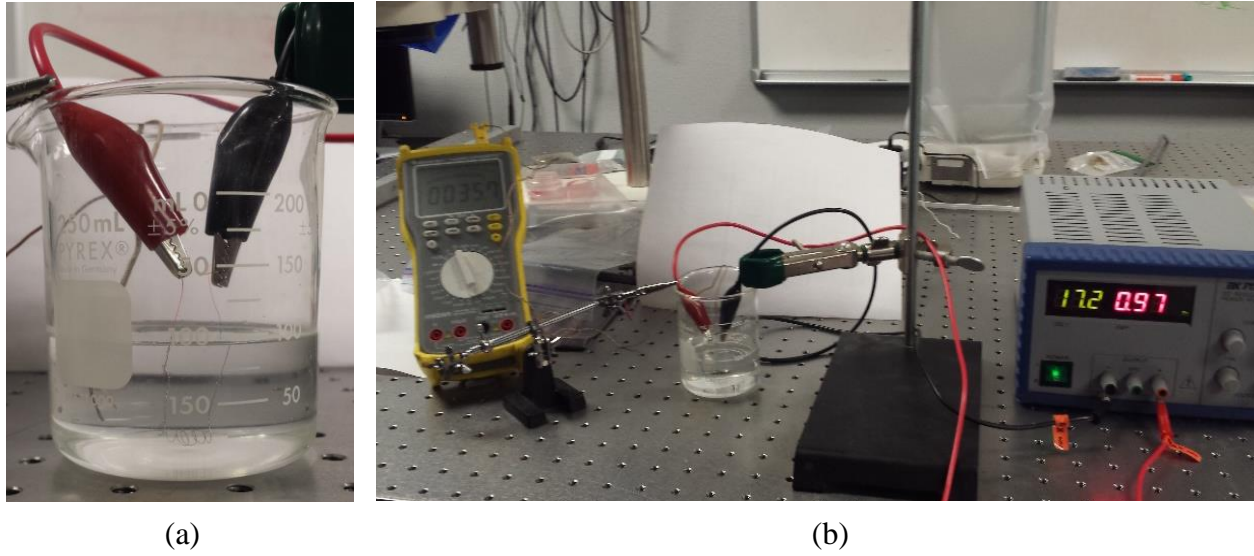
Figure 121: A nichrome wire acts as an immersion heater in water with an applied voltage

For the meso-scale evaporation experiment, a DAQ analog output controlled the voltage across the nichrome wire. A Burr Brown OPA544T high-voltage, high-current operational amplifier supplied the voltage to the heater. The op-amp allowed the heater to receive significantly higher voltages than that provided by the DAQ analog output, thus preventing damage to the DAQ. A 0.1-ohm sense resistor placed between the op-amp output and the heater enabled for the monitoring of power consumed by the heater. Labview recorded voltages across the heater and sense resistor.
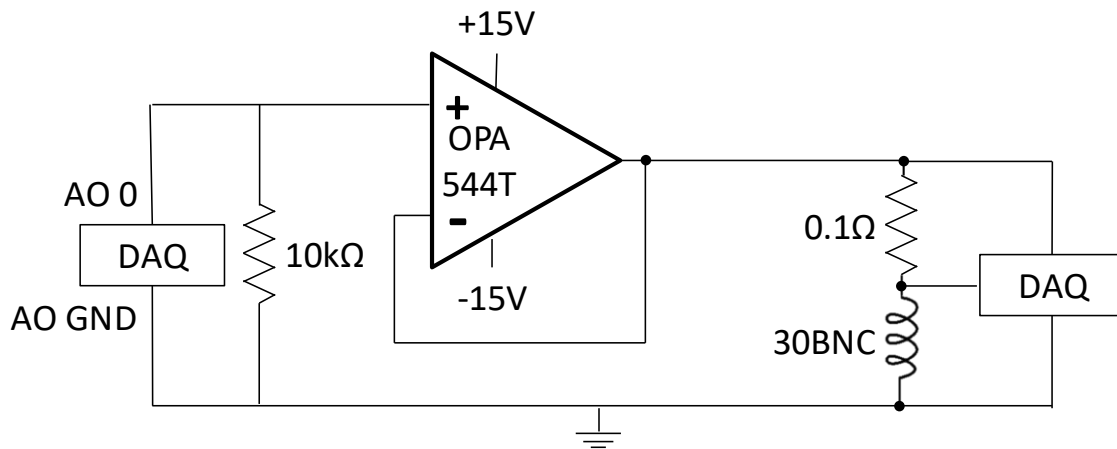
Figure 122: Electrical diagram for a nichrome wire resistance heater.

11.5.4 Peltier Heater
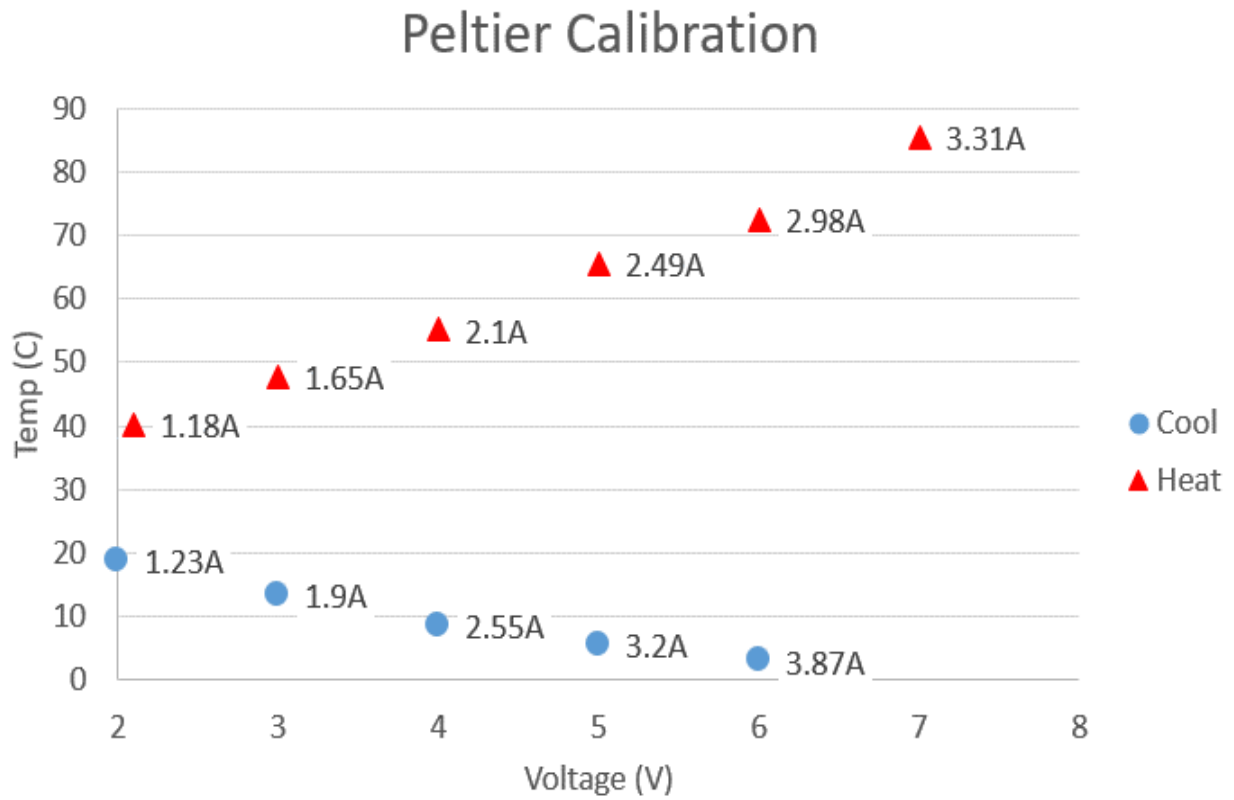
Figure 123: Peltier stage calibration indicated values necessary to maintain temperature.

11.5.5 LVDT

A linear variable differential transformer (LVDT) converts rectilinear motion to a corresponding electrical signal. This research used the LVDT to monitor the linear expansion of fluid during phase change into solid. An LVM110 signal conditioner controls the voltage supplied to the LVDT and conditions the electrical response from the LVDT. On the LVM110, dipswitches for S1 set to On/On/Off/Off indicated and output VRMS of 2.1 to 5.55, in master mode, and at a 2.5 kHz oscillator frequency. These settings conditioned the voltage to the test settings required by the LVDT. National Semiconductor 7815 and 7915 voltage regulators controlled the output voltage to +/- 15V for the LVM110 and AD595.
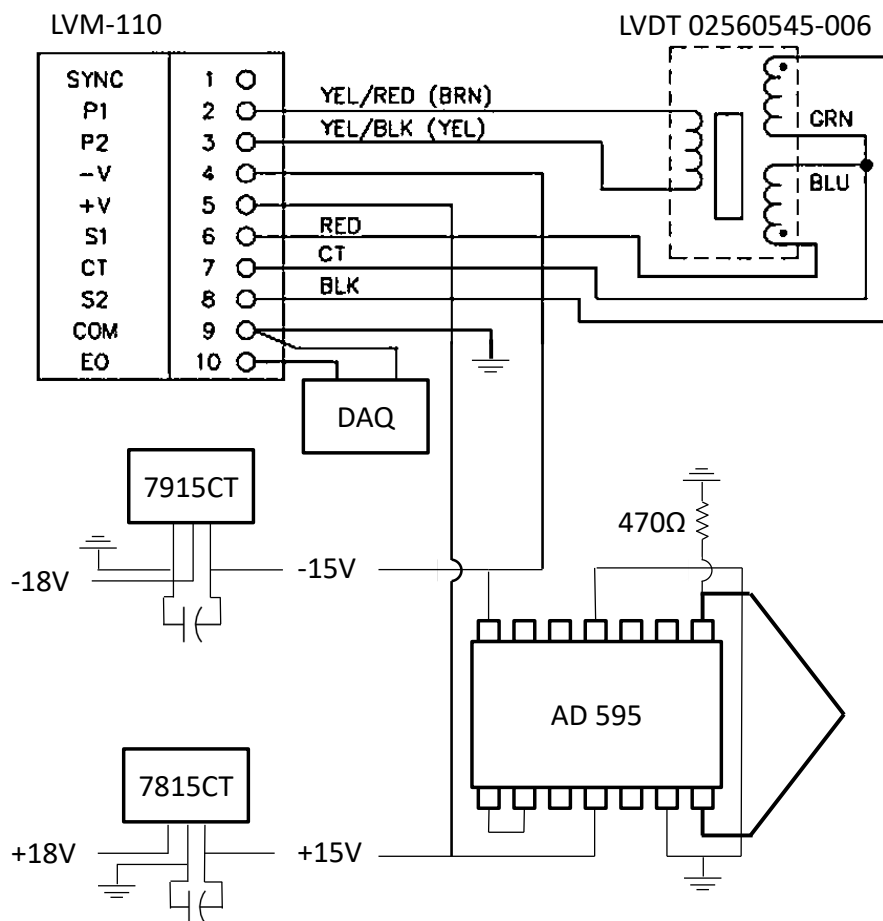
Figure 124: LVDT electrical diagram for recording both fluid expansion and temperature.

Figure 125: A 3D printed housing isolated the LVM110.

An E-1000 LVDT (part number 02560545-006) generated the output signal corresponding to linear displacement. The LVDT has a stoke length of +/- 1 inch and an operating temperature of -55°C to 95°C. Internal to the LVDT are three wound coils, a primary and two secondary. Movement of the core connecting rod (part number 05282946-006) affects the signal value between the coils, indicating a distance.

Figure 126: An E-1000 LVDT can detect axial movement with a total span of +/-1 inch.

11.6 EQUIPMENT

11.6.1 Stratasys Dimension Fused Deposition Modeling 3D Printer

3D printing, using a Dimension Elite Fused Deposition (FDM) printer, served a vital portion of the research conducted for this dissertation if only in a primarily supporting role. Throughout this documentation, lab setup pictures display various structural pieces from mounting hardware, brackets, clamps, electronics enclosures, and jigs. Another invaluable use was for the various prototypes that served as models, pre-machining fit checks, and sanity checks. All parts created using rapid prototyping saved tremendous amounts of time fabricating. 3D printing is a useful tool for quickly creating parts with minimal strength requirements, as there is no need to machine the piece out of a stronger material like aluminum or steel. When machining was necessary, i.e. aluminum and Teflon parts, rapid prototyping still served an important role in reducing the overall fabrication time. Initial testing of O-ring glands and press fits meant only one machine step was needed reducing lead time and cost for experiments. Additionally, at times an acetone vapor bath treated the surface of the 3D printed parts closing pores and smoothing the surface for a finished look. 3D printing proved to be an invaluable tool for supporting the research.

11.6.2 Laser Cutter

An Epilog 14000 Laser System Fusion M2 cut the nanochannel-filling chamber. Corel Draw in conjunction with epilog drivers generated a toolpath for the laser. Cutting depth and resolution varied based on the intensity and speed of the laser. The filling chamber utilized one half inch thick acrylic because it is nonporous and easy to machine.

11.6.3 Mettler Toledo Scale

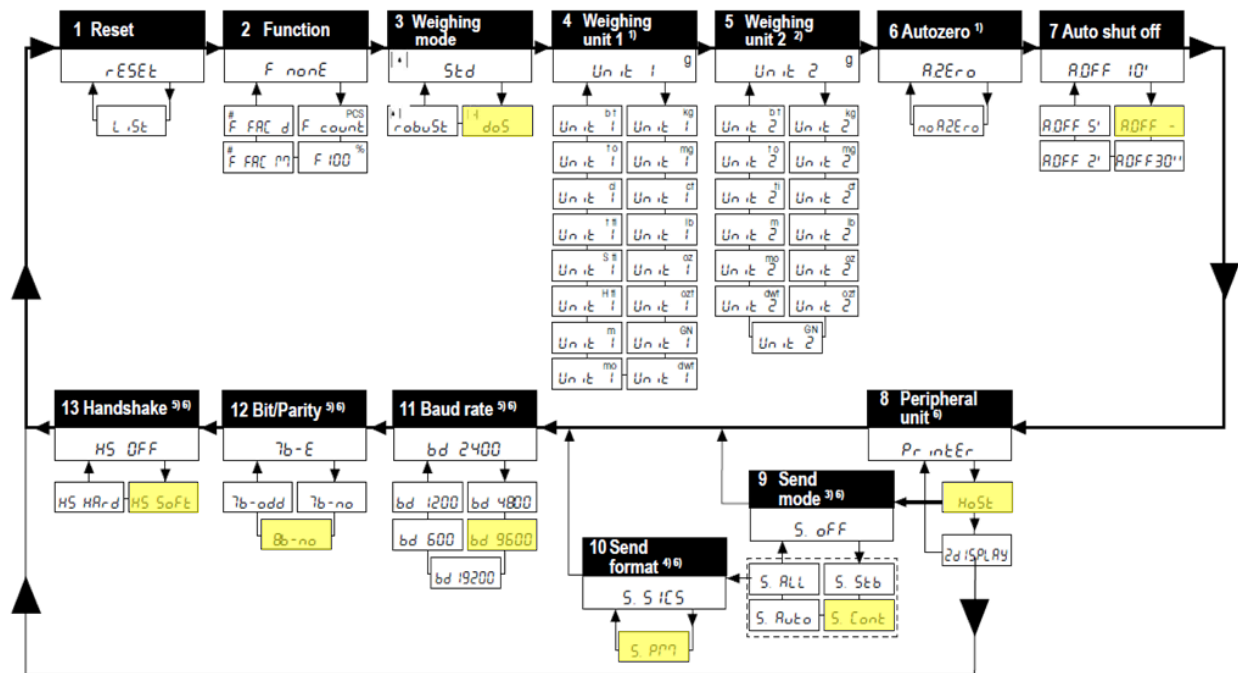Figure 127: Mass scale setup conditions indicate the data transmission method to the DAQ.

The control algorithm designed in Labview enabled real time mass measurement. VISA Overrun Error indicates a buildup in the number of bytes at serial port resulting in lagging data. Resetting the VISA if the bytes at port exceeded 32 mitigated the issue.
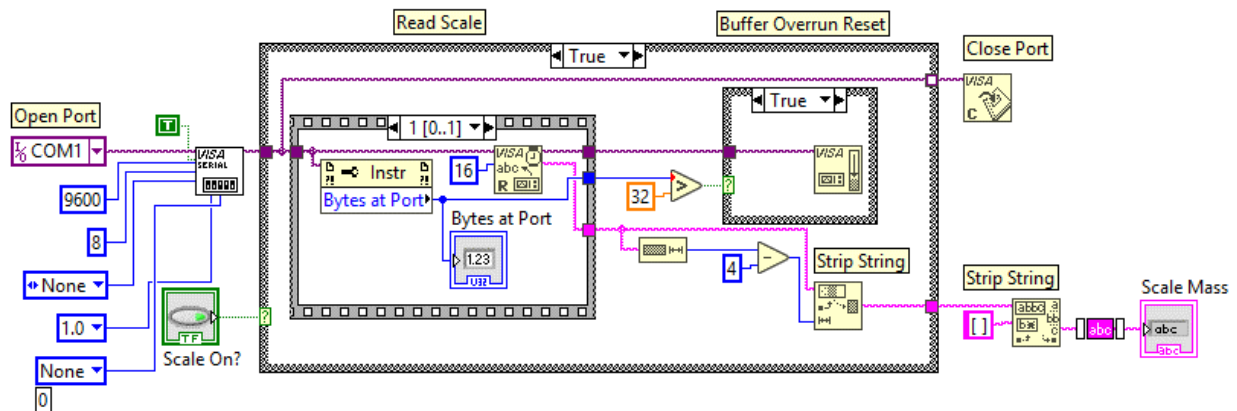

Figure 128: Mass scale control and data acquisition algorithm

11.6.4 Cincinnati Sub-Zero Micro Climate Chamber

A Cincinnati Sub-Zero MicroClimate chamber (Model No. MCBH-1.2-.33-.33-H/AC) controlled the testing environment for heat transfer in aqueous samples during phase change. The benchtop model has a temperature range of -70°C to 190°C with the ability to control humidity between 0 and 100%. The chamber has two control modes with single set point mode and profile programming for automated trials.

11.7 MICROFABRICATION METHODS

11.7.1 Cleaning

Wafer preparation includes removal of oils, organics, or particles from the surface. The general wafer cleaning process was as follows: five minutes in an acetone bath in a Pyrex crystallizing dish, followed by a 5 minute isopropyl alcohol (IPA) bath in a Pyrex crystallizing dish, and finished with a deionized water rinse. Acetone removes organic impurities from the wafer while IPA rinses the acetone. For a higher degree of cleaning, a bath of hydrogen peroxide (H_2O_2) and hydrochloric acid (HCl) decontaminated the wafer. Adding HCl to a premixed water and H_2O_2 solution generates a self-heating, boiling liquid, Figure 129. A 1:1:1 ratio of concentrated HCl to 30% H_2O_2 to H2O is a common etchant for PCB but also for wafer decontamination. Either a quartz or a Teflon container is preferable for the cleaning process. For extreme cleaning, a mixture of sulfuric acid (H_2SO_4) and hydrogen peroxide is necessary at a 3:1 ratio, respectively. The mixture, commonly known as piranha solution, is a strong oxidizing agent capable of removing organic matter. Piranha cleaning should be conducted in Pyrex glassware as it is a self-heating solution. After rinsing procedures, a nitrogen gun blew wafers dry to avoid water spots caused by mineral deposits.

Figure 129: HCL+H2O2 Wafer Decontamination

11.7.2 Photolithography

Photolithography is a fundamental microfabrication process to pattern parts on a substrate. Substrates consist of a variety of different mediums and materials including silicon, glass, and polymer. Generally, photolithography utilizes a photomask to transfer a pattern onto a wafer. A transparency mask has a resolution down to 5μm while a Pyrex max can achieve sub-micron level resolution. Photolithography is a two-step process. The first step is to transfer optically a pattern from a mask to a photosensitive polymer (photoresist). The second step is to develop the photoresist to realize the pattern.

For the patterning process, one must first consider the process flow and choose between the two types of photoresist: positive and negative. The chemical structure of positive photoresist changes when exposed to Ultra Violet (UV) light which increases the solubility making it easier

to remove. Negative photoresist polymerizes when exposed to UV light making it more difficult to remove. Depending on the photoresist viscosity, spin coating results in a thickness of a few to hundreds of microns. A soft bake is sometimes necessary to eliminate the remaining solvent in the photoresist, which inhibits mask contamination, bubbling, foaming, popping, dark erosion, etc. while increasing adhesion ("Softbake of Photoresist Films", 2013).

Next, align the mask to the wafer based on crystallography of the wafer, mask number for multiple step processes, etc. For this research, the author used a Karl Suss Electronic Vision aligner to expose the photoresist to UV light. Following exposure to UV, a hard bake is beneficial because it increases the thermal, chemical, and physical stability of the developed photoresist structures ("Hardbake of Photoresist Structures", 2013). Development of the photoresist removes the exposed area for positive photoresist but for negative photoresist leaves the exposed area untouched and instead removes the unexposed area. Completion of this step results in a patterned wafer that is ready for processing based on need and design followed by stripping the remaining resist.

Common mask aligners used for fabrication include the contact aligner, projection aligner, electron beam lithography, x-ray lithography, and soft lithography. A contact aligner (i.e. Karl Suss) typically has a resolution down to 1μm and either brings the mask in physical contact with the wafer or leaves a small gap between them to protect the substrate or mask. A projection aligner can shrink the projection of the mask onto the wafer five to ten times for increased spatial resolution. Electron beam lithography has nanoscale resolution via direct etch of the substrate by scanning a focused beam of electrons but can be very time consuming for larger features. X-ray lithography is similar to UV lithography but utilizes x-rays to treat the photoresist and creates high aspect ratio features. Soft lithography is a fabrication method used to pattern elastomeric materials

(i.e. Polydimethylsiloxane [PDMS] and Polymethyl methacrylate [PMMA]) and is a commonly used fabrication method in biomedical field. A litany of other fabrication methods exists but are too extensive to detail all.

11.7.3 Atomic Force Microscopy Nanolithography

Nanolithography is the branch of nanotechnology relating to the fabrication and study of devices on the nanoscale, 1-1000 nm. Nanolithography allows for the customization of the cross sectional area of nanochannels by scratching the surface of a glass substrate (Lee J & Huang A., 2009). Ideally, nanochannels have a constant circular cross-section enabling straightforward analysis and a simpler overall flow profile. Yet, due to the profile of the diamond tip, nanochannels have a wide, shallow, triangular cross section.

A Veeco PicoForce AFM using a Tap 190 DLC probe, shown in Figure 130, conducted the nanolithography process. The probe has a diamond-like-coating with a radius of less than 15nm ("Silicon AFM tapping mode probes," n.d.). The small scale of the tip allows for fabrication of a nanochannel on the same order of magnitude, yet larger, than the dimensions of the tip.
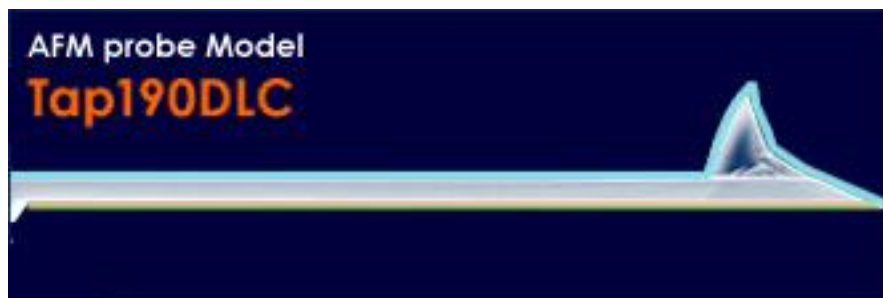

Figure 130: Tap 190 DLC AFM Probe Profile View

Single pass nanochannels scribed into a polymer substrate at varying forces determined the corresponding depth of cut, Figure 131. 6µm long scratches indicated a linear relationship between force and scratch depth. Five scratches in the polymer surface ranged between 10-30µN in 5µN

increments. Increasing the force applied during nanolithography results in channels of greater depth and width. The scratches were clean, but a common problem with nanolithography is material pile-up, observable as the bright spots on Figure 131. Material pile-up occurs because of material translocation rather than removal causing the material to deposit on the edge of the channels.
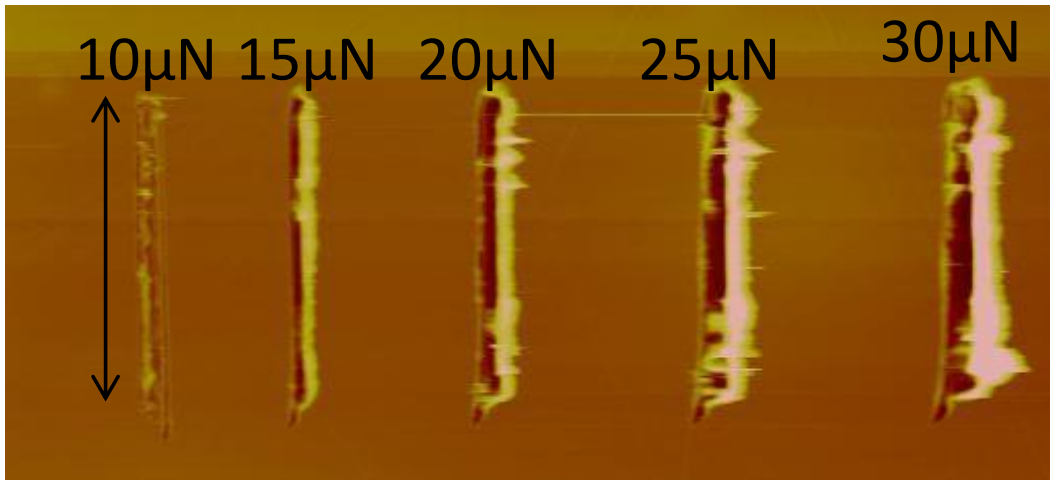

Figure 131: Nanolithography applied force variation test

Another test determined the repeatability of the nanolithography process. Figure 132 shows four single pass scratches made in a polymer surface under constant loading. For this particular material, the cutting depth was approximately 17 nm at a force of 10μN. Cutting depth measured in five different locations along the line showed some variability between measurements. The depth measurements in Figure 132(b) correspond to scratches I-IV in part Figure 132(a) respectively.
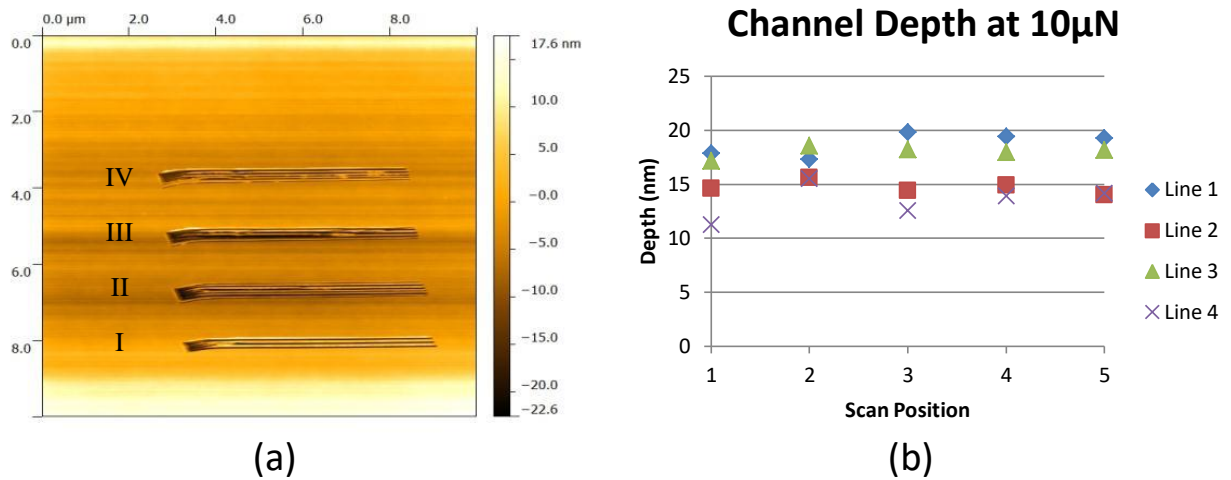
Figure 132: (a) Single pass nanolithography scratches (b) AFM depth of scratch

In preliminary work, this research studied the viability of AFM nanolithography to fabricate the nanochannel phase separator. Initial dimensions of the channels are 0.5μm wide, 30nm deep, and 6μm long, but are scalable based on AFM input parameters. Figure 133 shows that while channels width and depth were repeatable, the cross section was somewhat irregular. Additionally, tip wear becomes a factor with increasing number of channels scribed. Tips ploughed into hard surface like glass or silicon tend to lose their pyramidal structure resulting in a rounded profile (Killgore, & Geiss, & Hurley, 2011). Due to these irregularities and the potential unpredictable effect on fluid flow, this research proceeded with an alternate method of nanochannel fabrication.
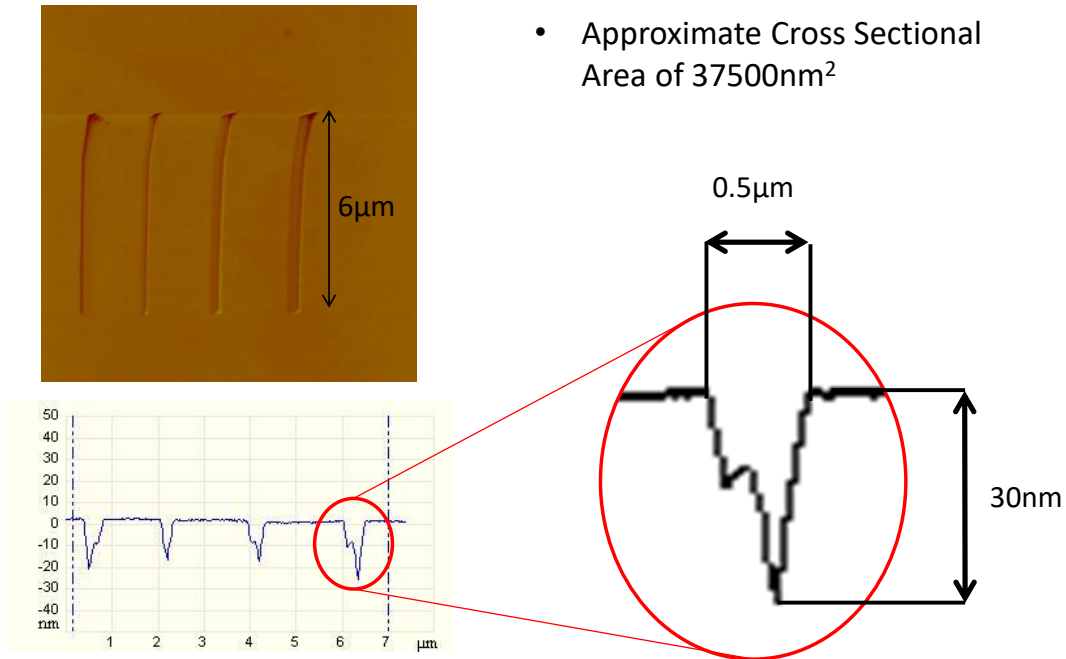
- Approximate Cross Sectional Area of 37500nm²

Figure 133: AFM nanolithography with v-channel profile

11.7.4 Packaging

11.7.4.1 Glass Drilling

Glass drilling is a very delicate process with how brittle glass is as a medium. Design of a peck drill process prevented swarf and minimized stress in the glass to avoid cracking. The peck drill is a repeating stepped process with the following order: a plunge into the substrate, slight retraction, and a pause. A computer numerical controlled mill regulated the feed rate and precision of the drilling process. The spindle speed was 2500 rotations per minute and the feed rate was 0.03 inches per minute. A 1/16 inch diamond drill bit allowed for a well-defined hole and a sacrificial glass slide proved necessary to prevent backside blowout when nearing completion of the drilling process.

11.7.4.2 Dicing

Wafer dicing is an essential step in the wafer fabrication process as it literally cuts down the wafer into a usable piece. Wafers used for this research were 4 inches in diameter while the devices were generally less than a half a square inch. Mounting a wafer to an adhesive backing on a metal frame prevents misalignment during cutting. After optical alignment, the dicing saw cuts the substrate into the desired square/rectangular sections. With a smaller form factor, the diced glass and silicon chips are wieldier for the nanochannel experiments.

11.7.4.3 Anodic Bonding

Anodic Bonding is common for bonding applications, as it is a "forgiving" process. The cleaner the surface the better the bond, but in a lower level cleanroom a bond is still achievable even with minor particles. Materials typically bonded anodically are silicon-silicon, silicon-glass, silicon- low temperature co-fired ceramics, and metal-glass. Bonding requires a clean flat surface on each mating surface. A high electrostatic field in addition to heat causes the diffusion of positive sodium ions (Na^+) in the glass towards the cathode. The movement of Na^+ results in a depletion layer in the glass adjacent to the silicon, which fills with drifting negative oxygen ions (O^-). The oxygen ions react with silicon to form an oxide layer, permanently bonding the glass and silicon.
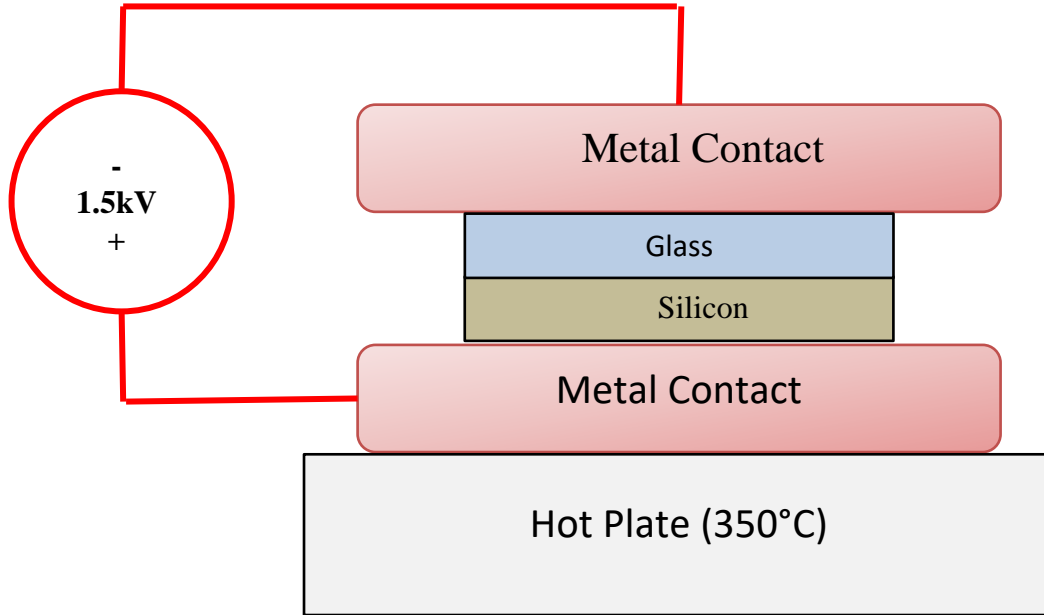
Figure 134: Ionic movement results in a strong bond between glass and silicon

An important note about anodic bonding is the importance of a matching coefficient of thermal expansion (CTE). With elevated temperatures, there is appreciable expansion in the material that contracts upon cooling. Two bonded materials with mismatched CTE's results in cracking and failure of the bond due to uncontrolled residual stresses. Borosilicate glass (Pyrex) and silicon have similar CTE's (3.3×10^{-6} K^{-1} and 2.7×10^{-6} K^{-1} respectively) making them a viable candidate for anodic bonding (Varshneya, 1993). Most microscope slides are made of soda lime glass that has a considerably different CTE (1×10^{-5} K^{-1}) from silicon and upon cooling results in a bond shown in the figure below (Varshneya, 1993).
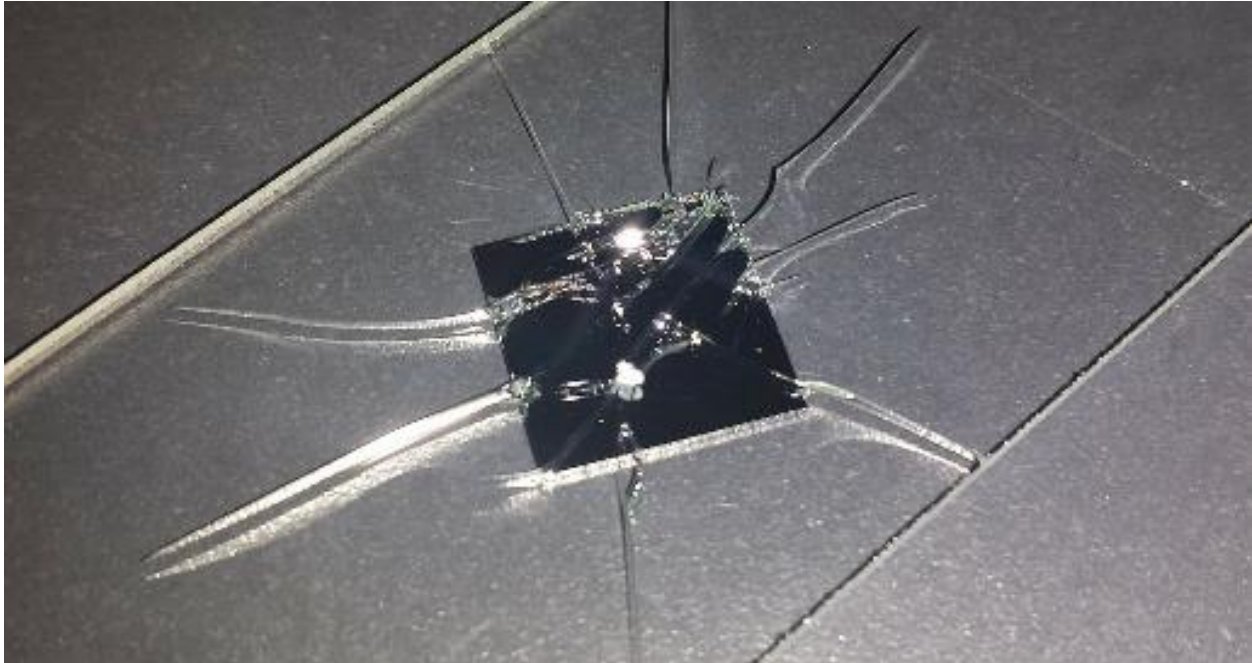
Figure 135: Mismatched coefficients of thermal expansion result in fracture of bonded glass.
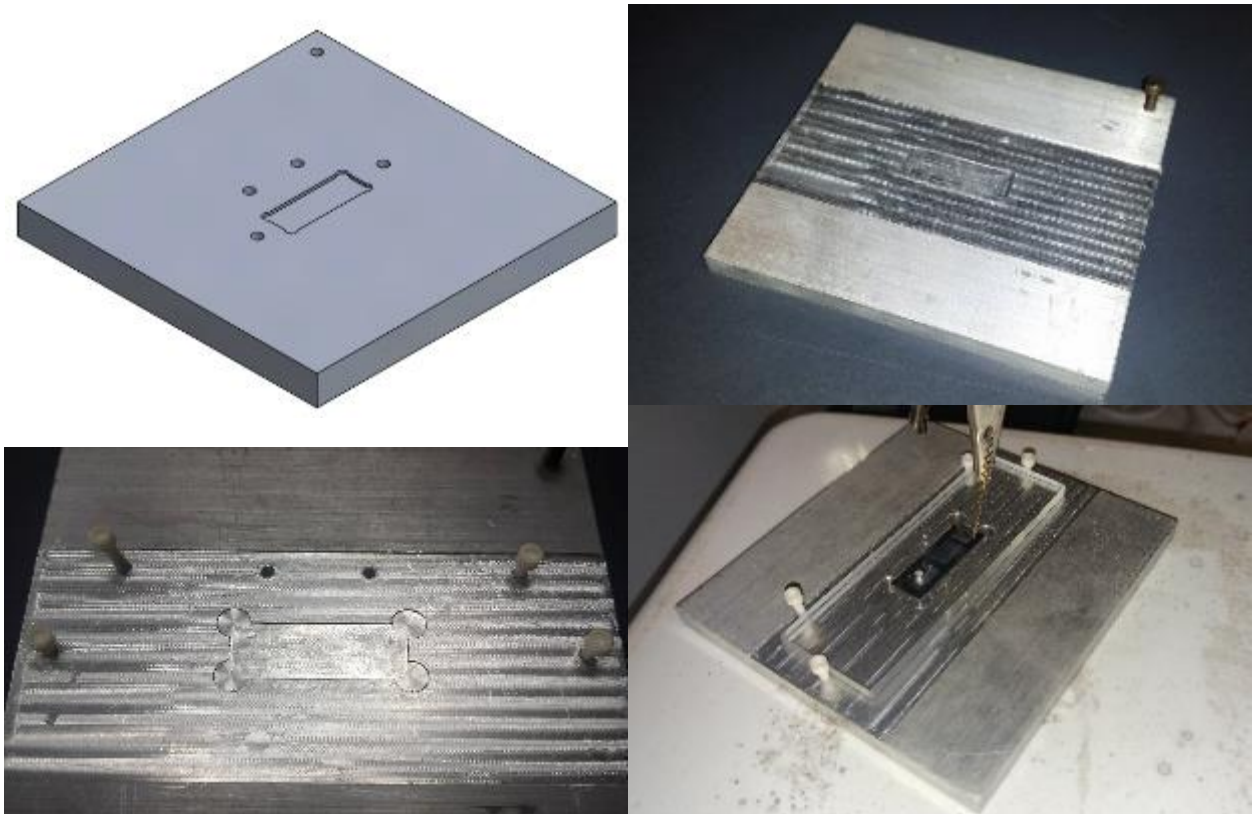

Figure 136: A bonding jig aligns the silicon chip to the glass slide for proper bonding.